

2021

Photodissociation of Gas-Phase Ions Investigated Using Combined Mass-Spectrometry, Ion- Mobility and Laser Spectroscopy

Samuel Jack Palmer Marlton

Follow this and additional works at: <https://ro.uow.edu.au/theses1>

University of Wollongong

Copyright Warning

You may print or download ONE copy of this document for the purpose of your own research or study. The University does not authorise you to copy, communicate or otherwise make available electronically to any other person any copyright material contained on this site.

You are reminded of the following: This work is copyright. Apart from any use permitted under the Copyright Act 1968, no part of this work may be reproduced by any process, nor may any other exclusive right be exercised, without the permission of the author. Copyright owners are entitled to take legal action against persons who infringe their copyright. A reproduction of material that is protected by copyright may be a copyright infringement. A court may impose penalties and award damages in relation to offences and infringements relating to copyright material.

Higher penalties may apply, and higher damages may be awarded, for offences and infringements involving the conversion of material into digital or electronic form.

Unless otherwise indicated, the views expressed in this thesis are those of the author and do not necessarily represent the views of the University of Wollongong.

Research Online is the open access institutional repository for the University of Wollongong. For further information contact the UOW Library: research-pubs@uow.edu.au

Photodissociation of Gas-Phase Ions Investigated Using Combined Mass-Spectrometry, Ion- Mobility and Laser Spectroscopy.

A thesis submitted in fulfilment of the requirements for the award of the degree:

Doctor of Philosophy

From:



UNIVERSITY
OF WOLLONGONG
AUSTRALIA

Molecular Horizons and School of Chemistry and Molecular Bio-Science

By

Samuel Jack Palmer Marlton

Supervised By
Prof. Adam J. Trevitt
Co-Supervised by
Prof. Todd Mitchell

2021

This page has been intentionally left blank.

Declaration

I, Samuel Jack Palmer Marlton, declare that this thesis is my own work and contains no material published by any other person unless due acknowledgment or reference has been made. This work has not been submitted for qualifications at any other university.

Samuel Jack Palmer Marlton

Acknowledgment

Thank you to my supervisor Prof. Adam Trevitt. The completion of this thesis would not have been possible without you. You have been supportive and enthusiastic while also giving me the opportunity to be creative and pursue scientific problems that I am passionate about. I have truly enjoyed my time during this project and a huge part of that is thanks to your supervision.

Thank you to my friends from the Laser Chemistry Lab at UOW. I would especially like to thank Ben “Franck-Condonyness” McKinnon, who I worked closely with throughout the project. Ben and I collaborated on all our projects and was especially critical to developing the pump-probe photodissociation setup. Thank you to Phillip Greißel, who acquired some of the pump-probe photodissociation results for indazoleH⁺ and benzimidazoleH⁺ (Chapter 6). Thank you to Boris “the Bear” Ucur, who was integral in getting the FAIMS running. Thank you to Brett “the Panda” Burns, Oisín “the Machine” Shiels, Paddy “Perfect Pitch” Kelly, and Jack “Goat-Life” Turner. Thank you to the past Laser Chemistry Lab Members that helped me along the way, Cameron Bright, Tassiani Sarreto, and Matthew Prendergast. Thank you to Alan Maccarone for your excellent technical support keeping our mass spectrometers alive. Thank you to our collaborators W.A. Donald, M.L. Coote and S.J. Blanksby for your help and insights.

Finally, I would like to thank my parents, my brother Jo, and my partner Loan. Your support means so much to me. A special thank you to Loan for being especially patient and supporting me.

Abstract

The photophysics and photochemistry of molecules are dependent on the interplay between multiple quantum states, which is challenging to model and especially challenging to control. This lack of control impedes development of photoinitiators, phototherapies and next-generation mass spectrometry tools. In this thesis, the influence of charge on the photodissociation of gas-phase ions is investigated using combined ion-mobility (field asymmetric ion-mobility spectrometry), photodissociation action spectroscopy and mass-spectrometry techniques along with quantum chemistry methods. Target molecules range from fundamental chromophores, photoinitiators and biologically relevant ions.

The electronic quantum states of Irgacure 2959 (a common photoinitiator) shift when complexed with a charged atom (H^+ , Li^+ , Na^+ , K^+ , Mg^{2+} , Zn^{2+} , or Ca^{2+}). The charged atom acts to establish an oriented electric field across the Irgacure 2959 chromophore, which shifts the electronic states. Photodissociation action spectra show that the first $^1\pi\pi^*$ state is red-shifted proportional to the electric field strength, with red-shifts $> 1\text{ eV}$. Quantum chemical calculations (SCS-CC2) show that a neighbouring $^3n\pi^*$, which facilitates the desired α -cleavage pathway, is blue-shifted by the oriented electric fields. The $^1\pi\pi^* - ^3n\pi^*$ energy gap is reduced, enhancing intersystem crossing rates as supported by detection of α -cleavage radical photoproducts. These results highlight the importance of photodissociation action spectroscopy that monitors photoproduct formation—not just photon absorption.

Quinazoline (1,3-diazanaphthalene) has two observable protonation sites. Protomer selection by ion-mobility thus selects the charge location and electric field orientation. Protomer assignment are provided by photodissociation action spectroscopy and MS-CASPT2 calculations. For 1-protonated quinazoline, the 0-0 transition of the 1L_a state is 27600 cm^{-1} and that of the 1B_b state is 42100 cm^{-1} . For 3-protonated quinazoline, the 0-0 transition of the 1L_a state is 26900 cm^{-1} and that of the 1B_b state is 41600 cm^{-1} . The protomers of quinazoline provide a benchmark system for protomer-specific kinetics and calculations.

Protonation isomers of (*S*)-nicotine are separated with field asymmetric ion-mobility spectrometry and analysed using photodissociation action spectroscopy. Protomer assignments are supported by quantum chemical calculations. Pyridine-protonated (*S*)-nicotine has a transition to a $^1\pi\pi^*$ state centred around 4.9 eV . Pyrrolidine-protonated (*S*)-nicotine has a

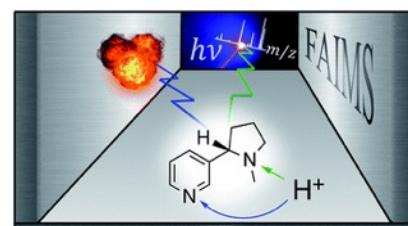
transition to a ${}^1\pi\pi^*$ state centred around 4.8 eV, as well as a shoulder on the low-energy side of the spectrum due to a transition to a ${}^1n\pi^*$ state.

A picosecond pump-probe photodissociation experimental arrangement is reported that probes excited-state dynamics. The role of the protonated N-N chemical group of indazole is targeted and compared to isomer that lacks this group, protonated benzimidazole. The ${}^1\pi\pi^*$ lifetimes of protonated indazole range from 390 ± 70 ps using 4.0 eV pump-photon energy and ≤ 18 ps using 4.6 eV. The ${}^1\pi\pi^*$ lifetimes of protonated benzimidazole are systematically longer, ranging from 4000 ± 1000 ps with a 4.6 eV pump-photon energy and 400 ± 200 ps with a 5.4 eV. The shorter excited-state lifetime of protonated indazole is attributed to a $\pi\sigma^*$ mediated elongation of the protonated N-N bond.

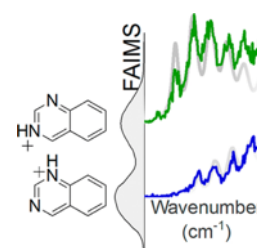
These results provide valuable new insights into the photochemistry and photophysics of protonated and ion-tagged chromophores.

Publications

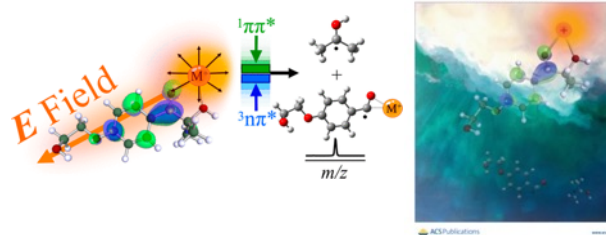
Marlton, S.J., McKinnon, B.I., Ucur, B., Maccarone, A.T., Donald, W.A., Blanksby, S.J. and Trevitt, A.J., **2019**. Selecting and identifying gas-phase protonation isomers of nicotineH⁺ using combined laser, ion mobility and mass spectrometry techniques. *Faraday discussions*, 217, pp.453-475.



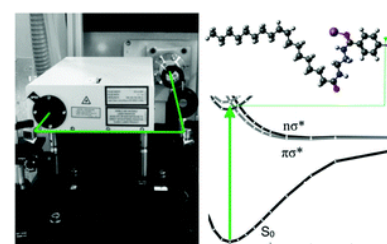
Marlton, S.J., McKinnon, B.I., Ucur, B., Bezzina, J.P., Blanksby, S.J. and Trevitt, A.J., **2020**. Discrimination between protonation isomers of quinazoline by ion mobility and uv-photodissociation action spectroscopy. *The journal of physical chemistry letters*, 11(10), pp.4226-4231.



Marlton, S.J., McKinnon, B.I., Hill, N.S., Coote, M.L. and Trevitt, A.J., **2021**. Electrostatically Tuning the Photodissociation of the Irgacure 2959 Photoinitiator in the Gas Phase by Cation Binding. *Journal of the American Chemical Society*, 143(5), pp.2331-2339.



Narreddula, V.R., McKinnon, B.I., **Marlton, S.J.**, Marshall, D.L., Boase, N.R., Poad, B.L., Trevitt, A.J., Mitchell, T.W. and Blanksby, S.J., **2021**. Next-generation derivatization reagents optimized for enhanced product ion formation in photodissociation-mass spectrometry of fatty acids. *Analyst*, 146(1), pp.156-169.



Marlton, S.J., McKinnon, B.I., Greißel, P., Shiels, O.J., Ucur, B. and Trevitt, A.J., **2021**. Picosecond Excited-State Lifetimes of Protonated Indazole and Benzimidazole: The Role of the NN bond. *The Journal of Chemical Physics*. 155(18), pp.184302

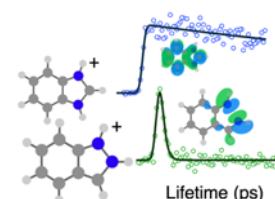


Table of Contents

Abstract.....	V
Publications.....	VII
Table of Figures.....	XI
Table of Tables.....	XVII
1. Introduction.....	1
1.1 How does UV-vis PD action spectroscopy work?.....	4
1.2 Constitutional Isomers.....	6
1.3 Assignment of Protomers.....	8
1.4 Room temperature UVPD.....	9
1.5 Cryogenic UVPD.....	11
1.6 Pump-Probe Photodissociation.....	14
1.7 UV Hole Burning.....	16
1.8 Ion Mobility Coupled with Photodissociation.....	17
1.9 Ion Mobility Coupled with Spectroscopy.....	18
1.10 Tandem IMS.....	21
1.11 Circular Dichroism.....	22
1.11 Final Thoughts.....	23
1.12 Thesis Outline:.....	24
2. Experimental Methods and Developments.....	44
2.0 Overview.....	44
2.1 List of Instruments.....	44
2.2 Photodissociation Action Spectroscopy.....	47
2.3 Field Asymmetric Ion Mobility Spectrometry.....	48
2.4 Picosecond Laser.....	53
2.5 Pump-Probe and Delay Stage.....	55
2.5.1 Pump-Probe Data Analysis.....	59
2.5.2 Pump Probe Validation:.....	61
3. Irgacure 2959 Clusters.....	68
3.1 Abstract.....	69
3.2 Introduction.....	70
3.3 Results and Discussion.....	72
3.3.1 Structures.....	72
3.3.2 Action Spectroscopy.....	73
3.3.3 $^1\pi\pi^*$ State Shift by M^+ and M^{2+} cations.....	75
3.3.4 Photodissociation Pathways.....	81
3.4 Conclusion.....	85

3.SI.0 Experimental	91
3.SI.0.0 Materials:.....	91
3.SI.0.1 Photodissociation Action Spectroscopy:.....	91
3.SI.0.2 Computational Details:.....	92
3.SI.1 Low m/z Threshold for Mass Spectra.....	93
3.SI.2 Orientation of Static Electric Field.....	93
3.SI.3 Additional Structure Energies and Assignments.....	94
3.SI.4 Single Wavelength PD Mass Spectra.....	97
3.SI.5 Additional Gaussian Fits to PD Action Spectra	98
3.SI.6 Coulomb's Law	99
3.SI.7 Centre of Mass to Cation Distances	99
3.SI.8 Orbitals relating to Figure 6	100
4. QuinazolineH⁺	117
4.1 Abstract.....	118
4.2 Introduction.....	119
4.3 Results and Discussion	120
4.4 Conclusion	127
4.SI.1 Detailed Experimental.....	132
4.SI.1.1 Materials.....	132
4.SI.1.2 Cylindrical FAIMS-Photodissociation Action Spectroscopy.....	132
4.SI.1.3 Computational Details.....	133
4.SI.2 FAIMS Ionograms spectra with varying dispersion voltages	134
4.SI.3 Photodissociation Mass Spectra	135
4.SI.4 Product Energies and Action Spectrum of Protonated Benzonitrile	136
4.SI.5 QZH ⁺ action spectrum without FAIMS separation.....	139
4.SI.6 Assignments of Transitions and Orbital Analysis.....	140
4.SI.6.1 CAM-B3LYP Orbitals	140
4.SI.6.2 MS-CASPT2//CASSCF Active Space	142
4.SI.6.3 Transition Dipoles	143
4.SI.7 Laser Power Dependence	144
4.SI.8 Action Spectra with Vibronic Assignments.....	145
4.SI.9 1QZH ⁺ Characterisation of Imaginary Frequency Coordinate.....	147
5. NicotineH⁺	154
5.1 Abstract.....	155
5.2 Introduction.....	156
5.3 Experimental.....	158
5.3.1 Materials	158

5.3.2 Cylindrical FAIMS-Mass Spectrometry	158
5.3.3 Planar-FAIMS-Mass Spectrometry	159
5.3.4 Photodissociation Action Spectroscopy.....	159
5.3.5 Computational Details	160
5.4 Results and Discussion	161
5.4.1 Calculations.....	161
5.4.2 Photodissociation and Collision-Induced Dissociation	162
5.4.3 Action Spectroscopy	165
5.4.4 Action Spectroscopy Compared to Calculations	167
5.4.5 FAIMS	171
5.5 Conclusions.....	176
5.SI NicotineH ⁺ Supporting Information.....	182
6. IndazoleH⁺ and BenimidazoleH⁺	191
6.1 Abstract.....	192
6.2 Introduction.....	193
6.3 Experimental.....	195
6.3.1 Photodissociation action spectroscopy mass spectrometry.....	195
6.3.2 Photodissociation pump-probe spectroscopy mass spectrometry.....	196
6.3.3 Computational Details	197
6.4 Results and Discussion	199
6.4.1 Photodissociation Action Spectroscopy.....	199
6.4.2 Pump-Probe PD	200
6.4.3 Minimum Energy Crossing Points and PES	203
6.5 Discussion	206
6.6 Conclusions.....	208
6.SI.1 Active Space for CASSCF calculations	216
6.SI.2 Additional Details for Linear and Curved Interpolation	218
6.SI.3 Additional Details for L _a and L _b State Character Analysis.....	219
6.SI.4 Photodissociation products and Pump-probe PD mass spectra.....	225
SI.5 Single Averages of Pump-Probe Photodissociation Plots.....	227
6.SI.6 MS-CASPT2 Deactivation pathways.....	230
7. Conclusions.....	252
7.1 The Effects of Charge	252
7.2 Experimental Results and Quantum Chemical Calculations	256
7.3 Implications and Future Directions.....	257

Table of Figures

Figure 1.1: UV PD action spectra for (a) quinolineH ⁺ and (b) isoquinolineH ⁺ ions. Adapted from Ref. ¹¹¹ . These spectra are both taken using a THERMO LTQ linear ion trap. A diagram of how a THERMO LTQ (c) or a Bruker AMAZON mass spectrometer (d) can be adapted to allow optical access to the ion trap is shown. (c) and (d) adapted from Dang, A., Korn, J.A., Gladden, J., Mozzone, B. and Tureček, F., 2019 . <i>Journal of The American Society for Mass Spectrometry</i> , 30(9), pp.1558-1564 Copyright 2019 American Chemical Society (Ref. ⁷⁵).....	7
Figure 1.2: UV PD action spectra for para-aminobenzoic acid (PABA) ions in different solvent following different PD products. The spectra correspond to two protomers co-populated in the ion trap, which are distinguishable by their different action spectra and PD products. Adapted from Ref. 29. ²⁹	10
Figure 1.3: (a) Cryogenic spectra of LFH ⁺ (black) compared with Franck-Condon simulations for two protomers (red and blue). Both protomers are assigned as contributing to the experimental spectrum. Adapted from Ref. 138. ¹³³ (b) Schematic diagram of the cryogenic BerlinTrap apparatus used to acquire these spectra. (b) Adapted from Ref. 82. ⁸²	13
Figure 1.4: (a) Cryogenic UV PD action spectra of tyrosineH ⁺ ions. (b) Pump-probe PD plots following the PD yield of tyrosineH ⁺ ions as a function of time delay between the pump and probe pulses (right). By setting the pump pulse to excite a vibronic peak for only one isomer, each isomer can be selected and its lifetime can be selectively probed. (a) and (b) adapted with permission from Soorkia, S., Broquier, M. and Grégoire, G., 2014 . <i>The Journal of Physical Chemistry Letters</i> , 5(24), pp.4349-4355. Copywrite 2014 American Chemical Society. ¹⁴⁹ (c) Schematic of experimental setup. (c) adapted with permission from Alata, I., Bert, J., Broquier, M., Dedonder, C., Féraud, G., Grégoire, G., Soorkia, S., Marceca, E. and Jouvét, C., 2013 . <i>The journal of Physical Chemistry A</i> , 117(21), pp.4420-4427. Copywrite 2013 American Chemical Society. ⁸³	15
Figure 1.5: (a) Some low energy isomers of noradrenaline-Na ⁺ . (b) Cryogenic UV-PD hole burning spectra of noradrenaline-Na ⁺ isomers. (c) Cryogenic UV-PD spectrum containing exhibiting the spectrum of all isomers generated by ESI. Figures (a), (b) and (c) reproduced from Ref. 175 with permission from the Royal Society of Chemistry. ¹⁷⁰ By setting a “probe” laser pulse to selectively excite one isomer, the PD from that isomer is detected. By introducing a second laser, an isomer selective spectrum can be generated whereby the spectrum dips when the second laser “burns” out the population of the isomer being selected by the “probe”. (d) Schematic of experimental setup. (d) Adapted from Ref. 84. ⁸⁴	16
Figure 1.6: (b) Drift IMS arrival time plots for C _n ⁺ clusters. Mass spectra of linear C ₉ ⁺ without laser irradiation (a) and after laser PD (c) and mass spectra of cyclic C ₉ ⁺ without laser irradiation (b) and after laser PD (d). Adapted from Ref. 175. ¹⁷⁵ (i) Schematic of experimental setup adapted from Ref. 93. ⁹³	18
Figure 1.7: (a) Drift IMS for benzocaineH ⁺ generated using acetonitrile or a mixture of methanol and water as the ESI solvent. (b) IRMPD spectra of the ion-mobility selected protomers and isomers of benzocaine-H ⁺ . (c) IRMPD mass spectra. (d) Calculated IR spectra for different benzocaineH ⁺ protomers. Structures and relative ground state energies for different protomers and isomers of protonated benzocaine (e). Schematic of the experimental setup (f). Adapted from Warnke, S., Seo, J., Boschmans, J., Sobott, F., Scrivens, J.H., Bleiholder, C., Bowers, M.T., Gewinner, S., Schöllkopf, W., Pagel, K. and von Helden, G., 2015 . <i>Journal of the American Chemical Society</i> , 137(12), pp.4236-4242. Original article is in the public domain. ¹¹⁹	20
Figure 1.8: (a) Arrival time distributions measured by the IMS2 drift region for <i>trans</i> azobenzene (that was selected by its mobility in the IMS1 region). The traces correspond to light off (black trace) and 440 nm photoaction (red dashes). (b) Action spectrum following the photoisomerization to the <i>cis</i> isomer as a function of wavelength. (c) Structures of protonated <i>cis</i> azobenzene and <i>trans</i> azobenzene. (d) Schematic of the tandem ion-mobility experimental setup. (a), (b) and (d) adapted with permission	

from Bull, J.N., Scholz, M.S., Carrascosa, E. and Bieske, E.J., **2018**. *Physical Chemistry Chemical Physics*, 20(1), pp.509-513. Copywrite 2018 American Chemical Society. ²¹⁸ 22

Figure 2.1: (A) Schematic of an example experimental setup containing the key experimental components deployed in this thesis. (B) Timing diagram of the experimental arrangement that ensures only the desired number of laser pulses enters the ion trap with each mass-spectrometer cycle. T is the time between laser repetitions, x is a programable delay and τ is the time delay between the pump and probe pulses. Figure B adapted from Hansen, C.S., Kirk, B.B., Blanksby, S.J., O’Hair, R.A. and Trevitt, A.J., **2013**. *Journal of The American Society for Mass Spectrometry*, 24(6), pp.932-940. Copywrite 2013 American Chemical Society. 46

Figure 2.2: Schematic of the cylindrical FAIMS used to separate ions (top) with dotted lines showing the paths of different types of ions (red, blue, and green). Zoomed in segment of the FAIMS showing the zig-zag trajectory that the ions take due to the asymmetric voltage waveform (bottom). A waveform for the asymmetric voltage is shown (blue line with yellow fill) where the height of this waveform determined by the dispersion voltage and a correction from the compensation voltage (red arrows at bottom). Example data is shown on the right, where the two protomers of quinazolineH⁺ are separated as a function of compensation voltage and appear as two peaks on a FAIMS ionogram. Data taken from References 7. ⁶ 49

Figure 2.3: (A) FAIMS ionograms of quinazolineH⁺ at several dispersion voltage values. (B) DV plot following the compensation voltage of peak throughput for 1-quinazolineH⁺ and 3-quinazolineH⁺ as a function of dispersion voltage. (C) Schematic illustration of characteristic DV plots for ion Types A, B, and C, which are indicative of the dynamic clustering and de-clustering properties of an ion. Data adapted from Reference 7. ⁶ 52

Figure 2.4: Schematic (not to scale) showing paths that the tuneable pump (blue) and 532 nm probe (green) travel. There is a lower-level, with dotted lines to represent the beam, connected by two periscopes to an upper-level, with solid lines to represent the beam path. (A) Top-down view with labels indicating the distances travelled on the lower level. (B) Top-down view zoomed in on the upper-level. (C) Diagonal view to show the three-dimensional layout of the top level and bottom level. The starting point is marked by **, which corresponds to the point that beams are split off. 56

Figure 2.5: Delay stage at three different positions, minimum distance (top), maximum distance (bottom), and an intermediate distance (middle). The delay stage can move a total of 220 mm, which corresponds to a change in beam path of 440 mm and a change in arrival time of light to the ion trap of 1430 ps. 58

Figure 2.6: Temporal overlap of the pump and probe pulses following electrical current signal measured by a white LED as a function of pump-probe delay. The wavelength of both pump and probe is 532 nm. 59

Figure 2.7: Pump-probe photodissociation mass spectra taken (A) with negative delay (532 nm probe before 270 nm pump), (B) zero delay (pump and probe irradiating ions simultaneously), and (C) positive delay (pump before probe). (C) shows a pump-probe PD plot following the intensity of the *m/z* 65 photoproduct as a function of time delay between the pump and probe pulse. Data from reference 19. ¹⁹ 61

Figure 2.8: (A) Measured time constants following the formation of the *m/z* 107 photofragment of protonated tyrosine with varying internal energies (given in cm⁻¹) above the 284.4 nm 0-0 transition. (B) Pump probe of protonated tyrosine following formation of the *m/z* 107 photoproduct. Data points plotted as circles in (A) are from references 18 and 21. ^{18, 21} 62

Figure 2.9: (A) Measured time constants following the formation of the *m/z* 107 photofragment of protonated *para*-dimethylaminopyridine with varying internal energies (given in cm⁻¹) above the 299.2 nm 0-0 transition. (B and C) Pump probe of protonated dimethyl aminopyridine following formation of the *m/z* 107 and *m/z* 80 photoproducts. Data points plotted as circles in (A) are from reference 20. ²⁰ 63

Figure 3.1: Alignment of transition dipoles for the $n\pi^*$ and $\pi\pi^*$ transitions for Irgacure as described by Hill *et al.* ¹¹ 72

Figure 3.2: Lowest energy structures for Irg-M⁺ and Irg-M²⁺-Irg complexes as calculated using the M06-2X method. 73

Figure 3.3: Photodissociation action spectra of Irgacure 2959 M^{Q+} complexes (M^{Q+} = H⁺, Li⁺, Na⁺, K⁺, Mg²⁺, Zn²⁺, Ca²⁺). Single Gaussian functions (blue) are fit to the lowest energy transition.

Additional Gaussian functions used for fitting are shown in Figure 3.15 of Supporting Information. Green sticks are the calculated vertical transition energies (E_{vert}) for each lowest energy structure using SCS-CC2 with bar heights equal to the oscillator strengths for each respective transition. 75

Figure 3.4: Dominant orbital transitions for the first $\pi \rightarrow \pi^*$ transition and $n \rightarrow \pi^*$ transition of neutral Irgacure 2959 (M06-2X/def2-TZVP) with predicted oscillator strengths (f). 77

Figure 3.5: Plot of $^1\pi\pi^*$ shift of Irg- M^{Q+} relative to neutral Irg calculated by TD-DFT versus (A) the experimental value from the photodissociation action spectra and (B) the shift as modelled by a point charge. 79

Figure 3.6: Energy shift of the transition to the first $^1\pi\pi^*$ state for Irg- M^{Q+} as a function of the electric field strength E . (A) Diamonds are the experimental peak position; error bars are the \pm HWHM of the fitted Gaussian. Black line is a linear regression fit to experimental data. (B) Triangles are the vertical excitation energies of the transition to the $^1\pi\pi^*$ state (M06-2X/def2-TZVP). The green trace is the $^1\pi\pi^*$ transition energy (M06-2X/def2-TZVP) under static electric fields of different strengths and the blue trace follows a $^1\pi\sigma^*$ state which interacts with the $^1\pi\pi^*$ state at higher E values (see text). 81

Figure 3.7: Two α -cleavage pathways where (A) the lowest energy singlet state is $^1n\pi^*$ character and follows and multistep mechanism and the simpler case (B) where the lowest energy singlet state is $^1\pi\pi^*$ character. 82

Figure 3.8: Vertical transition energies to the first $^1\pi\pi^*$ state (green rectangles), the first $^3n\pi^*$ state (blue rectangles), the first $^3\pi\pi^*$ state (red rectangles) and the first $^3n\pi^*$ state (purple rectangles) calculated using SCS-CC2/def2-TZVP. Values are compared to the lowest energy feature observed in the action spectra (black diamonds). 84

Figure 3.9: Alignment of the static electric field electric field applied to neutral Irg. The static electric field is applied exclusively along the x axis of neutral irgacure (XYZ coordinates in Section 3.SI.9). 93

Figure 3.10: Relative energies of Irg- M^{Q+} Structures calculated using M06-2X within 1 eV of the lowest ground state energy structure for each respective Irg- M^{Q+} ion. Structures with greater than 1 eV were not included. 94

Figure 3.11: Structure **E** barrier to form Structure **A** as calculated using M06-2X/def2-SVP. 95

Figure 3.12: Structure **B** barrier to form Structure **A** as calculated using M06-2X/def2-SVP. 96

Figure 3.13: Relative energies of Irg- M^{2+} -Irg structures calculated using M06-2X/def2-SVP. Irg- Ca^+ -Irg Structure **5** did not converge. 96

Figure 3.14: PD mass spectra for Irg- M^+ and Irg- M^{2+} -Irg ions taken at photon energies $\lambda = E_{\text{exp}}$ where E_{exp} is the energy at the centre of a Gaussian function fitted to the action spectrum (see main text). ... 97

Figure 3.15: Photodissociation action spectra of Irgacure 2959 M^{Q+} complexes ($M^{Q+} = \text{H}^+, \text{Li}^+, \text{Na}^+, \text{K}^+, \text{Mg}^{2+}, \text{Zn}^{2+}, \text{Ca}^{2+}$). Single Gaussian functions (blue) are fit to the lowest energy transition. Additional Gaussian functions for higher energy transitions are shown (red line) along with the sum of Gaussians (grey line). Green sticks are the calculated transition energies (E_{vert}) for each lowest energy structure using SCS-CC2/def2-TZVP. 98

Figure 3.16: Distance between M^{Q+} cation and the centre of mass of the chromophore (taken as the centre of mass of the labelled atoms which are the benzene carbons, C_7 , O_1 and O_2) as calculated using M06-2X for (A) Irg- M^+ and (B) Irg- M^{2+} -Irg. 99

Figure 3.17: The orbitals contributing to the $\pi\pi^*$ and $\pi\sigma^*$ transitions which undergo an avoided crossing in Figure 3.17 and Figure 6B of the main text. 100

Figure 4.1: (A) FAIMS ionogram following the m/z 131 signal of singly protonated quinazoline. Spectra are acquired using $\text{DV} = 5000$ V. The peaks observed at -8 V and -3 V are assigned to protomers of QZH^+ . Further evidence substantiating the FAIMS protomer assignment is obtained from photodissociation action spectroscopy. Figure 4.1(B): Dispersion plot following QZH^+ (m/z 131) in N_2 buffer gas. The green trace is assigned as 3QZH^+ and the blue trace is assigned as 1QZH^+ . Errors are 2σ as determined by fitting gaussians to FAIMS peaks. Dipole moments are calculated using CAM-B3LYP/aug-cc-pVDZ. 121

Figure 4.2: Photodissociation action spectra of QZH^+ with (A): no FAIMS selection, (B): FAIMS CV = -8 V and (C): FAIMS CV = -3V. 123

Figure 4.3: Photodissociation action spectra of QZH^+ at CV -8 V (A and E) and -3 V (C and G) following the yield of m/z 104 (thick line) and m/z 77 (thin line). Franck-Condon simulations of vibronic transitions to the S_1 ($^1\text{L}_a$) state for (B) 3QZH^+ and (D) 1QZH^+ and the S_5 ($^1\text{B}_b$) state for (F)

3QZH ⁺ and (H) 1QZH ⁺ are shown as sticks and also convoluted with Lorentzian functions (FWHM 220 cm ⁻¹ for S ₁ and 440 cm ⁻¹ for S ₅). CASSCF(12,11) calculations are shifted to match the experimental origin and vibrations scaled by 0.90 as described in the text.	126
Figure 4.4: Change in FAIMS ionogram following QZH ⁺ (<i>m/z</i> 131) with changing dispersion voltage.	134
Figure 4.5: Photodissociation mass spectra of QZH ⁺ at 360 nm (A and B) and 230 nm (C and D) where blue traces (top) correspond to -3 V compensation voltage (assigned as the 1QZH ⁺ protomer) and green traces (bottom) -8 V compensation voltage (assigned as 3QZH ⁺ protomer). The branching ratio of photoproducts (<i>m/z</i> 51: <i>m/z</i> 77: <i>m/z</i> 104) is 0.0:1.0:1.0 for 1QZH ⁺ and 0.0:1.0:4.0 for 3QZH ⁺ at 360 nm and 0.15:1.0:62.0 (1QZH ⁺) and 0.3:1.0:48.0 (3QZH ⁺) at 230 nm.	135
Figure 4.6: Photoproduct energies of most stable plausible <i>m/z</i> 104 and <i>m/z</i> 77 fragments. Energies calculated with DLPNO-CCSD(T)/aug-cc-pVDZ using MP2/aug-cc-pVDZ geometries and zero-point energy correction. Fragments shown in grey form hydrogen isocyanide. S ₁ and S ₅ photon energies (orange band) shown are origin energies for 3QZH ⁺ , which has a lower energy origin for both states and action spectra are plotted aligning with product energies.	136
Figure 4.7: (A) PD action scan of the photo-product <i>m/z</i> 104 formed from PD of QZH ⁺ protomers using 266 nm light. (B) PD action spectra of protonated benzonitrile. (C-F) EOM-CCSD/aug-cc-pVDZ vertical excitation energy calculations of the four lowest energy possible structures of the <i>m/z</i> 104 photo-product. The difference between the sum of the photo-product and HCN above QZH ⁺ is shown in eV under each structure as calculated with DLPNO-CCSD(T)/aug-cc-pVDZ using MP2/aug-cc-pVDZ structures and frequencies.	138
Figure 4.8: PD action spectra of QZH ⁺ without FAIMS separation (both protomers present). Black trace follows formation of <i>m/z</i> 104 and red trace follows formation of <i>m/z</i> 77.	139
Figure 4.9: Molecular orbitals for 1QZH ⁺ and 3QZH ⁺ as calculated with CAM-B3LYP/aug-cc-pVDZ.	140
Figure 4.10: Active space of 1QZH ⁺ and 3QZH ⁺ used for CASSCF(12,11) and CASPT2(12,11) calculations.	142
Figure 4.11: Transition dipole moments for the three lowest ¹ ππ* transitions of QZH ⁺ protomers as calculated with CAM-B3LYP.	143
Figure 4.12: Laser power dependence of QZH ⁺ at 303 nm (A) without FAIMS, (B) with -3 V compensation voltage, (C) with -8 V compensation voltage and at 240 nm (D) without FAIMS, (C) with -3 V compensation voltage, (D) with -8 V compensation voltage. Circles correspond to photoproduct signal of the <i>m/z</i> 104 photoproduct. Triangles correspond to photoproduct signal of the <i>m/z</i> 77 photoproduct. Light blue, light green and orange are fits of eq. 4.S1 to data following formation of the <i>m/z</i> 77 photoproduct. Dark blue, dark green and red lines are fits of eq. 4.S1 to data following formation of the <i>m/z</i> 104 photoproduct.	144
Figure 4.13: ¹ L _a region of QZH ⁺ including assignments of vibrational quanta. PD action spectra of (A) -8 V and (C) -3 V following the formation of <i>m/z</i> 104 (shown in (A) dark green and (C) dark blue) and <i>m/z</i> 77 (shown in (A) light green and (C) light blue). Franck-Condon simulations of vibronic transitions for (B) 3QZH ⁺ and (D) 1QZH ⁺ . Calculations were performed using CASSCF(12,11) and vibrations are offset by a scaling factor of 0.90. Transitions are fit with Lorentzians of FWHM 220 cm ⁻¹ . See Figure 4.15 for vibrations.	145
Figure 4.14: ¹ B _b region of QZH ⁺ including assignments of vibrational quanta. PD action spectra of (A) -8 V and (C) -3 V following the formation of <i>m/z</i> 104 (shown in (A) dark green and (C) dark blue) and <i>m/z</i> 77 (shown in (A) light green and (C) light blue). Franck-Condon simulations of vibronic transitions for (B) 3QZH ⁺ and (D) 1QZH ⁺ . Calculations were performed using CASSCF(12,11) and vibrations are offset by a scaling factor of 0.90. Transitions were fitted with Lorentzians of FWHM 440 cm ⁻¹ . See Figure 4.15 for vibrations.	146
Figure 4.15: Schematic illustration of the optically active vibrational modes of QZH ⁺ protomers with energies as calculated using CASSCF(12,11) with a scaling factor of 0.90.	147
Figure 4.16: (A and E) CAM-B3LYP, (B and F) CC2, (C and G) CASSCF, and (D and H) MS-CASPT2 energies along the (left) CAM-B3LYP L _a imaginary frequency and along the (right) analogous out of plane vibration as calculated with CASSCF(12,11).	147
Figure 5.1: Optimised structures for the lowest energy conformers of the two protomers of nich ⁺ . Their relative energies are given in kcal/mol as calculated using M06-2X/aug-cc-pVDZ.	161

Figure 5.2: (top) The CID and (bottom) PD ($\lambda=266$ nm) product mass spectra of nicH^+ (m/z 163). Spectra are normalised to the total ion count.	163
Figure 5.3: (A) The PD (266 nm) spectrum of nicH^+ with methanol (blue line) and acetonitrile (green line) as the ESI solvent. (B) A difference spectrum (methanol – acetonitrile). (C) Bias calculated for the seven major photoproduct ions as calculated using Eq. (5.1).	164
Figure 5.4: UVPD action spectra of nicH^+ generated by (A) ESI from acetonitrile with 1% formic acid and (B) methanol with 1% formic acid. The spectra follow the signal of the m/z 84 product ion (blue trace) and the m/z 132 product ion (green trace). Vertical bars represent vertical transition energies as calculated with CC2/cc-pVDZ based on geometries optimised with MP2/cc-pVDZ for PYRI- nicH^+ (blue bars) and PYRO- nicH^+ (green bars). Calculated transitions are all offset by -0.35 eV relative to their predicted values. Additional scans over the high energy portion of the spectra (<i>ca.</i> 5.5 eV) are appended to both (A) and (B).	166
Figure 5.5: Calculated natural transition orbitals (NTOs) for the major transitions using CAM-B3LYP/aug-cc-pVDZ. The charging proton is circled in red.	170
Figure 5.6: (A) Cylindrical-FAIMS ionogram of m/z 163 nicH^+ . (B) Cylindrical-FAIMS ionogram of photoproducts (PD 266 nm) for m/z 132 (green line) and m/z 84 (blue line). (C) FAIMS-modulated action spectra of photoproducts assigned to PYRO- nicH^+ (m/z 130 + 132 in green) and PYRI- nicH^+ (m/z 80+ 84 in blue) acquired at FAIMS CV voltages of -16.5 V (B) and -11.5 V (D). The square and diamond symbols link the compensation voltage value used for the respective action scans to the position on the FAIMS ionogram.	173
Figure 5.7: (A) PD mass spectra of nicH^+ with FAIMS CV voltages -11.5 V (blue) and -16.5 V (green). (B) Bar graph showing the bias values of several photo-products to formation from nicH^+ with a CV voltage of -11.5 V and -16.5 V.	174
Figure 5.8: Planar-FAIMS multiple-reaction monitoring scans following the formation of the m/z 84 CID product ions (red) from and m/z 132 (blue) which correspond to fragmentation from different promoters of nicH^+ (m/z 163) comparing acetonitrile (dashed-line) and methanol (solid line) as the solvent.	175
Figure 5.9: (A) CID spectra of planar-FAIMS separated nicH^+ protomers in a SCIEX 5500 with SelexION attachment. The green spectrum originates from ions isolated at 4.5 CV and are assigned as pyrrolidine protonated nicH^+ . The inverted blue spectrum originates from ions isolated at 6.5 CV and are assigned as pyridine protonated nicH^+ . (B) Bar graph showing the bias of several CID product ions to formation from nicH^+ with a CV voltage of 4.5 V and 6.5 V.	175
Figure 5.10: Structure of (<i>S</i>)-(-)-Nicotine including degrees of freedom which differentiate the conformers.	184
Figure 5.11: Optimised structures for twelve conformers of nicH^+ their relative energies in kcal/mol as calculated using M06-2X/aug-cc-pVDZ.	185
Figure 5.12: Electronic excitation energies of the first four states of protonated PYRI- nicH^+ (blue) and PYRO- nicH^+ (green) as the pyrrolidine ν_2 angle (A) or χ angle (B) was scanned. Transition energies were calculated using M06-2X/aug-cc-pVDZ. States of interest are plotted with bold lines. The -0.5 eV shift applied in the TD-DFT simulated electronic spectra was not applied to values presented in this table.	185
Figure 5.13: Calculated TD-DFT vertical transition energies for PYRI- nicH^+ (blue) and PYRO- nicH^+ (green). Three TD-DFT levels of theory were used (A) M06-2X, (B) CAM-B3LYP, (C) ω B97X-D, all with the aug-cc-pVDZ basis set. The transitions were fitted with Gaussian functions with a FWHM of 0.3 eV. Transitions have been offset -0.5 eV, as explained in the text. (D) Shows transitions calculated using CC2/cc-pVDZ from geometries which were optimised using MP2/cc-pVDZ. CC2 transitions have been offset by -0.35 eV as explained in the text.	186
Figure 5.14: Intensity photodissociation action plots showing the changing intensities of all nicH^+ photodissociation fragments between 60 m/z and 150 m/z . ESI solvents (A) acetonitrile and (B) methanol were used. The difference between image (A) and (B) is plotted in (C).	187
Figure 5.15: Normalised action spectra of fragments of nicH^+ after partial separation of the protomers of nicH^+ by FAIMS at -11.5 V (A) and -16.5 V (B).	188
Figure 5.16: Power dependence experiments showing change in 266 nm photo-fragment signal with increasing laser power for all photoproduct ions.	188

Figure 6.1: Schematic of the experimental setup.	196
Figure 6.2: UV Photo-dissociation action spectra of benzimidazoleH ⁺ (top) and indazoleH ⁺ (bottom) following loss of HCN (27 Da) to form the <i>m/z</i> 92 photoproduct. The black trace follows a rolling average of the three adjacent data points. Unshifted vertical transition energies calculated using CCSDR(3)/TZVP employing ω B97X-D/aug-cc-pVDZ geometries are shown (vertical bars).	200
Figure 6.3: Pump-probe photodissociation spectra of indazoleH ⁺ following the <i>m/z</i> 65 photoproduct. Pump photon energies are indicated. Probe photon energy is 2.33 eV (532 nm). Several traces are truncated to a maximum delay of 690 ps by experimental limitations early in the data collection. Multiple repeat experiments are combined and presented for data corresponding to pump energies of 4.0 eV (310 nm), 4.2 eV (295 nm) and 4.6 eV (270 nm). Individual experiments are presented in Figure 6.14 of Supporting Information.	201
Figure 6.4: Pump-probe photodissociation spectra of benzimidazoleH ⁺ following the <i>m/z</i> 65 photoproduct for all pump wavelengths except 4.6 eV (270 nm), which follows the 92 <i>m/z</i> fragment (solid circles). Pump photon energies are indicated. Probe photon energy is 2.33 eV (532 nm). Several traces are truncated to a maximum delay of 690 ps by experimental limitations earlier in the data collection. Multiple repeat experiments are combined and presented for data taken using 4.6 eV (270 nm) and 4.9 eV (255 nm) pump photons. Individual experiments are presented in Figure 6.15 of Supporting Information.	202
Figure 6.5: Plot of the decay lifetime of benzimidazoleH ⁺ (blue) and indazoleH ⁺ (green) as a function of pump photon energy. The dotted line indicates the instrument response function (IRF), which corresponds to the 13 ps laser cross-correlation.	203
Figure 6.6: Calculated potential energy surface interpolating between the optimised ground state of indazoleH ⁺ and several optimised crossing points. Panel (A) is constructed by linear interpolation between the ground state and an optimised ¹ L _a / ¹ $\pi\sigma^*$ (S ₂ /S ₁) MECP followed by linear interpolation to an optimised ¹ $\pi\sigma^*$ /S ₀ (S ₁ /S ₀) MECP. Ground state and MECP geometries were optimised using CASSCF(12,11)/cc-pVDZ and electronic energies were calculated using MS-CASPT2/cc-pVDZ. (B) MS-CASPT2 calculated key orbitals that contribute to the $\pi\sigma^*$ state for indazoleH ⁺ (isovalue = 0.05). The orbitals are presented with the ¹ $\pi\sigma^*$ /S ₀ MECP nuclear geometry, which is located in (A) by the arrow.	205
Figure 6.7: Calculated potential energy surfaces interpolating between the optimised ground state of benzimidazoleH ⁺ and an optimised ¹ L _b /S ₀ (S ₁ /S ₀) MECP. This surface is constructed by curved interpolation between the optimised S ₀ geometry and an optimised ¹ L _b /S ₀ (S ₁ /S ₀) MECP. Ground state and MECP geometries were optimised using CASSCF(12,11)/cc-pVDZ and electronic energies were calculated using MS-CASPT2/cc-pVDZ.	206
Figure 6.8: Active space for CASSCF(12,11)/cc-pVDZ calculations of indazoleH ⁺ . The s* and s orbitals on the N ₁ -H bond were rotated out for s* and s orbitals on either the N ₂ -H bond or the N ₂ -C ₃ bond to describe states involving these orbitals.	216
Figure 6.9: Active space for CASSCF(12,11)/cc-pVDZ calculations of benzimidazoleH ⁺	217
Figure 6.10: The π and π^* orbitals that contribute to the L _a and L _b transitions calculated using (A and B) CCSDR(3)/TZVP and (C) MS-CASPT2/cc-pVDZ//CASSCF(12,11)/cc-pVDZ. Dotted lines in (B) and (C) correspond to orbital contributions that are much weaker (amplitudes ~ 0.25) than those in bold (amplitudes > 0.5). The ordering of B ₁ (p) and A ₂ (p) orbitals in (A) have been swapped to simplify comparison to previous studies.	221
Figure 6.11: ω B2PLYP/aug-cc-pVTZ transition densities for L _a and L _b states of indazoleH ⁺ and benzimidazoleH ⁺ calculated in ORCA/4.2.1 using ω B97X-D/aug-cc-pVDZ geometries.	223
Figure 6.12: Bias between HCN loss and N ₂ loss for indazoleH ⁺ as a function of photon energy.	225
Figure 6.13: PD mass spectrum of indazoleH ⁺ using with no laser irradiation (black trace in A), with only 532 nm irradiation (green trace in A), with only 270 nm laser irradiation (black trace in B), and with 270 nm + 532 nm laser irradiation (green trace in B). PD mass spectrum of benzimidazoleH ⁺ using with no laser irradiation (black trace in C), with only 532 nm irradiation (green trace in C), with only 250 nm laser irradiation (black trace in D), and with 250 nm + 532 nm laser irradiation (green trace in D). The asterisk at <i>m/z</i> 105 indicates an artefact peak.	226
Figure 6.14: Pump-probe photodissociation spectra of indazoleH ⁺ following the <i>m/z</i> 65 photoproduct. A range of pump photon wavelengths were used with a probe wavelength of 2.33 eV (532 nm).	

Asterisk denotes measurement affected by the instrument response function (~13 ps). Several data sets are truncated to a maximum delay of 690 ps by experimental limitations earlier in the data collection. 227

Figure 6.15: Pump-probe photodissociation spectra of indazoleH⁺ following the *m/z* 65 photoproduct for all pump wavelengths except 4.6 eV (270 nm), which follows the 92 *m/z* fragment. A range of pump photon wavelengths were used with a probe wavelength of 2.33 eV (532 nm). Several data sets are truncated to a maximum delay of 690 ps by experimental limitations earlier in the data collection. 228

Figure 6.16: (A) Plot of the decay lifetime of benzimidazoleH⁺ (blue) and indazoleH⁺ (green) as a function of the photon energy relative to the calculated zero-point energy corrected 0-0 of the ¹L_a state—this value is 3.85 eV for indazoleH⁺ and 4.46 eV for benzimidazole and these values employed excited state geometries with C₁ symmetry. The dotted line indicates the instrument response function (13 ps). The 0-0 energies were calculated using CCSDR(3)/TZVP electronic energies and ωB97X-D/aug-cc-pVDZ geometries and vibrational frequencies. 229

Figure 6.17: Structures of CASSCF(12,11)/cc-pVDZ optimised MECP between excited states and the ground state with—where applicable—the non-bonding σ* orbital participating in the deactivation for benzimidazoleH⁺ (A) and indazoleH⁺ (B). The MS-CASPT2/cc-pVDZ energies of these S₁/S₀ MECPs are shown. 230

Figure 6.18: Calculated PESs interpolating between the optimised ground state of indazoleH⁺ or benzimidazoleH⁺ and several optimised crossing points. PESs show either linear interpolation between the ground state (GS) and an optimised S₂/S₁ MECP followed by linear interpolation of internal coordinates (LIIC) to an optimised S₁/S₀ MECP (A,C,E), or LIIC directly to an optimised S₁/S₀ MECP (B,D,G), or curvilinear interpolation of internal coordinates (curved LIIC) directly to an optimised S₁/S₀ MECP (F,H). Details of curvilinear interpolation are given in Section SI.3. Ground state and crossing point geometries were optimised using CASSCF(12,11)/cc-pVDZ and electronic energies were calculated using MS-CASPT2/cc-pVDZ. The first two ³ππ* triplet states are thin, blue dotted lines and the first ³πσ* state is represented as purple dotted lines. 232

Figure 7.1: Summary of photodissociation action spectra presented in this thesis. From top to bottom: 3-quinazolineH⁺, 1-quinazolineH⁺, indazoleH⁺, benzimidazoleH⁺, PYRI-nicotineH⁺, PYRO-nicotineH⁺, irgacure-K⁺, irgacure-Na⁺, irgacure-Li⁺, irgacure-H⁺, irgacure-Mg²⁺-irgacure, irgacure-Ca²⁺-irgacure, and irgacure-Zn²⁺-irgacure. 253

Figure 7.2: Differences in electron density in the ground state and excited state. Purple regions indicate decreased electron density in the excited state and orange regions indicate increased electron density in the excited state. Arrows emphasise the net direction of electron density transfer between the ground and excited state. Calculations employed the SCS-CC2/def2-SVP method. 254

Figure 7.3: Electrostatic potential surfaces for 1QZH⁺, 3QZH⁺, benzimidazoleH⁺ and indazoleH⁺. Calculated using ωB97X-D/def2-TZVP, with an iso-value of 0.004 and a range of 0.0 (red) to 0.25 (blue), where darker blue indicates regions of greater positive potential. 256

Figure 7.4: Comparisons between ωB97X-D and experiment (green), SCS-CC2 and experiment (blue) and ωB97X-D and SCS-CC2 (purple). The data are presented with a y = x function as a guide for where the data points would lie if there was perfect agreement (grey dotted line). Additionally, the data points are fit with a linear function that has gradient = 1 and a y offset (solid lines). 257

Figure 7.5: Structures of thioxanthone-M⁺ and acetophenone-M⁺ 258

Figure 7.6: Structures of MTT, protonated phenyl-pyrazole, protonated 7-azaindazole protomers and some allopurinol protomers. 259

Figure 7.7: Structures of distonic radical ion protomers of protonated dehydro-quinazoline. 260

Table of Tables

Table 2.1: Some key parameters for the two mass spectrometers used in this research. 47

Table 2.2: Key FAIMS parameters used in chapters 4 and 5. 53

Table 2.3: Key parameters for different lasers employed in this thesis. 54

Table 3.1: Centre (E_{exp}) and half width half maximum (HWHM) of Gaussian fit to experimental data. Vertical excitation (E_{vert}) energies and oscillator strengths (f) to the first $^1\pi\pi^*$ state for each ion as calculated using SCS-CC2 and TD-DFT. DNC denotes that the TD-DFT calculation did not converge. ^a SCS-CC2 calculations employed the def2-TZVP basis set for Irg- M^+ ions and the def2-SVP basis set for Irg- M^{2+} -Irg ions.	76
Table 3.2: Calculated distances between chromophore centre of mass (COM) and charged atom, electric field strength (V/M) calculated using Coulomb's law, transition energy (E_{exp}) shift determined from the PD action spectrum, TD-DFT vertical transition energy shifts (E_{vert}) and E_{vert} calculated by replacing M^{Q+} with a point charge.	78
Table 3.3: Energy gap between the (vertical) $^1\pi\pi^*$ and $^3n\pi^*$ states as calculated using SCS-CC2/def2-TZVP. Experimental ratio between photo-dissociation leading to α -cleavage ($\phi_{\alpha\text{-cleavage}}$) and total observed photo-dissociation yield (ϕ_{products}). Experimental ratio between photo-dissociation leading to α -cleavage ($\phi_{\alpha\text{-cleavage}}$) and total observed depletion of the precursor ion yield ($\phi_{\text{depletion}}$).	85
Table 3.4: Low m/z cut-off values for PD mass spectra of Irg- M^+ and Irg- M^{2+} -Irg ions.	93
Table 3.5: TD-DFT vertical excitation energies (E_{vert}) for the first state calculated to have oscillator strength ($f > 0.01$) of Irg- M^+ structures within 0.4 eV of the minimum energy structure A compared to experimental results (E_{exp}). Calculations employed the M06-2X/def2-TZVP level of theory. Energies of Structure A are shown in bold.	95
Table 4.1: 3QZH ⁺ : Experimental adiabatic transition (0-0) energies, MS-CASPT2 adiabatic transition energies, and CAM-B3LYP adiabatic and vertical transition energies, oscillator strength, and key orbital contributions (> 20 %). H = HOMO, L = LUMO. Structures with imaginary frequencies are shown in square brackets. The * denotes states that did not converge.	125
Table 4.2: 1QZH ⁺ : Experimental adiabatic transition (0-0) energies, MS-CASPT2 adiabatic transition energies, and CAM-B3LYP adiabatic and vertical transition energies, oscillator strength, and key orbital contributions (> 20 %). H = HOMO, L = LUMO. Structures with imaginary frequencies are shown in square brackets. The * denotes states that did not converge.	125
Table 4.3: Calculated vertical transition energies with key orbital contributions of 3QZH ⁺ using CAM-B3LYP. H = HOMO, L = LUMO.	141
Table 4.4: Calculated vertical transition energies with key orbital contributions of 1QZH ⁺ using CAM-B3LYP. H = HOMO, L = LUMO.	141
Table 5.1: Calculated vertical transition energies and key orbitals for the (<i>W</i> , <i>trans</i> , <i>anti</i>) PYRO-nicH ⁺ using CC2/cc-pVDZ and CAM-B3LYP/aug-cc-pVDZ. H = HOMO and L = LUMO.	168
Table 5.2: Calculated vertical transition energies and key orbitals for (<i>S</i> , <i>trans</i> , <i>anti</i>) PYRI-nicH ⁺ using CC2/cc-pVDZ and CAM-B3LYP/aug-cc-pVDZ. H = HOMO and L = LUMO.	169
Table 5.3: Relative energies of different conformers of PYRO-nicH ⁺ relative to the PYRI-nicH ⁺ (<i>S</i> , <i>trans</i> , <i>anti</i>) global minimum in kcal/mol as calculated with four different DFT levels of theory with the aug-cc-pVDZ basis set as well as the MP2 method with the cc-pVDZ basis set. Omitted values converged to another structure upon optimisation. Labels are according to the naming system implemented by Yoshida <i>et al.</i> [REF 34 in main text] and represents (pyrrolidine ring conformational region, relative placement of the methyl group to the pyridine ring, χ angle region).	182
Table 5.4: Relative energies of different conformers of PYRI-nicH ⁺ relative to the PYRI-nicH ⁺ (<i>S</i> , <i>trans</i> , <i>anti</i>) global minimum in kcal/mol as calculated with four different DFT levels of theory with the aug-cc-pVDZ basis set as well as the MP2 method with the cc-pVDZ basis set. Omitted values converged to another structure upon optimisation. Labels are according to the naming system implemented by Yoshida <i>et al.</i> [REF 34 in main text] and represents (pyrrolidine ring conformational region, relative placement of the methyl group to the pyridine ring, χ angle region).	183
Table 5.5: Experimental and Calculated vertical transition energies for the (<i>W</i> , <i>trans</i> , <i>anti</i>) isomer of PYRO-nicH ⁺ . TD-DFT calculations were performed with M06-2X and ω B97X-D with the aug-cc-pVDZ basis set.	183
Table 5.6: Experimental and Calculated vertical transition energies for the (<i>S</i> , <i>trans</i> , <i>anti</i>) isomer of PYRI-nicH ⁺ . TD-DFT calculations were done with M06-2X and ω B97X-D with the aug-cc-pVDZ basis set.	184
Table 6.1: Amplitudes of orbital contributions to the $L_a \rightarrow S_0$ and $L_b \rightarrow S_0$ states of cnH^+ and nnH^+ as calculated using CCSDR(3)/TZVP. Where relevant, ω B2PLYP/aug-cc-pVTZ amplitudes are shown	

in brackets and MS-CASPT2/cc-pVDZ amplitudes for corresponding configurations are shown in square brackets. Contributions with values less than 0.20 are omitted. 222

Table 6.2: Vertical transition energies and adiabatic transition energies for the 1L_a —both planar and OOP—and 1L_b states of benzimidazoleH⁺ and indazoleH⁺ (the OOP 1L_b state optimisations did not converge). All values are in eV. ^a Planar adiabatic transitions calculated with MS-CASPT2 employed optimised geometries and reference wavefunctions using CASSCF(10,9)/cc-pVDZ with only the full π system active space. ^b The symmetry for MS-CASPT2 vertical transitions is A' due to non-symmetric orbitals in the active space slightly breaking C_{2v} symmetry. Note that all planar “adiabatic” geometries give imaginary frequencies and do not correspond to true minima. The OOP adiabatic for the 1L_b state of benzimidazoleH⁺ did not converge and so 1L_b OOP adiabatic energies are not included. 224

Table 6.3: MS-CASPT2/cc-pVDZ energies of the S_1/S_0 MECP and maximum energy along the PESs towards optimised CIs for indazoleH⁺. All values are in eV. 231

Table 6.4: MS-CASPT2/cc-pVDZ energies of maximum barrier energy along the PESs towards optimised CIs for benzimidazoleH⁺. All values are in eV. 231

Table 7.1: Summary table of neutral and cationic ions spectroscopically probed in this thesis. 255

This page has been intentionally left blank.

INTRODUCTION

1. Introduction

The presence and proximity of charge are known to affect photochemistry in a variety of contexts. For example, when DNA nucleobases are protonated¹ their excited state lifetimes are altered depending on the protonation site,² which can in turn dictate the extent of DNA damage.³ In protein environments, charge affects the fluorescence emission energy as well as yield, this is observed for tryptophan excited states.⁴ Also, intramolecular charges have been recently flagged as promising agents for generating electric fields to tune photochemistry.⁵⁻⁹

The use of oriented electric fields (OEFs) as a method to control chemical reactivity has taken off in recent years.¹⁰⁻¹⁵ This interest arises from evidence that suitably oriented OEFs can provide systematic control over chemical reactivity—for example, by lowering the energy barrier of rate-limiting transition states.^{16, 17} Although most of these studies investigate OEF perturbing ground state molecules, the prospects for OEFs to be a controllable parameter in excited-state photochemical reactivity is also highlighted by computational predictions for photochemical CO₂ capture,⁵ photoisomerism,^{6, 7} and photoinitiators.^{8, 9}

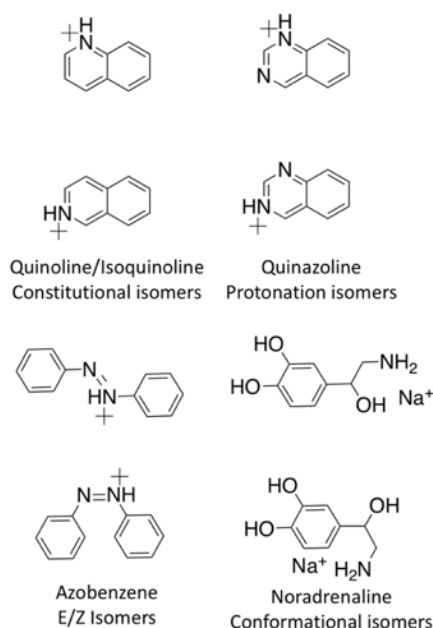
There is a pressing need for new photoinitiators. Currently, mercury lamps in industry are being phased out in accordance with the Minamata convention.¹⁸ Thus, new photoinitiators must have good photochemical efficiency and appropriate excitation energies for next generation LED sources. With the wide variety of LED sources, new photoinitiators can be tailored to match the LED output more precisely. This can reduce the damage to co-located molecules—particularly relevant for biological photoinitiator applications. It is predicted that appropriate OEFs can optimise the excitation energy of photoinitiators and optimise the energy gap between key excited states to optimise photochemical efficiency.^{8, 9} To realise these goals, and verify these predictions, methods for experimentally controlling the orientation and strength of these electric fields are required.

Experimental studies have reported OEF effects on the photoproperties of photoinitiators using metal ions in solution.^{19, 20} The deployment of OEF strategies in solution is a crucial step towards OEFs being implemented for practical use. However, homogeneous solution-phase studies are complicated by solvent-shell orientation, hydrogen bonding affecting excited states, and cation binding site variations. Improved control over the strength and orientation of OEFs

is desirable to verify OEF models and help guide future applications of OEFs to control photochemistry.

In this thesis, combined mass spectrometry, ion-mobility and photodissociation (PD) techniques are employed to investigate the effects of charge and charge location on the spectroscopic and photophysical properties of ions. Because an OEF can be applied to a molecule by adding a charge tag (either covalently or non-covalently),^{5-9, 19, 20} mass spectrometry is an appropriate choice for investigating OEFs. This thesis also reports combined mass spectrometry, ion-mobility and photodissociation methods that have been developed for distinguishing and characterising charged isomers. This allowed detailed study of the impact of orientation of the electric field generated by the charge. This introduction will, therefore, focus on combined mass-spectrometry and photodissociation techniques—especially UV/vis (PD) action spectroscopy as well as combinations of ion-mobility and UV/vis photodissociation action spectroscopy—with particular emphasis on distinguishing isomers and characterising their photoproperties.

In the field of mass-spectrometry the existence of isomers is considered to be a major bottleneck, in particular for fields like metabolomics,²¹ lipidomics,²² and mass spectrometry imaging.²³ Since the basis of mass spectrometry is the measurement of ions by their mass to charge ratio, to distinguish between isomers requires additional strategies. Over the decades, innovative strategies have been deployed to distinguish isomers including ion-mobility methods,²⁴ collision-induced dissociation,^{25, 26} ion-molecule reactions like ozone induced dissociation,^{27, 28} and photodissociation.^{29, 30} Since whole research fields are devoted to conformational analysis there have been enormous advances in this area, particularly coupling ion mobility and mass spectrometry. Nevertheless, structural isomers present significant challenges and within this isomer grouping there is huge diversity.



Scheme 1.1: The constitutional isomers quinolineH⁺, isoquinolineH⁺. The protomers of quinazolineH⁺. The E/Z isomers of protonated azobenzene. The conformational isomers of sodium-noradrenaline complexes.

In the 1970s, reports emerged of UV and visible tuneable laser photodissociation of mass selected ions as a method that can distinguish isomers. For example, the isomers of C₇H₈⁺ (radical cations of toluene, cycloheptatriene, and norbornadiene) were reported to have different electronic PD action spectra.³¹ At that point in time, lasers generally lacked broadband UV-Vis tunability so pioneering action spectroscopy experiments coupled arc-lamp/monochromator light sources with ion cyclotron resonance ion trap mass spectrometry.³¹⁻³³ Works by Dunbar and Beauchamp groups are landmark and remain heavily cited.^{31, 32, 34, 35}

Since these pioneering experiments, there have been two major technical advancements that have drastically broadened the scope and application of PD action spectroscopy, these are ESI/MALDI ionisation sources and tuneable UV-VIS mid-band OPO laser sources. Use of ESI/MALDI has become widespread amongst biological, chemical and physical sciences because they enable the study of an enormous variety of ions in the gas phase. Many authoritative reviews exist on these topics.³⁶⁻³⁸ The second key development is the tuneable mid-band OPO laser, which is now widely available, moderately priced (for a table-top laser systems) and becoming increasingly turn-key. These systems are typically pulsed, with repetition rates commonly (but not limited to) 10–100 Hz and pulse widths *ca.* 5–10 ns and also available in picosecond pulse-width. The technical advantages of these OPO laser systems

are the broadband tunability and good pulse energies (mJ), where scanning from NIR through the visible and into the UV is relatively straightforward. High energy cut offs are typically around 210–225 nm, depending on the system. However, various vendors offer a range of other options including deeper UV extensions, higher repetition rates of on the order of kilohertz, high pulse energies on the order of joules, IR wavelength extensions, small footprint, “rugged” housings and more. There are some limitations and downsides to common OPO laser systems. For example, OPO laser systems have pulse energy that vary significantly over large scanning ranges and beam output can be rather divergent with irregular beam spot energy distribution. These factors can be problematic when power normalisation is required for scans over large wavelength ranges. Ultimately, however, OPO laser systems provide robust light sources for acquiring PD action spectra of gas-phase ions.

A major portion of the current research in photodissociation spectroscopy utilises UV-vis PD action spectroscopy coupled with ion traps, both room temperature and cryogenic. Ion-mobility strategies such as drift mobility and field asymmetric ion mobility for pre-selection of ions. In this introduction some advantages of these techniques are discussed, as well as what they have taught us about a variety of isomer ions. In targeting the scope of this introduction, IR PD techniques, such as IRMPD³⁹⁻⁴⁶ and IRPD,⁴⁷⁻⁵¹ and *m/z* selected photoelectron (PE) spectroscopy⁵²⁻⁵⁵ are not covered in detail with the exception of a few select examples. The interested reader is directed to these corresponding references. This introduction also focuses on ions generated using ESI. Although other techniques are used to generate ions for action spectroscopy, for example electron impact ionisation⁵⁶⁻⁵⁸ and supersonic expansion followed by photoionisation.⁵⁹ Finally, this introduction is not an extensive review of all PD action spectroscopy or ion mobility. The reader is directed to the following reviews on for ion-mobility,^{24, 60-62} the history of ion spectroscopy,^{31, 33, 63} advances and developments in ion spectroscopy,⁶⁴ UV-vis photodissociation action spectroscopy,⁶⁵ lasers and mass spectrometry for structure determination,⁶⁶ conformer resolved photoinduced dynamics for neutral and ionic peptides,⁶⁷ action spectroscopy of DNA radical cations,⁶⁸ gas-phase dynamics including isomer selective spectroscopy,⁶⁹ biological relevant ions with room temperature⁷⁰⁻⁷² and cryogenic ion spectroscopy.^{73, 74}

1.1 How does UV-vis PD action spectroscopy work?

Typically, UV-vis PD action spectroscopy is a method that measures the yield of photoproduct ions as a function of photon energy of selected precursor ions. Although details can vary, the procedure is generally as follows. The use of ESI in the source serves two purposes, to transfer the sample into the gas phase and to ionise the target ions, usually *via* protonation or deprotonation. Charge can also be provided by complexation with cations (*e.g.* H⁺, Na⁺, K⁺, NH₄⁺) or anions (*e.g.* Cl⁻, I⁻) or, alternatively, the target species may be a native cation or anion. At some point, *m/z* isolation of the target ions is performed often in a quadrupole ion guide or an ion trap. This is a vital step that removes interference from other ions and provides an essentially background-free baseline for detecting product ions. The target ions are then irradiated with laser photons. Following this, a mass spectrum is recorded and the intensity of any product ions resulting from the laser is measured against the total ion count. This sequence may be repeated many times depending on the signal to noise ratio desired. The laser wavelength is then changed, at the desired step size, and the process is repeated. At each laser wavelength, the PD yield is recorded either as the sum of all the photoproducts or a single *m/z* photoproduct ion's spectrum can be plotted as a subset. Individual product ions can have different PD action spectra, which might signify different photodissociation pathways for a precursor ion or that there are different populations of precursor ions (*e.g.* isomers). The PD yield must also take into account any ions that are not laser dependent and variations in laser energy.

There have been a range of strategies and configurations of action spectroscopy, including commercial⁷⁵⁻⁷⁹ and custom built ion-traps⁸⁰ or commercial triple-quadrupole MS arrangements,⁸¹ cryogenic ion traps,^{74, 82-89} as well as other designs that emphasise ion mobility selection⁹⁰⁻⁹³ or ion storage rings.^{94, 95} All these arrangements allow laser access to selected ions to induce photodissociation. Some of these setups include ion mobility stages, which will be discussed in detail later.

Photodissociation action spectroscopy is an indirect spectroscopic method. For ions, direct gas-phase absorption measurements are not routinely possible since gas-phase ions are typically available in relatively low number density compared to solution phase systems. The number of ions that can be generated by ESI—and subsequently selected in the mass spectrometer—can range from tens of millions down to a few tens (much lower than the number density in solution phase absorption, which is normally well above 10¹² molecules *per* cubic centimetre or nanomolar concentrations). For a gas phase ion packet, if there are only ten photons being

absorbed from a laser pulse made up of trillions of photons, then the reduction of photon flux due to absorption (relative to the photon flux of the initial pulse) will be practically unmeasurable. Alternatively, PD action spectroscopy relies on detection of photoproduct ion at different m/z value from the selected precursor ions, which is essentially a background-free measurement. Weak dissociation events are easily recorded even if only a few product ions are generated for a MS cycle. PD action spectroscopy, therefore, generates a count of ten on a background signal of zero, whereas gas phase absorption would generate a count of ten on a background of trillions.

Another inherent advantage of PD action spectroscopy using mass spectrometry is that it introduces an element of selection and control because it allows for the selection of ions by their m/z ratio. As such, background signal and contamination are often eliminated. Of course, this m/z selection alone does not allow for selection of isomers or isobaric contaminants.

Although separation and identification of isomers is an active area of research development, one strategy for addressing isomer separation—namely, ion mobility separation of isomers—will be discussed later. Another notable method for separation is chromatography, which was recently coupled to IRMPD spectroscopy.^{43, 96, 97} Even though PD action spectroscopy and ion mobility separation can be well used in combination, spectroscopic techniques can provide a detailed characterisation of isomers.

1.2 Constitutional Isomers

There are many examples of UV/vis PD action spectroscopy studies that interrogate isomeric ions separated before introduction to the mass spectrometer. In this context, separation means that pure samples of the structural isomers are available so—provided no isomerisation occurs upon delivery of ions into the laser interaction region—these isomers can be investigated and compared. Such studies include substituted pyridines,⁹⁸⁻¹⁰¹ azaindoles,^{102, 103} diazabenzenes,^{104, 105} and diazanaphthalenes,¹⁰¹ as well as for anionic systems: deprotonated azaindole,¹⁰³ nitrophenolate ions,¹⁰⁶⁻¹⁰⁸ molecular-iodide clusters,¹⁰⁹ and the isomers protonated quinoline and isoquinoline.^{110, 111}

A simple starting point is the case of the protonated quinoline and isoquinoline structural isomers. The PD action spectra for the $S_1 \leftarrow S_0$ transitions of isoquinolineH⁺ and quinolineH⁺

are shown in Figure 1.1. These spectra are constructed by tracking the three major product ions, which are the same for both precursor ions.

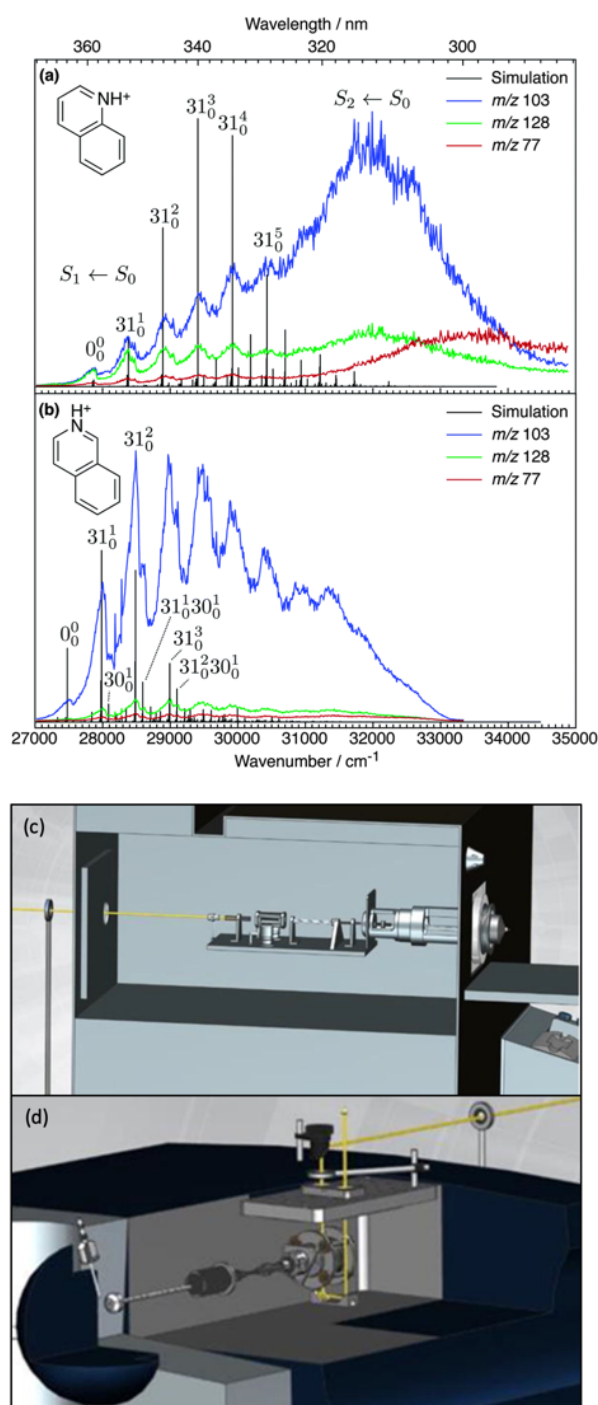


Figure 1.1: UV PD action spectra for (a) quinolineH⁺ and (b) isoquinolineH⁺ ions. Adapted from Ref. 111.¹¹¹ These spectra are both taken using a THERMO LTQ linear ion trap. A diagram of how a THERMO LTQ (c) or a Bruker AMAZON mass spectrometer (d) can be adapted to allow optical access to the ion trap is shown. (c) and (d) adapted from Dang, A., Korn, J.A., Gladden, J., Mozzone, B. and Tureček, F., **2019**. *Journal of The American Society for Mass Spectrometry*, 30(9), pp.1558-1564 Copyright 2019 American Chemical Society (Ref. 75).⁷⁵

The pure electronic transition ($v' = 0 \leftarrow v'' = 0$), termed the 0-0 transition, is often the key value for assigning experimental spectra because it is a clearly defined value in both calculations and experiment.^{112, 113} The difference in the 0-0 energy of protonated isoquinolineH⁺ and quinolineH⁺ is small (200 cm⁻¹), which is a difference that is challenging to confidently calculate with excited state methods. Note that a hot-band was incorrectly assigned as the 0-0 for isoquinolineH⁺ in the original publication.¹¹¹ The 0-0 energies of the two isomers were subsequently measured by Jouvét and co-workers at cryogenic temperatures to be within 200 cm⁻¹ of one another for this transition.¹¹⁰ This difficulty in characterising small differences between 0-0 energies is compounded by the fact that excited state calculations tend to be less accurate and less robust than ground state calculations. Time dependant density functional theory (TD-DFT) calculations have typical absolute uncertainties on the order of 2000 cm⁻¹ and the coupled cluster method CC2, (which is the gold standard method for excited state calculations of medium sized molecules,) has typical uncertainties of *ca.* 1000 cm⁻¹. Methods like EOM-CCSDT have typical errors of above 200 cm⁻¹ and are too expensive to be routinely used for molecules of this size.¹¹⁴ The fact that EOM-CCSDT and other high level methods—which reach chemical accuracy (< 1 kcal/mol or 350 cm⁻¹)—may not correctly predict the energetic ordering between these isomers emphasises a challenge in assigning these quinolineH⁺ and isoquinolineH⁺. In this study, these isomers were generated from standards where the identity of the isomer was known. Nevertheless, techniques need to be developed that separate and detect isomers present in the one sample. To this end, Coughlan *et al.* used these quinolineH⁺ and isoquinolineH⁺ reference spectra to assign isoquinolineH⁺ and quinolineH⁺ separated using differential ion mobility spectrometry (DMS).¹¹⁵ Therefore, these isomer resolved spectra can serve as references for future diagnostic applications.

1.3 Assignment of Protomers

A common structural variable that gives rise to isomers is variation in protonation site. Isomers that only differ in their protonation site are termed protomers.* When multiple favourable protonation sites are present, the protomers present in solution may be transferred through to the gas phase following ESI, along with protomers that are favoured in the gas phase.^{42, 116-119} However, the protomer populations generated by ESI are affected by the ESI conditions and

* The term “protomer” is also used in biology to refer to units of proteins. In this thesis, the term protomer is always used to refer to protonation isomers.

do not necessarily reflect the statistically preferred distributions in either the gas phase or the solution phase.¹¹⁶⁻¹¹⁹ Because protomer populations are affected by ESI (and because the exact mechanisms by which ions are formed in ESI is not fully understood) it can be difficult to predict which isomers are going to be present in the experiment. This uncertainty means that the protomers present need to be assigned and characterised.

1.4 Room temperature UVPD

Matthews and Dessent reported UVPD action spectra of protomer isomers co-populated in an ion trap in their study of *para*-aminobenzoic acid (PABA).²⁹ The room temperature action spectra could be deconvoluted to two protomers of PABA, as is shown in Figure 1.2. Figure 1.2a shows the spectrum of the O-protonated form and Figure 1.2b shows the spectrum of the N-protonated form. Because there are major differences in the spectra of these protomer ions and the major product ions are characteristic to the protomer precursor ions, the isomers are clearly distinguished. Since these product ions are—for the most part—unique to the precursor protomer ion, any isomerization between protomers subsequent to photoactivation must be minimal. However, depending on the structure of the molecule, the availability of proton scrambling pathways and the difference in the protonatable functional groups, some protomers give rise to the same photoproduct ions. Nevertheless, the protomers of PABA have different photoproduct ions and spectroscopic differences.

Fragment ions can give insights into protomer assignment. For example, Figure 1.2b follows H atom loss and loss a neutral NH₃ fragment (−17 Da), which has previously been assigned as forming from the N protomer by ground state dissociation.^{120, 121} Therefore, based on the photoproducts, one can begin to assign the spectra to different protomers without even analysing their spectral profile.

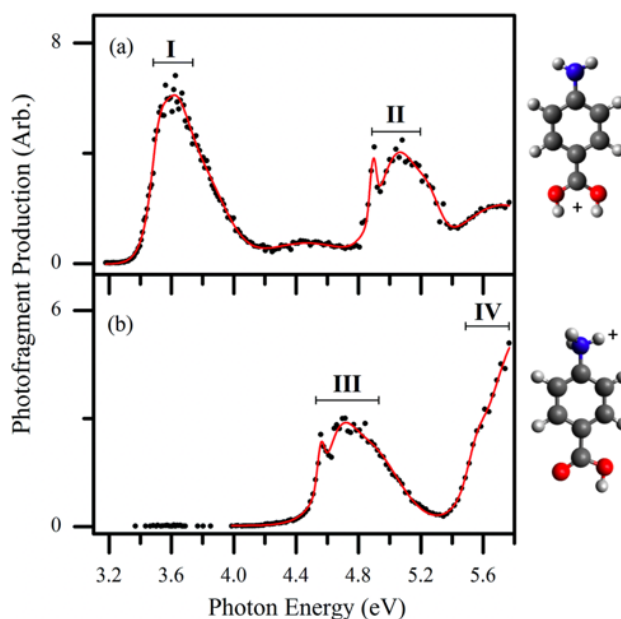


Figure 1.2: UV PD action spectra for para-aminobenzoic acid (PABA) ions in different solvent following different PD products. The spectra correspond to two protomers co-populated in the ion trap, which are distinguishable by their different action spectra and PD products. Adapted from Ref. 29.²⁹

For direct assignment of isomers, photodissociation action spectroscopy can be compared to calculated spectroscopic transitions. For example, the first electronic transition for the O-protonated form of PABA is calculated to be centred around 3.58 eV (using the high level MRCI method) and the peak in the experimental spectrum (Figure 1.2a) is centred around 3.51 eV. Similarly, the calculated first transition of N protonated PABA is calculated to be 4.50 eV, which is close to the experimental transition around 4.56 eV (Figure 1.2b). This agreement between calculations and experimental spectra, in addition to other observed states, provides an unequivocal assignment of these spectra. When the spectra of isomers are different enough (like the O and N protomers of PABA) low resolution PD action spectroscopy definitively reveals co-located isomers.

The Dessent group has also deployed PD action spectroscopy to study protomers of flavin ions¹²² and nicotinamide.¹²³ In these experiments, the various isomers are co-located in the ion trap. Other UV PD studies on nucleobases^{124, 125} distinguished between multiple protomers. These studies showed how excitation energy and non-radiative decay depends on protonation site, which is noteworthy considering protonation resembles the hydrogen bonding and isomerism that occurs for nucleobases in DNA. From the PD action spectra of these molecules, their intrinsic photoproperties can be deduced. These properties include absorption transitions and non-radiative decay mechanisms. This is benchmark information to understand the effect

of more complex environments, including solvent shifts or other environments. UV PD has also been employed to understand how structural changes affect the photochemistry of sunscreens, for example, by distinguishing and characterising how the binding site of a salt cation can inhibit the excited state proton transfer that affect the photostability of sunscreen agents.¹²⁶⁻¹²⁸

Nucleobase radical cation isomers,^{68, 129-132} as well as several other biologically relevant radical cation isomers have been analysed by Turaček and co-workers using UV action spectroscopy in a modified commercial ion trap, which takes advantage of the inert ion trap environment. Reactive radical ions, which would otherwise be transient intermediates that quickly react away, can be isolated and stored for the acquisition of PD spectra.

The Turaček group has also compared the results from the two most common commercial mass spectrometers that are modified for PD action spectroscopy (THERMO LTQ and Bruker AmaZon). These modified setups are shown in Figure 1.1C and 1D.⁷⁵ The main difference between these arrangements is that for the linear ion trap (THERMO LTQ) optical access is afforded through a window on the rear of the mass spectrometer, whereas optical access is afforded through a window on the top of mass spectrometer to the 3D ion trap (Bruker AmaZon) with a clear path in and out of the instrument. The spectra in Figure 1.1 were acquired using a THERMO LTQ mass spectrometer, whereas the spectra in Figure 1.2 from Dessent and co-workers were acquired using a Bruker AmaZon mass spectrometer. It is evident that both configurations are suited for PD action spectroscopy, however, these spectra should not be used to directly compare the performance of the two mass spectrometer setups because they also employed different lasers, different spectral ranges, and different ions. For direct comparisons between equivalent instruments using a THERMO LTQ and a Bruker AmaZon mass spectrometer see Ref. 75.⁷⁵

Although there are many cases where room temperature PD action spectroscopy can distinguish isomers, there will be many instances where the spectra of isomers are inherently too broad, featureless and/or overlapping.

1.5 Cryogenic UVPD

As is well established, vibronic spectra are generally sharper and better resolved when ions are cooled in cryogenic ion traps as this greatly restricts vibrational state population and narrows rotational state distributions. PD action spectroscopy of ions confined in cryogenically cooled environments is conducted in a similar manner to the previously described room temperature experiments except that the temperature of the ions is cooled to *ca.* 3-50 K using a buffer gas, which is typically He. Figure 1.3b shows a schematic of a setup employing a cryogenic ion trap as shown in Ref. 82.⁸² The ions are generated by ESI and guided into a 22-pole ion trap, which is cooled by a He cryostat. With the colder ions, hot band intensities and temperature broadening are significantly reduced or eliminated and the general sharpness of the spectra can be vastly improved.

Cryogenic ion-trap PD action spectroscopy has been used to characterise the protonation or metalation-site isomers for ions of flavins,¹³³⁻¹³⁵ nucleobases,^{2, 136} polycyclic aromatic amines,^{137, 138} distinguishing between different spin states of high-spin ions,^{139, 140} and to disentangle E and Z double-bond isomers of hemithioindigo¹⁴¹ and the green fluorescent protein chromophore,¹⁴² lipid isomers¹⁴³ and carbohydrates.¹⁴⁴ Similar experiments have measured electron photodetachment (rather than PD) as a function of wavelength for deprotonomers of cytosine anions.⁵²

The PD action spectra of protonated lumiflavin (LFH⁺) is shown in Figure 1.3 (from the study of Dopfer and co-workers).¹³³ A lower resolution spectrum is recorded using a mid-band OPO laser (linewidth *ca.* 4 cm⁻¹) and the high-resolution spectrum is acquired using a dye laser (linewidth *ca.* 0.014 cm⁻¹). The first major peak (at 0 cm⁻¹) is assigned as the origin of the O protomer. Aided by the simulated spectra, it is apparent that the two protomer contribute to the experimental spectra. The N-protomer origin (0-0) is assigned at +74 cm⁻¹ from the O-protomer 0-0. Several low frequency excited state vibrational quanta are assigned within a few 100 cm⁻¹ above the 0-0 transition arising from both protomers. This vibronic structure allows for assignment of two protomers based on comparison with FC simulations and calculated 0-0 transition energies. The O2⁺ protomer (red simulation) is planar in the excited state and is dominated by in-plane vibrations and the geometry of the N1 protomer (blue simulation) is non-planar in the excited state and has a spectrum that has several active low-frequency out of plane vibrations. This illustrates how biological flavins can have their photoproperties altered by the protonation site, which implicates the importance of the flavin's environment to its photoproperties. Furthermore, the flavin's environment can also be altered by metal binding

site, as other studies using cryogenic PD action spectroscopy have observed that changing the metal binding site can dramatically shift the 0-0 transition energy for the first $^1\pi\pi^*$ state of flavin ions.¹³³⁻¹³⁵

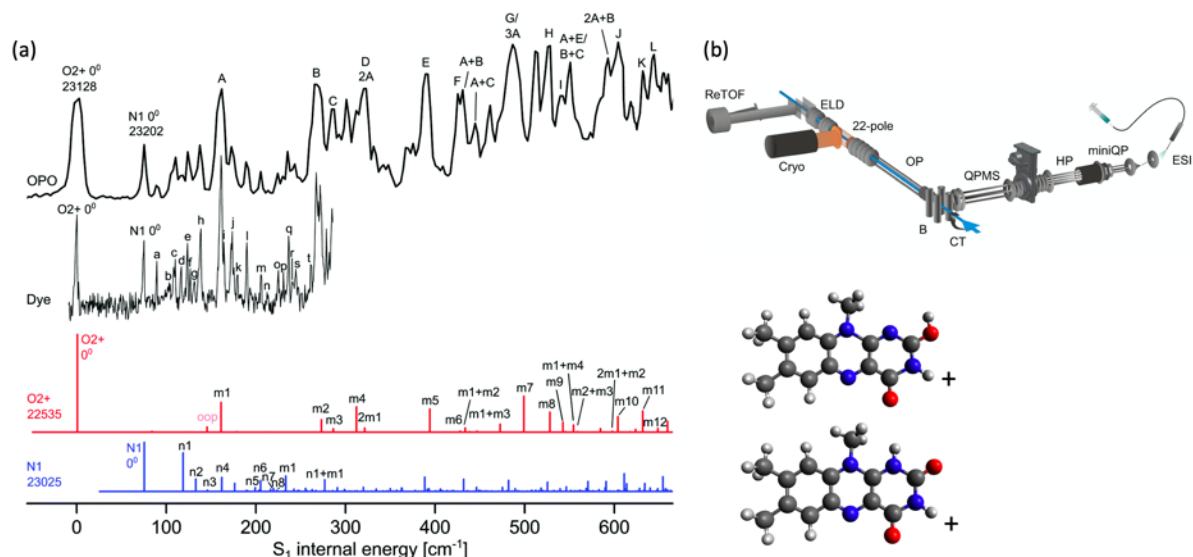


Figure 1.3: (a) Cryogenic spectra of LFH+ (black) compared with Franck-Condon simulations for two protomers (red and blue). Both protomers are assigned as contributing to the experimental spectrum. Adapted from Ref. 138.¹³³ (b) Schematic diagram of the cryogenic BerlinTrap apparatus used to acquire these spectra. (b) Adapted from Ref. 82.⁸²

For protomers of lumiflavin under cryogenic conditions, the vibronic spectra are used for convincing assignment of isomers.^{133, 134, 137, 138, 145-148} Assignment is achieved by comparison between experimental and calculated results, which typically involves FC simulations and calculated 0-0 transition energies. The interplay between experiment and computation is important in this area of research. Accurate calculations are often needed to assign experimental spectra and calculations need experimental references for benchmarking and development.

Natural linewidths recorded using cryogenic ion PD spectroscopy can be used to estimate excited state lifetimes based on the uncertainty principle.^{2, 102, 104} This is possible because rotational broadening of vibronic peaks should be minimised at low temperatures. Using cryogenic ion PD spectroscopy, two protomers of protonated uracil were determined to have excited state lifetimes of 40 fs and 2 ns (where the 2 ns lifetime was measured using pump-probe).^{2, 104} This difference between lifetimes was attributed to the different energy gaps between the $\pi\pi^*$ and $n\pi^*$ states. Thereby, the effect of lone pairs and protonation site on the photostability of DNA nucleobases was spectroscopically observed.

1.6 Pump-Probe Photodissociation

When the vibronic peak linewidths are significantly narrow so that peak overlap is reduced, it is possible to tune a laser to selectively excite a vibronic transition of only one isomer, leaving the other unaffected. Taking advantage of this, Soorkia *et al.* selectively excited conformers of protonated tyrosine ions using resonant transitions. By then introducing a second (probe) laser pulse, they measured pump-probe PD spectra for various conformers (see Figure 1.4).¹⁴⁹ A schematic of the experimental setup is also shown in Figure 1.4c, all isomers are isolated in the ion-trap (Paul trap), which is cooled by a cryostat. Both the pump and probe pulses (see fragmentation laser in Figure 1.4c) irradiate the ion cloud in the ion-trap.

This type of isomer-selective pump-probe experiment was employed to investigate protonated tyrosine isomers¹⁴⁹ and nucleobase isomers.^{136, 150} Protonated tyrosine conformers are found to have similar excited state lifetimes at 1610 cm^{-1} above the 0-0 transition (*ca.* 450 ps). On the other hand, the $^1n\pi^*$ lifetimes of protonated cytosine varied by over an order of magnitude and, as previously mentioned, the excited state lifetimes of uracil varied by almost five orders of magnitude.

Other groups have employed combined femtosecond or picosecond pump-probe with photodissociation mass-spectrometry to interrogate the excited state lifetimes of ions in tandem time-of-flight mass spectrometers,¹⁵¹⁻¹⁵³ triple-quadrupole mass spectrometers,¹⁵⁴ ion storage rings,^{155, 156} custom built ion traps at room temperature¹⁵⁷⁻¹⁵⁹ and cryogenically cooled,^{100, 104, 150, 160} and commercial ion traps.¹⁶¹⁻¹⁶⁴ There are also setups using electronic delays for pump-probe photodissociation on the nanosecond to millisecond timescale.^{136, 150, 164-169} Excited state dynamics of few gas-phase ions have been investigated experimentally or computationally, especially relative to solution-phase species.

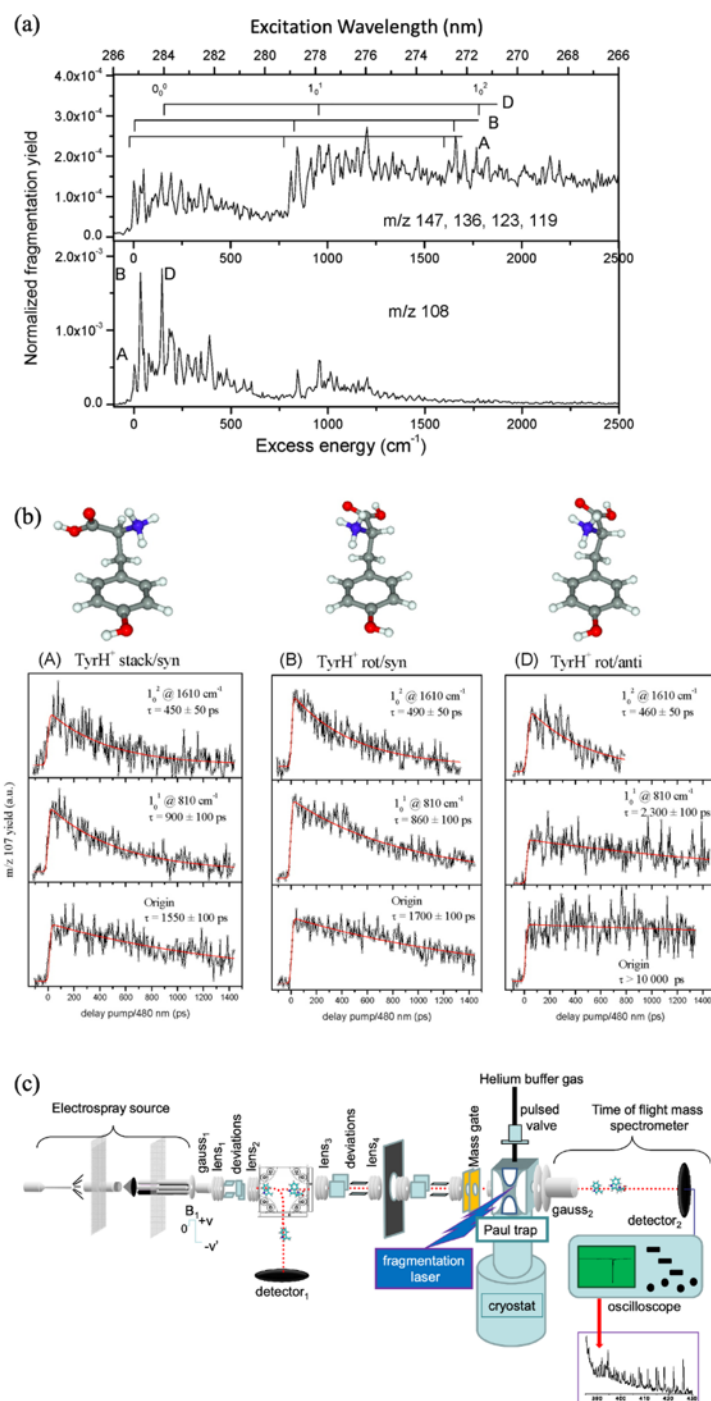


Figure 1.4: (a) Cryogenic UV PD action spectra of tyrosineH⁺ ions. (b) Pump-probe PD plots following the PD yield of tyrosineH⁺ ions as a function of time delay between the pump and probe pulses (right). By setting the pump pulse to excite a vibronic peak for only one isomer, each isomer can be selected and its lifetime can be selectively probed. (a) and (b) adapted with permission from Soorkia, S., Broquier, M. and Grégoire, G., **2014**. *The Journal of Physical Chemistry Letters*, 5(24), pp.4349-4355. Copyright 2014 American Chemical Society.¹⁴⁹ (c) Schematic of experimental setup. (c) adapted with permission from Alata, I., Bert, J., Broquier, M., Dedonder, C., Féraud, G., Grégoire, G., Soorkia, S., Marceca, E. and Juvet, C., **2013**. *The journal of Physical Chemistry A*, 117(21), pp.4420-4427. Copyright 2013 American Chemical Society.⁸³

1.7 UV Hole Burning

Co-populated isomer populations can be selectively probed by excitation of specific vibronic transitions. Hole burning spectroscopy takes advantage of this to selectively obtain a spectrum of only one isomer. This requires two lasers. When the first laser (referred to as the burn laser) is tuned to excite a particular isomer, the population of only that isomer is depleted either by dissociation or removal of population from the ground state. Depletion can be observed by introducing another laser (referred to as the probe laser) that records a change in photoproduct yield. In this experiment the burn laser is scanned and depletes isomer populations, while the probe laser is fixed and detects the isomer-specific depletion.

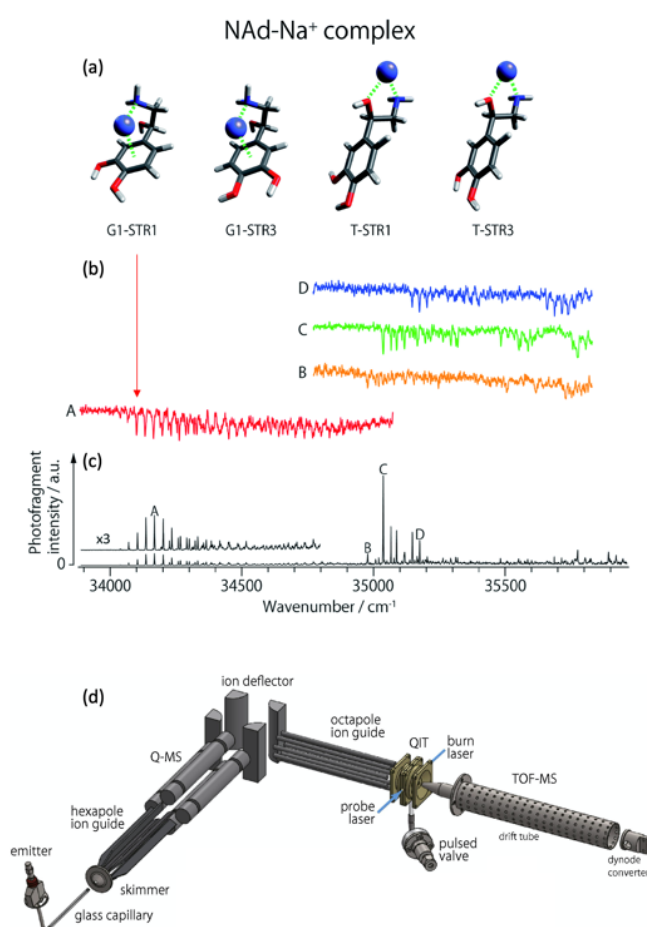


Figure 1.5: (a) Some low energy isomers of noradrenaline- Na^+ . (b) Cryogenic UV-PD hole burning spectra of noradrenaline- Na^+ isomers. (c) Cryogenic UV-PD spectrum containing exhibiting the spectrum of all isomers generated by ESI. Figures (a), (b) and (c) reproduced from Ref. 175 with permission from the Royal Society of Chemistry.¹⁷⁰ By setting a “probe” laser pulse to selectively excite one isomer, the PD from that isomer is detected. By introducing a second laser, an isomer selective spectrum can be generated whereby the spectrum dips when the second laser “burns” out the population of the isomer being selected by the “probe”. (d) Schematic of experimental setup. (d) Adapted from Ref. 84.⁸⁴

Hole burning spectra are presented in Figure 1.5 where isomer selective spectra for four noradrenaline- Na^+ conformers (red, orange, green and blue lines) are extracted from an experiment with all isomers co-populated in the trap. The different spectra are acquired by scanning the burn laser and setting the probe laser to selectively excite one of the peaks A, B, C, or D shown in Figure 1.5c. A schematic example of an experimental arrangement for hole burning is shown in Figure 1.5d (reproduced from Ref. 84⁸⁴), which shows ions are generated by ESI, m/z selected with a quadrupole mass spectrometer (labelled Q-MS), and guided into the ion-trap where they are cooled by pulsed He and irradiated by the burn and probe lasers. This hole burning experiment was used to assign the vibronic progression labelled A (red trace) to a closed structure where the Na^+ interacts with the aromatic π system. This isomer was not observed for the noradrenaline- Li^+ ion (not shown), which may explain the different effect that Li^+ and Na^+ has on the inhibition of noradrenaline molecular recognition.

Biomolecular ions of considerable structural flexibility like polypeptides and proteins have been analysed using combined cryogenic and IR and UV hole burning and double resonance experiments.^{51, 171-173} For more on cold ion spectroscopy, the interested reader is directed to the following reviews for biological ions by Boyarkin and co-workers^{73, 174} and Soorkia *et al.*⁶⁷

1.8 Ion Mobility Coupled with Photodissociation

Ion mobility in its various forms is an additional tool to separate ions by physical properties including size, dipole, buffer-gas affinity *etc.* Coupling ion mobility with PD spectroscopy, isomers can first be separated and then spectroscopically investigated. Ion mobility combined with spectroscopy can also provide a reference spectrum of one isomer, which can be valuable particularly for understanding results when separation is not possible.

Koyasu *et al.* generated isomers of C_9^+ with laser vaporisation of graphite. Various C_9^+ isomers were separated using drift ion mobility spectrometry (IMS) and then irradiated with 355 nm photons to induce photodissociation (see Figure 1.6 and Scheme 1.4 for a simplified workflow of this experiment). In IMS, ions drift through a cell that contains a gas, typically N_2 or He. As the ions drift, their mobility is affected by the ion-molecule collisions as quantified by the collision cross section (CCS). Two types of C_n^+ isomers are reported in this experiment, linear and cyclic. The linear isomers have a larger CCS and they tumble through the collision cell with a longer arrival time (peak labelled A in Figure 1.6b). The cyclic isomers are more

compact with a smaller CCS and, therefore, have the arrival time (peaks labelled B in Figure 1.6b).

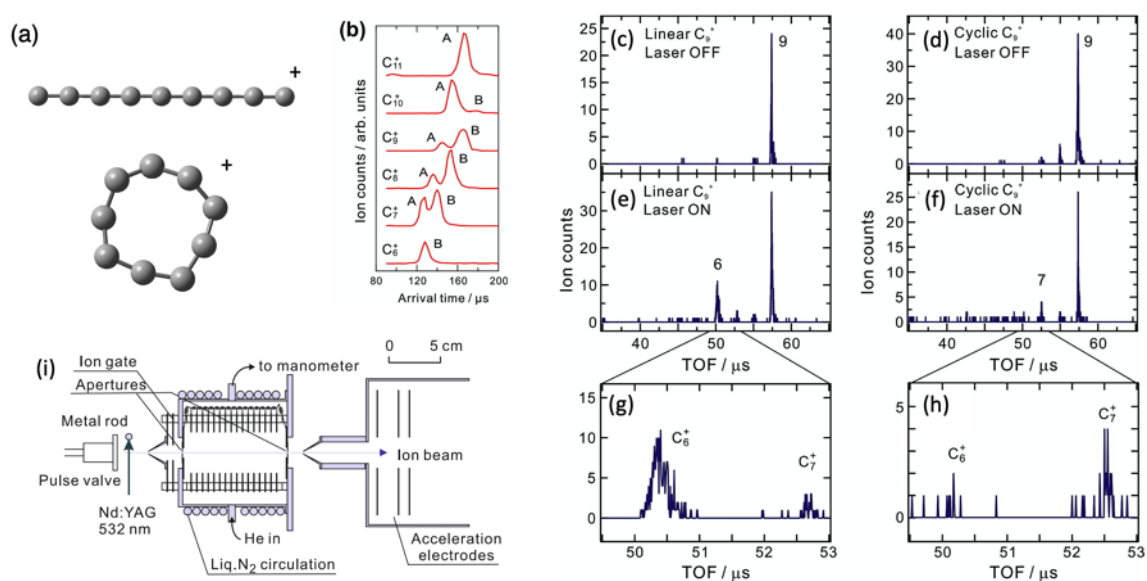


Figure 1.6: (b) Drift IMS arrival time plots for C_n^+ clusters. Mass spectra of linear C_9^+ without laser irradiation (a) and after laser PD (c) and mass spectra of cyclic C_9^+ without laser irradiation (b) and after laser PD (d). Adapted from Ref. 175.¹⁷⁵ (i) Schematic of experimental setup adapted from Ref. 93.⁹³

Because the two C_9^+ isomers are separated, the ratio between C_6^+ and C_7^+ formation is determined, where the linear isomer favours C_6^+ and the cyclic isomer favours C_7^+ . Because they are separated, the difference is obvious, which is a clear advantage of the combined ion mobility and PD mass spectrometry arrangement

Some other examples of ion mobility coupled with photoelectron spectroscopy or PD using set wavelengths are other carbon cluster ions,^{176, 177} silicon cluster ions,¹⁷⁷ trisaccharides,¹⁷⁸ DNA anions,^{179, 180} proteins,¹⁸¹⁻¹⁸⁵ flavins,⁹² and glycans.¹⁸⁶ Also, fixed wavelength arrangements have been used for more exotic experiments such ion-mobility selected gas-phase fluorescence.¹⁸⁷⁻¹⁸⁹

1.9 Ion Mobility Coupled with Spectroscopy

Ion-mobility and PD action spectroscopy reveals considerable detail about ions and isomer populations. Protomers of benzocaine H^+ were separated using ion mobility and then assigned using IRMPD.¹¹⁹ Figure 1.7b shows that the mobility selected IRMPD spectrum of isomer II matches the calculated spectrum for the N-protomer of benzocaine H^+ , and the spectrum of I

matches the calculated spectrum of the O-protomer. The IRMPD spectra exhibit several diagnostic peaks (like the N-protomer peak at 1250 cm^{-1} or the O-protomer peak at 1550 cm^{-1}). These peaks in the IRMPD spectra allow for unambiguous assignment of the two ion-mobility separated species. Notably, CID generates the same photoproducts for both protomers and, therefore, does not provide clear assignments. However, one could even argue that these protomers could be assigned using IRMPD without separation—although the result would be less definitive without separation. Even though the IMS points to additional isomers, (isomers II and II'), the IRMPD spectra of these isomers appears almost identical. The populations of these protomers and isomers can be measured by variation of the ESI solvent (Figure 1.7a).

Although most of the focus of this thesis is UV and visible photodissociation, IR PD strategies are another tool that is well suited for combined ion mobility and spectroscopy. Ion mobility combined with room temperature IR PD has been used to distinguish isomers of sacharides,¹⁹⁰ amino acids,¹⁹¹ amino acid clusters,¹⁹² small molecules,¹⁹³ metal-oxide clusters,¹⁹⁴ and β -sheet formation.¹⁹⁵ Combined ion mobility and cryogenic IR PD studies have distinguished isomers of peptides¹⁹⁶⁻¹⁹⁸ and glycans.¹⁹⁹⁻²⁰⁴ Gas-phase infrared spectroscopy of glycan isomers was also recently reviewed.²⁰⁵ In the case of many systems mentioned here, especially some glycan isomers, the difference between isomers is very slight and these isomers cannot always be distinguished using one technique alone (*i.e.* just ion mobility or just IR PD). It is only when ion mobility is combined with IR PD that these isomers can be clearly distinguished.

Another ion-mobility method for separation of ions is FAIMS.^{115, 117, 206} While traditional drift IMS separates ions by their cross-sectional mobility in a low-strength electric field alone, the FAIMS method separates ions by both their mobility in a low strength electric field and their mobility in a high strength electric field. These mobilities are unique to each ion, which allows for separation of isomers. A detailed description of FAIMS is discussed the following Experimental Chapter.

Drift IMS and FAIMS each have advantages and disadvantages. While FAIMS can provide separation that is not easily afforded using drift IMS,²⁰⁷ FAIMS separation can activate ions²⁰⁸ and possibly cause structural rearrangements. Drift IMS provides collisional cross section (CCS) values for separated species. These CCS values provide information about ion shape and can be compared other reference CCSs and calculated values. Therefore, even before using

PD, the CCS values can inform structural assignments of different isomers separated with IMS. A method to measure CCS using FAIMS results and machine learning is emerging,²⁰⁹ which is promising but not as routine as CCS measurements with drift IMS.

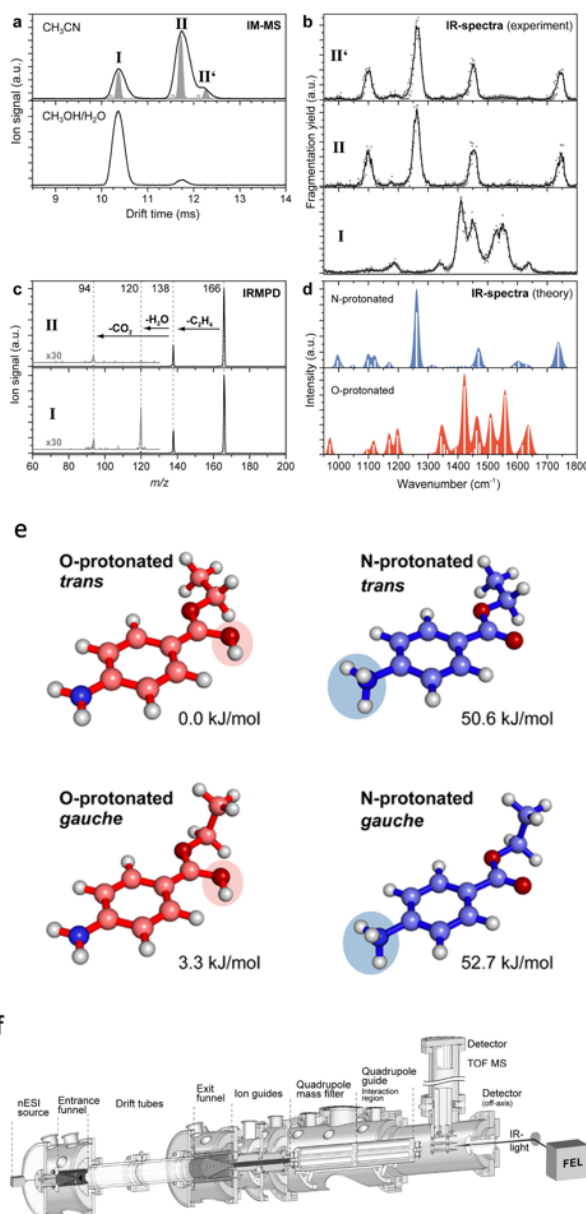


Figure 1.7: (a) Drift IMS for benzocaineH⁺ generated using acetonitrile or a mixture of methanol and water as the ESI solvent. (b) IRMPD spectra of the ion-mobility selected protomers and isomers of benzocaine-H⁺. (c) IRMPD mass spectra. (d) Calculated IR spectra for different benzocaineH⁺ protomers. Structures and relative ground state energies for different protomers and isomers of protonated benzocaine (e). Schematic of the experimental setup (f). Adapted from Warnke, S., Seo, J., Boschmans, J., Sobott, F., Scrivens, J.H., Bleiholder, C., Bowers, M.T., Gewinner, S., Schöllkopf, W., Pagel, K. and von Helden, G., **2015**. *Journal of the American Chemical Society*, 137(12), pp.4236-4242. Original article is in the public domain.¹¹⁹

Examples of experiments that combine ion mobility with PD action spectroscopy are FAIMS separation with cryogenic UV/vis PD spectroscopy of peptides from the Rizzo group,^{196, 210, 211} FAIMS separation with room temperature UV/vis PD spectroscopy from the Hopkins group,^{115, 212-215} and drift mobility separation with room temperature photodissociation and photoisomerization from the Bieske group^{91, 216-229} and the Dugourd group.^{230, 231}

1.10 Tandem IMS

Tandem IMS has been combined with photoactivation to observe photoisomerism. This is possible because photoisomerism can alter the ion CCS. The Bieske group^{91, 216-229} and the Dugourd group^{230, 231} have both deployed this strategy. The tandem ion mobility setup uses an IMS-IMS-QMF configuration with two drift ion mobility regions (IMS1 and IMS2). A schematic of this experimental setup is shown in Figure 1.8, along with an ion mobility spectrum and photoisomerization action spectrum of protonated *trans* azobenzene reproduced from Ref. 218.²¹⁸

The *trans* isomer of protonated azobenzene is selected in the first ion mobility step (IMS1) so only this isomer is present. This is confirmed by the IMS2 arrival time distribution, which displays only one peak (black trace in Figure 1.8a). If the mobility selected ions are irradiated by a laser between IMS1 and IMS2, photoisomerism can be induced as revealed by the signal from the *cis* isomer and the depletion of the *trans* (dotted line in Figure 1.8b). The *cis* isomer peak is assigned by its arrival time from the IMS2 spectrum.

Tandem ion mobility makes up a major proportion of the studies using combined ion-mobility and UV/vis action spectroscopy due to studies by the Bieske group^{91, 216-229} as well as the Dugourd group.^{230, 231} The example of protonated azobenzene highlights several key points about this technique. Ion mobility selection can allow for isomer specific investigation, tandem ion mobility can be used to study photoisomerism and the connection between conformational isomers.

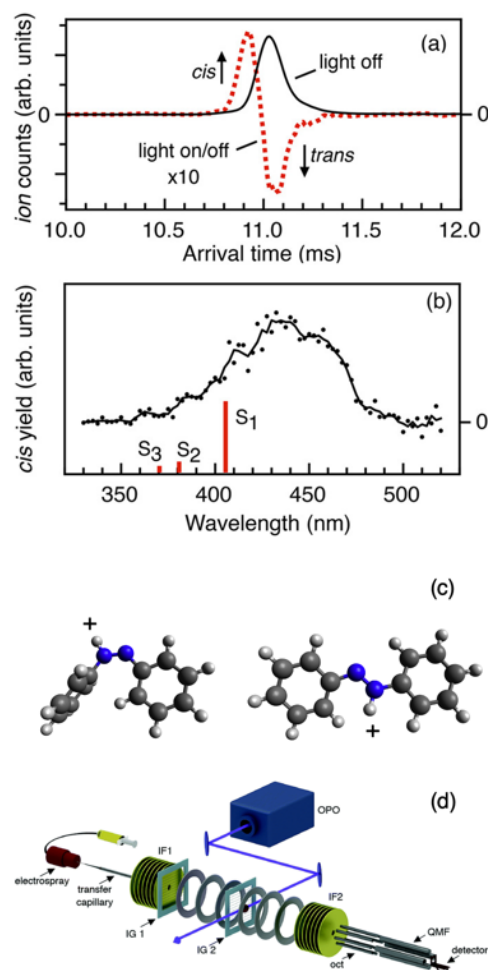
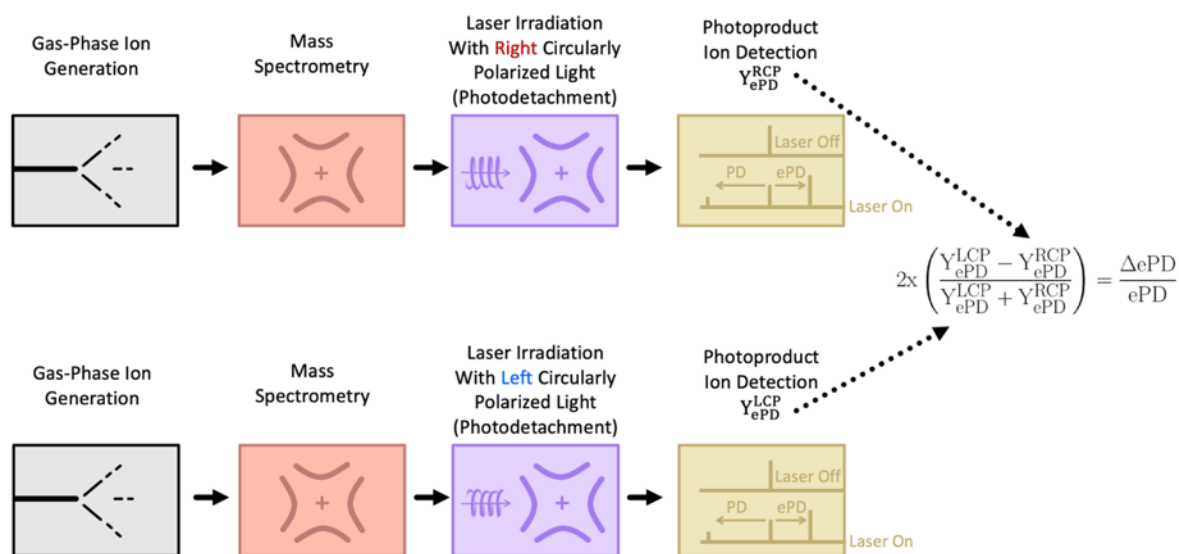


Figure 1.8: (a) Arrival time distributions measured by the IMS2 drift region for *trans* azobenzene (that was selected by its mobility in the IMS1 region). The traces correspond to light off (black trace) and 440 nm photoaction (red dashes). (b) Action spectrum following the photoisomerization to the *cis* isomer as a function of wavelength. (c) Structures of protonated *cis* azobenzene and *trans* azobenzene. (d) Schematic of the tandem ion-mobility experimental setup. (a), (b) and (d) adapted with permission from Scholz, M. S.; Bull, J. N.; Coughlan, N. J.; Carrascosa, E.; Adamson, B. D.; Bieske, E. J., 2017. *The Journal of Physical Chemistry A*, 121 (34), pp. 6413-6419. Copyright 2018 American Chemical Society.²¹⁸

1.11 Circular Dichroism

Chirality is a structural parameter of molecules, which impacts their biological and toxicological behaviour.²³² The chirality of a molecule is typically measured using circular dichroism (CD) spectroscopy. CD spectroscopy takes advantage of the fact that stereoisomers have different absorption properties in left and right circularly polarised light. Development of gas phase PD techniques for distinguishing stereoisomers has been rapidly expanding in the past few years.

Recently, experimental gas phase PD setups have successfully distinguished between stereoisomers of small chiral ions with linearly polarised light.^{233, 234} Experimental setups using circular polarised light to generate gas-phase CD action spectra have also been developed recently. Gas-phase CD action spectra have been reported for small ions in a cryogenic ion trap^{235, 236} and large DNA polyanions at room temperature.²³⁷ Photoelectron circular dichroism of amino acid anions was also recently reported.²³⁸



Scheme 1.2: Simplified workflow for gas-phase circular dichroism photodetachment.

Rather than the total yield of photodissociation (or electron photodetachment) measured for standard action spectroscopy, the data points for gas phase CD action spectroscopy results follow the normalised difference in electron photodetachment (ePD) yield when polyanions were irradiated using left circularly polarised and right circularly polarised light. This approach shows the capability of gas phase ePD and PD to generate CD action spectra and probe higher-order chirality of DNA.²³⁷ With this comes the inherent advantages of mass spectrometry, where lower concentrations are required and lower purity is acceptable because background artifacts can be reduced when ions are selected by their m/z ratio.

1.11 Final Thoughts

Structure and charge have impacts on chemical reactivity, and combined mass spectrometry are well suited to investigate these links. However, isomers pose unique challenges and studies benefit from additional strategies including ion mobility techniques and cryogenic cooling.

In this introduction, techniques for distinguishing between and characterising different isomers that involve UV and visible photodissociation were discussed. Some isomers (such as protomers) cannot be straightforwardly introduced for separate experiments and often require spectroscopic characterisation with multiple isomers copulated in the ion trap. Cryogenic spectroscopy can reduce spectral congestion and help reveal otherwise unobserved vibronic details. Ion-mobility is an important enhancement to PD that can allow for separation and selective probing of different isomers photoproperties. Spectra of certain isomer ions can be buried when they are co-populated but are revealed if they are separated using ion mobility before PD action spectroscopy. Photoisomerism can be investigated by combined laser and tandem ion mobility strategy can probe photoisomerism in the gas phase. Finally, chiral isomers can be distinguished using PD or electron photodetachment in circularly polarised light in a gas-phase CD setup and the renewed interest in this area.

As techniques for distinguishing isomers develop, future efforts may implement these techniques into routine mass spectrometry workflows. Mass spectrometry imaging shows that different lipid isomers occupy different regions of the brain, however, disentangling these isomers required novel combinations of mass spectrometry techniques.²³ Commercial mass spectrometers like the Orbitrap Fusion Lumos (THERMO) have an incorporated fixed-wavelength 213 nm laser for PD. The prospect of using tuneable lasers, VUV tunability, and PD ion spectroscopy techniques to routinely visualise the spatial distribution of structural isomers or chiral isomers is an intriguing future direction. These PD techniques have the advantage of requiring small amounts of analyte and do not demand high standards of sample purity because of the selectivity afforded by mass spectrometry and ion mobility. Therefore, PD action spectroscopy could be a useful tool to characterise the roles isomers play in biological processes using mass spectrometry imaging, in analytical chemistry, lipidomics, and metabolomics.

1.12 Thesis Outline:

- Chapter 2 describes the experimental setup used in this thesis. This chapter summarises the photodissociation action spectroscopy setup and details the implementation of Field Asymmetric Ion Mobility Spectrometry and Pump-Probe photodissociation into the experimental workflow.
- Chapter 3 of this thesis shows an example where photochemistry of the irgacure 2959 photoinitiator is controlled by oriented electric fields created by charge tags (H^+ , Li^+ ,

Na⁺, K⁺, Mg²⁺, Zn²⁺, Ca²⁺) that form cluster isomers with locked-in electric field orientation. This chapter is derived from the publication: Marlton, S.J., McKinnon, B.I., Hill, N.S., Coote, M.L. and Trevitt, A.J., **2021**. *Journal of the American Chemical Society*, 143(5), pp.2331-2339.

- Chapter 4 of this thesis shows an example where the separation and selection of protomers of quinazoline using field asymmetric ion mobility spectrometry (FAIMS) and their characterisation using PD action spectroscopy. The protomers of quinazoline differ only in their protonation site, which equates to different charge locations and, hence, different electric field orientations. This provides a good model system for investigating the effects of charge location because the protomers can be selected with FAIMS. This chapter is derived from the publication: Marlton, S.J., McKinnon, B.I., Ucur, B., Bezzina, J.P., Blanksby, S.J. and Trevitt, A.J., **2020**. *The Journal of Physical Chemistry Letters*, 11(10), pp.4226-4231.
- Chapter 5 of this thesis follows FAIMS selection and PD action spectroscopy of the protomers of nicotine. This chapter contrasts the previous two, as the protomers of nicotine are differentiated by through-bond effects (rather than electric field effects). This chapter is derived from the publication: Marlton, S.J., McKinnon, B.I., Ucur, B., Maccarone, A.T., Donald, W.A., Blanksby, S.J. and Trevitt, A.J., **2019**. *Faraday discussions*, 217, pp.453-475.
- Chapter 6 of this thesis explores the excited state dynamics of two constitutional isomers (protonated indazole and protonated benzimidazole) using picosecond pump-probe photodissociation. The excited state lifetime of protonated indazole is shown to be much shorter than that of protonated benzimidazole due to a facile excited-state deactivation pathway involving breaking of the N-N bond. This result shows that the N-N bond deactivation pathway is available for protonated systems. Furthermore, this chapter shows the utility of the pump-probe photodissociation setup developed during this project, which can be extended to other species to investigate the effects of charge and charge location on the excited state dynamics of gas-phase ions. This chapter has been accepted to the *Journal of Chemical Physics*, after it is published it will be found at <https://aip.scitation.org/journal/jcp>.
- Chapter 7 provides some final thoughts, which summarise the results of this thesis, describe the outcomes, and describe some possible future directions.

References

1. Tuna, D.; Sobolewski, A. L.; Domcke, W., Mechanisms of ultrafast excited-state deactivation in adenosine. *The Journal of Physical Chemistry A* **2014**, *118* (1), 122-127.
2. Berdakin, M.; Féraud, G.; Dedonder-Lardeux, C.; Jouvet, C.; Pino, G. A., Excited states of protonated DNA/RNA bases. *Physical Chemistry Chemical Physics* **2014**, *16* (22), 10643-10650.
3. Boldissar, S.; de Vries, M. S., How nature covers its bases. *Physical Chemistry Chemical Physics* **2018**, *20* (15), 9701-9716.
4. Vivian, J. T.; Callis, P. R., Mechanisms of tryptophan fluorescence shifts in proteins. *Biophysical Journal* **2001**, *80* (5), 2093-2109.
5. Blyth, M. T.; Noble, B. B.; Russell, I. C.; Coote, M. L., Oriented Internal Electrostatic Fields Cooperatively Promote Ground-and Excited-State Reactivity: A Case Study in Photochemical CO₂ Capture. *Journal of the American Chemical Society* **2019**, *142* (1), 606-613.
6. Kempfer-Robertson, E. M.; Thompson, L. M., Effect of Oriented External Electric Fields on the Photo and Thermal Isomerization of Azobenzene. *The Journal of Physical Chemistry A* **2020**, *124* (18), 3520-3529.
7. Avdic, I.; Kempfer-Robertson, E. M.; Thompson, L. M., Oriented External Electric Field Tuning of Unsubstituted Azoheteroarene Thermal Isomerization Half-Lives. *The Journal of Physical Chemistry A* **2021**.
8. Hill, N. S.; Coote, M. L., Internal Oriented Electric Fields as a Strategy for Selectively Modifying Photochemical Reactivity. *Journal of the American Chemical Society* **2018**, *140* (50), 17800-17804.
9. Hill, N. S.; Coote, M. L., Strategies for Red-Shifting Type I Photoinitiators: Internal Electric Fields versus Lewis Acids versus Increasing Conjugation. *Australian Journal of Chemistry* **2019**, *72* (8), 627-632.
10. Ciampi, S.; Darwish, N.; Aitken, H. M.; Díez-Pérez, I.; Coote, M. L., Harnessing electrostatic catalysis in single molecule, electrochemical and chemical systems: a rapidly growing experimental tool box. *Chemical Society Reviews* **2018**, *47* (14), 5146-5164.
11. Shaik, S.; Ramanan, R.; Danovich, D.; Mandal, D., Structure and reactivity/selectivity control by oriented-external electric fields. *Chemical Society Reviews* **2018**, *47* (14), 5125-5145.
12. Stuyver, T.; Danovich, D.; Joy, J.; Shaik, S., External electric field effects on chemical structure and reactivity. *Wiley Interdisciplinary Reviews: Computational Molecular Science* **2019**, e1438.
13. Shaik, S.; Mandal, D.; Ramanan, R., Oriented electric fields as future smart reagents in chemistry. *Nature Chemistry* **2016**, *8* (12), 1091.
14. Shaik, S.; Danovich, D.; Joy, J.; Wang, Z.; Stuyver, T., Electric-Field Mediated Chemistry: Uncovering and Exploiting the Potential of (Oriented) Electric Fields to Exert Chemical Catalysis and Reaction Control. *Journal of the American Chemical Society* **2020**, *142* (29), 12551-12562.
15. Stuyver, T.; Ramanan, R.; Mallick, D.; Shaik, S., Oriented (Local) Electric Fields Drive the Millionfold Enhancement of the H-Abstraction Catalysis Observed for Synthetic Metalloenzyme Analogues. *Angewandte Chemie International Edition* **2020**, *59* (20), 7915-7920.

16. Meir, R.; Chen, H.; Lai, W.; Shaik, S., Oriented electric fields accelerate Diels–Alder reactions and control the endo/exo selectivity. *ChemPhysChem* **2010**, *11* (1), 301-310.
17. Aragonès, A. C.; Haworth, N. L.; Darwish, N.; Ciampi, S.; Bloomfield, N. J.; Wallace, G. G.; Diez-Perez, I.; Coote, M. L., Electrostatic catalysis of a Diels–Alder reaction. *Nature* **2016**, *531* (7592), 88.
18. Mackey, T. K.; Contreras, J. T.; Liang, B. A., The Minamata Convention on Mercury: Attempting to address the global controversy of dental amalgam use and mercury waste disposal. *Science of the Total Environment* **2014**, *472*, 125-129.
19. Noble, B. B.; Mater, A. C.; Smith, L. M.; Coote, M. L., The effects of Lewis acid complexation on type I radical photoinitiators and implications for pulsed laser polymerization. *Polymer Chemistry* **2016**, *7* (41), 6400-6412.
20. Robertson, P. A.; Bishop, H. M.; Orr-Ewing, A. J., Tuning the Excited-State Dynamics of Acetophenone Using Metal Ions in Solution. *The Journal of Physical Chemistry Letters* **2021**, *12*, 5473-5478.
21. Uppal, K.; Walker, D. I.; Liu, K.; Li, S.; Go, Y.-M.; Jones, D. P., Computational metabolomics: a framework for the million metabolome. *Chemical Research in Toxicology* **2016**, *29* (12), 1956-1975.
22. Blanksby, S. J.; Mitchell, T. W., Advances in mass spectrometry for lipidomics. *Annual Review of Analytical Chemistry* **2010**, *3*, 433-465.
23. Paine, M. R.; Poad, B. L.; Eijkel, G. B.; Marshall, D. L.; Blanksby, S. J.; Heeren, R. M.; Ellis, S. R., Mass spectrometry imaging with isomeric resolution enabled by ozone-induced dissociation. *Angewandte Chemie International Edition* **2018**, *57* (33), 10530-10534.
24. Wu, Q.; Wang, J.-Y.; Han, D.-Q.; Yao, Z.-P., Recent advances in differentiation of isomers by ion mobility mass spectrometry. *TrAC Trends in Analytical Chemistry* **2020**, *124*, 115801.
25. Demireva, M.; Armentrout, P., Relative Energetics of the Gas Phase Protomers of p-Aminobenzoic Acid and the Effect of Protonation Site on Fragmentation. *The Journal of Physical Chemistry A* **2021**, *125* (14), 2849-2865.
26. Lam, A. K.; O'Hair, R. A., Isomer differentiation via collision-induced dissociation: The case of protonated α -, β 2-and β 3-phenylalanines and their derivatives. *Rapid Communications in Mass Spectrometry* **2010**, *24* (12), 1779-1790.
27. Campbell, J. L.; Yang, A. M.-C.; Melo, L. R.; Hopkins, W. S., Studying gas-phase interconversion of tautomers using differential mobility spectrometry. *Journal of The American Society for Mass Spectrometry* **2016**, *27* (7), 1277-1284.
28. Thomas, M. C.; Mitchell, T. W.; Harman, D. G.; Deeley, J. M.; Nealon, J. R.; Blanksby, S. J., Ozone-induced dissociation: elucidation of double bond position within mass-selected lipid ions. *Analytical Chemistry* **2008**, *80* (1), 303-311.
29. Matthews, E.; Dessent, C. E., Experiment and theory confirm that UV laser photodissociation spectroscopy can distinguish protomers formed via electrospray. *Physical Chemistry Chemical Physics* **2017**, *19* (26), 17434-17440.
30. Brodbelt, J. S., Photodissociation mass spectrometry: new tools for characterization of biological molecules. *Chemical Society Reviews* **2014**, *43* (8), 2757-2783.
31. Dunbar, R. C.; Fu, E. W., Photodissociation spectroscopy of gaseous toluene (C₇H₈⁺) cations. *Journal of the American Chemical Society* **1973**, *95* (8), 2716-2718.
32. Freiser, B.; Beauchamp, J., Acid-base properties of molecules in excited electronic states utilizing ion cyclotron resonance spectroscopy. *Journal of the American Chemical Society* **1977**, *99* (10), 3214-3225.
33. Dunbar, R. C., In the beginning was H₂⁺: Mass spectrometry and the molecular spectroscopy of gas-phase ions. *International Journal of Mass Spectrometry* **2015**, *377*, 159-171.

34. Dunbar, R. C., Photodissociation of the methyl chloride (CH₃Cl⁺) and nitrous oxide (N₂O⁺) cations. *Journal of the American Chemical Society* **1971**, *93* (18), 4354-4358.
35. Casassa, M. P.; Bomse, D. S.; Beauchamp, J.; Janda, K. C., Infrared photochemistry of ethylene clusters. *The Journal of Chemical Physics* **1980**, *72* (12), 6805-6806.
36. El-Aneed, A.; Cohen, A.; Banoub, J., Mass spectrometry, review of the basics: electrospray, MALDI, and commonly used mass analyzers. *Applied Spectroscopy Reviews* **2009**, *44* (3), 210-230.
37. Konermann, L.; Ahadi, E.; Rodriguez, A. D.; Vahidi, S., Unraveling the mechanism of electrospray ionization. *Analytical Chemistry* **2013**, *85* (1), 2-9.
38. Awad, H.; Khamis, M. M.; El-Aneed, A., Mass spectrometry, review of the basics: ionization. *Applied Spectroscopy Reviews* **2015**, *50* (2), 158-175.
39. van Outersterp, R. E.; Martens, J.; Berden, G.; Koppen, V.; Cuyckens, F.; Oomens, J., Mass spectrometry-based identification of ortho-, meta- and para-isomers using infrared ion spectroscopy. *Analyst* **2020**, *145* (18), 6162-6170.
40. Müntst, M. G.; Ončák, M.; Beyer, M. K.; van der Linde, C., Infrared spectroscopy of CO₃^{•-}(H₂O) 1, 2 and CO₄^{•-}(H₂O) 1, 2. *The Journal of Chemical Physics* **2021**, *154* (8), 084301.
41. Cruz-Ortiz, A. F.; Jara-Toro, R. A.; Berdakin, M.; Loire, E.; Pino, G. A., Gas phase structure and fragmentation of [Cytosine-Guanine] Ag⁺ Ag⁺ complex studied by mass-resolved IRMPD spectroscopy. *The European Physical Journal D* **2021**, *75* (4), 1-11.
42. Cismesia, A. P.; Nicholls, G. R.; Polfer, N. C., Amine vs. carboxylic acid protonation in ortho-, meta-, and para-aminobenzoic acid: An IRMPD spectroscopy study. *Journal of Molecular Spectroscopy* **2017**, *332*, 79-85.
43. Schindler, B.; Laloy-Borgna, G.; Barnes, L.; Allouche, A.-R.; Bouju, E.; Dugas, V.; Demesmay, C.; Compagnon, I., Online separation and identification of isomers using infrared multiple photon dissociation ion spectroscopy coupled to liquid chromatography: application to the analysis of disaccharides regio-isomers and monosaccharide Anomers. *Analytical Chemistry* **2018**, *90* (20), 11741-11745.
44. Wu, R.; Hamlow, L.; He, C.; Nei, Y.-w.; Berden, G.; Oomens, J.; Rodgers, M., N₃ and O₂ protonated conformers of the cytosine mononucleotides coexist in the gas phase. *Journal of the American Society for Mass Spectrometry* **2017**, *28* (8), 1638-1646.
45. Laskin, J.; Futrell, J. H., Activation of large ions in FT-ICR mass spectrometry. *Mass Spectrometry Reviews* **2005**, *24* (2), 135-167.
46. Brodbelt, J. S.; Wilson, J. J., Infrared multiphoton dissociation in quadrupole ion traps. *Mass Spectrometry Reviews* **2009**, *28* (3), 390-424.
47. Mitra, S.; Duong, C. H.; McCaslin, L. M.; Gerber, R. B.; Johnson, M. A., Isomer-specific cryogenic ion vibrational spectroscopy of the D₂ tagged Cs⁺ (HNO₃)(H₂O) n= 0–2 complexes: ion-driven enhancement of the acidic H-bond to water. *Physical Chemistry Chemical Physics* **2020**, *22* (8), 4501-4507.
48. Perez, E. H.; Menges, F. S.; Cattaneo, M.; Mayer, J. M.; Johnson, M. A., Characterization of the non-covalent docking motif in the isolated reactant complex of a double proton-coupled electron transfer reaction with cryogenic ion spectroscopy. *The Journal of Chemical Physics* **2020**, *152* (23), 234309.
49. Chatterjee, K.; Dopfer, O., Vibrational Spectroscopy of a Potential Interstellar Ion: Protonated Methyl Formate. *The Astrophysical Journal* **2020**, *898* (1), 92.
50. Andris, E.; Navrátil, R.; Jašík, J.; Terencio, T.; Srnc, M.; Costas, M.; Roithová, J., Chasing the Evasive Fe□ O Stretch and the Spin State of the Iron (IV)–Oxo Complexes by Photodissociation Spectroscopy. *Journal of the American Chemical Society* **2017**, *139* (7), 2757-2765.

51. DeBlase, A. F.; Harrilal, C. P.; Lawler, J. T.; Burke, N. L.; McLuckey, S. A.; Zwier, T. S., Conformation-Specific Infrared and Ultraviolet Spectroscopy of Cold [YAPAA+ H]⁺ and [YGPAA+ H]⁺ Ions: A Stereochemical “Twist” on the β -Hairpin Turn. *Journal of the American Chemical Society* **2017**, *139* (15), 5481-5493.
52. Zhu, G. Z.; Qian, C. H.; Wang, L. S., Tautomer-Specific Resonant Photoelectron Imaging of Deprotonated Cytosine Anions. *Angewandte Chemie International Edition* **2019**, *58* (23), 7856-7860.
53. Weichman, M. L.; DeVine, J. A.; Levine, D. S.; Kim, J. B.; Neumark, D. M., Isomer-specific vibronic structure of the 9-, 1-, and 2-anthracenyl radicals via slow photoelectron velocity-map imaging. *Proceedings of the National Academy of Sciences* **2016**, *113* (7), 1698-1705.
54. Bull, J. N.; Anstöter, C. S.; Verlet, J. R., Fingerprinting the Excited-State Dynamics in Methyl Ester and Methyl Ether Anions of Deprotonated para-Coumaric Acid. *The Journal of Physical Chemistry A* **2020**, *124* (11), 2140-2151.
55. Woodhouse, J. L.; Assmann, M.; Parkes, M. A.; Grounds, H.; Pacman, S. J.; Anderson, J. C.; Worth, G. A.; Fielding, H. H., Photoelectron spectroscopy of isolated luciferin and infraluciferin anions in vacuo: competing photodetachment, photofragmentation and internal conversion. *Physical Chemistry Chemical Physics* **2017**, *19* (34), 22711-22720.
56. Dryza, V.; Chalyavi, N.; Sanelli, J. A.; Bieske, E. J., Electronic absorptions of the benzylium cation. *The Journal of Chemical Physics* **2012**, *137* (20), 204304.
57. Jacovella, U.; da Silva, G.; Bieske, E. J., Unveiling New Isomers and Rearrangement Routes on the C₇H₈⁺ Potential Energy Surface. *The Journal of Physical Chemistry A* **2019**, *123* (4), 823-830.
58. Jacovella, U.; Scholz, M. S.; Bieske, E. J., Electronic Spectrum of the Tropylium Cation in the Gas Phase. *The Journal of Physical Chemistry Letters* **2020**, *11* (20), 8867-8872.
59. Krechkivska, O.; Liu, Y.; Lee, K. L. K.; Nauta, K.; Kable, S. H.; Schmidt, T. W., Triple-Resonance Spectroscopy Reveals the Excitation Spectrum of Very Cold, Isomer-Specific Protonated Naphthalene. *The Journal of Physical Chemistry Letters* **2013**, *4* (21), 3728-3732.
60. Gabelica, V.; Marklund, E., Fundamentals of ion mobility spectrometry. *Current Opinion in Chemical Biology* **2018**, *42*, 51-59.
61. Lanucara, F.; Holman, S. W.; Gray, C. J.; Eyers, C. E., The power of ion mobility-mass spectrometry for structural characterization and the study of conformational dynamics. *Nature Chemistry* **2014**, *6* (4), 281-294.
62. d'Atri, V.; Causon, T.; Hernandez-Alba, O.; Mutabazi, A.; Veuthey, J. L.; Cianferani, S.; Guillarme, D., Adding a new separation dimension to MS and LC-MS: What is the utility of ion mobility spectrometry? *Journal of Separation Science* **2018**, *41* (1), 20-67.
63. Dunbar, R. C., Photodissociation of trapped ions. *International Journal of Mass Spectrometry* **2000**, *200* (1-3), 571-589.
64. Zeng, H. J.; Yang, N.; Johnson, M. A., Introductory lecture: advances in ion spectroscopy: from astrophysics to biology. *Faraday Discussions* **2019**, *217*, 8-33.
65. Tureček, F., UV-vis spectroscopy of gas-phase ions. *Mass Spectrometry Reviews* **2021**.
66. Guasco, T. L.; Johnson, M. A., Applications of Lasers and Mass Spectrometry in Molecular Spectroscopy and Molecular Structure Determination. In *Emerging Trends in Chemical Applications of Lasers*, ACS Publications: 2021; pp 277-306.
67. Soorkia, S.; Jouvét, C.; Grégoire, G., UV photoinduced dynamics of conformer-resolved aromatic peptides. *Chemical Reviews* **2019**, *120* (7), 3296-3327.

68. Tureček, F. e., Flying DNA Cation Radicals in the Gas Phase: Generation and Action Spectroscopy of Canonical and Noncanonical Nucleobase Forms. *The Journal of Physical Chemistry B* **2021**.
69. Zettergren, H.; Domaracka, A.; Schlathölter, T.; Bolognesi, P.; Díaz-Tendero, S.; Łabuda, M.; Tosić, S.; Maclot, S.; Johnsson, P.; Steber, A., Roadmap on dynamics of molecules and clusters in the gas phase. *The European Physical Journal D* **2021**, *75* (5), 1-53.
70. Antoine, R.; Dugourd, P., Visible and ultraviolet spectroscopy of gas phase protein ions. *Physical Chemistry Chemical Physics* **2011**, *13* (37), 16494-16509.
71. Hendricks, N. G.; Julian, R. R., Leveraging ultraviolet photodissociation and spectroscopy to investigate peptide and protein three-dimensional structure with mass spectrometry. *Analyst* **2016**, *141* (15), 4534-4540.
72. Reilly, J. P., Ultraviolet photofragmentation of biomolecular ions. *Mass Spectrometry Reviews* **2009**, *28* (3), 425-447.
73. Rizzo, T. R.; Stearns, J. A.; Boyarkin, O. V., Spectroscopic studies of cold, gas-phase biomolecular ions. *International Reviews in Physical Chemistry* **2009**, *28* (3), 481-515.
74. Boyarkin, O. V.; Kopysov, V., Cryogenically cooled octupole ion trap for spectroscopy of biomolecular ions. *Review of Scientific Instruments* **2014**, *85* (3), 033105.
75. Dang, A.; Korn, J. A.; Gladden, J.; Mozzone, B.; Tureček, F., UV-Vis Photodissociation Action Spectroscopy on Thermo LTQ-XL ETD and Bruker amaZon Ion Trap Mass Spectrometers: a Practical Guide. *Journal of The American Society for Mass Spectrometry* **2019**, *30* (9), 1558-1564.
76. Hansen, C. S.; Kirk, B. B.; Blanksby, S. J.; O'Hair, R. A.; Trevitt, A. J., UV photodissociation action spectroscopy of haloanilinium ions in a linear quadrupole ion trap mass spectrometer. *Journal of the American Society for Mass Spectrometry* **2013**, *24* (6), 932-940.
77. Matthews, E.; Sen, A.; Yoshikawa, N.; Bergström, E.; Dessent, C. E., UV laser photoactivation of hexachloroplatinate bound to individual nucleobases in vacuo as molecular level probes of a model photopharmaceutical. *Physical Chemistry Chemical Physics* **2016**, *18* (22), 15143-15152.
78. Bian, Q.; Forbes, M. W.; Talbot, F. O.; Jockusch, R. A., Gas-phase fluorescence excitation and emission spectroscopy of mass-selected trapped molecular ions. *Physical Chemistry Chemical Physics* **2010**, *12* (11), 2590-2598.
79. Ly, T.; Julian, R. R., Residue-specific radical-directed dissociation of whole proteins in the gas phase. *Journal of the American Chemical Society* **2008**, *130* (1), 351-358.
80. Stockett, M. H.; Houmøller, J.; Stöckel, K.; Svendsen, A.; Brøndsted Nielsen, S., A cylindrical quadrupole ion trap in combination with an electrospray ion source for gas-phase luminescence and absorption spectroscopy. *Review of Scientific Instruments* **2016**, *87* (5), 053103.
81. Coughlan, N. J.; Carr, P. J.; Walker, S. C.; Zhou, C.; Guna, M.; Campbell, J. L.; Hopkins, W. S., Measuring Electronic Spectra of Differential Mobility-Selected Ions in the Gas Phase. *Journal of the American Society for Mass Spectrometry* **2020**.
82. Günther, A.; Nieto, P.; Müller, D.; Sheldrick, A.; Gerlich, D.; Dopfer, O., BerlinTrap: A new cryogenic 22-pole ion trap spectrometer. *Journal of Molecular Spectroscopy* **2017**, *332*, 8-15.
83. Alata, I.; Bert, J.; Broquier, M.; Dedonder, C.; Féraud, G.; Grégoire, G.; Soorkia, S.; Marceca, E.; Jouvét, C., Electronic spectra of the protonated indole chromophore in the gas phase. *The Journal of Physical Chemistry A* **2013**, *117* (21), 4420-4427.

84. Ishiuchi, S.-i.; Wako, H.; Kato, D.; Fujii, M., High-cooling-efficiency cryogenic quadrupole ion trap and UV-UV hole burning spectroscopy of protonated tyrosine. *Journal of Molecular Spectroscopy* **2017**, *332*, 45-51.
85. Kang, H.; Féraud, G.; Dedonder-Lardeux, C.; Jouvet, C., New method for double-resonance spectroscopy in a cold quadrupole ion trap and its application to UV-UV hole-burning spectroscopy of protonated adenine dimer. *The Journal of Physical Chemistry Letters* **2014**, *5* (15), 2760-2764.
86. Wang, X.-B.; Wang, L.-S., Development of a low-temperature photoelectron spectroscopy instrument using an electrospray ion source and a cryogenically controlled ion trap. *Review of Scientific Instruments* **2008**, *79* (7), 073108.
87. Xu, S.; Gozem, S.; Krylov, A. I.; Christopher, C. R.; Weber, J. M., Ligand influence on the electronic spectra of monocationic copper-bipyridine complexes. *Physical Chemistry Chemical Physics* **2015**, *17* (47), 31938-31946.
88. Jasik, J.; Navrátil, R.; Němec, I.; Roithová, J., Infrared and Visible Photodissociation Spectra of Rhodamine Ions at 3 K in the Gas Phase. *The Journal of Physical Chemistry A* **2015**, *119* (51), 12648-12655.
89. Redwine, J. G.; Davis, Z. A.; Burke, N. L.; Oglesbee, R. A.; McLuckey, S. A.; Zwier, T. S., A novel ion trap based tandem mass spectrometer for the spectroscopic study of cold gas phase polyatomic ions. *International Journal of Mass Spectrometry* **2013**, *348*, 9-14.
90. Adamson, B.; Coughlan, N.; Continetti, R.; Bieske, E., Changing the shape of molecular ions: photoisomerization action spectroscopy in the gas phase. *Physical Chemistry Chemical Physics* **2013**, *15* (24), 9540-9548.
91. Adamson, B.; Coughlan, N.; Markworth, P.; Continetti, R.; Bieske, E., An ion mobility mass spectrometer for investigating photoisomerization and photodissociation of molecular ions. *Review of Scientific Instruments* **2014**, *85* (12), 123109.
92. Bellina, B.; Brown, J. M.; Ujma, J.; Murray, P.; Giles, K.; Morris, M.; Compagnon, I.; Barran, P. E., UV photodissociation of trapped ions following ion mobility separation in a Q-ToF mass spectrometer. *Analyst* **2014**, *139* (24), 6348-6351.
93. Misaizu, F.; Hori, N.; Tanaka, H.; Komatsu, K.; Furuya, A.; Ohno, K., Isomer-selected photoreactions of gas-phase cluster ions. *The European Physical Journal D* **2009**, *52* (1), 59-62.
94. Andersen, J. U.; Hvelplund, P.; Nielsen, S. B.; Tomita, S.; Wahlgreen, H.; Møller, S. P.; Pedersen, U. V.; Forster, J. S.; Jørgensen, T. J., The combination of an electrospray ion source and an electrostatic storage ring for lifetime and spectroscopy experiments on biomolecules. *Review of Scientific Instruments* **2002**, *73* (3), 1284-1287.
95. Thomas, R. D.; Schmidt, H. T.; Andler, G.; Björkhage, M.; Blom, M.; Brännholm, L.; Bäckström, E.; Danared, H.; Das, S.; Haag, N., The double electrostatic ion ring experiment: A unique cryogenic electrostatic storage ring for merged ion-beams studies. *Review of Scientific Instruments* **2011**, *82* (6), 065112.
96. Depland, A. D.; Renois-Predelus, G.; Schindler, B.; Compagnon, I., Identification of sialic acid linkage isomers in glycans using coupled InfraRed Multiple Photon Dissociation (IRMPD) spectroscopy and mass spectrometry. *International Journal of Mass Spectrometry* **2018**, *434*, 65-69.
97. Jaravel, L.; Schindler, B.; Randon, J.; Compagnon, I.; Demesmay, C.; Dugas, V., Off-line coupling of capillary isotachopheresis separation to IRMPD spectroscopy for glycosaminoglycans analysis: Application to the chondroitin sulfate disaccharides model solutes. *Journal of Chromatography A* **2020**, *1617*, 460782.
98. Broquier, M.; Soorkia, S.; Dedonder-Lardeux, C.; Jouvet, C.; Theulé, P.; Grégoire, G., Twisted intramolecular charge transfer in protonated amino pyridine. *The Journal of Physical Chemistry A* **2016**, *120* (21), 3797-3809.

99. Garcia, R. L.; Nieuwjaer, N.; Desfrancois, C.; Lecomte, F.; Leite, S.; Manil, B.; Broquier, M.; Grégoire, G., Vibronic spectra of protonated hydroxypyridines: contributions of prefulvenic and planar structures. *Physical Chemistry Chemical Physics* **2017**, *19* (12), 8258-8268.
100. Soorkia, S.; Broquier, M.; Grégoire, G., Multiscale excited state lifetimes of protonated dimethyl aminopyridines. *Physical Chemistry Chemical Physics* **2016**, *18* (34), 23785-23794.
101. Bezzina, J. P., Photochemistry of Fundamental Nitrogen Containing Aromatic Heterocycles. *Master of Philosophy Thesis, School of Chemistry, University of Wollongong* **2018**.
102. Noble, J. A.; Marceca, E.; Dedonder, C.; Phasayavan, W.; Féraud, G.; Inceesungvorn, B.; Jouvét, C., Influence of the N atom position on the excited state photodynamics of protonated azaindole. *Physical Chemistry Chemical Physics* **2020**.
103. Noble, J. A.; Marceca, E.; Dedonder, C.; Jouvét, C., Influence of the N atom and its position on electron photodetachment of deprotonated indole and azaindole. *Physical Chemistry Chemical Physics* **2020**, *22* (46), 27290-27299.
104. Pino, G. A.; Féraud, G.; Broquier, M.; Grégoire, G.; Soorkia, S.; Dedonder, C.; Jouvét, C., Non-radiative processes in protonated diazines, pyrimidine bases and an aromatic azine. *Physical Chemistry Chemical Physics* **2016**, *18* (30), 20126-20134.
105. Hansen, C. S., Ultraviolet photodissociation of protonated pyridine derivatives: action spectroscopy and mass spectrometry. *Doctor of Philosophy Thesis, School of Chemistry, University of Wollongong* **2016**.
106. Dodson, L. G.; Zagorec-Marks, W.; Xu, S.; Smith, J. E.; Weber, J. M., Intrinsic photophysics of nitrophenolate ions studied by cryogenic ion spectroscopy. *Physical Chemistry Chemical Physics* **2018**, *20* (45), 28535-28543.
107. Wanko, M.; Houmøller, J.; Støchkel, K.; Kirketerp, M.-B. S.; Petersen, M. Å.; Nielsen, M. B.; Nielsen, S. B.; Rubio, A., Substitution effects on the absorption spectra of nitrophenolate isomers. *Physical Chemistry Chemical Physics* **2012**, *14* (37), 12905-12911.
108. Houmøller, J.; Wanko, M.; Rubio, A.; Nielsen, S. B., Effect of a Single Water Molecule on the Electronic Absorption by o- and p-Nitrophenolate: A Shift to the Red or to the Blue? *The Journal of Physical Chemistry A* **2015**, *119* (47), 11498-11503.
109. Uleanya, K.; Dessent, C. E. H., Investigating the Mapping of Chromophore Excitations onto the Electron Detachment Spectrum: Photodissociation Spectroscopy of Iodide Ion-Thiouracil Clusters. *Physical Chemistry Chemical Physics* **2021**.
110. Féraud, G.; Domenianni, L.; Marceca, E.; Dedonder-Lardeux, C.; Jouvét, C., Photodissociation Electronic Spectra of Cold Protonated Quinoline and Isoquinoline in the Gas Phase. *The Journal of Physical Chemistry A* **2017**, *121* (13), 2580-2587.
111. Hansen, C. S.; Blanksby, S. J.; Trevitt, A. J., Ultraviolet photodissociation action spectroscopy of gas-phase protonated quinoline and isoquinoline cations. *Physical Chemistry Chemical Physics* **2015**, *17* (39), 25882-25890.
112. Loos, P.-F. o.; Galland, N.; Jacquemin, D., Theoretical 0–0 Energies with Chemical Accuracy. *The Journal of Physical Chemistry Letters* **2018**, *9* (16), 4646-4651.
113. Loos, P.-F.; Jacquemin, D., Chemically Accurate 0–0 Energies with Not-so-Accurate Excited State Geometries. *Journal of Chemical Theory and Computation* **2019**, *15* (4), 2481-2491.
114. Loos, P.-F.; Scemama, A.; Jacquemin, D., The Quest for Highly Accurate Excitation Energies: A Computational Perspective. *The Journal of Physical Chemistry Letters* **2020**, *11* (6), 2374-2383.

115. Coughlan, N. J.; Carr, P. J.; Walker, S. C.; Zhou, C.; Guna, M.; Campbell, J. L.; Hopkins, W. S., Measuring electronic spectra of differential mobility-selected ions in the gas phase. *Journal of the American Society for Mass Spectrometry* **2020**, *31* (2), 405-410.
116. Xia, H.; Attygalle, A. B., Untrapping kinetically trapped ions: the role of water vapor and ion-source activation conditions on the gas-phase protomer ratio of benzocaine revealed by ion-mobility mass spectrometry. *Journal of The American Society for Mass Spectrometry* **2017**, *28* (12), 2580-2587.
117. Marlton, S. J.; McKinnon, B. I.; Ucur, B.; Maccarone, A. T.; Donald, W. A.; Blanksby, S. J.; Trevitt, A. J., Selecting and identifying gas-phase protonation isomers of nicotineH⁺ using combined laser, ion mobility and mass spectrometry techniques. *Faraday Discussions* **2019**, *217*, 453-475.
118. Chandran, J.; Zheng, Z.; Thomas, V. I.; Rajalakshmi, C.; Attygalle, A. B., LC-MS analysis of p-aminosalicylic acid under electrospray ionization conditions manifests a profound solvent effect. *Analyst* **2020**, *145* (15), 5333-5344.
119. Warnke, S.; Seo, J.; Boschmans, J.; Sobott, F.; Scrivens, J. H.; Bleiholder, C.; Bowers, M. T.; Gewinner, S.; Schöllkopf, W.; Pagel, K., Protomers of benzocaine: solvent and permittivity dependence. *Journal of the American Chemical Society* **2015**, *137* (12), 4236-4242.
120. Schmidt, J.; Meyer, M. M.; Spector, I.; Kass, S. R., Infrared multiphoton dissociation spectroscopy study of protonated p-aminobenzoic acid: does electrospray ionization afford the amino-or carboxy-protonated ion? *The Journal of Physical Chemistry A* **2011**, *115* (26), 7625-7632.
121. Tian, Z.; Kass, S. R., Gas-phase versus liquid-phase structures by electrospray ionization mass spectrometry. *Angewandte Chemie* **2009**, *121* (7), 1347-1349.
122. Matthews, E.; Cercola, R.; Dessent, C., Protomer-Dependent Electronic Spectroscopy and Photochemistry of the Model Flavin Chromophore Alloxazine. *Molecules* **2018**, *23* (8), 2036.
123. Matthews, E.; Dessent, C. E., Locating the proton in nicotinamide protomers via low-resolution UV action spectroscopy of electrosprayed solutions. *The Journal of Physical Chemistry A* **2016**, *120* (46), 9209-9216.
124. Pitzer, M.; Ozga, C.; Küstner-Wetekam, C.; Reiß, P.; Knie, A.; Ehresmann, A.; Jahnke, T.; Giuliani, A.; Nahon, L., State-dependent fragmentation of protonated uracil and uridine. *The Journal of Physical Chemistry A* **2019**, *123* (16), 3551-3557.
125. Pedersen, S. Ø.; Byskov, C. S.; Turecek, F.; Nielsen, S. B., Structures of protonated thymine and uracil and their monohydrated gas-phase ions from ultraviolet action spectroscopy and theory. *The Journal of Physical Chemistry A* **2014**, *118* (24), 4256-4265.
126. Berenbeim, J. A.; Wong, N. G.; Cockett, M. C.; Berden, G.; Oomens, J.; Rijs, A. M.; Dessent, C. E., Unravelling the Keto–Enol Tautomer Dependent Photochemistry and Degradation Pathways of the Protonated UVA Filter Avobenzone. *The Journal of Physical Chemistry A* **2020**, *124* (15), 2919-2930.
127. Wong, N. G.; Berenbeim, J. A.; Hawkrige, M.; Matthews, E.; Dessent, C. E., Mapping the intrinsic absorption properties and photodegradation pathways of the protonated and deprotonated forms of the sunscreen oxybenzone. *Physical Chemistry Chemical Physics* **2019**, *21* (26), 14311-14321.
128. Berenbeim, J. A.; Wong, N. G.; Cockett, M. C.; Berden, G.; Oomens, J.; Rijs, A. M.; Dessent, C. E., Sodium cationization can disrupt the intramolecular hydrogen bond that mediates the sunscreen activity of oxybenzone. *Physical Chemistry Chemical Physics* **2020**, *22* (35), 19522-19531.
129. Huang, S. R.; Dang, A.; Tureček, F. e., Ground and Excited States of Gas-Phase DNA Nucleobase Cation-Radicals. A UV–vis Photodissociation Action Spectroscopy and

- Computational Study of Adenine and 9-Methyladenine. *Journal of the American Society for Mass Spectrometry* **2020**, *31* (6), 1271-1281.
130. Lesslie, M.; Lawler, J. T.; Dang, A.; Korn, J. A.; Bím, D.; Steinmetz, V.; Maître, P.; Tureček, F.; Ryzhov, V., Cytosine Radical Cations: A Gas-Phase Study Combining IRMPD Spectroscopy, UVPD Spectroscopy, Ion–Molecule Reactions, and Theoretical Calculations. *ChemPhysChem* **2017**, *18* (10), 1293-1301.
131. Dang, A.; Nguyen, H. T.; Ruiz, H.; Piacentino, E.; Ryzhov, V.; Tureček, F. e., Experimental evidence for noncanonical thymine cation radicals in the gas phase. *The Journal of Physical Chemistry B* **2018**, *122* (1), 86-97.
132. Dang, A.; Liu, Y.; Tureček, F. e., Uv–vis action spectroscopy of guanine, 9-methylguanine, and guanosine cation radicals in the gas phase. *The Journal of Physical Chemistry A* **2019**, *123* (15), 3272-3284.
133. Müller, D.; Dopfer, O., Vibronic optical spectroscopy of cryogenic flavin ions: the O₂⁺ and N1 tautomers of protonated lumiflavin. *Physical Chemistry Chemical Physics* **2020**, *22* (33), 18328-18339.
134. Müller, D.; Dopfer, O., Optical spectroscopy of cryogenic metalated flavins: The O₂⁽⁺⁾ isomers of M⁺ lumiflavin (M= Li–Cs). *Journal of Photochemistry and Photobiology* **2020**, *3*, 100009.
135. Müller, D.; Nieto, P.; Miyazaki, M.; Dopfer, O., Effect of alkali ions on optical properties of flavins: vibronic spectra of cryogenic M⁺ lumiflavin complexes (M= Li–Cs). *Faraday Discussions* **2019**, *217*, 256-275.
136. Broquier, M.; Soorkia, S.; Pino, G. A.; Dedonder-Lardeux, C.; Jouvét, C.; Gregoire, G., Excited State Dynamics of Cold Protonated Cytosine Tautomers: Characterization of Charge Transfer, Inter System Crossing and Internal Conversion Processes. *The Journal of Physical Chemistry A* **2017**, *121* (34), 6429-6439.
137. Noble, J. A.; Dedonder-Lardeux, C.; Mascetti, J.; Jouvét, C., Electronic Spectroscopy of Protonated 1-Aminopyrene in a Cold Ion Trap. *Chemistry–An Asian Journal* **2017**, *12* (13), 1523-1531.
138. Noble, J. A.; Broquier, M.; Gregoire, G.; Soorkia, S.; Pino, G.; Marceca, E.; Dedonder-Lardeux, C.; Jouvét, C., Tautomerism and electronic spectroscopy of protonated 1- and 2-aminonaphthalene. *Physical Chemistry Chemical Physics* **2018**, *20* (9), 6134-6145.
139. Andris, E.; Navrátil, R.; Jasík, J.; Puri, M.; Costas, M.; Que Jr, L.; Roithová, J., Trapping iron (III)–oxo species at the boundary of the “Oxo Wall”: insights into the nature of the Fe (III)–O bond. *Journal of the American Chemical Society* **2018**, *140* (43), 14391-14400.
140. Andris, E.; Navrátil, R.; Jašík, J.; Sabenya, G.; Costas, M.; Srnec, M.; Roithová, J., Spin-State-Controlled Photodissociation of Iron (III) Azide to an Iron (V) Nitride Complex. *Angewandte Chemie International Edition* **2017**, *56* (45), 14057-14060.
141. Navrátil, R.; Wiedbrauk, S.; Jašík, J.; Dube, H.; Roithová, J., Transforming hemithioindigo from a two-way to a one-way molecular photoswitch by isolation in the gas phase. *Physical Chemistry Chemical Physics* **2018**, *20* (10), 6868-6876.
142. Zagorec-Marks, W.; Foreman, M. M.; Verlet, J. R.; Weber, J. M., Cryogenic Ion Spectroscopy of the Green Fluorescent Protein Chromophore in Vacuo. *The Journal of Physical Chemistry Letters* **2019**, *10* (24), 7817-7822.
143. Sapparbaev, E.; Yamaletdinov, R.; Boyarkin, O. V., Identification of Isomeric Lipids by UV Spectroscopy of Noncovalent Complexes with Aromatic Molecules. *Analytical Chemistry* **2021**.
144. Sapparbaev, E.; Kopysov, V.; Aladinskaia, V.; Ferrieres, V.; Legentil, L.; Boyarkin, O. V., Identification and Quantification of Any Isoforms of Carbohydrates by 2D UV-MS Fingerprinting of Cold Ions. *Analytical Chemistry* **2020**, *92* (21), 14624-14632.

145. Nieto, P.; Müller, D.; Sheldrick, A.; Günther, A.; Miyazaki, M.; Dopfer, O., Effect of alkali ions on optical properties of flavins: vibronic spectra of cryogenic M⁺ lumichrome ions (M= Li–Cs) in the gas phase. *Physical Chemistry Chemical Physics* **2018**, *20* (34), 22148-22158.
146. Féraud, G.; Esteves-Lopez, N.; Dedonder-Lardeux, C.; Jouvét, C., UV spectroscopy of cold ions as a probe of the protonation site. *Physical Chemistry Chemical Physics* **2015**, *17* (39), 25755-25760.
147. Patzer, A.; Schütz, M.; Jouvét, C.; Dopfer, O., Experimental Observation and Quantum Chemical Characterization of the S₁ ← S₀ Transition of Protonated Naphthalene–Argon Clusters. *The Journal of Physical Chemistry A* **2013**, *117* (39), 9785-9793.
148. Alata, I.; Broquier, M.; Dedonder, C.; Jouvét, C.; Marceca, E., Electronic excited states of protonated aromatic molecules: Protonated Fluorene. *Chemical Physics* **2012**, *393* (1), 25-31.
149. Soorkia, S.; Broquier, M.; Grégoire, G., Conformer-and mode-specific excited state lifetimes of cold protonated tyrosine ions. *The Journal of Physical Chemistry Letters* **2014**, *5* (24), 4349-4355.
150. Dezalay, J.; Broquier, M.; Soorkia, S.; Grégoire, G., Excited state dynamics of protonated keto uracil: intersystem crossing pathways in competition. *The European Physical Journal D* **2021**, *75* (1), 1-11.
151. Papanikolas, J. M.; Vorsa, V.; Nadal, M. E.; Campagnola, P. J.; Gord, J. R.; Lineberger, W., I₂⁻ photofragmentation/recombination dynamics in size-selected I₂⁻(CO₂)_n cluster ions: Observation of coherent I... I⁻ vibrational motion. *The Journal of Chemical Physics* **1992**, *97* (9), 7002-7005.
152. Vorsa, V.; Nandi, S.; Campagnola, P. J.; Larsson, M.; Lineberger, W., Recombination dynamics of photodissociated I₂⁻ in size selected Ar and CO₂ clusters. *The Journal of Chemical Physics* **1997**, *106* (4), 1402-1410.
153. Sanov, A.; Sanford, T.; Nandi, S.; Lineberger, W. C., Spin-orbit relaxation and recombination dynamics in I₂⁻(CO₂)_n and I₂⁻(OCS)_n cluster ions: A new type of photofragment caging reaction. *The Journal of Chemical Physics* **1999**, *111* (2), 664-675.
154. Hervé, M.; Boyer, A.; Brédy, R.; Compagnon, I.; Allouche, A.-R.; Lépine, F., Controlled ultrafast ππ*-πσ* dynamics in tryptophan-based peptides with tailored micro-environment. *Communications Chemistry* **2021**, *4* (1), 1-7.
155. Svendsen, A.; Kiefer, H. V.; Pedersen, H. B.; Bochenkova, A. V.; Andersen, L. H., Origin of the intrinsic fluorescence of the green fluorescent protein. *Journal of the American Chemical Society* **2017**, *139* (25), 8766-8771.
156. Kiefer, H. V.; Gruber, E.; Langeland, J.; Kusocek, P. A.; Bochenkova, A. V.; Andersen, L. H., Intrinsic photoisomerization dynamics of protonated Schiff-base retinal. *Nature Communications* **2019**, *10* (1), 1-9.
157. Kang, H.; Jouvét, C.; Dedonder-Lardeux, C.; Martrenchard, S.; Charriere, C.; Grégoire, G.; Desfrancois, C.; Schermann, J.; Barat, M.; Fayeton, J., Photoinduced processes in protonated tryptamine. *The Journal of Chemical Physics* **2005**, *122* (8), 084307.
158. Kang, H.; Dedonder-Lardeux, C.; Jouvét, C.; Grégoire, G.; Desfrancois, C.; Schermann, J.-P.; Barat, M.; Fayeton, A., Control of bond-cleaving reactions of free protonated tryptophan ion by femtosecond laser pulses. *The Journal of Physical Chemistry A* **2005**, *109* (11), 2417-2420.
159. Kang, H.; Jouvét, C.; Dedonder-Lardeux, C.; Martrenchard, S.; Grégoire, G.; Desfrancois, C.; Schermann, J.-P.; Barat, M.; Fayeton, J., Ultrafast deactivation mechanisms of protonated aromatic amino acids following UV excitation. *Physical Chemistry Chemical Physics* **2005**, *7* (2), 394-398.

160. Dezalay, J.; Broquier, M.; Soorkia, S.; Hirata, K.; Ishiuchi, S.-i.; Fujii, M.; Grégoire, G., Excited-state proton transfer in protonated adrenaline revealed by cryogenic UV photodissociation spectroscopy. *Physical Chemistry Chemical Physics* **2020**, *22* (20), 11498-11507.
161. Liedy, F.; Böppler, F.; Waldt, E.; Nosenko, Y.; Imanbaew, D.; Bhunia, A.; Yadav, M.; Diller, R.; Kappes, M. M.; Roesky, P. W., Photodynamics and Luminescence of Mono- and Tri-Nuclear Lanthanide Complexes in the Gas Phase and in Solution. *ChemPhysChem* **2018**, *19* (22), 3050-3060.
162. Kruppa, S.; Böppler, F.; Klopper, W.; Walg, S.; Thiel, W.; Diller, R.; Riehn, C., Ultrafast excited-state relaxation of a binuclear Ag (I) phosphine complex in gas phase and solution. *Physical Chemistry Chemical Physics* **2017**, *19* (34), 22785-22800.
163. Kruppa, S. V.; Böppler, F.; Holzer, C.; Klopper, W.; Diller, R.; Riehn, C., Vibrational coherence controls molecular fragmentation: Ultrafast photodynamics of the [Ag₂Cl]⁺ scaffold. *The Journal of Physical Chemistry Letters* **2018**, *9* (4), 804-810.
164. MacAleese, L.; Hermelin, S.; Hage, K. E.; Chouzenoux, P.; Kulesza, A.; Antoine, R.; Bonacina, L.; Meuwly, M.; Wolf, J.-P.; Dugourd, P., Sequential proton coupled electron transfer (PCET): dynamics observed over 8 orders of magnitude in time. *Journal of the American Chemical Society* **2016**, *138* (13), 4401-4407.
165. Bouakil, M.; Chirot, F.; Girod, M.; Dugourd, P.; MacAleese, L., Secondary structure effects on internal proton transfer in poly-peptides. *Structural Dynamics* **2020**, *7* (2), 024302.
166. Bouakil, M.; Kulesza, A.; Daly, S.; MacAleese, L.; Antoine, R.; Dugourd, P., Visible multiphoton dissociation of chromophore-tagged peptides. *Journal of the American Society for Mass Spectrometry* **2017**, *28* (10), 2181-2188.
167. Scutelnic, V.; Prlj, A.; Zabuga, A.; Corminboeuf, C. m.; Rizzo, T. R., Infrared spectroscopy as a probe of electronic energy transfer. *The Journal of Physical Chemistry Letters* **2018**, *9* (12), 3217-3223.
168. Zabuga, A. V.; Kamrath, M. Z.; Boyarkin, O. V.; Rizzo, T. R., Fragmentation mechanism of UV-excited peptides in the gas phase. *The Journal of Chemical Physics* **2014**, *141* (15), 10B609_1.
169. Yang, N.; Edington, S. C.; Choi, T. H.; Henderson, E. V.; Heindel, J. P.; Xantheas, S. S.; Jordan, K. D.; Johnson, M. A., Mapping the temperature-dependent and network site-specific onset of spectral diffusion at the surface of a water cluster cage. *Proceedings of the National Academy of Sciences* **2020**, *117* (42), 26047-26052.
170. Ishiuchi, S.-i.; Wako, H.; Xantheas, S. S.; Fujii, M., Probing the selectivity of Li⁺ and Na⁺ cations on noradrenaline at the molecular level. *Faraday Discussions* **2019**, *217*, 396-413.
171. Dean, J. C.; Burke, N. L.; Hopkins, J. R.; Redwine, J. G.; Ramachandran, P.; McLuckey, S. A.; Zwier, T. S., UV photofragmentation and IR spectroscopy of cold, G-type β-O-4 and β-β dilignol-alkali metal complexes: structure and linkage-dependent photofragmentation. *The Journal of Physical Chemistry A* **2015**, *119* (10), 1917-1932.
172. Nagornova, N. S.; Rizzo, T. R.; Boyarkin, O. V., Exploring the Mechanism of IR-UV Double-Resonance for Quantitative Spectroscopy of Protonated Polypeptides and Proteins. *Angewandte Chemie* **2013**, *125* (23), 6118-6121.
173. Stearns, J. A.; Seaiby, C.; Boyarkin, O. V.; Rizzo, T. R., Spectroscopy and conformational preferences of gas-phase helices. *Physical Chemistry Chemical Physics* **2009**, *11* (1), 125-132.
174. Boyarkin, O. V., Cold ion spectroscopy for structural identifications of biomolecules. *International Reviews in Physical Chemistry* **2018**, *37* (3-4), 559-606.

175. Koyasu, K.; Ohtaki, T.; Hori, N.; Misaizu, F., Isomer-resolved dissociation of small carbon cluster cations, $C_7^+–C_{10}^+$. *Chemical Physics Letters* **2012**, *523*, 54-59.
176. Fromherz, R.; Ganteför, G.; Shvartsburg, A. A., Isomer-resolved ion spectroscopy. *Physical review letters* **2002**, *89* (8), 083001.
177. Moriyama, R.; Ohtaki, T.; Hosoya, J.; Koyasu, K.; Misaizu, F., Isomer-separated photodissociation of large sized silicon and carbon cluster ions: Drift tube experiment combined with a tandem reflectron mass spectrometer for $Si\ 24^+–Si\ 27^+$ and $C\ 32^+–C\ 38^+$. *The European Physical Journal D* **2013**, *67* (1), 1-5.
178. Zucker, S. M.; Lee, S.; Webber, N.; Valentine, S. J.; Reilly, J. P.; Clemmer, D. E., An ion mobility/ion trap/photodissociation instrument for characterization of ion structure. *Journal of the American Society for Mass Spectrometry* **2011**, *22* (9).
179. Vonderach, M.; Ehrler, O. T.; Matheis, K.; Weis, P.; Kappes, M. M., Isomer-selected photoelectron spectroscopy of isolated DNA oligonucleotides: phosphate and nucleobase deprotonation at high negative charge states. *Journal of the American Chemical Society* **2012**, *134* (18), 7830-7841.
180. Vonderach, M.; Ehrler, O. T.; Weis, P.; Kappes, M. M., Combining ion mobility spectrometry, mass spectrometry, and photoelectron spectroscopy in a high-transmission instrument. *Analytical Chemistry* **2011**, *83* (3), 1108-1115.
181. Vonderach, M.; Winghart, M.-O.; MacAleese, L.; Chirot, F.; Antoine, R.; Dugourd, P.; Weis, P.; Hampe, O.; Kappes, M. M., Conformer-selective photoelectron spectroscopy of α -lactalbumin derived multianions in the gas phase. *Physical Chemistry Chemical Physics* **2014**, *16* (7), 3007-3013.
182. Warnke, S.; Baldauf, C.; Bowers, M. T.; Pagel, K.; von Helden, G., Photodissociation of conformer-selected ubiquitin ions reveals site-specific cis/trans isomerization of proline peptide bonds. *Journal of the American Chemical Society* **2014**, *136* (29), 10308-10314.
183. Warnke, S.; von Helden, G.; Pagel, K., Analyzing the higher order structure of proteins with conformer-selective ultraviolet photodissociation. *Proteomics* **2015**, *15* (16), 2804-2812.
184. Simon, A.-L.; Chirot, F.; Choi, C. M.; Clavier, C.; Barbaire, M.; Maurelli, J.; Dagany, X.; MacAleese, L.; Dugourd, P., Tandem ion mobility spectrometry coupled to laser excitation. *Review of Scientific Instruments* **2015**, *86* (9), 094101.
185. Theisen, A.; Yan, B.; Brown, J. M.; Morris, M.; Bellina, B.; Barran, P. E., Use of ultraviolet photodissociation coupled with ion mobility mass spectrometry to determine structure and sequence from drift time selected peptides and proteins. *Analytical Chemistry* **2016**, *88* (20), 9964-9971.
186. Morrison, K. A.; Clowers, B. H., Differential fragmentation of mobility-selected glycans via ultraviolet photodissociation and ion mobility-mass spectrometry. *Journal of the American Society for Mass Spectrometry* **2017**, *28* (6), 1236-1241.
187. Frankevich, V.; Martinez-Lozano Sinues, P.; Barylyuk, K.; Zenobi, R., Ion mobility spectrometry coupled to laser-induced fluorescence. *Analytical Chemistry* **2013**, *85* (1), 39-43.
188. Frankevich, V. E.; Barylyuk, K. V.; Sinues, P. M.-L.; Zenobi, R., Ion mobility spectrometry coupled to laser-induced fluorescence for probing the electronic structure and conformation of gas-phase ions. *Journal of Analytical Chemistry* **2014**, *69* (13), 1215-1219.
189. Guo, K.; Ni, K.; Song, X.; Li, K.; Tang, B.; Yu, Q.; Qian, X.; Wang, X., Ion distribution profiling in an ion mobility spectrometer by laser-induced fluorescence. *Analytical Chemistry* **2018**, *90* (7), 4514-4520.

190. Hernandez, O.; Isenberg, S.; Steinmetz, V.; Glish, G. L.; Maitre, P., Probing mobility-selected saccharide isomers: selective ion–molecule reactions and wavelength-specific IR activation. *The Journal of Physical Chemistry A* **2015**, *119* (23), 6057-6064.
191. Berthias, F.; Maatoug, B.; Glish, G. L.; Moussa, F.; Maitre, P., Resolution and assignment of differential ion mobility spectra of sarcosine and isomers. *Journal of The American Society for Mass Spectrometry* **2018**, *29* (4), 752-760.
192. Seo, J.; Warnke, S.; Pagel, K.; Bowers, M. T.; von Helden, G., Infrared spectrum and structure of the homochiral serine octamer–dichloride complex. *Nature Chemistry* **2017**, *9* (12), 1263.
193. Schindler, B.; Depland, A. D.; Renois-Predelus, G.; Karras, G.; Concina, B.; Celep, G.; Maurelli, J.; Loriot, V.; Constant, E.; Bredy, R., FAIMS-MS-IR spectroscopy workflow: a multidimensional platform for the analysis of molecular isoforms. *International Journal for Ion Mobility Spectrometry* **2017**, *20* (3), 119-124.
194. Marianski, M.; Seo, J.; Mucha, E.; Thomas, D. A.; Jung, S.; Schlögl, R.; Meijer, G.; Trunschke, A.; von Helden, G., Structural Characterization of Molybdenum Oxide Nanoclusters Using Ion Mobility Spectrometry–Mass Spectrometry and Infrared Action Spectroscopy. *The Journal of Physical Chemistry C* **2018**, *123* (13), 7845-7853.
195. Seo, J.; Hoffmann, W.; Warnke, S.; Huang, X.; Gewinner, S.; Schöllkopf, W.; Bowers, M. T.; von Helden, G.; Pagel, K., An infrared spectroscopy approach to follow β -sheet formation in peptide amyloid assemblies. *Nature Chemistry* **2017**, *9* (1), 39-44.
196. Voronina, L.; Rizzo, T. R., Spectroscopic studies of kinetically trapped conformations in the gas phase: the case of triply protonated bradykinin. *Physical Chemistry Chemical Physics* **2015**, *17* (39), 25828-25836.
197. Masson, A.; Kamrath, M. Z.; Perez, M. A.; Glover, M. S.; Rothlisberger, U.; Clemmer, D. E.; Rizzo, T. R., Infrared Spectroscopy of Mobility-Selected H⁺-Gly-Pro-Gly-Gly (GPGG). *Journal of the American Society for Mass Spectrometry* **2015**, *26* (9), 1444-1454.
198. Voronina, L.; Masson, A.; Kamrath, M.; Schubert, F.; Clemmer, D.; Baldauf, C.; Rizzo, T., Conformations of prolyl–peptide bonds in the bradykinin 1–5 fragment in solution and in the gas phase. *Journal of the American Chemical Society* **2016**, *138* (29), 9224-9233.
199. Masellis, C.; Khanal, N.; Kamrath, M. Z.; Clemmer, D. E.; Rizzo, T. R., Cryogenic vibrational spectroscopy provides unique fingerprints for glycan identification. *Journal of the American Society for Mass Spectrometry* **2017**, *28* (10), 2217-2222.
200. Ben Faleh, A.; Warnke, S.; Rizzo, T. R., Combining ultrahigh-resolution ion-mobility spectrometry with cryogenic infrared spectroscopy for the analysis of glycan mixtures. *Analytical Chemistry* **2019**, *91* (7), 4876-4882.
201. Warnke, S.; Ben Faleh, A.; Scutelnic, V.; Rizzo, T. R., Separation and identification of glycan anomers using ultrahigh-resolution ion-mobility spectrometry and cryogenic ion spectroscopy. *Journal of The American Society for Mass Spectrometry* **2019**, *30* (11), 2204-2211.
202. Bansal, P.; Yatsyna, V.; AbiKhodr, A. H.; Warnke, S.; Ben Faleh, A.; Yalovenko, N.; Wysocki, V. H.; Rizzo, T. R., Using SLIM-Based IMS-IMS Together with Cryogenic Infrared Spectroscopy for Glycan Analysis. *Analytical Chemistry* **2020**, *92* (13), 9079-9085.
203. Yalovenko, N.; Yatsyna, V.; Bansal, P.; AbiKhodr, A. H.; Rizzo, T. R., Analyzing glycans cleaved from a biotherapeutic protein using ultrahigh-resolution ion mobility spectrometry together with cryogenic ion spectroscopy. *Analyst* **2020**, *145* (20), 6493-6499.
204. Kim Greis, D.; Mucha, E.; Lettow, M.; Thomas, D. A.; Kirschbaum, C.; Moon, S.; Alonso Pardo-Vargas, P.; von Helden, G.; Meijer, G.; Gilmore, K., The impact of leaving group anomericity on the structure of glycosyl cations of protected galactosides. *ChemPhysChem* **2020**, *21* (17), 1905.

205. Gray, C. J.; Compagnon, I.; Flitsch, S. L., Mass spectrometry hybridized with gas-phase InfraRed spectroscopy for glycan sequencing. *Current Opinion in Structural Biology* **2020**, *62*, 121-131.
206. Marlton, S. J.; McKinnon, B. I.; Ucur, B.; Bezzina, J. P.; Blanksby, S. J.; Trevitt, A. J., Discrimination between protonation isomers of quinazoline by ion mobility and UV-photodissociation action spectroscopy. *The Journal of Physical Chemistry Letters* **2020**, *11* (10), 4226-4231.
207. Zhang, J. D.; Donor, M. T.; Rolland, A. D.; Leeming, M. G.; Wang, H.; Trevitt, A. J.; Kabir, K. M.; Prell, J. S.; Donald, W. A., Protonation isomers of highly charged protein ions can be separated in FAIMS-MS. *International Journal of Mass Spectrometry* **2020**, *457*, 116425.
208. Ieritano, C.; Featherstone, J.; Haack, A.; Guna, M.; Campbell, J. L.; Hopkins, W. S., How Hot Are Your Ions in Differential Mobility Spectrometry? *Journal of the American Society for Mass Spectrometry* **2020**, *31* (3), 582-593.
209. Ieritano, C.; Lee, A.; Crouse, J.; Bowman, Z.; Mashmouhi, N.; Crossley, P. M.; Friebe, B. P.; Campbell, J. L.; Hopkins, W. S., Determining Collision Cross Sections from Differential Ion Mobility Spectrometry. *Analytical Chemistry* **2021**.
210. Papadopoulos, G.; Svendsen, A.; Boyarkin, O. V.; Rizzo, T. R., Conformational distribution of bradykinin [bk+ 2 H]²⁺ revealed by cold ion spectroscopy coupled with FAIMS. *Journal of the American Society for Mass Spectrometry* **2012**, *23* (7), 1173-1181.
211. Kamrath, M. Z.; Rizzo, T. R., Combining ion mobility and cryogenic spectroscopy for structural and analytical studies of biomolecular ions. *Accounts of Chemical Research* **2018**, *51* (6), 1487-1495.
212. Coughlan, N. J.; Stockett, M. H.; Kjær, C.; Ashworth, E. K.; Bulman Page, P. C.; Meech, S. R.; Brøndsted Nielsen, S.; Blancafort, L.; Hopkins, W. S.; Bull, J. N., Action spectroscopy of the isolated red Kaede fluorescent protein chromophore. *The Journal of Chemical Physics* **2021**, *155* (12), 124304.
213. Heldmaier, F. V.; Coughlan, N. J.; Haack, A.; Huard, R.; Guna, M.; Schneider, B. B.; Le Blanc, J. Y.; Campbell, J. L.; Nooijen, M.; Hopkins, W. S., UVPD spectroscopy of differential mobility-selected prototropic isomers of protonated adenine. *Physical Chemistry Chemical Physics* **2021**, *23* (35), 19892-19900.
214. Mashmouhi, N.; Juhász, D. R.; Coughlan, N. J.; Schneider, B. B.; Le Blanc, J. Y.; Guna, M.; Ziegler, B. E.; Campbell, J. L.; Hopkins, W. S., UVPD Spectroscopy of Differential Mobility-Selected Prototropic Isomers of Rivaroxaban. *The Journal of Physical Chemistry A* **2021**, *125* (37), 8187-8195.
215. Coughlan, N. J.; Fu, W.; Guna, M.; Schneider, B. B.; Le Blanc, J. Y.; Campbell, J. L.; Hopkins, W. S., Electronic spectroscopy of differential mobility-selected prototropic isomers of protonated para-aminobenzoic acid. *Physical Chemistry Chemical Physics* **2021**, *23* (36), 20607-20614.
216. Adamson, B. D.; Coughlan, N. J.; da Silva, G.; Bieske, E. J., Photoisomerization action spectroscopy of the carbocyanine dye DTC⁺ in the gas phase. *The Journal of Physical Chemistry A* **2013**, *117* (50), 13319-13325.
217. Markworth, P. B.; Adamson, B. D.; Coughlan, N. J.; Goerigk, L.; Bieske, E. J., Photoisomerization action spectroscopy: flicking the protonated merocyanine-spiropyran switch in the gas phase. *Physical Chemistry Chemical Physics* **2015**, *17* (39), 25676-25688.
218. Scholz, M. S.; Bull, J. N.; Coughlan, N. J.; Carrascosa, E.; Adamson, B. D.; Bieske, E. J., Photoisomerization of protonated azobenzenes in the gas phase. *The Journal of Physical Chemistry A* **2017**, *121* (34), 6413-6419.

219. Bull, J. N.; Carrascosa, E.; Mallo, N.; Scholz, M. S.; Da Silva, G.; Beves, J. E.; Bieske, E. J., Photoswitching an isolated donor–acceptor stenhouse adduct. *The Journal of Physical Chemistry Letters* **2018**, *9* (3), 665-671.
220. Bull, J. N.; Buntine, J. T.; Carrascosa, E.; Stockett, M. H.; Bieske, E. J., Action spectroscopy of deprotomer-selected hydroxycinnamate anions. *The European Physical Journal D* **2021**, *75* (2), 1-12.
221. Jacovella, U.; Carrascosa, E.; Buntine, J. T.; Ree, N.; Mikkelsen, K. V.; Jevric, M.; Moth-Poulsen, K.; Bieske, E. J., Photo-and Collision-Induced Isomerization of a Charge-Tagged Norbornadiene–Quadricyclane System. *The Journal of Physical Chemistry Letters* **2020**, *11* (15), 6045-6050.
222. Bull, J. N.; Carrascosa, E.; Giacomozzi, L.; Bieske, E. J.; Stockett, M. H., Ion mobility action spectroscopy of flavin dianions reveals deprotomer-dependent photochemistry. *Physical Chemistry Chemical Physics* **2018**, *20* (29), 19672-19681.
223. Kjær, C.; Bull, J. N.; Carrascosa, E.; Nielsen, S. B.; Bieske, E. J., Action spectroscopy of isomer-selected luciferin anions. *The European Physical Journal D* **2021**, *75* (3), 1-9.
224. Bull, J. N.; West, C. W.; Anstöter, C. S.; da Silva, G.; Bieske, E. J.; Verlet, J. R., Ultrafast photoisomerisation of an isolated retinoid. *Physical Chemistry Chemical Physics* **2019**, *21* (20), 10567-10579.
225. Bull, J. N.; Coughlan, N. J.; Bieske, E. J., Protomer-Specific Photochemistry Investigated Using Ion Mobility Mass Spectrometry. *The Journal of Physical Chemistry A* **2017**, *121* (32), 6021-6027.
226. Bull, J. N.; Buntine, J. T.; Scholz, M. S.; Carrascosa, E.; Giacomozzi, L.; Stockett, M. H.; Bieske, E. J., Photodetachment and photoreactions of substituted naphthalene anions in a tandem ion mobility spectrometer. *Faraday Discussions* **2019**, *217*, 34-46.
227. Bull, J. N.; Scholz, M. S.; Carrascosa, E.; Bieske, E. J., From E to Z and back again: reversible photoisomerisation of an isolated charge-tagged azobenzene. *Physical Chemistry Chemical Physics* **2018**, *20* (1), 509-513.
228. Bull, J. N.; Scholz, M. S.; Carrascosa, E.; Da Silva, G.; Bieske, E. J., Double molecular photoswitch driven by light and collisions. *Physical Review Letters* **2018**, *120* (22), 223002.
229. Bull, J. N.; Silva, G. d.; Scholz, M. S.; Carrascosa, E.; Bieske, E. J., Photoinitiated Intramolecular Proton Transfer in Deprotonated para-Coumaric Acid. *The Journal of Physical Chemistry A* **2019**, *123* (20), 4419-4430.
230. Choi, C. M.; Simon, A.-L.; Chirot, F.; Kulesza, A.; Knight, G.; Daly, S.; MacAleese, L.; Antoine, R.; Dugourd, P., Charge, color, and conformation: spectroscopy on isomer-selected peptide ions. *The Journal of Physical Chemistry B* **2016**, *120* (4), 709-714.
231. Czerwinska, I.; Kulesza, A.; Choi, C.; Chirot, F.; Simon, A.-L.; Far, J.; Kune, C.; De Pauw, E.; Dugourd, P., Supramolecular influence on cis–trans isomerization probed by ion mobility spectrometry. *Physical Chemistry Chemical Physics* **2016**, *18* (47), 32331-32336.
232. Smith, S. W., Chiral toxicology: it's the same thing... only different. *Toxicological sciences* **2009**, *110* (1), 4-30.
233. Murashima, H.; Fujihara, A., Wavelength dependence of chiral recognition using ions between photoexcited tryptophan and sugars. *Chemical Physics* **2020**, *536*, 110818.
234. Murashima, H.; Fujihara, A., Quantification of monosaccharide enantiomers using optical properties of hydrogen-bonded tryptophan. *Analytical Biochemistry* **2021**, 114151.
235. Eun, H. J.; Min, A.; Jeon, C. W.; Yoo, I. T.; Heo, J.; Kim, N. J., Chiral and Isomeric Discrimination of Chiral Molecular Ions by Cold Ion Circular Dichroism Spectroscopy. *The Journal of Physical Chemistry Letters* **2020**, *11* (11), 4367-4371.

Chapter 1: Introduction

236. Yoo, I. T.; Eun, H. J.; Min, A.; Jeon, C. W.; Jeong, J.; Heo, J.; Kim, N. J., Ultraviolet Photodissociation Circular Dichroism Spectroscopy of Protonated L-Phenylalanyl-L-Alanine in a Cryogenic Ion Trap. *Physical Chemistry Chemical Physics* **2021**.
237. Daly, S.; Rosu, F.; Gabelica, V., Mass-resolved electronic circular dichroism ion spectroscopy. *Science* **2020**, *368* (6498), 1465-1468.
238. Krüger, P.; Weitzel, K.-M., Photoelectron Circular Dichroism in the Photodetachment of Amino Acid Anions. *Angewandte Chemie* **2021**.

This page has been intentionally left blank.



EXPERIMENTAL

2. Experimental Methods and Developments

2.0 Overview

This section describes the experimental arrangements and techniques involved in this thesis. Various instrumentation arrangements are deployed, most of which involve a combination of mass spectrometry (MS) and laser photodissociation (PD). The setup for PD action spectroscopy has been described in detail elsewhere.¹ Therefore, this chapter will focus on the additions developed for experiments in this project—namely, field asymmetric ion mobility spectrometry (FAIMS), which is an ion mobility technique that allows the separation of ions that have the same mass to charge (m/z) ratios; and a picosecond pump-probe setup to investigate time-resolved excited state dynamics.

A schematic of the coupled FAIMS with ion trap arrangement setup is shown in Figure 2.1A and contains the major components used in this thesis. Gas-phase ions are first generated using electrospray ionization (ESI). Next ions can be separated and selected using FAIMS. Ions selected using FAIMS are then transported through an S-lens and ion guides into a linear ion trap, where they are selected by their m/z and stored at 0.4 mTorr (for the low pressure ion trap). At this stage, the ions have been selected by both FAIMS (which can separate isomers) and by their m/z —therefore, the ion trap contains an isomerically pure ion population with insignificant contamination.

2.1 List of Instruments

- **LTQ XL:** A THERMO mass spectrometer that contains a linear ion trap.
- **LTQ VELOS:** A THERMO mass spectrometer that contains a low-pressure and high-pressure linear ion trap as well as an S-lens to increase ion count.
- **Field Asymmetric Ion Mobility Spectrometer (FAIMS):** A type of non-linear ion-mobility. The FAIMS referred to here has a cylindrical electrode geometry and is produced by THERMO.
- **Differential Mobility Spectrometer (DMS):** Another FAIMS device that has linear electrode geometries. This instrument could be referred to as a FAIMS instrument but will be referred to here as DMS to distinguish it from the THERMO FAIMS. The DMS (SELXION) is produced by SCIEX and is coupled to a triple quadrupole mass spectrometer.

- **OPO Laser system (INDI):** A 10 Hz nanosecond laser system, which comprises a Spectra-Physics Quanta-Ray INDI Nd:YAG pump laser, the 355 nm third harmonic of which is used to pump an OPO (GWU-Lasertechnik Flexiscan).
- **OPO Laser system (EKSPLA):** A 20 Hz nanosecond laser system (NT342), which comprises a Nd:YAG pump laser, the 355 nm third harmonic of which is used to pump an OPO.
- **Picosecond OPG Laser system (EKSPLA):** A 20 Hz picosecond laser system (PL2551, EKSPLA), which comprises a diode pumped Nd:YVO₄ master oscillator, diode pumped Nd:YAG regenerative amplifier and flash lamp pumped Nd:YAG power amplifier, which generates picosecond 1064 nm light. The third harmonic of this pulse is used to pump an OPG (PG401 OPG, EKSPLA).
- **Fixed Wavelength nanosecond Nd:YAG Laser (Continuum, MINILITE):** A 10 Hz nanosecond Nd:YAG laser operating with SHG to form 532 nm light followed by a second SHG to form 266 nm light. Operation using 1064 nm, 532 nm, and 355 nm light is also possible.
- **Laser Power Meter:** Laser power measurements were taken using a GENTEC 11MAESTRO power meter.
- **Mechanical Shutter:** The mechanical shutter used was a SH05 ½ inch optical beam shutter with a Thorlabs SC10 shutter controller.
- **Digital Delay Generator:** Two delay generators were used to synchronise the timing of the lasers, mass spectrometers and mechanical shutters. For interfacing to the LTQ XL, a Quantum Composers 9520 delay generator was used. For interfacing to the LTQ VELOS, a Stanford Research Systems DG645 delay generator was used.
- **Mechanical Delay Stage:** The delay stage used was a Thorlabs that has a maximum movement of 220 mm, which corresponds to a change in optical path distance of 440 mm (1466 ps time delay). The minimum step size is 0.67 fs.

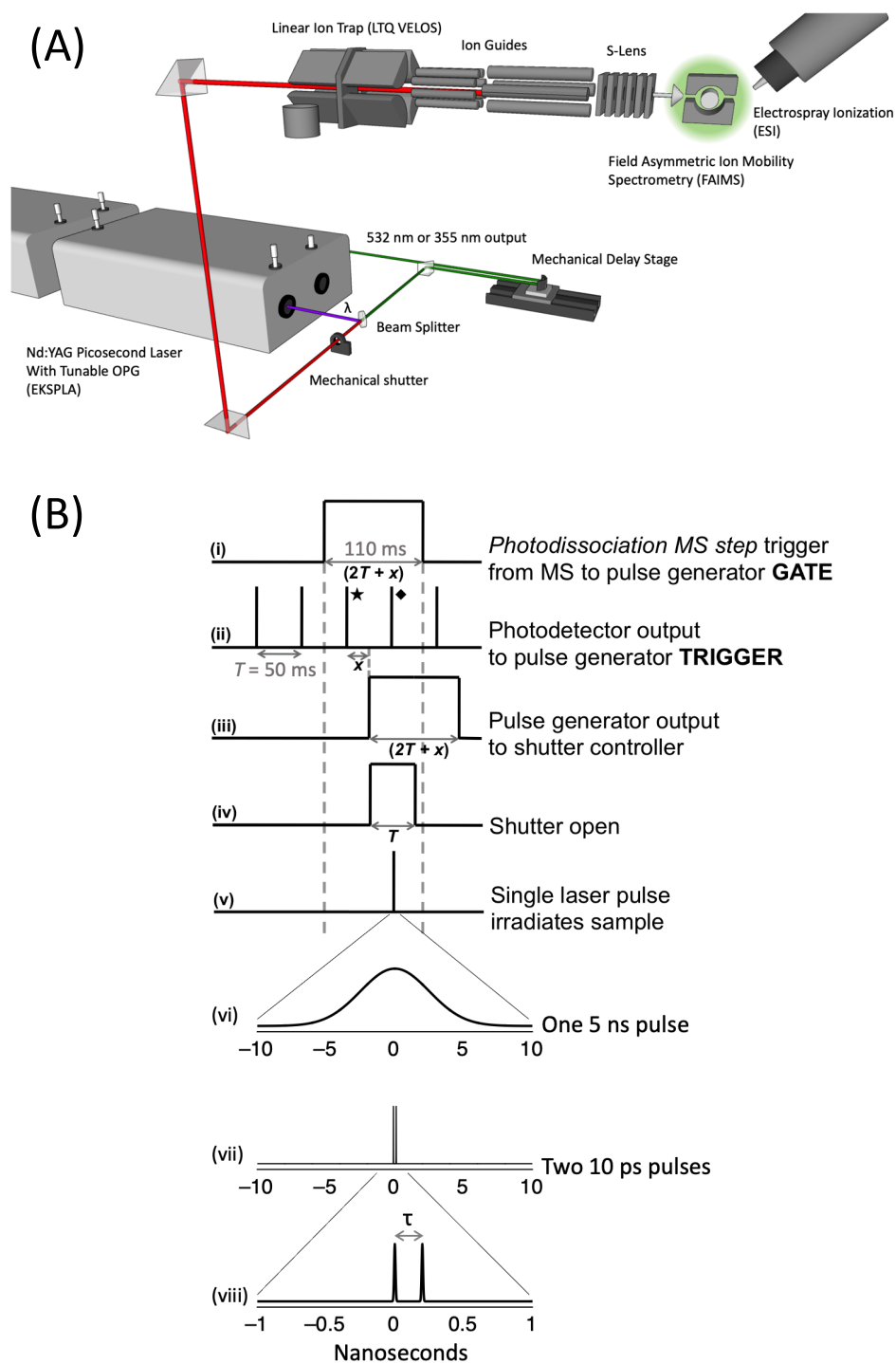


Figure 2.1: (A) Schematic of an example experimental setup containing the key experimental components deployed in this thesis. (B) Timing diagram of the experimental arrangement that ensures only the desired number of laser pulses enters the ion trap with each mass-spectrometer cycle. T is the time between laser repetitions, x is a programmable delay and τ is the time delay between the pump and probe pulses. Figure B adapted from Hansen, C.S., Kirk, B.B., Blanksby, S.J., O’Hair, R.A. and Trevitt, A.J., **2013**. *Journal of The American Society for Mass Spectrometry*, 24(6), pp.932-940. Copyright 2013 American Chemical Society.

2.2 Photodissociation Action Spectroscopy

The PD action spectroscopy method involves laser irradiation of m/z selected ions, irradiating them with a laser, and detecting the photoproducts. The experimental setup for PD action spectroscopy was—for the most part—in place at the beginning of this project. It is described in detail elsewhere and will only be described briefly here.¹

The PD action spectroscopy experiments employed one of two commercial linear quadrupole ion trap mass spectrometers Thermo Fisher Scientific LTQ VELOS or LTQ XL. Some key parameters for these two mass spectrometers are shown in Table 2.1. These mass spectrometers operate with ion-traps under vacuum (0.4 mTorr for the low-pressure VELOS ion-trap,² and 2.5 mTorr for the XL ion-trap³). The average time between hard-sphere collisions for a He atom in the ion trap is *ca.* 300 μs for the low-pressure ion trap of the VELOS and *ca.* 5 μs for the LTQ XL. The excited state processes observed here are likely to be collision free.

Table 2.1: Some key parameters for the two mass spectrometers used in this research.

Mass-Spectrometer	Chapter	Pressure in Ion-Trap	Ave. time between He collisions	S-Lens
LTQ XL	Chapters 4,5,6	2.5 mTorr	5 μs	No
LTQ VELOS (low-pressure trap)	Chapters 1,6	0.4 mTorr	300 μs	Yes

Ions are generated using electrospray ionisation (ESI). FAIMS electrodes are positioned in between the ESI needle and the inlet of the mass spectrometer. Once inside the mass spectrometer, ions are guided by ion optics towards a linear ion trap. The Thermo VELOS mass spectrometer has a stacked ring ion guide (or S-lens)^{4,5} among the ion optics, which increases ion throughput but can lead to ion heating—otherwise, the ion optics do not normally significantly affect the ions.

After the ion optics, ions are stored in a linear ion trap, isolated by their m/z , then stored in the trap for between 100 ms and 300 ms. While stored in the ion trap, the ions are irradiated by a single laser pulse. While stored in the ion trap, the ions are irradiated by a single laser pulse.

This laser pulse is directed through the long axis of the ion trap *via* a quartz window at the rear of the mass spectrometer providing very good spatial overlap between the trapped ion cloud and the laser pulse. After either ~ 50 ms or ~ 100 ms (depending on the laser repetition rate), the ions are scanned out of the ion trap and detected to create a PD mass spectrum. This process is repeated across a range of wavelengths to create a PD action spectrum, which follows the PD yield as a function of laser photon energy. The PD action spectrum is normalised by total ion count and by the laser power, which is measured after an action scan using a laser power meter (GENTEC MAESTRO). This process is automated with a in-house built LabView program.

A timing diagram is shown in Figure 2.1B. The ion-storage step of the mass-spectrometer is the gate signal. Following the gate signal, the next laser pulse is then registered as the trigger signal. After a delay of x time (normally 25 ms), a signal is sent to open a mechanical shutter and allow in one nanosecond laser pulse to irradiate the ions. For pump-probe experiments, two picosecond laser pulses are allowed into the ion trap with a relative delay of τ picoseconds (discussed in detail in section 2.5).

2.3 Field Asymmetric Ion Mobility Spectrometry

Field asymmetric ion mobility spectrometry (FAIMS) experiments were performed as a front-end separation technique. Ions are separated using FAIMS before being guided into a mass spectrometer for subsequent analysis—usually by photodissociation action spectroscopy. A schematic showing FAIMS separation is shown in Figure 2.2. A commercial FAIMS cell was employed (Thermo-Fischer Scientific).

The FAIMS mechanism employs an electric field which oscillates between high-field and low-field regimes to separate ions. Ions drift with the flow of an inert buffer gas (normally N_2 or He) at approximately atmospheric pressure. The flow of this gas guides ions between two electrodes. The oscillating voltage applied across these electrodes is called the separation voltage or dispersion voltage (DV). This voltage oscillates between a high voltage, which creates a high-field regime, and a low voltage, which creates a low-field regime. The low field regime lasts for longer than the high field regime so that the integration of the waveform is zero. For example, if the high field regime has a voltage that is twice that of the low field, then the high field regime is set to half the time as the low field. These electric fields, which arise from the DV, displace the ions laterally with respect to the flow of the buffer gas. The direction

of gas-flow is shown in Figure 2.2 as arrows. The low-field and high-field regimes have opposite polarity and, hence, displace ions in opposite directions (see Figure 2.2 bottom). The displacement of ions in the low-field regime is determined by their low-field mobility and the displacement of the ions in the high-field is determined by their high-field mobility. These mobilities are unique to each ion and so different ions will have different trajectories.

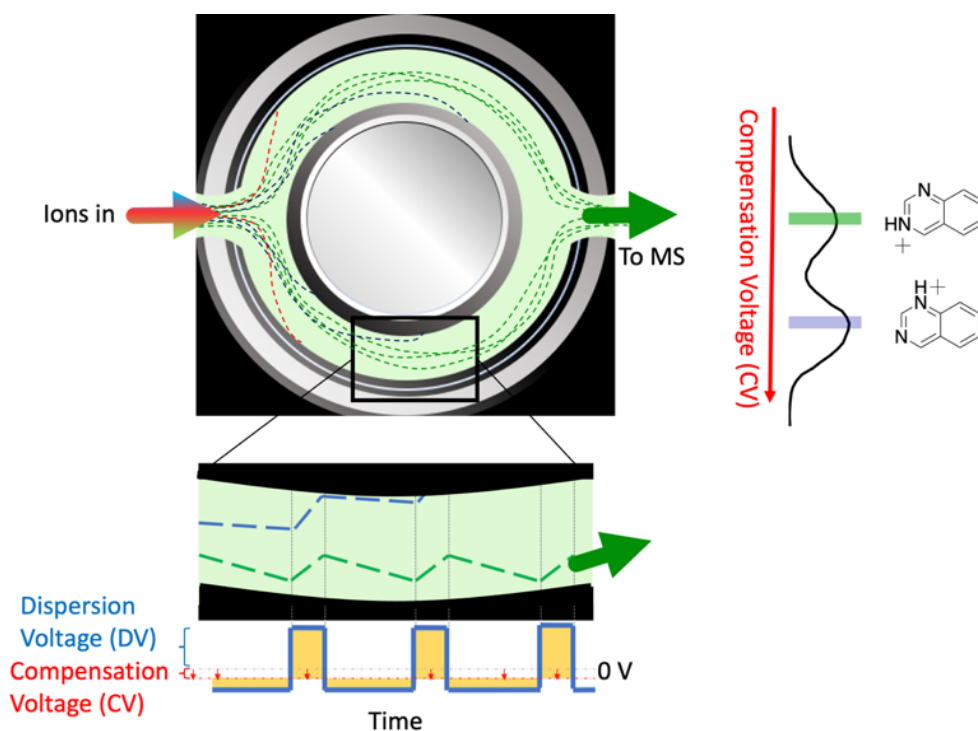


Figure 2.2: Schematic of the cylindrical FAIMS used to separate ions (top) with dotted lines showing the paths of different types of ions (red, blue, and green). Zoomed in segment of the FAIMS showing the zig-zag trajectory that the ions take due to the asymmetric voltage waveform (bottom). A waveform for the asymmetric voltage is shown (blue line with yellow fill) where the height of this waveform determined by the dispersion voltage and a correction from the compensation voltage (red arrows at bottom). Example data is shown on the right, where the two protomers of quinazolineH⁺ are separated as a function of compensation voltage and appear as two peaks on a FAIMS ionogram. Data taken from References 7.⁶

An ion will have a stable trajectory if it has a net-zero displacement in the high-field and low-field regimes. The ion will, therefore, pass between the FAIMS electrodes and into the mass spectrometer for detection (see the dotted green trajectory in Figure 2.2). However, an ion with an unstable trajectory has a net displacement in the high-field and low-field regions that causes it to approach one of the FAIMS electrodes—this ion eventually collides with the electrode and is not detected (see blue trajectory in Figure 2.2). Only ions with stable trajectories are detected and all ions with unstable trajectories are filtered out.

The unstable trajectories can be selectively corrected by applying a DC voltage across the electrodes, which is termed the compensation voltage (CV). By applying the CV, the ions that would have had stable trajectories without the CV now have unstable trajectories and are filtered out. This CV can be scanned to create a spectrum, which is referred to as an “ionogram” and tracks transmission of ions through the FAIMS. An example of an ionogram is shown in Figure 2.2, where the two protomers of quinazolineH⁺ are separated as a function of CV. Therefore, ions are separated in FAIMS by their mobility in high-field and low-field regimes and can be selectively detected (or selectively filtered out) by applying an appropriate CV. After FAIMS has selected an ion of interest, this ion is guided into a mass spectrometer for further analysis.

It is observed in Figure 2.3A that at low dispersion voltage values no separation is observed and the ionogram shows one peak. As dispersion voltage increases, the two protomers are separated and two peaks are resolved in the ionogram. This information can be summarised in a DV plot (shown in Figure 2.3B), which follows the CV value at which an ion is detected a function of DV. From the DV plots, information about the ions, (as well as the ion’s interaction with ambient neutral gasses), can be extracted.^{6, 7} In FAIMS, the ions undergo dynamic clustering and de-clustering with the neutral gas involving the ions clustering with the neutral gas in the low field regime, and then these clusters boiling off in the high field regime.⁸ As such, the extent of clustering and de-clustering will change the relative low and high field mobility of an ion. This is partly because a cluster will have a larger collisional cross section than the bare ion and will, therefore, have a lower mobility.

The dynamic clustering and de-clustering in FAIMS gives rise to three typical types of ion, namely Type A, Type B, and Type C. Recently, a non-typical Type D ion was observed.^{9, 10} A schematic illustration of the characteristic dispersion plots for the three common ion-types are shown in Figure 2.3C. The shape of the dispersion curves is determined by the strength of clustering between the ions and surrounding gas: whether they form strong clusters or bounce off each other like hard spheres. The three typical ion types can be summarised as ions that act approximately as hard spheres in high and low field regimes (Type C), ions that have strong clustering with surrounding gas (Type A), and ions that have strong clustering at lower DV but act more like hard spheres at increasing DV (Type B). Type A ions are expected to all exhibit Type B behaviour eventually when a high enough DV is reached. Nevertheless, the propensity

for an ion to remain Type A can be used to assess how strongly that ion binds with the neutral gas.

As an example of relating the FAIMS DV plots to ion-neutral interactions, Figure 2.3B presents the DV plot for two protomers of quinazolineH⁺. The blue trace (1-quinazolineH⁺) begins to exhibit Type B behaviour at high DV, although, the CV values are not observed to rise as dramatically as the example shown in Figure 2.3C. The green trace (3-quinazolineH⁺) exhibits weaker Type B behaviour, following an almost Type A-like curve. Because the blue trace becomes more hard-sphere-like at high DV values, (as is typical of Type B ions), while the green trace continues to have strong clustering behaviour (as is typical of Type A ions), one can infer that the ion responsible for the green trace (3-quinazolineH⁺) has stronger ion-neutral interactions. This can be related back to the properties of the ions as, for example, the 3-quinazolineH⁺ has stronger ion-neutral clustering and has a larger dipole moment than 1-quinazolineH⁺, which affects the strength of non-covalent interactions between the ion and the surrounding neutral gas.

Some key parameters used for FAIMS are the CV, DV, buffer gas composition and buffer gas flow rate. These parameters change how well two ions can be separated and resolved but also can affect the ion signal. There is often a trade-off between resolving power and ion signal and so it can take some optimisation to find the ideal conditions.

The DV was, for the most part, set to the maximum value of 5000 V, which normally corresponds to the maximum separation. However, larger DV leads to heating of the ions, which can cause isomerism become problematic for more flexible structures¹¹ and separation can be challenging to achieve at DV values below 3800 V (see Figure 2.3A). Fortunately, after FAIMS separation the use of PD action spectroscopy can provide evidence to characterise any isomerism.

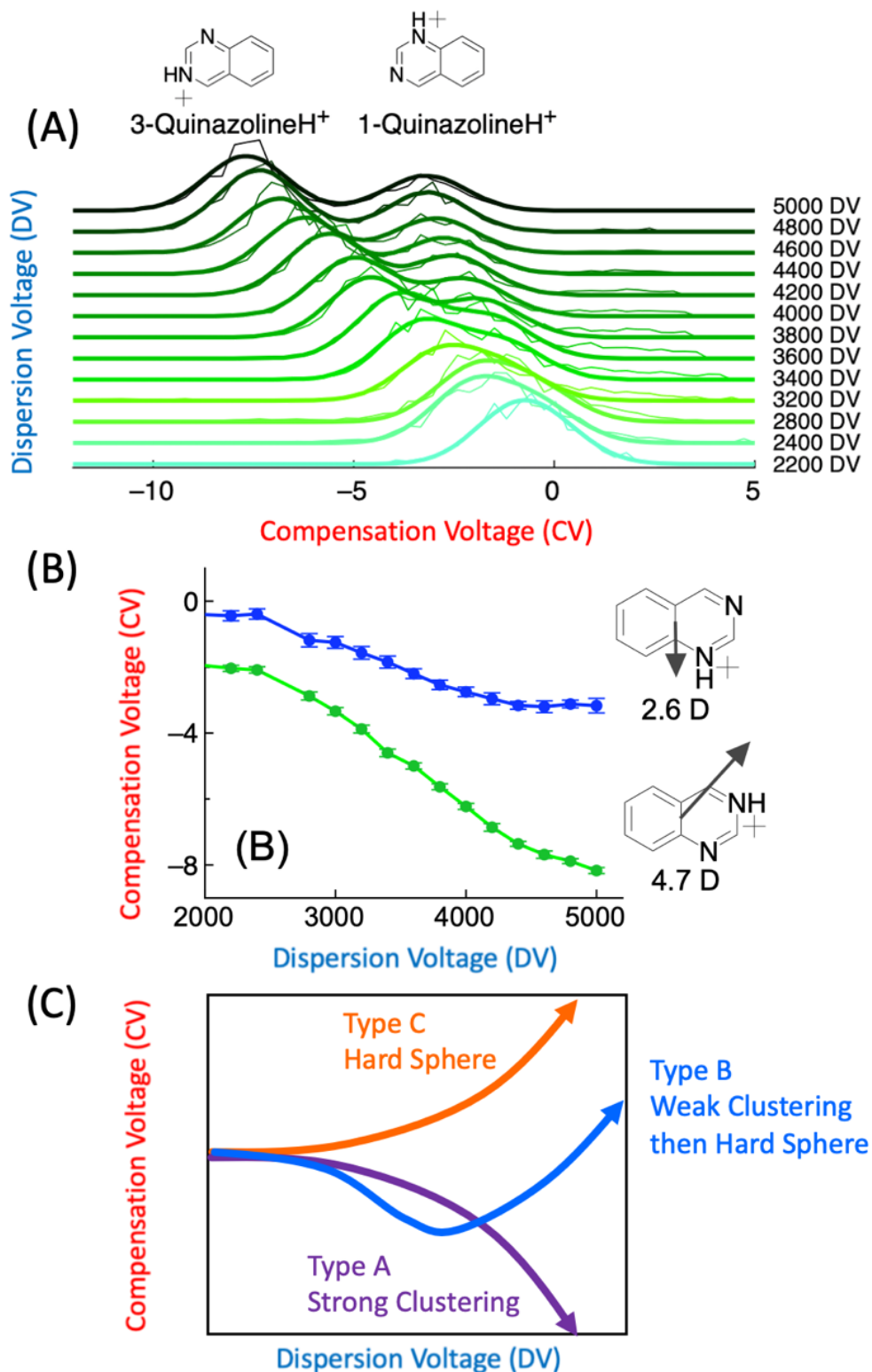


Figure 2.3: (A) FAIMS ionograms of quinazolineH⁺ at several dispersion voltage values. (B) DV plot following the compensation voltage of peak throughput for 1-quinazolineH⁺ and 3-quinazolineH⁺ as a function of dispersion voltage. (C) Schematic illustration of characteristic DV plots for ion Types A, B, and C, which are indicative of the dynamic clustering and de-clustering properties of an ion. Data adapted from Reference 7. ⁶

Chapter 2: Experimental

Buffer gas composition can also affect FAIMS separation. Although the buffer gas is often doped with organic molecules to enhance the dynamic clustering and de-clustering to drive improved FAIMS separation,^{10, 12, 13} this thesis focuses on the buffer gas compositions containing He and N₂ only. While He can improve FAIMS separation, the use of He must often be limited because of the high, *ca.* kV voltages used in FAIMS: high He concentrations can allow these voltages to arc and discharge. Some key FAIMS parameters used for acquiring the data presented in Chapter 4 and Chapter 5 are shown in Table 2.2.

Table 2.2: Key FAIMS parameters used in chapters 4 and 5.

Used in Chapter	Buffer Gas Flow Rate	Buffer Gas Composition	Dispersion Voltage
Chapter 4	3.5 L/min	100 % N ₂	5000 V
Chapter 5	3.5 L/min	50 % N ₂ 50 % He	5000 V

Cylindrical FAIMS provides some ion focusing which increases ion throughput and therefore increases signal at the expense of resolving power.^{14, 15} In contrast, linear FAIMS electrode geometries have increased resolving power but lower ion throughput in principle. A linear FAIMS (DMS SELEXION) coupled to a triple quadrupole mass spectrometer (SCIEX 5500) is also used in this thesis. The resolving power of the linear FAIMS (DMS SELEXION) was observed to be better than that of the cylindrical FAIMS. Hopkins and co-workers have successfully coupled linear FAIMS with PD action spectroscopy in a triple quadrupole mass spectrometer.¹⁶ However, because we do not have the capability to undertake PD action spectroscopy experiments coupled with linear FAIMS, (and we do have the capability to undertake PD action spectroscopy with cylindrical FAIMS), most of the FAIMS experiments in this thesis employ a cylindrical FAIMS geometry. Further information about the FAIMS mechanism is provided elsewhere.^{14, 17}

2.4 Picosecond Laser

To analyse processes on the picosecond timescale, laser pulses with duration on the picosecond timescale or shorter are required. At the beginning of this project, only nanosecond lasers were included in the experimental arrangement and so a new arrangement was developed that

includes a picosecond laser system (PL2251, EKSPLA). A comparison between key parameters of the nanosecond and picosecond laser systems is shown in Table 2.3. The picosecond laser is coupled with an OPG to generate tuneable wavelength light (PG401 OPG, EKSPLA). Generation of tuneable photons with pulse durations on the picosecond scale starts with the master oscillator. The master oscillator has a diode pumped Nd:YVO₄ rod that creates a pulse train with a repetition rate of 87 MHz (*ca.* 10 ns period between pulses). This is achieved by passive mode-locking, whereby light oscillating in a resonant cavity with “locked” fixed phase periodically creates a short pulse of higher intensity by constructive interference. The light in the cavity is made up of longitudinal modes, which have supported frequencies defined by the length of the cavity. The short pulse of higher intensity (resulting from mode-locking) then exits the master oscillator through a saturable absorber, which transmits light of high intensity and attenuates light of lower intensity. Therefore, the high intensity pulse passes through the saturable absorber and the lower intensity wings of the pulse are attenuated. This process produces a pulse train of short pulses with the time interval between pulses T equal to the time it takes for the light to do a round trip around the laser cavity t_{rt} (or the reciprocal of the frequency difference between the different modes) and the pulse width is approximately equal to the time interval between pulses divided by the number of oscillating modes N so that: $dt_p = t_{rt} / N$.

Table 2.3: Key parameters for different lasers employed in this thesis.

Pump Laser	Wavelength Tunability	Used in Chapter	Pulse Width	Rep. Rate	Typical Pulse Energy
Quanta Ray INDI	GWU-Lasertechnik FlexiScan OPO	Chapters 4, 5, 6	<i>ca.</i> 5 ns	10 Hz	0.1–5 mJ
EKSPLA NT342	EKSPLA NT342 OPO	Chapter 3	<i>ca.</i> 5 ns	20 Hz	0.1–10 mJ
EKSPLA PL2251	EKSPLA PG401 OPG	Chapter 6	<i>ca.</i> 10 ps	20 Hz	0.05–0.5 mJ

The pulse from the master oscillator is then passed into a regenerative amplifier. Once the pulse has entered the gain medium, a Pockels cell is turned on blocking the exit and the pulse becomes trapped. As the pulse is reflected within the regenerative amplifier, it passes through

the regenerative amplifier's diode pumped Nd:YAG gain medium. After a certain number of round trips, the pulse is amplified to maximum. At a pre-determined time, the Pockels cell is switched off and the pulse can leave the regenerative amplifier. The pulse then undergoes two passes through a power amplifier for further amplification. The power amplifier has an Nd:YAG gain medium and is pumped by two flash lamps.

After amplification, the picosecond pulse, (which at this point has a wavelength of 1064 nm), is passed through a second harmonic generator (SHG) to generate 532 nm light and a third harmonic generator (THG) to generate 355 nm light. Either the 532 nm pulse is picked off to become the probe pulse for pump probe experiments, or *ca.* 10 % of the 355 nm pulse is picked off to become the probe pulse. What remains of the 355 nm pulse is used to pump an optical parametric generator (OPG) to generate tuneable light.

The outputs of this laser that are used for pump-probe experiments are tuneable light output from the OPG (with range 213–340 nm and 340–700 nm) and either 532 nm, 355 nm, 266 nm or 1064 nm light, which are the harmonics of the fundamental Nd:YAG 1064 nm pulse that can be picked off before entering the OPG. The tuneable light from the OPG is used as the pump pulse and one of the harmonics (532 nm in this thesis) is used as the probe pulse. These pulses are output with a repetition rate of 20 Hz and have a cross correlation estimated to be 12 ± 1 ps (as will be discussed later). Typical laser powers are *ca.* 100 μ J for the tuneable light and *ca.* 3 mJ for 532 nm light. The linewidth of the tuneable output is *ca.* 10 cm^{-1} . Although this setup cannot probe effects that happen faster than the picosecond timescale, it provides a good compromise between spectroscopic precision (due to the 10 cm^{-1} linewidth), time resolution (due to the 13 ps limit of detection) and robustness. Some key parameters for the picosecond laser are shown in Table 2.2 in comparison to the two nanosecond lasers used in this project.

2.5 Pump-Probe and Delay Stage

For pump-probe photodissociation experiments, the tuneable (pump) and 532 nm (probe) laser pulses must be guided into the ion-trap at known delays. The delay must also be adjustable. The pump and probe paths must have significant spatial overlap with the ion-cloud within the ion-trap. The pump and the probe must have enough pulse energy to achieve sufficient signal.

The delay between laser pulses needs to be known. To control timing on the order of picoseconds requires a delay stage configuration. Using the speed of light (c), the time that a laser pulse takes to travel a pathlength L is simply

$$t = \frac{L}{c} \quad (\text{Eq. 2.1})$$

For reference, the time it takes light to travel 1 mm is 3.3 ps. Therefore, because the pump and probe pulse come from the same source and are only split off after the SHG and THG crystals, one can control the relative timings of the two pulses by manipulating their relative pathlengths. The relative pathlengths can be estimated by measuring the distance that each laser pulse travels (shown in Figure 2.4) and the relative delay can be fine-tuned by passing one of the pulses (in this case, the 532 nm probe pulse) through a mechanical delay stage (shown in Figure 2.5).

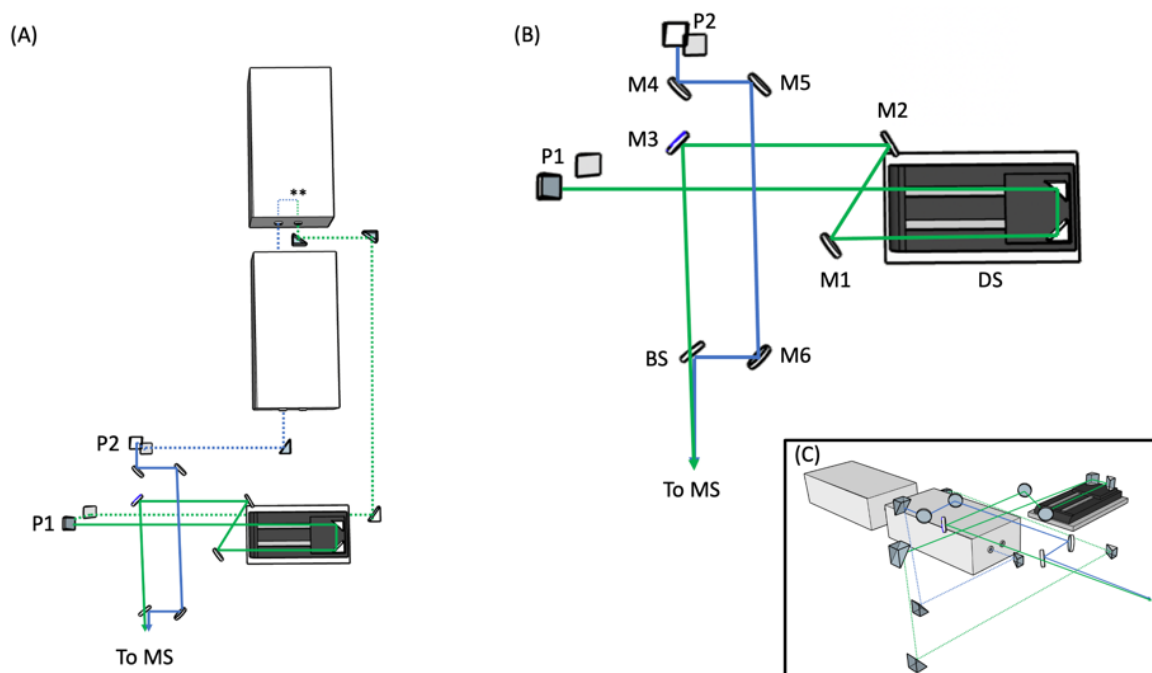


Figure 2.4: Schematic (not to scale) showing paths that the tuneable pump (blue) and 532 nm probe (green) travel. There is a lower-level, with dotted lines to represent the beam, connected by two periscopes to an upper-level, with solid lines to represent the beam path. (A) Top-down view with labels indicating the distances travelled on the lower level. (B) Top-down view zoomed in on the upper-level. (C) Diagonal view to show the three-dimensional layout of the top level and bottom level. The starting point is marked by **, which corresponds to the point that beams are split off.

Chapter 2: Experimental

The pathlengths of the two pulses were designed so that they had approximately equal length. The tuneable path is measured to be roughly 5020 mm in length, while the 532 nm path is measured to be roughly 4780 – 5220 mm depending on the position of the delay stage. The optical delay stage (THORLABS ODL220M) is shown in Figure 2.5. This stage has a maximum movement of 220 mm, which corresponds to a change in optical path distance of 440 mm and a change in arrival time of the light at the ion trap of 1466 ps. The minimum step size corresponds to 0.67 fs and so the time resolution of the pump-probe PD experiments are not limited by the mechanical delay stage. The relative arrival time can be adjusted so that the pump pulse arrives before the probe, or so the pump pulse arrives after the probe, or so that the pump and probe arrive at the same time.

To characterise the time-resolution of a pump-probe experiment, the laser cross correlation must be determined. As the pump and probe delay is scanned, their overlap has a Gaussian profile, the standard deviation of this Gaussian profile is the laser cross correlation. To measure the laser cross-correlation, the delay stage was scanned as the pump and probe laser pulses were focused onto a LED. The LED acts as a photodiode that absorbs light and generates electrical current. When both the pump and probe pulses temporally overlap, the electrical current signal generated by the LED spikes. By scanning the delay stage and measuring the electrical current signal, the overlap of the two pulses is measured (Figure 2.6). By fitting this data to a single Gaussian function, the standard deviation of the Gaussian gives the laser cross-correlation. Using this method, a cross-correlation of 12 ± 1 ps was determined.

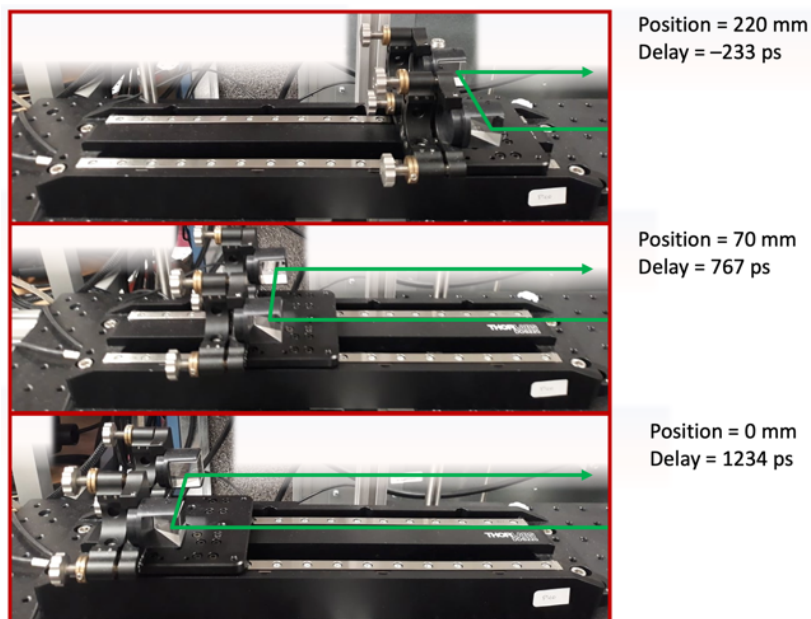


Figure 2.5: Delay stage at three different positions, minimum distance (top), maximum distance (bottom), and an intermediate distance (middle). The delay stage can move a total of 220 mm, which corresponds to a change in beam path of 440 mm and a change in arrival time of light to the ion trap of 1430 ps.

Over the course of an experiment, the delay stage will be set to an initial position—normally starting at position 0 mm, which corresponds to the maximum delay between the pump and probe pulses. The pump and probe delay is fixed as the laser pulses with a 20 Hz repetition rate. Ions are isolated and stored in the ion trap for 110 ms, during this time a mechanical shutter is triggered and opens for 25 ms, allowing for one pump and one probe pulse to enter the ion-trap. If ions absorb the laser pulses, they may form photodissociation products, which are recorded as a mass spectrum. Approximately 50 mass spectra are taken at this time delay point. The delay stage then moves by a predetermined interval (normally 1 mm, 2 mm or 5 mm), which changes the time delay between the pump and probe pulses and the process of recording mass spectra is repeated.

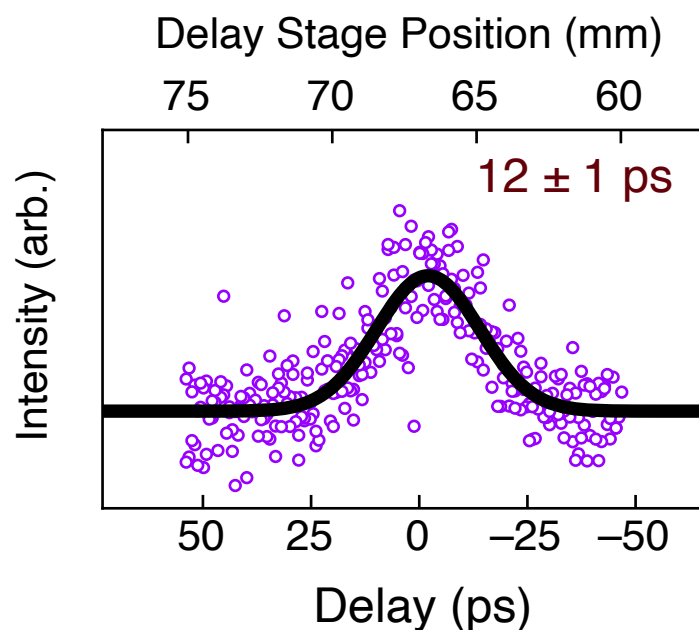


Figure 2.6: Temporal overlap of the pump and probe pulses following electrical current signal measured by a white LED as a function of pump-probe delay. The wavelength of both pump and probe is 532 nm.

2.5.1 Pump-Probe Data Analysis

To calculate the PD yield, the sum of all photoproduct ion signal is divided by the sum of the total spectrum (total ion count). For PD action spectroscopy, these yields are also divided by the laser power for a given wavelength, but for pump-probe PD the laser power is constant throughout the experiment and so the PD yield is not normalised to laser power.

The PD yield of the m/z 65 photoproduct from protonated indazole (indazoleH⁺) is shown as a function of pump-probe delay in Figure 2.7D. Individual data points in Figure 2.7D correspond to a PD mass spectrum, (which are the average of *ca.* 50 mass spectra). Three PD mass spectra are shown in Figure 2.7 at different pump-probe delays, one with negative delay in Figure 2.7A (532 nm probe before 270 nm pump), zero delay in Figure 2.7B (pump and probe irradiating ions simultaneously), and positive delay in Figure 2.7C (pump before probe). There is an increase in the intensity yield of the m/z 65 photoproduct when the pump and probe pulse arrive simultaneously (Figure 2.7B). Note that the m/z 92 photoproduct in Figures 2.7A, 2.7B, and 2.7C has consistent intensity—this shows that transient absorption of a photon will not necessarily translate into a change in PD yield.

Figure 2.7D and 2.7E show pump-probe photodissociation plots of indazoleH⁺ using different pump photon energies. Following the workflow of Soorkia *et al.*,¹⁸ the data points corresponding to *m/z* 65 photoproduct yield as a across a range of pump-probe delay times is fit with a function shown in Equation 2.2 using the Levenberg-Marquardt algorithm.

$$S(t) = 1/2 \left(1 + \operatorname{erf} \frac{t - t_0}{l_0} \right) \exp - \frac{t - t_0}{\tau} \quad (\text{Eq. 2.2})$$

This equation convolutes an error function (erf) with a mono-exponential decay, where l_0 is the laser cross correlation (estimated to be 13 ps), t_0 is time zero, τ is the time constant for the exponential decay. This time constant τ can correspond to the lifetime of an excited state. The lifetime in Figure 2.7E is 110 ps, whereas the lifetime in Figure 2.7D is shorter than the time resolution of the laser and, hence, the signal only increases off baseline when both laser pulses temporally overlap (similar to Figure 2.6). The errors presented in this thesis are all $\pm 2\sigma$ and, in the case of pump-probe PD lifetimes, σ corresponds to the standard deviation output from the Levenberg-Marquardt fit.

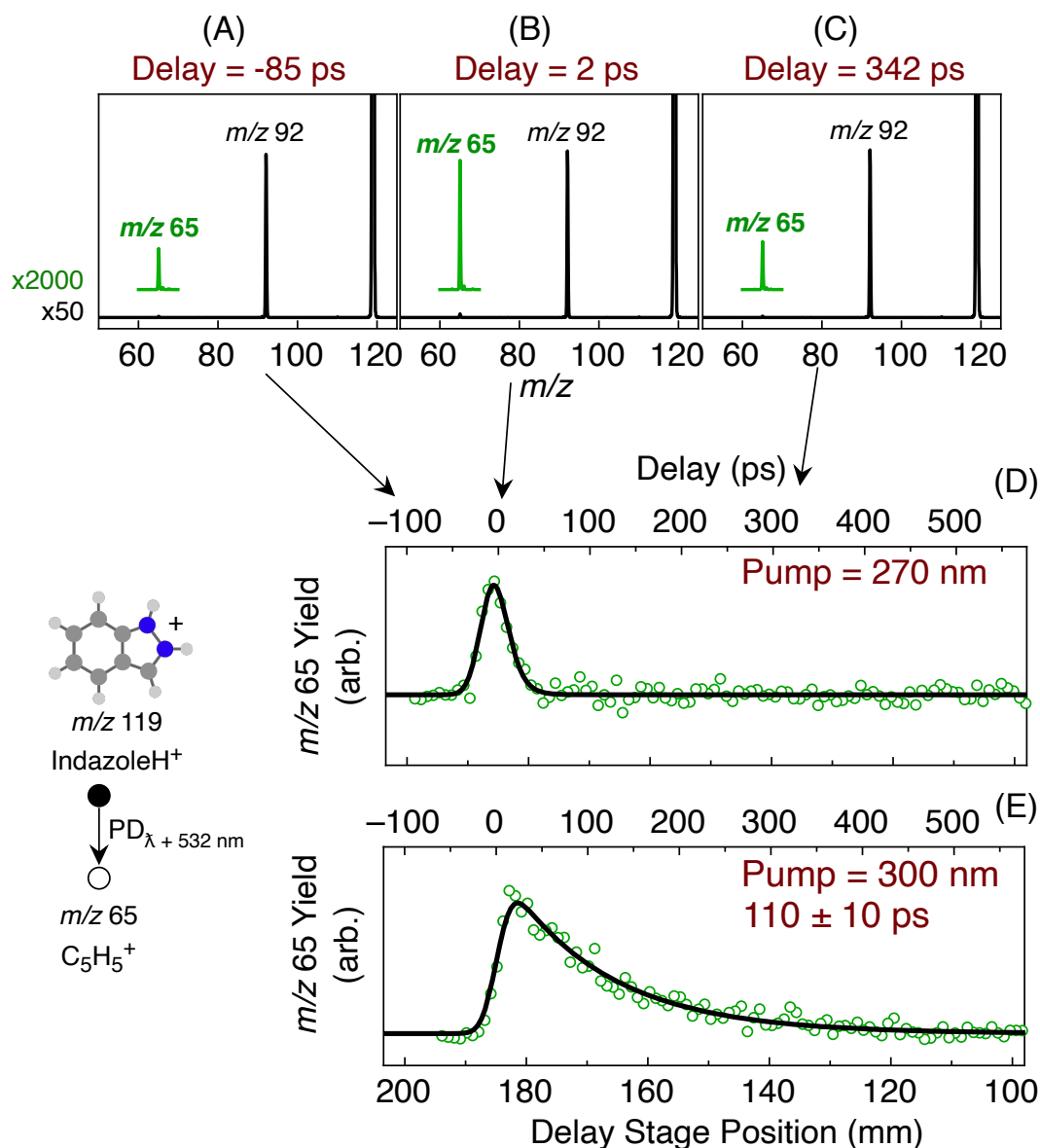


Figure 2.7: Pump-probe photodissociation mass spectra taken (A) with negative delay (532 nm probe before 270 nm pump), (B) zero delay (pump and probe irradiating ions simultaneously), and (C) positive delay (pump before probe). (C) shows a pump-probe PD plot following the intensity of the m/z 65 photoproduct as a function of time delay between the pump and probe pulse. Data from reference 19.¹⁹

2.5.2 Pump Probe Validation:

To benchmark this pump-probe configuration, comparisons here are made between our room temperature pump-probe experimental setup and a pump-probe experimental setup employing a cryogenic ion trap. However, because the ions are at different temperatures for the different experiments, it is necessary to account for the differences in internal energy. The method for accounting for the different internal energies follows that of Soorkia *et al.* who compared room temperature and cryogenic temperature lifetimes measured by ion-trap pump probe PD.¹⁸

Measurements using a cryogenic ion trap are plotted as circles in Figure 2.8¹⁸ and 2.9²⁰ (with the exception of the data point at 5500 cm⁻¹ in Figure 2.8A, which was taken at a femtosecond laser at an estimated temperature of ~355 K).²¹ Data taken with the setup used in the present study are plotted as squares in Figures 2.8A and 2.9A with an estimated temperature of 300 K. The results reported in this thesis were a combination of two separate experiments with a total of *ca.* 200 laser shots *per* step. The results from reference 18 were averages of 5 scans with 160 laser shots *per* step. The results from reference 21 were averages of ten to twenty scans with 100 laser shots *per* step. Internal energy is calculated by taking into account the energy above the 0-0 transition in addition to the internal energy from temperature. The internal energy from temperature is calculated by finding the average internal energy of a collection of harmonic oscillators (where the harmonic oscillators are the vibrational modes of protonated tyrosine calculated using the ω B97X-D/aug-cc-pVDZ method) populated by a statistical Boltzmann distribution at 300K.

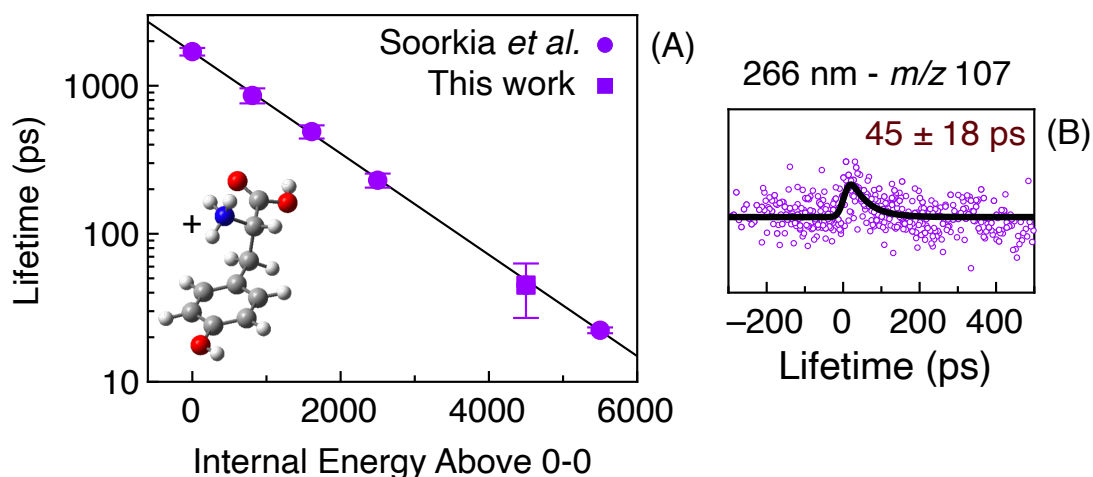


Figure 2.8: (A) Measured time constants following the formation of the m/z 107 photofragment of protonated tyrosine with varying internal energies (given in cm⁻¹) above the 284.4 nm 0-0 transition. (B) Pump probe of protonated tyrosine following formation of the m/z 107 photoproduct. Data points plotted as circles in (A) are from references 18 and 21.^{18, 21}

This method was also repeated for protonated 4-dimethyl-aminopyridine and 2-aminopyridine (Figures 2.8 and 2.9). In both cases, the vibrational modes were calculated using ω B97X-D/aug-cc-pVDZ method. The internal energy above 0-0 was then calculated as the internal energy of the ions at room temperature plus the excess pump-photon energy relative to the 0-0 transition energy. Our results at room temperature agree well with those of the previous studies. Notably, our error bars are larger than those of the previous studies, this may be due to

differences in pump-probe PD yield at room temperature compared to cryogenic temperature, or possibly because we have included fewer averages. Nevertheless, the agreement between these studies is satisfactory.

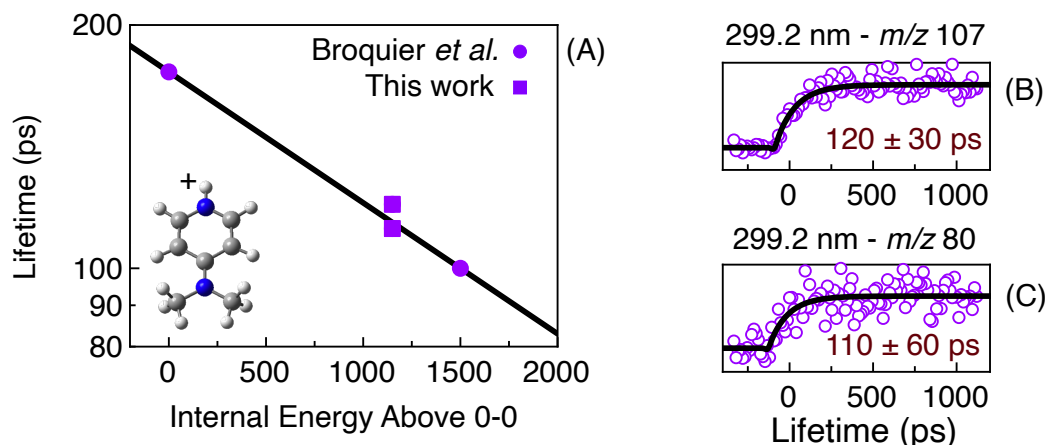


Figure 2.9: (A) Measured time constants following the formation of the m/z 107 photofragment of protonated *para*-dimethylaminopyridine with varying internal energies (given in cm⁻¹) above the 299.2 nm 0-0 transition. (B and C) Pump probe of protonated dimethyl aminopyridine following formation of the m/z 107 and m/z 80 photoproducts. Data points plotted as circles in (A) are from reference 20.²⁰

References

1. Hansen, C. S.; Kirk, B. B.; Blanksby, S. J.; O'Hair, R. A.; Trevitt, A. J., UV photodissociation action spectroscopy of haloanilinium ions in a linear quadrupole ion trap mass spectrometer. *Journal of The American Society for Mass Spectrometry* **2013**, *24* (6), 932-940.
2. Olsen, J. V.; Schwartz, J. C.; Griep-Raming, J.; Nielsen, M. L.; Damoc, E.; Denisov, E.; Lange, O.; Remes, P.; Taylor, D.; Splendore, M., A dual pressure linear ion trap Orbitrap instrument with very high sequencing speed. *Molecular & Cellular Proteomics* **2009**, *8* (12), 2759-2769.
3. Harman, D. G.; Blanksby, S. J., Investigation of the gas phase reactivity of the 1-adamantyl radical using a distonic radical anion approach. *Organic & Biomolecular Chemistry* **2007**, *5* (21), 3495-3503.
4. Wouters, E. R.; Splendore, M.; Mullen, C.; Schwartz, J. C.; Senko, M.; Duniach, J.-J.; Jose, S. In *Implementation of a progressively spaced stacked ring ion guide on a linear ion trap mass spectrometer*, 57th Amer. Soc. Mass Spectrom. Annual Conf. on Mass Spectrometry & Allied Topics, Philadelphia, PA, May 31–June, 2009.
5. Guan, S.; Marshall, A. G., Stacked-ring electrostatic ion guide. *Journal of the American Society for Mass Spectrometry* **1996**, *7* (1), 101-106.
6. Marlton, S. J.; McKinnon, B. I.; Ucur, B.; Bezzina, J. P.; Blanksby, S. J.; Trevitt, A. J., Discrimination between protonation isomers of quinazoline by ion mobility and UV-

photodissociation action spectroscopy. *The Journal of Physical Chemistry Letters* **2020**, *11* (10), 4226-4231.

7. Campbell, J. L.; Le Blanc, J. Y.; Schneider, B. B., Probing electrospray ionization dynamics using differential mobility spectrometry: the curious case of 4-aminobenzoic acid. *Analytical Chemistry* **2012**, *84* (18), 7857-7864.

8. Haack, A.; Crouse, J.; Schlüter, F.-J.; Benter, T.; Hopkins, W. S., A first principle model of differential ion mobility: the effect of ion-solvent clustering. *Journal of the American Society for Mass Spectrometry* **2019**, *30* (12), 2711-2725.

9. Crouse, J.; Haack, A.; Benter, T.; Hopkins, W. S., Understanding Nontraditional Differential Mobility Behavior: A Case Study of the Tricarbostannatrane Cation, N(CH₂CH₂CH₂)₃Sn⁺. *Journal of the American Society for Mass Spectrometry* **2020**, *31* (4), 796-802.

10. Mashmoushi, N.; Juhász, D. R.; Coughlan, N. J.; Schneider, B. B.; Le Blanc, J. Y.; Guna, M.; Ziegler, B. E.; Campbell, J. L.; Hopkins, W. S., UVPD Spectroscopy of Differential Mobility-Selected Prototropic Isomers of Rivaroxaban. *The Journal of Physical Chemistry A* **2021**.

11. Ieritano, C.; Featherstone, J.; Haack, A.; Guna, M.; Campbell, J. L.; Hopkins, W. S., How Hot Are Your Ions in Differential Mobility Spectrometry? *Journal of the American Society for Mass Spectrometry* **2020**, *31* (3), 582-593.

12. Wei, M. S.; Kemperman, R. H.; Yost, R. A., Effects of solvent vapor modifiers for the separation of opioid isomers in micromachined FAIMS-MS. *Journal of The American Society for Mass Spectrometry* **2019**, *30* (5), 731-742.

13. Campbell, J. L.; Zhu, M.; Hopkins, W. S., Ion-molecule clustering in differential mobility spectrometry: lessons learned from tetraalkylammonium cations and their isomers. *Journal of the American Society for Mass Spectrometry* **2014**, *25* (9), 1583-1591.

14. Buryakov, I.; Krylov, E.; Nazarov, E.; Rasulev, U. K., A new method of separation of multi-atomic ions by mobility at atmospheric pressure using a high-frequency amplitude-asymmetric strong electric field. *International Journal of Mass Spectrometry and Ion Processes* **1993**, *128* (3), 143-148.

15. Guevremont, R.; Purves, R. W., Atmospheric pressure ion focusing in a high-field asymmetric waveform ion mobility spectrometer. *Review of Scientific Instruments* **1999**, *70* (2), 1370-1383.

16. Coughlan, N. J.; Carr, P. J.; Walker, S. C.; Zhou, C.; Guna, M.; Campbell, J. L.; Hopkins, W. S., Measuring electronic spectra of differential mobility-selected ions in the gas phase. *Journal of the American Society for Mass Spectrometry* **2020**, *31* (2), 405-410.

17. Shvartsburg, A. A., *Differential ion mobility spectrometry: nonlinear ion transport and fundamentals of FAIMS*. CRC Press: 2008.

18. Soorkia, S.; Broquier, M.; Grégoire, G., Conformer- and mode-specific excited state lifetimes of cold protonated tyrosine ions. *The Journal of Physical Chemistry Letters* **2014**, *5* (24), 4349-4355.

19. Marlton, S. J. P.; McKinnon, B. I.; Greißel, P.; Shiels, O. J.; Ucur, B.; Trevitt, A. J., Picosecond Excited-State Lifetimes of Protonated Indazole and Benzimidazole: The Role of the NN bond. *The Journal of Chemical Physics* **2021**.

20. Soorkia, S.; Broquier, M.; Grégoire, G., Multiscale excited state lifetimes of protonated dimethyl aminopyridines. *Physical Chemistry Chemical Physics* **2016**, *18* (34), 23785-23794.

21. Kang, H.; Jouvét, C.; Dedonder-Lardeux, C.; Martrenchard, S.; Gregoire, G.; Desfrancois, C.; Schermann, J.-P.; Barat, M.; Fayeton, J., Ultrafast deactivation mechanisms of protonated aromatic amino acids following UV excitation. *Physical Chemistry Chemical Physics* **2005**, *7* (2), 394-398.

This page has been intentionally left blank.

IRGACURE 2959 CLUSTERS

3. Irgacure 2959 Clusters

This chapter outlines how the electronic quantum states of a photoinitiator (irgacure 2959) can be shifted experimentally using oriented electric fields. The contents are reproduced verbatim from the peer-reviewed and publication:

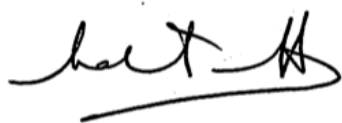
Marlton, S.J., McKinnon, B.I., Hill, N.S., Coote, M.L. and Trevitt, A.J., 2021. Electrostatically Tuning the Photodissociation of the Irgacure 2959 Photoinitiator in the Gas Phase by Cation Binding. *Journal of the American Chemical Society*, 143(5), pp.2331-2339.

Author Contributions

S.J.P Marlton performed all calculations and experiments presented in this work. S.J.P Marlton prepared the manuscript with input from all authors. S.J.P Marlton prepared the manuscript with input from all authors. B, J McKinnon contributed to analysis of the data. M, Coote and N, Hill contributed to conception of the study.

Certification

I, Prof. Adam J. Trevitt, as Samuel J. P. Marlton's primary supervisor, and the principal investigator for this project, agree with and certify the author contributions described above.

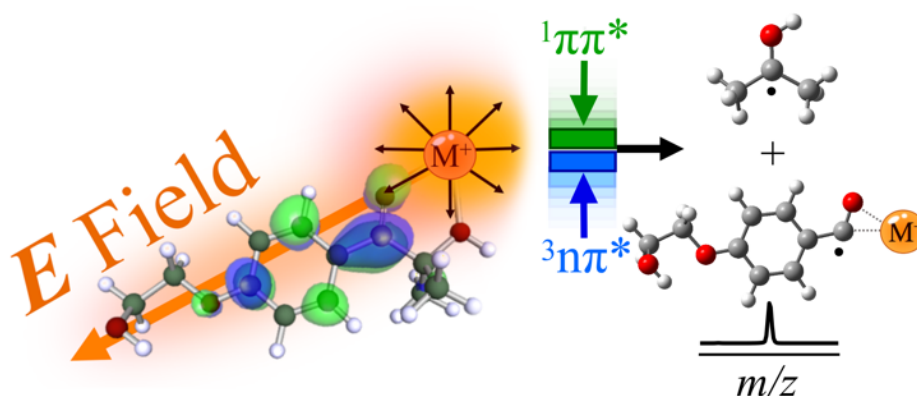


Adam J. Trevitt

07/12/2021

3.1 Abstract.

The low-lying electronic states of Irgacure 2959, a Norrish-type I photoinitiator, complexed with a single metal cation are investigated in the gas-phase by photodissociation action spectroscopy. Analysis of the band-shifts using quantum chemical calculations (TD-DFT and SCS-CC2) reveals the underlying influence of the charge on the key electronic energy levels. Since the cations (H^+ , Li^+ , Na^+ , K^+ , Zn^{2+} , Ca^{2+} and Mg^{2+}) bind at varying distances, the magnitude of the electric field at the center of the chromophore due to the cation is altered and this shifts the electronic states by different amounts. Photodissociation action spectra of cation-Irg complexes show that absorption transitions to the first $^1\pi\pi^*$ state are red shifted with a magnitude proportional to the electric field strength (with red shifts > 1 eV) and, in most cases, the cation is essentially acting as a point-charge. Calculations show that a neighboring $^3n\pi^*$ state, a key state for the α -cleavage pathway, is destabilized (blue-shifted) by the orientated electric field. As such, if the $^1\pi\pi^* - ^3n\pi^*$ energy gap is reduced, increased inter-system crossing rates are expected resulting in higher yields of the desired radical photoproducts and this is controlled by the orientated electric field arising from the cation.



3.2 Introduction.

Theoretical and experimental investigations—particularly in combination—are providing new insights into the control of chemical reactivity using oriented electric field (OEFs).¹⁻⁶ Recent experiments have shown OEFs can enhance ground state reactivity in a variety of contexts including homogenous catalysts in solution,⁷ single-molecules at junctions⁸ and charged groups interacting with radicals in the gas phase.⁹ Recently, Coote and co-workers used computational predictions to rationalize how OEFs can be used to tune the photodissociation properties of radical photoinitiators by shifting the key excited electronic quantum levels implicated in photodissociation.^{10, 11} This requires the coordinated shifting of the absorption transition with the other states implicated in the dissociation to the desired products.

Following absorption of a photon, it is often the interplay between the spectroscopically prepared excited state and the neighbouring “dark” excited state(s) that mediate the photodissociation efficiency.¹⁰⁻¹³ As a result, the photon energy corresponding to the maximum absorption cross-section does not necessarily correspond to the maximum photodissociation efficiency.¹³⁻¹⁵ As red shifting the active wavelengths of photoinitiators is often sought after, since lower energy photons are generally less expensive and are less damaging to other co-located molecules, it is vital that *both* the absorption transition and the other key states shift in accord to maintain high photodissociation yields. Predicting the impact of chemical modification, or application of OEFs, on photoactivity is not straightforward as different excited states have different polarities and polarizabilities and thus respond differently.^{10, 11, 16} This in turn has complex follow-on effects on intersystem crossing rates, triplet lifetimes and other factors affecting photodissociation. To study these processes, experiments that probe both excitation and dissociation as a function of photon energy are required and gas-phase photodissociation action spectroscopy—combining laser photodissociation with *m/z*-selected ions—is well suited to investigate the fundamental processes of photoinitiator systems.

Gas-phase photodissociation (PD) action spectroscopy provides information on the structural characterization of ions including the position of metal cations complexed to chromophores¹⁷⁻²³ and the location of protonation sites.²⁴⁻³² PD action spectroscopy of ions complements other experimental strategies examining the effect of electric fields on molecular reactivity.^{9, 33-39}

This paper focuses on the photodissociation of Irgacure 2959 (Irg), 2-hydroxy-4-(2-hydroxyethoxy)-2-methylpropiophenone, a well-known photoinitiator based on acetophenone with Norrish type-I photo-chemistry^{10, 11} and popular for use in bio-printing.⁴⁰⁻⁴² Irg absorbs in the UV region with an absorption maximum at $\lambda = 273$ nm.⁴³ Following absorption, the desired α -cleavage photodissociation mechanism of Irg is summarized as a $^1\pi\pi^* \rightarrow ^1n\pi^* \rightarrow ^3\pi\pi^* \rightarrow ^3n\pi^* \rightarrow \alpha$ -cleavage.^{10-12, 44} Because neutral Irg has an S_1 state with $^1n\pi^*$ character, the $S_1 (^1n\pi^*) \rightarrow T_n (^3\pi\pi^*)$ ISC pathway—the second step—should be favourable (El-Sayed Rules).⁴⁵ Ultimately, dissociation from the $^3n\pi^*$ state correlates to $\bullet C_9H_9O_3 + \bullet C_3H_6OH$ α -hydroxyalkyl radical.⁴⁴ The quantum yield of α -cleavage from Irg is $\phi_\alpha = 0.29$ in acetonitrile.⁴³ Irg has a strong $\pi \rightarrow \pi^*$ transition ($\epsilon = 16200$ M⁻¹ cm⁻¹ in acetonitrile),⁴⁶ which is excited, for example, in the cross linking of hydrogels.⁴⁷ Alternatively, to reduce damage in bio-applications, lower energy photons ($\lambda > 320$ nm) can be used and this directly accesses the weaker $n \rightarrow \pi^*$ transition ($\epsilon = 4$ M⁻¹ cm⁻¹ for $\lambda = 365$ nm in ethanol)^{40-42, 48} and thus requires longer irradiation times.^{47, 49} This trade-off highlights the need to balance the efficiency of the absorbing transition, which often coincides with higher energy photons, with yields of α -cleavage and other photo-initiated chemistry.

Hill *et al.* recently outlined that oriented electric fields can be used to (a) decrease the excitation energy of Irg and (b) increase the efficiency of α -cleavage pathway.¹¹ Their study targeted that fact that the transition dipoles for the $^1\pi\pi^*$ and $^3n\pi^*$ states are anti-aligned (as depicted schematically in Figure 3.1) and thus are likely perturbed by OEFs in opposite directions. In addition, the $\pi\pi^*$ states are highly polarizable, which greatly enhances their stabilization (> 1 eV) in the presence of an appropriately aligned field. Thus, suitable modification with a charged group or metal cation can lower the $^1\pi\pi^*$ state to become the S_1 and then, in the absence of any lower lying $^1n\pi^*$, the $S_1 (^1\pi\pi^*) \rightarrow T_n (^3n\pi^*)$ ISC pathway can dominate and enhance α -cleavage.¹⁰⁻¹² The efficiency of this pathway will be influenced by the energy gap between the $^1\pi\pi^*$ and $^3n\pi^*$ states and a smaller energy gap is expected to increase the ISC rate and increase α -cleavage yields.¹⁰⁻¹²

Motivated by these predictions, the present study targets Irg bound to metal cations in the gas phase. Using PD action spectroscopy together with mass spectrometry allows for investigation of the energy shift of the $^1\pi\pi^*$ states of Irgacure in the presence of different cations (M^{Q+}) along

with detection of the photoproduct ions. It is observed that the energies of the electronic quantum states are shifted by the presence of the M^{Q+} ions which altered the (a) the absorption profile and (b) subsequent photodissociation.

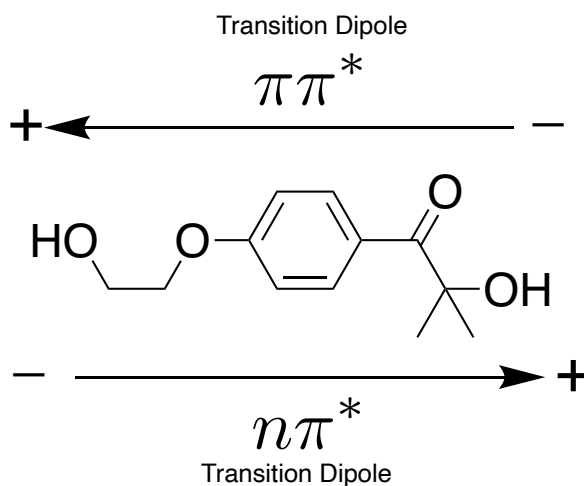


Figure 3.1: Alignment of transition dipoles for the $n\pi^*$ and $\pi\pi^*$ transitions for Irgacure as described by Hill *et al.*¹¹

3.3 Results and Discussion

3.3.1 Structures

In order to characterize the effect of oriented electric fields (OEFs) arising from the presence of M^{Q+} charged atoms on the electronic quantum states of Irg, it is first necessary to determine the preferred location of the charged atom. Based on the m/z values of the ions, the M^+ cations gave rise to complexes of one Irg molecule and one M^+ , whereas the M^{2+} cations gave rise to complexes comprising two Irg molecules clustered one M^{2+} , with essentially no reproducible signal detected for single Irg- M^{2+} clusters. Figure 3.2 shows structure of M^+ ($M^+ = H^+, Li^+, Na^+, K^+$) ions complexed with one Irgacure 2959 molecule, which are labelled Irg- M^{Q+} in general. Figure 3.2 also shows structures for $M^{2+} = Zn^{2+}, Mg^{2+}, Ca^{2+}$ clusters and these are labelled as Irg- M^{Q+} -Irg. The relative energies of other calculated Irg- M^{Q+} structures are shown in Figure 3.10 in Supporting Information. In all cases, Structure A (M^{Q+} binding to the ketone and hydroxide oxygens), as shown in Figure 3.2, is the lowest energy structure.

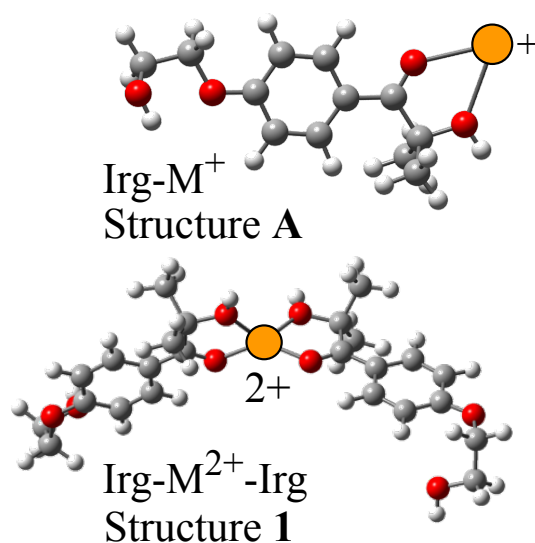


Figure 3.2: Lowest energy structures for Irg-M⁺ and Irg-M²⁺-Irg complexes as calculated using the M06-2X method.

It is known that thermodynamically less-favoured gas-phase structures can survive ESI since they are kinetically trapped.⁵⁰⁻⁵⁴ However it is determined that structures other than the minimum-energy structure A can be excluded from the ensuing analysis based on DFT energies and based on their predicted electronic spectra residing above the 3.0 eV to 5.0 eV range. Also, structures could be excluded based on low isomerization barriers to form Structure A. For additional details relating to the structure assignment see Supporting Information Section 3.SI.2.

The lowest energy structure of Irg-M²⁺-Irg (labelled Structure 1) has the hydroxy and ketone oxygens bound to the M^{Q+} ion. This Irg-M²⁺-Irg structure has some underlying C₂-like symmetry for the chromophore but not for the flexible hydroxyethane tails. Based on the relative energies of Irg-M²⁺-Irg structures as calculated with M06-2X (Figure 3.13 of Supporting Information), the following analysis assumes the results are related to Structure 1.

3.3.2 Action Spectroscopy

Figure 3.3 contains the photodissociation spectra (black line) of Irg-M⁺ and Irg-M²⁺-Irg ions alongside SCS-CC2 calculated vertical transitions below 5.0 eV (green bars). The PD action spectra are plotted as the sum of all photoproduct intensities. Representative product mass spectra are shown Figure 3.14 of the Supporting Information. The Na⁺ and K⁺ complexes

form α -cleavage pathway products as a dominant photoproduct pathway, the Li^+ system shows small amounts and the H^+ and the M^{2+} cases exhibit a range of photoproducts.

The lowest energy peaks in experimental action spectra are fitted with a Gaussian function (blue line in Figure 3.3), which is used to assign the position of maximum PD efficiency. Additional Gaussian functions are fitted to include the higher energy peaks and are shown in Figure 3.15 of Supporting Information. A single Gaussian function is used to fit the monocation systems Irg-Li^+ , Irg-Na^+ and Irg-K^+ , where there is one predicted bright transition. For Irg-H^+ however, there is a peak before a shoulder (around 3.65 eV) so a single Gaussian was fitted to this leading peak with a second smaller Gaussian to the shoulder. Fitting one Gaussian to the whole band shifts the centre peak position by less than 0.01 eV. For the dication systems, two bright absorption transitions are predicted and thus these are fitted with two Gaussian functions. The centre of this blue Gaussian fit (labelled E_{exp}) will be used and compared with calculated vertical transition energies, although it is worth noting that experimental assignment of the vertical transition energy is subjective.^{24, 55, 56}

The E_{exp} values are listed in Table 3.1 along with TD-DFT and SCS-CC2 vertical transition energies (E_{vert}) for Structure A of Irg-M^+ and Structure 1 of Irg-M^{2+} -Irg. The E_{vert} values calculated using SCS-CC2 and TD-DFT generally agree with E_{exp} , assuming the peak maximum corresponds to the vertical transition energy, but with a systematic overestimation of *ca.* 0.3 eV for SCS-CC2 and *ca.* 0.5 eV for TD-DFT, which is consistent with other reports using these methods.^{24, 28, 55, 57} Two features are observed for $\text{Irg-M}^{\text{Q}+}$ -Irg complexes in the PD action spectra and these are predicted by the SCS-CC2 calculations. Using these calculations, the experimental PD spectra are assigned to the $\pi \rightarrow \pi^*$ transitions of either Structure A for $\text{Irg-M}^{\text{Q}+}$ or Structure 1 for $\text{Irg-M}^{\text{Q}+}$ -Irg, for each cation.

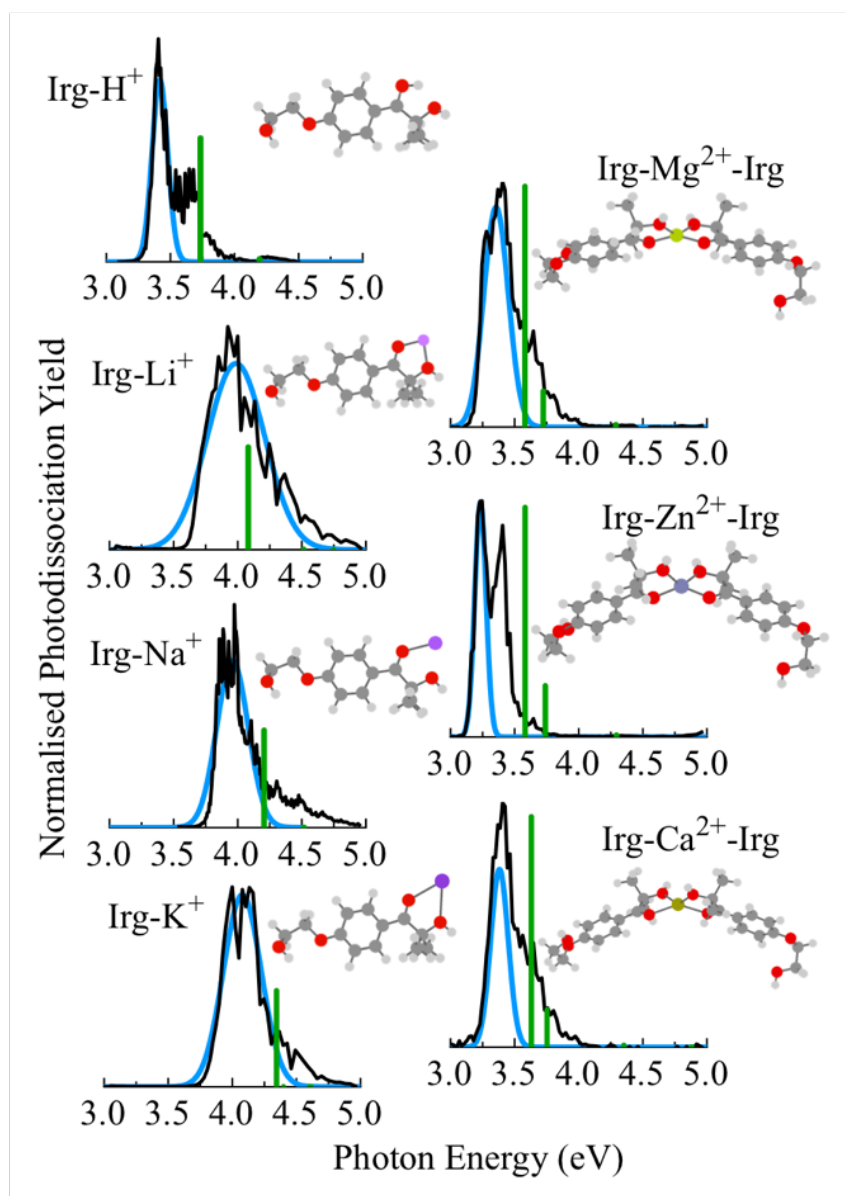


Figure 3.3: Photodissociation action spectra of Irgacure 2959 M^{Q+} complexes ($M^{Q+} = H^+, Li^+, Na^+, K^+, Mg^{2+}, Zn^{2+}, Ca^{2+}$). Single Gaussian functions (blue) are fit to the lowest energy transition. Additional Gaussian functions used for fitting are shown in Figure 3.15 of Supporting Information. Green sticks are the calculated vertical transition energies (E_{vert}) for each lowest energy structure using SCS-CC2 with bar heights equal to the oscillator strengths for each respective transition.

3.3.3 ${}^1\pi\pi^*$ State Shift by M^+ and M^{2+} cations.

Neutral Irg has an S_1 state with ${}^1n\pi^*$ character and an S_2 state with ${}^1\pi\pi^*$ character. Figure 3.4 shows the dominant contributing orbitals to these S_1 and S_2 transitions. The highest occupied π and lowest unoccupied π^* orbitals are primarily localized across the phenyl ring (C_{1-6}) in addition to on the ether oxygen and the ketone C_7O_1 groups (for atom labelling see Figure 3.16(A)) and these groups comprise the chromophore of Irg. The ${}^1\pi\pi^*$ transition shown in Figure 3.4 involves a redistribution of the electron density around aromatic ring as well as an

increase around the ketone moiety. In contrast, the ${}^1n\pi^*$ transition shifts electron density from the C=O lone pair into the broader π system. The important result of this is that the corresponding transition dipoles for these states are oppositely aligned, as shown in Figure 3.1.

Table 3.1: Centre (E_{exp}) and half width half maximum (HWHM) of Gaussian fit to experimental data. Vertical excitation (E_{vert}) energies and oscillator strengths (f) to the first ${}^1\pi\pi^*$ state for each ion as calculated using SCS-CC2 and TD-DFT. DNC denotes that the TD-DFT calculation did not converge. ^aSCS-CC2 calculations employed the def2-TZVP basis set for Irg- M^+ ions and the def2-SVP basis set for Irg- M^{2+} -Irg ions.

	E_{exp} (eV)	<i>Exp.</i> HWHM (eV)	E_{vert} SCS- CC2 ^a (eV)	<i>Oscillator</i> Strength SCS-CC2 (f)	E_{vert} TD-DFT (eV)	<i>Oscillator</i> Strength TD-DFT (f)
<i>Irg-H⁺</i>	3.42	0.07	3.73	0.76	4.11	0.66
<i>Irg-Li⁺</i>	3.97	0.24	4.08	0.63	4.36	0.56
<i>Irg-Na⁺</i>	3.96	0.14	4.21	0.60	4.47	0.53
<i>Irg-K⁺</i>	4.08	0.17	4.35	0.59	4.55	0.52
<i>Irg-Mg²⁺-Irg</i>	3.36	0.11	3.58	1.52	3.90	1.34
<i>Irg-Zn²⁺-Irg</i>	3.23	0.05	3.58	1.45	3.86	1.24
<i>Irg-Ca²⁺-Irg</i>	3.38	0.08	3.63	1.46	DNC	DNC

As described by other groups, the transition-dipole axis can be thought of as a reaction-axis for OEF control over chemical reactivity.¹⁻³ As such, if an electric field was oriented from a positive point-charge at the position as M^{Q+} , near the ketone and OH groups as shown in both cases in Figure 3.2, then the electric field arising from the cation will stabilize (red shift) the ${}^1\pi\pi^*$ state and destabilize (blue-shift) the ${}^1n\pi^*$ state. That is, the field from the cation works with the $\pi \rightarrow \pi^*$ transition but works against the $n \rightarrow \pi^*$ transition.¹⁰⁻¹² Ultimately, the stabilization of the $\pi\pi^*$ state is in large part due to its polarizability, which leads to significant stabilization despite its almost negligible dipole in the absence of the cation.¹⁰⁻¹²

Experimentally, it is known that the absorption maximum of neutral Irg in acetonitrile is $\lambda_{\text{max}} = 273 \text{ nm}$ (4.54 eV),^{43, 44} which corresponds to the $\pi \rightarrow \pi^*$ transition. The gas-phase λ_{max} for neutral Irg is not reported, so in the absence of this value the experimental red shifts (Figure 3.3) are reported here as shifts relative to this reported acetonitrile λ_{max} value. The experimental

shifts, assigned as transitions to the ${}^1\pi\pi^*$ state of each system, are listed in Table 3.2 along with the TD-DFT calculated shift. Figure 3.16 shows the distances between the centre of mass (COM) of the chromophore and the charged atom and are listed in Table 3.2. From the results, the mono-cations give rise to red shifts up to 1.18 eV measured for Irg- H^+ . It is apparent that as the effective radius of mono-cationic M^+ atom increases, its binding distance from the chromophore increases (see Figure 3.16A and Table 3.2). For the di-cationic Irg- M^{2+} -Irg systems shifts are over 1 eV, relative to neutral Irg are measured. Shifting of electronic^{20, 21} and vibrational⁵⁸ transitions due to bound M^{Q+} cations has been reported in gas-phase action spectra by other groups. Electrostatic shifts of electronic states have also been induced using metal chlorides in solution.¹² Overall, the Irg- M^{Q+} action spectra reveal that the amount of red shift for the ${}^1\pi\pi^*$ transition increases as the charge increases from +1 to +2. Also, the trend is for the red shift to increase as the M^{Q+} positions closer to the chromophore.

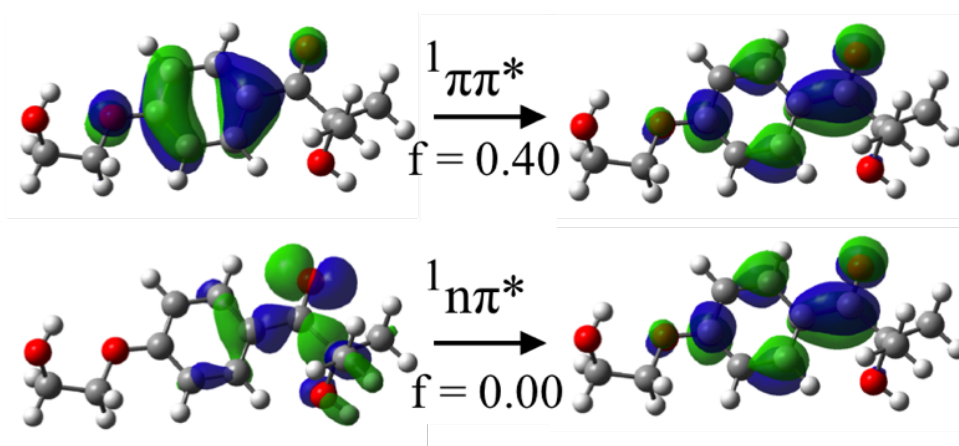


Figure 3.4: Dominant orbital transitions for the first $\pi \rightarrow \pi^*$ transition and $n \rightarrow \pi^*$ transition of neutral Irgacure 2959 (M06-2X/def2-TZVP) with predicted oscillator strengths (f).

Figure 3.5A shows a plot of the experimental red shift for the transition to the ${}^1\pi\pi^*$ state compared to the calculated TD-DFT red shift, where there is a good correlation. These calculations thus provide good predictions for the shift of the absorption transitions. To assess if the M^{Q+} cations are acting effectively as point charges—and hence if the underlying cause of the shift is primarily electrostatic³⁴—TD DFT excitation energies were recalculated with the geometry fixed but with M^{Q+} atoms replaced with point charges P^{Q+} ($Q = +1e$ or $Q = +2e$). Figure 3.5B shows the calculated ${}^1\pi\pi^*$ shifts plotted against the shifts calculated for point charges. The mono-cationic shifts are nearly identically to P^{1+} point charge values. The di-

cationic systems, on the other hand, have a reduced red shift compared to the P^{2+} point-charge values—falling off the linear trend. This may be due to some bonding interaction between the cation and the Irg molecules, thus reducing the effective charge of the M^{2+} cation. For the Irg- M^+ clusters, the correlation between the shift and the point charge values with the M^{Q+} cations supports the notion that the shifts are an electrostatic effect.³⁴

Table 3.2: Calculated distances between chromophore centre of mass (COM) and charged atom, electric field strength (V/M) calculated using Coulomb's law, transition energy (E_{exp}) shift determined from the PD action spectrum, TD-DFT vertical transition energy shifts (E_{vert}) and E_{vert} calculated by replacing M^{Q+} with a point charge.

	<i>Cation-Irg Distance (Å)</i>	<i>Electric Field Strength (V/m) $\times 10^9$</i>	<i>Field E_{exp} Shift</i>	<i>E_{vert} Shift of Ion (TD-DFT)</i>	<i>E_{vert} Shift with Point Charge (TD-DFT)</i>
<i>Irg-H^+</i>	4.07	8.69	-1.12	-0.990	-0.982
<i>Irg-Li^+</i>	4.95	5.89	-0.57	-0.738	-0.743
<i>Irg-Na^+</i>	5.33	5.07	-0.58	-0.629	-0.621
<i>Irg-K^+</i>	5.71	4.42	-0.46	-0.549	-0.510
<i>Irg-Mg^{2+}-Irg</i>	5.07	11.2	-1.19	-1.206	-1.343
<i>Irg-Zn^{2+}-Irg</i>	5.07	11.2	-1.31	-1.238	-1.364
<i>Irg-Ca^{2+}-Irg</i>	5.41	9.86	-1.16	DNC	-1.336

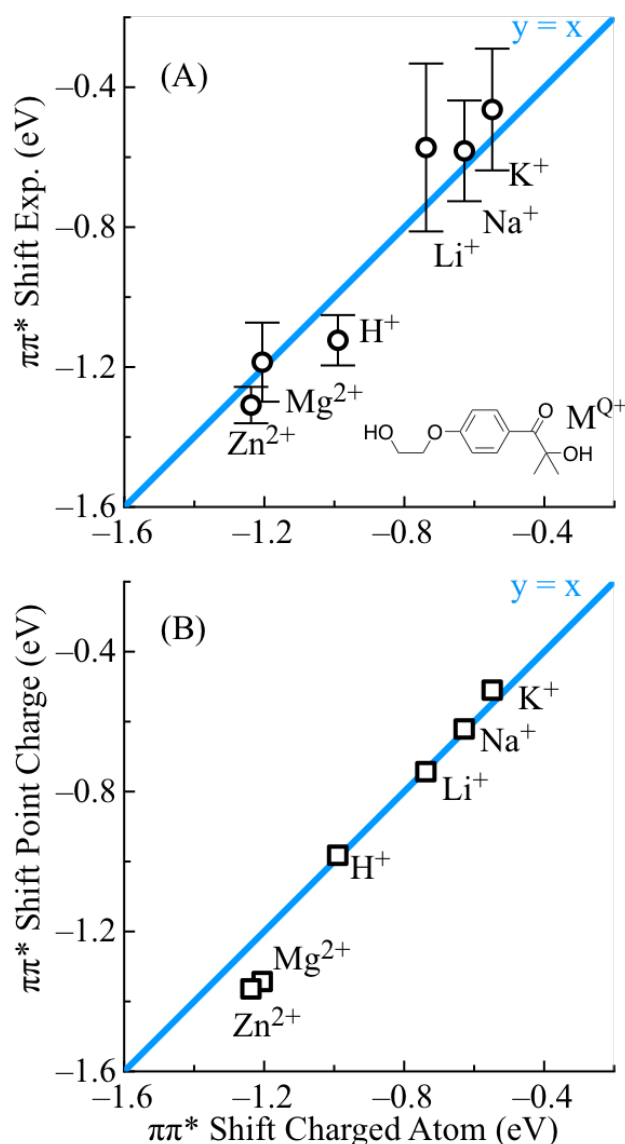


Figure 3.5: Plot of $^1\pi\pi^*$ shift of Irg- M^{Q+} relative to neutral Irg calculated by TD-DFT versus (A) the experimental value from the photodissociation action spectra and (B) the shift as modelled by a point charge.

To further explore the underlying cause of the band shift—and the influence of the metal cation—the electric field strength (E) is calculated using Coulomb's law⁴⁵ (as described in Section 3.SI.6 of Supporting Information). We note that this is a somewhat simplified approximation of the electric field strength, as it is simply the value of the electric field strength at a single distance to a point on the Irg chromophore and the charge Q_M (either $+1e$ or $+2e$). Values for each system are shown in Table 3.2. Figure 3.6A shows the plot of the experimental red shift (E_{exp} shift) of the $\pi \rightarrow \pi^*$ transition for each ion complex (relative to neutral Irg) against the electric field strength (E) calculated to arise from M^{Q+} (with error bars from the HWHM from the experimental band, *vide supra*). A fitted linear function (black line), shows

that the experimental band shift of the transition correlates with the electric field strength at the chromophore COM ($R^2 = 0.95$ and y-intercept of -0.06 ± 0.3 eV). Importantly, the fit passes through origin in accord with 0 V/m electric field affecting zero red shift. Recall that the $^1\pi\pi^*$ energy shifts in Figure 3.6 are referenced to the reported experimental value in acetonitrile solution.^{43,44} As a check, the $^1\pi\pi^*$ transition of neutral irgacure was calculated (M06-2X/def2-TZVP, acetonitrile PCM) to be 0.16 eV red shifted from the gas-phase value. This estimate for the gas-phase value falls within the uncertainty of the fitted y-intercept. In this case of Irg- M^{Q+} ions, and for other Norrish type-I photoinitiators,^{10,11} the charge-induced dipole alignment—moderated by the polarizability—provides a clear rationalization of the excited-state energy shift.

For the calculations, the vertical excitation energies to the $^1\pi\pi^*$ state of Irg- M^+ and Irg- M^{2+} -Irg ions relative to neutral Irg values are plotted in Figure 3.6B (triangles). The green trace is the vertical $^1\pi\pi^*$ excitation energy for neutral Irg in the presence of an increasing static electric field (oriented along the axis of neutral Irg as shown in Figure 3.9 of Supporting Information). It was found that at higher electric field values, the $^1\pi\pi^*$ state of interest interacted with a higher lying $^1\pi\sigma^*$ state (shown as blue trace) and this state is dramatically stabilized by the electric field. Although these states interact well-above the E field values for the mono cations, they become mixed around 9×10^9 V/m and invert at electric field strengths above 10×10^9 V/m (These $^1\pi\pi^*$ and $^1\pi\sigma^*$ orbitals are shown in Figure 3.17 of Supporting Information). State-mixing and orbital-mixing is a common feature of molecular species in OEFs.³ It is not suspected that the $^1\pi\sigma^*$ state is involved in the dissociation of the high-field (or any) complexes here. As mentioned above the dissociation products for the Irg- Na^+ and Irg- K^+ complexes cleanly photodissociate to α -cleavage pathway products, Irg- Li^+ does in small yields, but the Irg- H^+ complex and the Irg- M^{2+} -Irg systems do not. The α -pathway mechanisms are discussed in the next section.

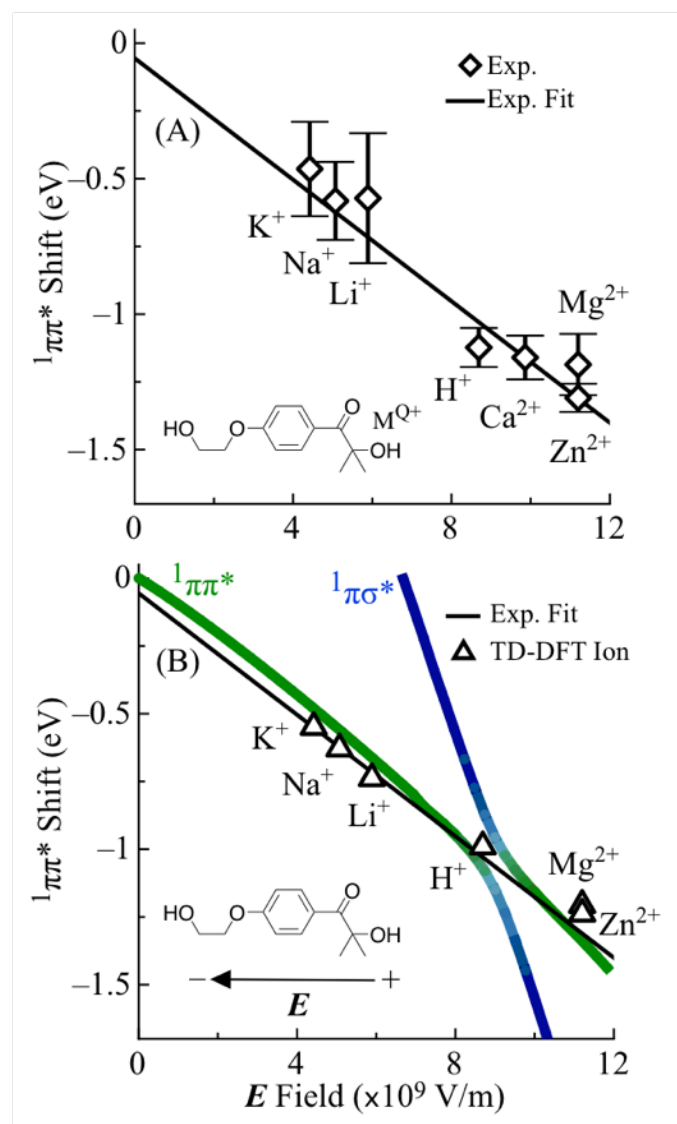


Figure 3.6: Energy shift of the transition to the first $^1\pi\pi^*$ state for Irg- M^{Q+} as a function of the electric field strength E . (A) Diamonds are the experimental peak position; error bars are the \pm HWHM of the fitted Gaussian. Black line is a linear regression fit to experimental data. (B) Triangles are the vertical excitation energies of the transition to the $^1\pi\pi^*$ state (M06-2X/def2-TZVP). The green trace is the $^1\pi\pi^*$ transition energy (M06-2X/def2-TZVP) under static electric fields of different strengths and the blue trace follows a $^1\pi\sigma^*$ state which interacts with the $^1\pi\pi^*$ state at higher E values (see text).

3.3.4 Photodissociation Pathways

We have shown that the proximity of the cation affects the amount of red shift for the key absorbing transition to the $^1\pi\pi^*$ state of Irg- M^{Q+} ions. This achieves the goal of decreasing the photon energy required for excitation. The next required step is efficient formation of radical products *via* α -cleavage. Two pathways resulting in α -cleavage are shown in Figure 3.7, these are canonical acetophenone-type pathway^{10, 11} (Figure 3.7A) and the more direct ISC pathway (Figure 3.7B). It is theorized that the efficiency of α -cleavage is enhanced when the canonical

acetophenone-type photo-dissociation pathway ($^1\pi\pi^* \rightarrow ^1n\pi^* \rightarrow ^3\pi\pi^* \rightarrow ^3n\pi^* \rightarrow \alpha\text{-cleavage}$) is negated by lowering the $^1\pi\pi^*$ state below the $^1n\pi^*$ state.^{11, 12} Once achieved, the S_1 state is $^1\pi\pi^*$, and this opens up the more direct $^1\pi\pi^* \rightarrow ^3n\pi^* \rightarrow \alpha\text{-cleavage}$ pathway.¹⁰⁻¹² This direct ISC from the S_1 ($^1\pi\pi^*$) to the T_n ($^3n\pi^*$) state must still compete with radiative decay and other non-radiative decay pathways but overall enhancement of ISC is afforded by the decreasing energy gap between the S_1 $^1\pi\pi^*$ state and the T_n $^3n\pi^*$ state.¹¹ Dissociation from $^3\pi\pi^*$ states is predicted to be slow^{12, 59} while ISC to the triplet manifold and $\alpha\text{-cleavage}$ from the $^3n\pi^*$ state is ultra-fast.⁴⁴

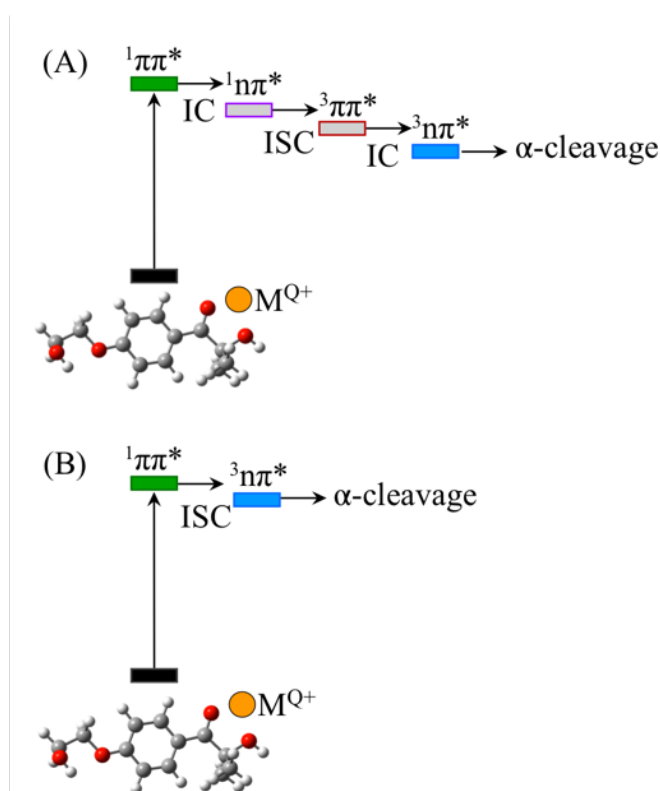


Figure 3.7: Two $\alpha\text{-cleavage}$ pathways where (A) the lowest energy singlet state is $^1n\pi^*$ character and follows a multistep mechanism and the simpler case (B) where the lowest energy singlet state is $^1\pi\pi^*$ character.

Using the framework shown in Figure 3.7, Figure 3.8 shows the vertical transition energies to the first $^1\pi\pi^*$, $^1n\pi^*$, $^3\pi\pi^*$ and $^3n\pi^*$ states of each Irg- M^{Q+} . The Irg- M^{Q+} -Irg complexes are excluded from this analysis because of their more complex dissociation mass spectra, which presumably arise from other mechanisms. To accurately characterize different spin states, the SCS-CC2 method was used to calculate vertical excitation of these various spin states. CC2 is a robust method for calculating the excitation energies of medium sized molecules and the SCS

correction improves results for open shell systems such as the triplet states investigated here.⁶⁰ Calculated $^1\pi\pi^*$ energies (green rectangles in Figure 3.8) are compared with experimental energies of the first $^1\pi\pi^*$ state (black diamonds in Figure 3.8) and agree well. Therefore, SCS-CC2 better reproduces absolute vertical transition energies, whereas TD-DFT performed well for relative energy shifts but consistently overestimated absolute transition energies by ~ 0.5 eV.

The encroachment of the M^+ cation to the chromophore (from Irg- K^+ to Irg- H^+) red shifts the transition to the $\pi\pi^*$ states (green and red rectangles in Figure 3.8) while raising the transition energy to the $n\pi^*$ states (blue and purple rectangles in Figure 3.8). It is worth noting that in the case of Irg- H^+ the $n\pi^*$ state is affected differently because the proton interacts with the n orbital in a way that cannot be described solely by electrostatic effects. For all Irg- M^{Q+} ions, the OEF arising from the presence of the cation stabilizes the $^1\pi\pi^*$ state such that it shifts *below* the energy of the $^1n\pi^*$ state thus it favours the ISC pathway from S_1 ($^1\pi\pi^*$) to the T_n ($^3n\pi^*$) state (in accordance with the El-Sayed rules). Because ISC can occur from the $^1\pi\pi^*$ state to the dissociative $^3n\pi^*$ state, the more direct $^1\pi\pi^* \rightarrow ^3n\pi^* \rightarrow \alpha$ -cleavage pathway (Figure 3.7B) can dominate.

In order to maximize α -cleavage yield, one can drive ISC to the desired dissociative $^3n\pi^*$ state by minimizing the energy gap between $^1\pi\pi^*$ and $^3n\pi^*$ states. This gap is calculated using SCS-CC2/def2-TZVP. The gas-phase PD experiments follow the formation of photoproduct ions and, as such, the PD yield of α -cleavage product ions can be reported as a fraction of the total product yield and also as a fraction of the total precursor ion depletion.

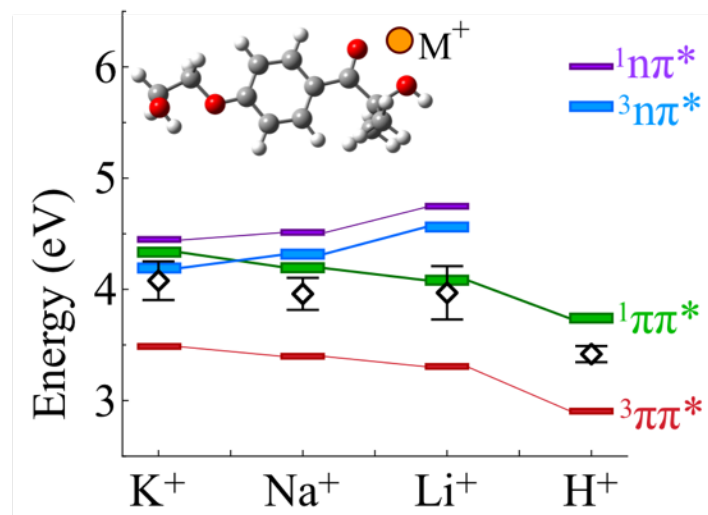


Figure 3.8: Vertical transition energies to the first $1\pi\pi^*$ state (green rectangles), the first $3n\pi^*$ state (blue rectangles), the first $3\pi\pi^*$ state (red rectangles) and the first $3n\pi^*$ state (purple rectangles) calculated using SCS-CC2/def2-TZVP. Values are compared to the lowest energy feature observed in the action spectra (black diamonds).

Table 3.3 shows the experimental ratio between the α -cleavage photoproduct ion yield $\phi_{\alpha\text{-cleavage}}$ and total PD photoproduct yield ϕ_{products} (or total depletion of the precursor ion $\phi_{\text{depletion}}$) for each Irg- M^{Q+} ion plotted against the energy gap between the first $1\pi\pi^*$ and $3n\pi^*$ states as calculated (SCS-CC2). The Irg- Na^+ and Irg- K^+ ions have the smallest energy gap between the first $1\pi\pi^*$ and $3n\pi^*$ states and dissociate with a yield of $\phi_{\alpha\text{-cleavage}} / \phi_{\text{products}} = 0.86$ (Irg- Na^+) and $\phi_{\alpha\text{-cleavage}} / \phi_{\text{products}} = 0.97$ (Irg- K^+). The higher α -cleavage yield of Irg- K^+ can be rationalized as the $3n\pi^*$ state being slightly lower in energy than $1\pi\pi^*$ state; the corresponding energy difference for Irg- Na^+ value is slightly positive but within the uncertainty of these values. With an unfavorably large energy gap of 0.5 eV, the Irg- Li^+ complex dissociated with a small yield of $\phi_{\alpha\text{-cleavage}} / \phi_{\text{products}} = 0.0008$. Therefore, under low pressure conditions in the gas-phase, other dissociation pathways can dominate for the Irg- Li^+ system.

The ratios of $\phi_{\alpha\text{-cleavage}} / \phi_{\text{depletion}}$ are lower than for $\phi_{\alpha\text{-cleavage}} / \phi_{\text{products}}$ because we suspect photoproducts are formed below the m/z threshold for the experiment. It is quite possible that α -cleavage resulting in $\bullet C_9H_9O_3 + \bullet C_3H_6OH + M^{Q+}$ is occurring and this would go undetected (and not contribute to the $\phi_{\alpha\text{-cleavage}}$ value). If this channel was taken into account, then the $\phi_{\alpha\text{-cleavage}} / \phi_{\text{depletion}}$ ratio would be expected to more closely match the $\phi_{\alpha\text{-cleavage}} / \phi_{\text{products}}$ value. Nevertheless, the $\phi_{\alpha\text{-cleavage}} / \phi_{\text{depletion}}$ values follow a similar trend to the $\phi_{\alpha\text{-cleavage}} / \phi_{\text{products}}$ values. Irg- K^+ has a yield of $\phi_{\alpha\text{-cleavage}} / \phi_{\text{depletion}} = 0.36$, while Irg- Li^+ has a yield of $\phi_{\alpha\text{-cleavage}} / \phi_{\text{depletion}} =$

0.00041. By tuning the energy gap between $^1\pi\pi^*$ and $^3n\pi^*$ quantum states the photochemistry of Irg is altered. This manifests in a yield of α -cleavage from Irg- K^+ is $\sim 10^4$ times larger than for Irg- Li^+ .

Table 3.3: Energy gap between the (vertical) $^1\pi\pi^*$ and $^3n\pi^*$ states as calculated using SCS-CC2/def2-TZVP. Experimental ratio between photo-dissociation leading to α -cleavage ($\phi_{\alpha\text{-cleavage}}$) and total observed photo-dissociation yield (ϕ_{products}). Experimental ratio between photo-dissociation leading to α -cleavage ($\phi_{\alpha\text{-cleavage}}$) and total observed depletion of the precursor ion yield ($\phi_{\text{depletion}}$).

	SCS-CC2	Exp.	Exp.	PD
	Energy Gap	$\phi_{\alpha\text{-cleavage}}$	$\phi_{\alpha\text{-cleavage}}$	Wavelength
	$^3n\pi^* - ^1\pi\pi^*$	ϕ_{products}	$\phi_{\text{depletion}}$	(nm)
Irg- K^+	-0.15	0.97	0.36	300
Irg- Na^+	0.11	0.86	0.0096	296
Irg- Li^+	0.48	0.0008	0.00041	310

3.4 Conclusion

Using ion trap mass spectrometry, M^{Q+} cations (H^+ , Li^+ , Na^+ , K^+ , Zn^{2+} , Ca^{2+} , Mg^{2+}) bound to Irg molecules—either one Irg molecule per M^+ monocationic atom or two Irg molecules per M^{2+} dicationic atom—resulting in electric fields of varying strengths that were oriented internally for each Irg molecule. Gas-phase UV PD spectroscopy, combined with TD-DFT calculations, showed that the first $^1\pi\pi^*$ transition was red shifted proportionally to the strength of the electric field arising from the M^{Q+} cation. Red shifts of the transitions to the $^1\pi\pi^*$ state are observed from the UVC to the UVB or UVA region (depending on the charged atom), in accordance with the predictions by Hill and Coote (2019)¹¹ that transition energies can be favorably controlled using OEFs.

The radical photoproduct yield of 97% following α -cleavage were measured for Irg- K^+ , which was the system with the smallest energy gap between the first $^1\pi\pi^*$ and $^3n\pi^*$ states (as calculated using SCS-CC2). In contrast, Irg- Li^+ ions with a $^1\pi\pi^*$ and $^3n\pi^*$ gap of 0.5 eV dissociated with 0.08% α -cleavage. Therefore, with the tuning the $^1\pi\pi^* - ^3n\pi^*$ energy gap with OEFs, photodissociation can be drastically altered. This study provides combined experimental and theoretical evidence that oriented electric fields can shift photochemical reactivity by

tuning the energies of electronic quantum states to affect absorption profiles and photodissociation pathways.

ACKNOWLEDGMENT

Funding from Australian Research Council grants (AJT: DP200100065 and LP180100550. MLC: CE140100012 and FL170100041) is gratefully acknowledged. This work was also supported by computational resources provided by the Australian Government through the National Computation Infrastructure under the National Computational Merit Allocation Scheme. S.J.P.M., B.I.M., acknowledge support from Australian Government Research Training Program Scholarships

References

1. Ciampi, S.; Darwish, N.; Aitken, H. M.; Díez-Pérez, I.; Coote, M. L., Harnessing electrostatic catalysis in single molecule, electrochemical and chemical systems: a rapidly growing experimental tool box. *Chemical Society Reviews* **2018**, *47* (14), 5146-5164.
2. Shaik, S.; Ramanan, R.; Danovich, D.; Mandal, D., Structure and reactivity/selectivity control by oriented-external electric fields. *Chemical Society Reviews* **2018**, *47* (14), 5125-5145.
3. Stuyver, T.; Danovich, D.; Joy, J.; Shaik, S., External electric field effects on chemical structure and reactivity. *Wiley Interdisciplinary Reviews: Computational Molecular Science* **2019**, e1438.
4. Shaik, S.; Mandal, D.; Ramanan, R., Oriented electric fields as future smart reagents in chemistry. *Nature Chemistry* **2016**, *8* (12), 1091.
5. Shaik, S.; Danovich, D.; Joy, J.; Wang, Z.; Stuyver, T., Electric-Field Mediated Chemistry: Uncovering and Exploiting the Potential of (Oriented) Electric Fields to Exert Chemical Catalysis and Reaction Control. *Journal of the American Chemical Society* **2020**, *142* (29), 12551-12562.
6. Stuyver, T.; Ramanan, R.; Mallick, D.; Shaik, S., Oriented (Local) Electric Fields Drive the Millionfold Enhancement of the H-Abstraction Catalysis Observed for Synthetic Metalloenzyme Analogues. *Angewandte Chemie International Edition* **2020**, *59* (20), 7915-7920.
7. Gorin, C. F.; Beh, E. S.; Kanan, M. W., An Electric Field-Induced Change in the Selectivity of a Metal Oxide-Catalyzed Epoxide Rearrangement. *Journal of the American Chemical Society* **2012**, *134* (1), 186-189.
8. Aragonès, A. C.; Haworth, N. L.; Darwish, N.; Ciampi, S.; Bloomfield, N. J.; Wallace, G. G.; Díez-Pérez, I.; Coote, M. L., Electrostatic catalysis of a Diels-Alder reaction. *Nature* **2016**, *531* (7592), 88.
9. Gryn'Ova, G.; Marshall, D. L.; Blanksby, S. J.; Coote, M. L., Switching radical stability by pH-induced orbital conversion. *Nature Chemistry* **2013**, *5* (6), 474.

10. Hill, N. S.; Coote, M. L., Internal Oriented Electric Fields as a Strategy for Selectively Modifying Photochemical Reactivity. *Journal of the American Chemical Society* **2018**, *140* (50), 17800-17804.
11. Hill, N. S.; Coote, M. L., Strategies for Red-Shifting Type I Photoinitiators: Internal Electric Fields versus Lewis Acids versus Increasing Conjugation. *Australian Journal of Chemistry* **2019**, *72* (8), 627-632.
12. Noble, B. B.; Mater, A. C.; Smith, L. M.; Coote, M. L., The effects of Lewis acid complexation on type I radical photoinitiators and implications for pulsed laser polymerization. *Polymer Chemistry* **2016**, *7* (41), 6400-6412.
13. Menzel, J. P.; Feist, F.; Tuten, B.; Weil, T.; Blinco, J. P.; Barner-Kowollik, C., Light-Controlled Orthogonal Covalent Bond Formation at Two Different Wavelengths. *Angewandte Chemie International Edition* **2019**, *58* (22), 7470-7474.
14. Wolf, T. J.; Voll, D.; Barner-Kowollik, C.; Unterreiner, A.-N., Elucidating the early steps in photoinitiated radical polymerization via femtosecond pump-probe experiments and DFT calculations. *Macromolecules* **2012**, *45* (5), 2257-2266.
15. Fast, D. E.; Lauer, A.; Menzel, J. P.; Kelterer, A.-M.; Gescheidt, G.; Barner-Kowollik, C., Wavelength-Dependent Photochemistry of Oxime Ester Photoinitiators. *Macromolecules* **2017**, *50* (5), 1815-1823.
16. Blyth, M. T.; Noble, B. B.; Russell, I. C.; Coote, M. L., Oriented Internal Electrostatic Fields Cooperatively Promote Ground-and Excited-State Reactivity: A Case Study in Photochemical CO₂ Capture. *Journal of the American Chemical Society* **2019**, *142* (1), 606-613.
17. Günther, A.; Nieto, P.; Berden, G.; Oomens, J.; Dopfer, O., IRMPD spectroscopy of metalated flavins: structure and bonding of M^{q+}-lumichrome complexes (M^{q+}= Li⁺-Cs⁺, Ag⁺, Mg²⁺). *Physical Chemistry Chemical Physics* **2014**, *16* (27), 14161-14171.
18. Gao, J.; Berden, G.; Rodgers, M.; Oomens, J., Interaction of Cu⁺ with cytosine and formation of i-motif-like C-M⁺-C complexes: alkali versus coinage metals. *Physical Chemistry Chemical Physics* **2016**, *18* (10), 7269-7277.
19. Nieto, P.; Günther, A.; Berden, G.; Oomens, J.; Dopfer, O., IRMPD spectroscopy of metalated flavins: structure and bonding of lumiflavin complexes with alkali and coinage metal ions. *The Journal of Physical Chemistry A* **2016**, *120* (42), 8297-8308.
20. Nieto, P.; Müller, D.; Sheldrick, A.; Günther, A.; Miyazaki, M.; Dopfer, O., Effect of alkali ions on optical properties of flavins: vibronic spectra of cryogenic M⁺ lumichrome ions (M= Li-Cs) in the gas phase. *Physical Chemistry Chemical Physics* **2018**, *20* (34), 22148-22158.
21. Müller, D.; Nieto, P.; Miyazaki, M.; Dopfer, O., Effect of alkali ions on optical properties of flavins: vibronic spectra of cryogenic M⁺ lumiflavin complexes (M= Li-Cs). *Faraday Discussions* **2019**, *217*, 256-275.
22. Taccone, M. n. I.; Cruz-Ortiz, A. F.; Dezalay, J.; Soorkia, S.; Broquier, M.; Grégoire, G.; Sánchez, C. n. G.; Pino, G. A., UV Photofragmentation of Cold Cytosine-M⁺ Complexes (M⁺: Na⁺, K⁺, Ag⁺). *The Journal of Physical Chemistry A* **2019**, *123* (36), 7744-7750.
23. Yang, B.; Wu, R.; Polfer, N.; Berden, G.; Oomens, J.; Rodgers, M., IRMPD action spectroscopy of alkali metal cation-cytosine complexes: effects of alkali metal cation size on gas phase conformation. *Journal of The American Society for Mass Spectrometry* **2013**, *24* (10), 1523-1533.
24. Marlton, S. J.; McKinnon, B. I.; Ucur, B.; Maccarone, A. T.; Donald, W. A.; Blanksby, S. J.; Trevitt, A. J., Selecting and identifying gas-phase protonation isomers of nicotineH⁺ using combined laser, ion mobility and mass spectrometry techniques. *Faraday Discussions* **2019**, *217*, 453-475.

25. Berdakin, M.; Féraud, G.; Dedonder-Lardeux, C.; Jouvét, C.; Pino, G. A., Excited states of protonated DNA/RNA bases. *Physical Chemistry Chemical Physics* **2014**, *16* (22), 10643-10650.
26. Féraud, G.; Esteves-Lopez, N.; Dedonder-Lardeux, C.; Jouvét, C., UV spectroscopy of cold ions as a probe of the protonation site. *Physical Chemistry Chemical Physics* **2015**, *17* (39), 25755-25760.
27. Noble, J. A.; Broquier, M.; Gregoire, G.; Soorkia, S.; Pino, G.; Marceca, E.; Dedonder-Lardeux, C.; Jouvét, C., Tautomerism and electronic spectroscopy of protonated 1- and 2-aminonaphthalene. *Physical Chemistry Chemical Physics* **2018**, *20* (9), 6134-6145.
28. Matthews, E.; Dessent, C. E., Locating the proton in nicotinamide protomers via low-resolution UV action spectroscopy of electrosprayed solutions. *The Journal of Physical Chemistry A* **2016**, *120* (46), 9209-9216.
29. Bull, J. N.; Coughlan, N. J.; Bieske, E. J., Protomer-Specific Photochemistry Investigated Using Ion Mobility Mass Spectrometry. *The Journal of Physical Chemistry A* **2017**, *121* (32), 6021-6027.
30. Matthews, E.; Dessent, C. E., Experiment and theory confirm that UV laser photodissociation spectroscopy can distinguish protomers formed via electrospray. *Physical Chemistry Chemical Physics* **2017**, *19* (26), 17434-17440.
31. Matthews, E.; Cercola, R.; Dessent, C., Protomer-Dependent Electronic Spectroscopy and Photochemistry of the Model Flavin Chromophore Alloxazine. *Molecules* **2018**, *23* (8), 2036.
32. Marlton, S. J.; McKinnon, B. I.; Ucur, B.; Bezzina, J. P.; Blanksby, S. J.; Trevitt, A. J., Discrimination Between Protonation Isomers of Quinazoline by Ion Mobility and UV-Photodissociation Action Spectroscopy. *The Journal of Physical Chemistry Letters* **2020**.
33. Aragones, A. C.; Haworth, N. L.; Darwish, N.; Ciampi, S.; Bloomfield, N. J.; Wallace, G. G.; Diez-Perez, I.; Coote, M. L., Electrostatic catalysis of a Diels–Alder reaction. *Nature* **2016**, *531* (7592), 88-91.
34. Yue, L.; Li, J.; Zhou, S.; Sun, X.; Schlangen, M.; Shaik, S.; Schwarz, H., Control of product distribution and mechanism by ligation and electric field in the thermal activation of methane. *Angewandte Chemie International Edition* **2017**, *56* (34), 10219-10223.
35. Marshall, D. L.; Gryn'ova, G.; Poad, B. L.; Bottle, S. E.; Trevitt, A. J.; Coote, M. L.; Blanksby, S. J., Experimental evidence for long-range stabilizing and destabilizing interactions between charge and radical sites in distonic ions. *International Journal of Mass Spectrometry* **2019**, *435*, 195-203.
36. Klinska, M.; Smith, L. M.; Gryn'ova, G.; Banwell, M. G.; Coote, M. L., Experimental demonstration of pH-dependent electrostatic catalysis of radical reactions. *Chemical Science* **2015**, *6* (10), 5623-5627.
37. Zhang, L.; Laborda, E.; Darwish, N.; Noble, B. B.; Tyrell, J. H.; Pluczyk, S.; Le Brun, A. P.; Wallace, G. G.; Gonzalez, J.; Coote, M. L., Electrochemical and electrostatic cleavage of alkoxyamines. *Journal of the American Chemical Society* **2018**, *140* (2), 766-774.
38. Noble, B. B.; Smith, L. M.; Coote, M. L., The effect of LiNTf₂ on the propagation rate coefficient of methyl methacrylate. *Polymer Chemistry* **2014**, *5* (17), 4974-4983.
39. Jiang, J. Y.; Smith, L. M.; Tyrell, J. H.; Coote, M. L., Pulsed laser polymerisation studies of methyl methacrylate in the presence of AlCl₃ and ZnCl₂—evidence of propagation catalysis. *Polymer Chemistry* **2017**, *8* (38), 5948-5953.
40. Geng, J.; Li, W.; Zhang, Y.; Thottappillil, N.; Clavadetscher, J.; Lilienkamp, A.; Bradley, M., Radical polymerization inside living cells. *Nature Chemistry* **2019**, *11* (6), 578-586.

41. Williams, C. G.; Malik, A. N.; Kim, T. K.; Manson, P. N.; Elisseff, J. H., Variable cytocompatibility of six cell lines with photoinitiators used for polymerizing hydrogels and cell encapsulation. *Biomaterials* **2005**, *26* (11), 1211-1218.
42. Fedorovich, N. E.; Oudshoorn, M. H.; van Geemen, D.; Hennink, W. E.; Alblas, J.; Dhert, W. J., The effect of photopolymerization on stem cells embedded in hydrogels. *Biomaterials* **2009**, *30* (3), 344-353.
43. Jockusch, S.; Landis, M. S.; Freiermuth, B.; Turro, N. J., Photochemistry and photophysics of α -hydroxy ketones. *Macromolecules* **2001**, *34* (6), 1619-1626.
44. Liu, M.; Li, M.-D.; Xue, J.; Phillips, D. L., Time-resolved spectroscopic and density functional theory study of the photochemistry of irgacure-2959 in an aqueous solution. *The Journal of Physical Chemistry A* **2014**, *118* (38), 8701-8707.
45. McNaught, A. D.; Wilkinson, A., *IUPAC. Compendium of Chemical Terminology, 2nd ed. (the "Gold Book")*. Blackwell Science Oxford: 1997; Vol. 1669.
46. Segurola, J.; Allen, N.; Edge, M.; Roberts, I., Photochemistry and photoinduced chemical crosslinking activity of acrylated prepolymers by several commercial type I far UV photoinitiators. *Polymer Degradation and Stability* **1999**, *65* (1), 153-160.
47. Tse, J. R.; Engler, A. J., Preparation of hydrogel substrates with tunable mechanical properties. *Current Protocols in Cell Biology* **2010**, *47* (1), 10.16. 1-10.16. 16.
48. Bryant, S. J.; Nuttelman, C. R.; Anseth, K. S., Cytocompatibility of UV and visible light photoinitiating systems on cultured NIH/3T3 fibroblasts in vitro. *Journal of Biomaterials Science, Polymer Edition* **2000**, *11* (5), 439-457.
49. Wang, Z.; Jin, X.; Dai, R.; Holzman, J. F.; Kim, K., An ultrafast hydrogel photocrosslinking method for direct laser bioprinting. *RSC Advances* **2016**, *6* (25), 21099-21104.
50. Xia, H.; Attygalle, A. B., Untrapping Kinetically Trapped Ions: The Role of Water Vapor and Ion-Source Activation Conditions on the Gas-Phase Protomer Ratio of Benzocaine Revealed by Ion-Mobility Mass Spectrometry. *Journal of The American Society for Mass Spectrometry* **2017**, *28* (12), 2580-2587.
51. Klyne, J.; Dopfer, O., Protonation and Sequential Microsolvation of 5-Hydroxyindole: Infrared Photodissociation Spectra of $5\text{HIH}^+-\text{L}_n$ with $\text{L} = \text{Ar}$ and N_2 ($n \leq 3$). *The Journal of Physical Chemistry B* **2018**, *122* (47), 10700-10713.
52. Campbell, J. L.; Yang, A. M.-C.; Melo, L. R.; Hopkins, W. S., Studying gas-phase interconversion of tautomers using differential mobility spectrometry. *Journal of The American Society for Mass Spectrometry* **2016**, *27* (7), 1277-1284.
53. Attygalle, A. B.; Xia, H.; Pavlov, J., Influence of Ionization Source Conditions on the Gas-Phase Protomer Distribution of Anilinium and Related Cations. *Journal of The American Society for Mass Spectrometry* **2017**, *28* (8), 1575-1586.
54. Patrick, A. L.; Cismesia, A. P.; Tesler, L. F.; Polfer, N. C., Effects of ESI conditions on kinetic trapping of the solution-phase protonation isomer of p-aminobenzoic acid in the gas phase. *International Journal of Mass Spectrometry* **2017**, *418*, 148-155.
55. Kulesza, A. J.; Titov, E.; Daly, S.; Włodarczyk, R.; Megow, J.; Saalfrank, P.; Choi, C. M.; MacAleese, L.; Antoine, R.; Dugourd, P., Excited States of Xanthene Analogues: Photofragmentation and Calculations by CC2 and Time-Dependent Density Functional Theory. *ChemPhysChem* **2016**, *17* (19), 3129-3138.
56. Avila Ferrer, F. J.; Cerezo, J.; Stendardo, E.; Improta, R.; Santoro, F., Insights for an accurate comparison of computational data to experimental absorption and emission spectra: beyond the vertical transition approximation. *Journal of Chemical Theory and Computation* **2013**, *9* (4), 2072-2082.
57. Laurent, A. D.; Jacquemin, D., TD-DFT benchmarks: A review. *International Journal of Quantum Chemistry* **2013**, *113* (17), 2019-2039.

58. Marsh, B. M.; Zhou, J.; Garand, E., Charge transfer in MOH (H₂O)⁺(M= Mn, Fe, Co, Ni, Cu, Zn) complexes revealed by vibrational spectroscopy of mass-selected ions. *Physical Chemistry Chemical Physics* **2015**, *17* (39), 25786-25792.
59. Ding, L.; Shen, L.; Chen, X.-B.; Fang, W.-H., Solvent effects on photoreactivity of valerophenone: a combined QM and MM study. *The Journal of organic chemistry* **2009**, *74* (23), 8956-8962.
60. Brückner, C.; Engels, B., Benchmarking singlet and triplet excitation energies of molecular semiconductors for singlet fission: Tuning the amount of HF exchange and adjusting local correlation to obtain accurate functionals for singlet–triplet gaps. *Chemical Physics* **2017**, *482*, 319-338.

Chapter 3

Supporting Information

3.SI.0 Experimental

3.SI.0.0 Materials:

Irgacure 2959 (Sigma Aldrich 98%) was dissolved in HPLC grade methanol to a concentration of $\sim 1 \mu\text{M}$. Either Lithium hydroxide, formic acid, potassium chloride, magnesium perchlorate, zinc acetate dihydrate and calcium carbonate were dissolved in HPLC methanol and Milli-Q water and added to separate Irgacure 2959 solutions with a final concentration of $\sim 100 \mu\text{M}$.

3.SI.0.1 Photodissociation Action Spectroscopy:

The methods used for photodissociation action spectroscopy are described in detail elsewhere.¹ Following Julian and co-workers,³ a commercial, linear quadrupole ion trap mass spectrometer (Thermo Fisher Scientific LTQ VELOS) has been coupled with a tunable Nd:YAG optical parametric oscillator laser (EKSPLA). Following electrospray ionisation (ESI), populations of either one Irg molecule bound to a single metal mono-cation (Irg- $\text{M}^{\text{Q}+}$) or two Irg molecules bound to a single metal di-cation (Irg- $\text{M}^{\text{Q}+}$ -Irg) were isolated and stored in the ion trap and then irradiated by a single laser pulse, which is directed through the long axis of the ion trap *via* a quartz window mounted at the rear of the mass spectrometer chamber.¹ This experimental arrangement results in good spatial overlap between the trapped ions and the laser pulse.⁴ Approximately 50 ms after the laser pulse, ions are scanned out of the ion trap to record a mass spectrum. These product mass spectra are recorded for a wavelength range spanning between 450 - 250 nm at a step size of either 2 nm for Li^+ , K^+ , Zn^{2+} , Ca^{2+} and Mg^{2+} , or a step size of 1 nm for H^+ and Na^+ . At each laser wavelength, *ca.* 150 mass spectra are recorded and averaged, each mass spectrum corresponding to photodissociation of Irg- M^+ or Irg- M^{2+} -Irg ions by a single laser pulse. The photoproduct yield is then normalized to total ion count as well as laser power as measured with a power meter (STANDA 10MVAA) placed in the beam path following each scan. Mass spectra were recorded with a low m/z threshold of between 60 m/z and 75 m/z depending on the precursor ion (see Table 3.4, Supporting

Information). Photodissociation action spectra are plotted as the sum of all photoproduct ion signal, normalized to total ion count and laser power.

The yield of α -cleavage photoproducts relative to depletion of the total photoproduct signal was calculated by dividing the ion count of the α -cleavage product signal by the total ion count of all photodissociation products. The yield of α -cleavage relative to depletion of the precursor ion was calculated by dividing the ion count of the α -cleavage product ions by the difference in “laser-on” and “laser-off” precursor ion intensity (300 mass spectra laser-on and 300 mass spectra laser-off).

3.SI.0.2 Computational Details:

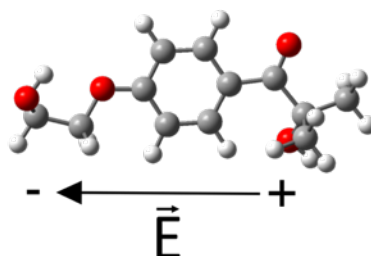
All calculations are relevant to gas phase systems. All density functional theory (DFT) and time dependent-density functional theory (TD-DFT) calculations were performed with the Gaussian16 program package,⁵ employing the M06-2X method.⁶ For DFT optimizations, the def2-TZVP basis set was used for Irg-M⁺ complexes and the def2-SVP basis set was utilized for the larger Irg-M²⁺-Irg complexes.^{7, 8} At least seven isomers of each Irg-M^{Q+} ion were optimized using M06-2X. For the lowest-energy gas-phase structures, TD-DFT excitation energies were calculated in Gaussian16. All TD-DFT vertical excitation energy calculations for both Irg-M⁺ and Irg-M²⁺-Irg complexes employed the def2-TZVP basis set.

Using the most stable structures—as calculated using M06-2X—the distance between the M^{Q+} cation and the center of mass (COM) of the (taken as the center of mass of the seven aromatic carbons, the ether oxygen and the ketone oxygen) was determined. These structures were also used to calculate TD-DFT vertical excitation energies with the M^{Q+} atom replaced with a point charge P^{Q+}.^{9, 10} The M06-2X geometry of neutral Irg was used to calculate TD-DFT vertical transition energies in the presence of a static electric field oriented along the long axis of the Irg molecule (see Supporting Information, Figure 3.9).

The lowest energy structure for each of the complexes were re-optimized using SCS-CC2^{11, 12} with the resolution of the identity approximation¹³ and using these geometries, SCS-CC2 excitation energies were computed using the TURBOMOLE (V7.2) program package.¹⁴ Irg-M^{Q+} calculations with SCS-CC2 made use of the def2-TZVP basis set while the def2-SVP basis set was used for calculations of Irg-M^{Q+}-Irg ions.

3.SI.1 Low m/z Threshold for Mass Spectra.**Table 3.4:** Low m/z cut-off values for PD mass spectra of Irg- M^+ and Irg- M^{2+} -Irg ions.

Ion	Low m/z Threshold
Irg- H^+	60
Irg- Li^+	60
Irg- Na^+	65
Irg- K^+	70
Irg- Mg^{2+} -Irg	75
Irg- Zn^{2+} -Irg	75
Irg- Ca^{2+} -Irg	75

3.SI.2 Orientation of Static Electric Field**Figure 3.9:** Alignment of the static electric field electric field applied to neutral Irg. The static electric field is applied exclusively along the x axis of neutral irgacure (XYZ coordinates in Section 3.SI.9).

3.SI.3 Additional Structure Energies and Assignments

The relative energies of Irg-M⁺ structures (within 1.0 eV of the lowest energy structure) are shown in Figure 3.10. For all Irg-M⁺ complexes, Structure **A** was found to have the lowest energy. TD-DFT vertical excitation energies (E_{vert}) of all structures within 0.5 eV of Structure **A** are shown in Table 3.5 and compared to experimental E_{exp} from PD action spectra. The E_{vert} values of Structure **A** for each ion agree well with the E_{exp} values with a systematic overestimation of ~ 0.5 eV which is typical of TD-DFT.^{2, 15, 16}

Although Structure **G** has a low relative energy (< 0.15 eV), all E_{vert} values for Structure **G** are significantly well above the experimental E_{exp} values and have low oscillator strengths ($f < 0.1$). E_{vert} values for Structure **D** also above 5.0 eV. Therefore, contribution of these structures to the PD action spectra can be essentially ruled out. The H⁺ cation binds similarly for Structure **A** and Structure **B** of Irg-H⁺ and therefore E field effects will not differ significantly for these two structures if a minor population of Structure **B** is formed, however the high energy of Structure **B** of Irg-H⁺ means it is not likely to be significantly present. While Irg-K⁺ Structure **B** and Structure **E** have E_{vert} values are plausibly close to the E_{exp} values, these have a low barrier of isomerisation to form Structure **A** and are therefore not likely to be kinetically trapped in this shallow well (see Figures 3.11 and 3.12). Therefore, of structures which are plausible to form based on their ground state energies (Structure **A** and Structure **G**), only Structure **A** can be expected to significantly appear within the 3.0 – 5.0 eV spectral range analysed here. Of structures with plausible TD-DFT energies (Structure **A**, Structure **B**, and Structure **E**), only Structure **A** can be expected based on ground state energies and low barriers of isomerisation.

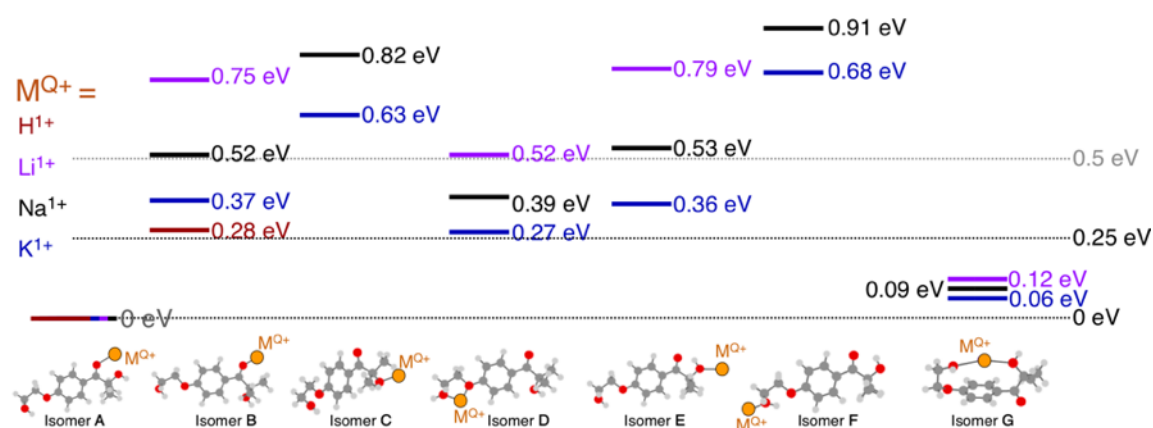


Figure 3.10: Relative energies of Irg-M^{Q+} Structures calculated using M06-2X within 1 eV of the lowest ground state energy structure for each respective Irg-M^{Q+} ion. Structures with greater than 1 eV were not included.

Table 3.5: TD-DFT vertical excitation energies (E_{vert}) for the first state calculated to have oscillator strength ($f > 0.01$) of Irg- M^+ structures within 0.4 eV of the minimum energy structure **A** compared to experimental results (E_{exp}). Calculations employed the M06-2X/def2-TZVP level of theory. Energies of Structure **A** are shown in bold.

Structure	TD-DFT E_{vert} of First State with $f > 0.01$	E_{exp}
H Structure B	4.04	3.42
H Structure A	4.11	3.42
Li Structure G	5.28	3.97
Li Structure A	4.29	3.97
Na Structure G	5.18	3.96
Na Structure D	5.5	3.96
Na Structure A	4.4	3.96
K Structure G	5.09	4.08
K Structure E	4.68	4.08
K Structure D	5.47	4.08
K Structure B	4.43	4.08
K Structure A	4.47	4.08

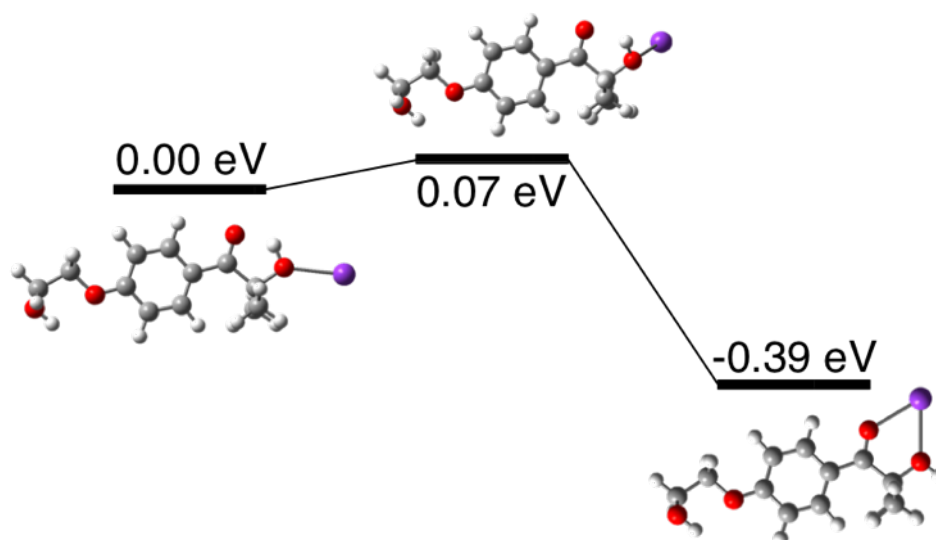


Figure 3.11: Structure **E** barrier to form Structure **A** as calculated using M06-2X/def2-SVP.

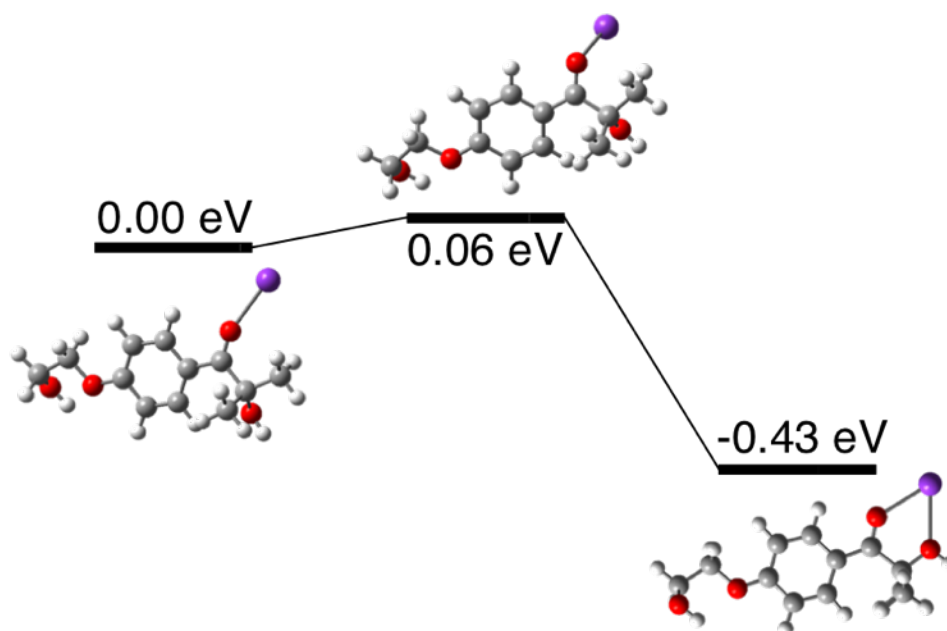


Figure 3.12: Structure **B** barrier to form Structure **A** as calculated using M06-2X/def2-SVP.

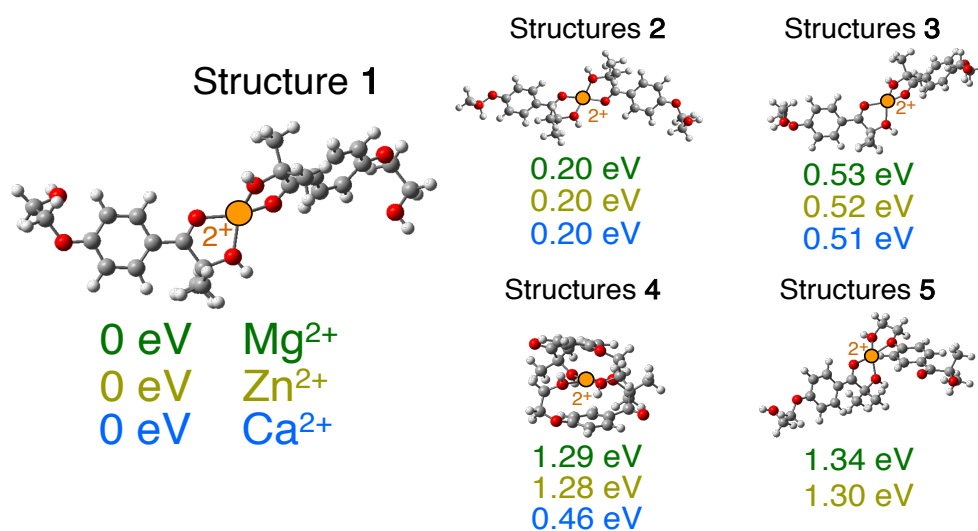


Figure 3.13: Relative energies of Irg- M^{2+} -Irg structures calculated using M06-2X/def2-SVP. Irg- Ca^{+} -Irg Structure **5** did not converge.

3.SI.4 Single Wavelength PD Mass Spectra

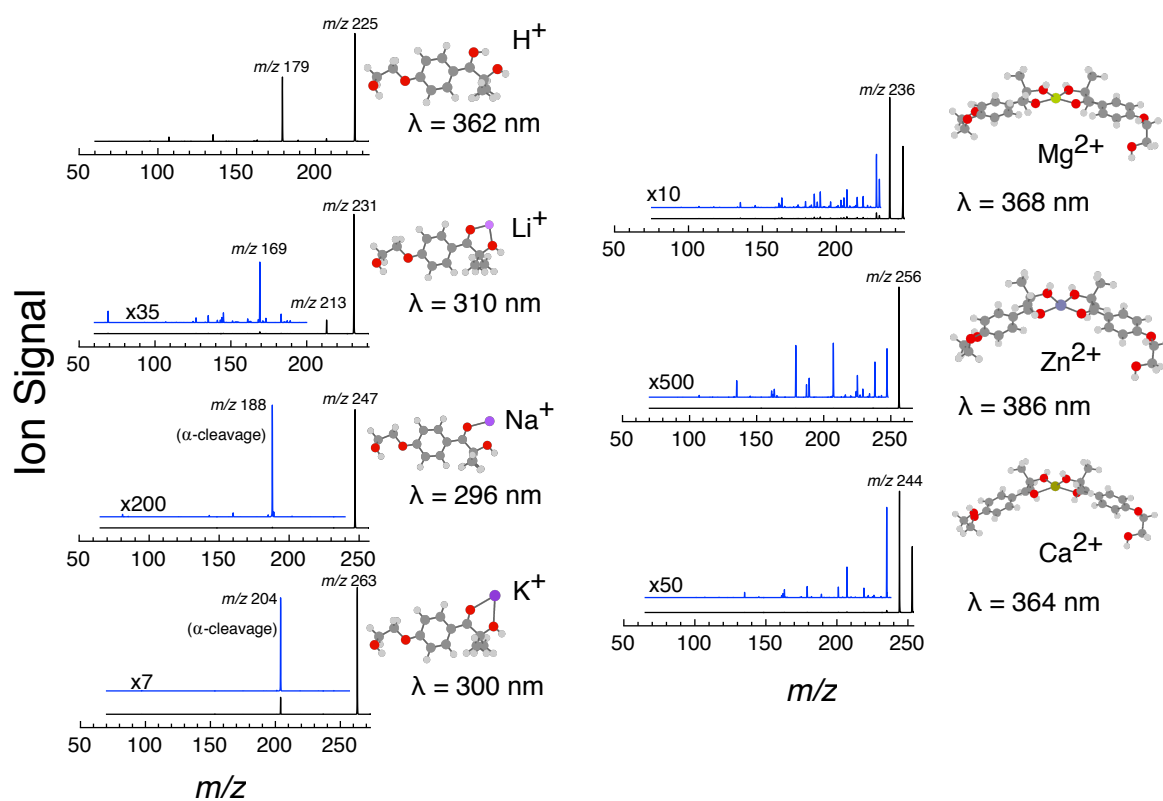


Figure 3.14: PD mass spectra for Irg-M⁺ and Irg-M²⁺-Irg ions taken at photon energies $\lambda = E_{\text{exp}}$ where E_{exp} is the energy at the centre of a Gaussian function fitted to the action spectrum (see main text).

3.SI.5 Additional Gaussian Fits to PD Action Spectra

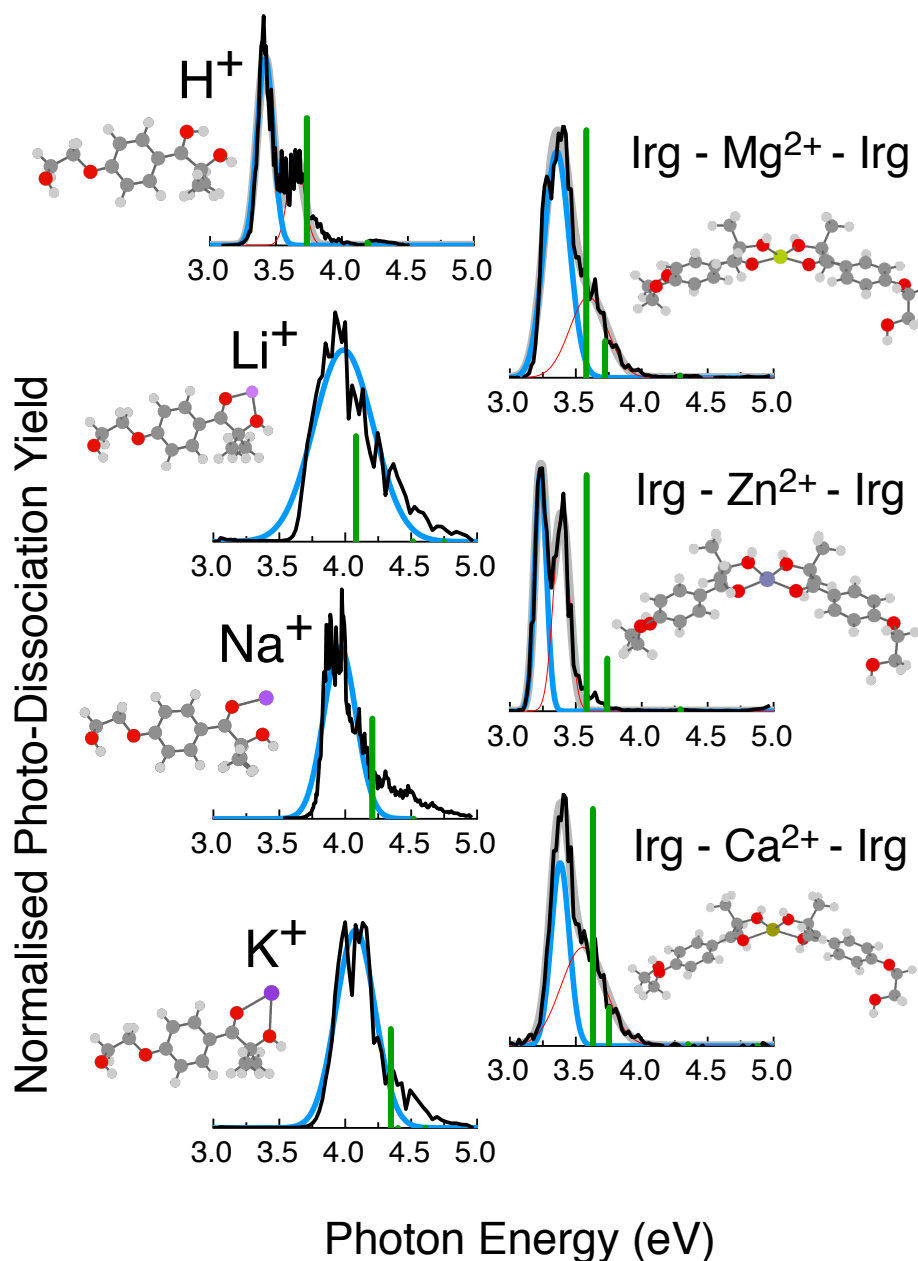


Figure 3.15: Photodissociation action spectra of Irgacure 2959 M^{Q+} complexes ($M^{Q+} = H^+, Li^+, Na^+, K^+, Mg^{2+}, Zn^{2+}, Ca^{2+}$). Single Gaussian functions (blue) are fit to the lowest energy transition. Additional Gaussian functions for higher energy transitions are shown (red line) along with the sum of Gaussians (grey line). Green sticks are the calculated transition energies (E_{vert}) for each lowest energy structure using SCS-CC2/def2-TZVP.

3.SI.6 Coulomb's Law

Equation 3.S1: Coulomb's law, where Q_M is the charge of the charged atom M^{Q+} , r is the distance between the charged atom M^{Q+} and the centre of mass of the chromophore (as calculated using M06-2X), and ϵ_0 is the permittivity of vacuum.¹⁷

$$E = \frac{1}{4\pi\epsilon_0} \frac{Q_M}{r^2} \quad (\text{Eq 3.S1})$$

3.SI.7 Centre of Mass to Cation Distances

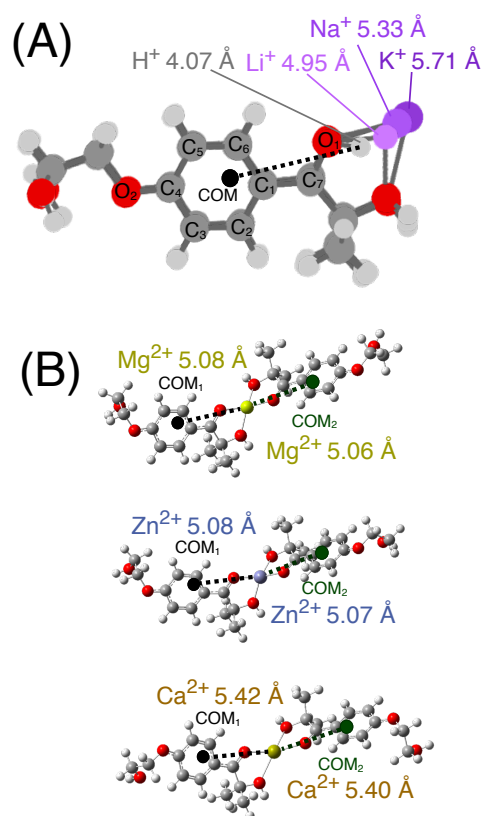


Figure 3.16: Distance between M^{Q+} cation and the centre of mass of the chromophore (taken as the centre of mass of the labelled atoms which are the benzene carbons, C_7 , O_1 and O_2) as calculated using M06-2X for (A) Irg- M^+ and (B) Irg- M^{2+} -Irg.

3.SI.8 Orbitals relating to Figure 6

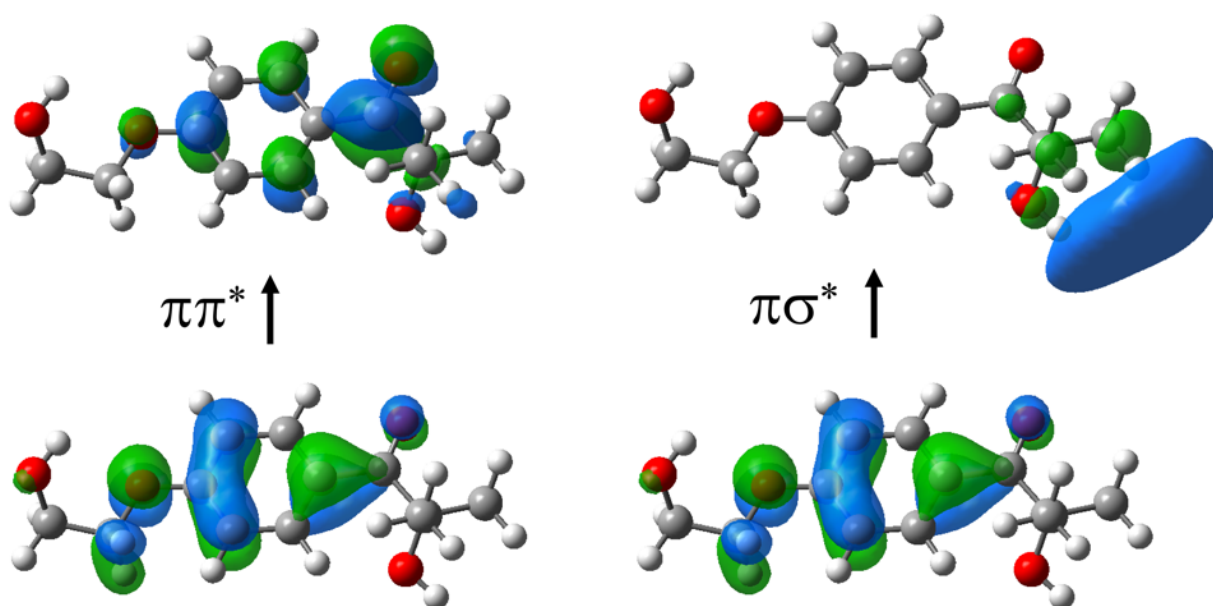


Figure 3.17: The orbitals contributing to the $\pi\pi^*$ and $\pi\sigma^*$ transitions which undergo an avoided crossing in Figure 3.17 and Figure 6B of the main text.

3.SI.9 XYZ Coordinates

M06-2X/ def2-TZVP

Irg (neutral)

-767.7753625

C	-1.145640	1.568588	-0.190220
C	0.225442	1.653668	-0.133726
C	1.022021	0.502473	-0.087155
C	0.392295	-0.737935	-0.097786
C	-0.992164	-0.838969	-0.147157
H	-1.766294	2.453643	-0.231752
H	0.715880	2.617770	-0.122430
H	0.978806	-1.643514	-0.084915
H	-1.450652	-1.816631	-0.154740
C	2.498499	0.709701	0.005878
O	2.949668	1.826374	0.110070
C	-1.764600	0.316277	-0.194513
O	-3.116778	0.322189	-0.251411
O	3.036727	-1.441067	-0.905140
C	4.876973	-0.009611	-0.290367
H	4.895678	0.416909	-1.292433
H	5.217585	0.747697	0.411652
H	5.562849	-0.859816	-0.249490
C	3.473682	-0.482317	0.054285
C	3.435022	-1.073457	1.465701
H	4.134042	-1.910525	1.526357
H	3.730944	-0.323807	2.200420

Chapter 3: Irgacure 2959 Clusters Supporting Information

H	2.437735	-1.433198	1.715199
C	-3.806649	-0.917327	-0.238907
H	-3.553529	-1.473370	0.668947
H	-3.535789	-1.510984	-1.117983
C	-5.279277	-0.581709	-0.248882
H	-5.515389	-0.022602	-1.161099
H	-5.860058	-1.504255	-0.251983
O	-5.652547	0.138079	0.901973
H	-5.090080	0.918442	0.950574
H	3.748090	-2.076655	-1.033174

Irg-H⁺

-768.1358753

C	1.274128	1.239573	0.059228
C	-0.078232	1.428896	-0.028409
C	-0.983627	0.341425	0.019728
C	-0.452207	-0.965809	0.162491
C	0.893023	-1.165360	0.248172
H	1.939391	2.088619	0.023852
H	-0.466378	2.432530	-0.134108
H	-1.099345	-1.827750	0.201684
H	1.312271	-2.155846	0.355628
C	-2.364254	0.614903	-0.082938
O	-2.726370	1.838176	-0.241865
C	1.779298	-0.067838	0.197067
O	3.057854	-0.357699	0.287234
O	-4.676190	0.437607	-0.104564
C	-3.476497	-1.331800	-1.226890
H	-3.493419	-0.764811	-2.158349
H	-2.596120	-1.967987	-1.227371
H	-4.354882	-1.978948	-1.188006
C	-3.518422	-0.390076	-0.024087
C	-3.552190	-1.111685	1.323514
H	-4.452516	-1.725123	1.352315
H	-2.690501	-1.753684	1.482463
H	-3.606157	-0.386032	2.134361
C	4.048534	0.684925	0.225232
H	3.917949	1.353565	1.079611
H	3.926035	1.232529	-0.711365
C	5.398619	0.008071	0.254155
H	6.166360	0.782092	0.277093
H	5.492577	-0.588650	1.166446
O	5.613397	-0.758143	-0.902285
H	5.138152	-1.590337	-0.827264
H	-5.378476	0.007081	-0.603337
H	-3.713487	1.851872	-0.295388

Irg-K⁺

-1367.5742213

C	1.794766	-1.115360	-0.171167
C	0.416678	-1.102049	-0.117790
C	-0.313312	0.091261	-0.092428
C	0.406060	1.297394	-0.128055
C	1.778830	1.302073	-0.181342
H	2.319926	-2.058344	-0.189874
H	-0.123526	-2.038040	-0.093453
H	-0.092617	2.253528	-0.114782
H	2.335004	2.228847	-0.209663
C	-1.779956	-0.033819	-0.028145
O	-2.301033	-1.139437	-0.008225

Chapter 3: Irgacure 2959 Clusters Supporting Information

C	2.490525	0.096618	-0.200157
O	3.820746	0.198950	-0.248573
O	-4.040861	0.662142	0.088342
C	-2.471580	2.015978	1.286792
H	-2.603597	1.386696	2.167065
H	-1.481487	2.459003	1.329827
H	-3.202556	2.826449	1.326811
C	-2.704546	1.195795	0.019195
C	-2.601730	2.013597	-1.267025
H	-3.327168	2.829257	-1.230837
H	-1.618537	2.449457	-1.415076
H	-2.830223	1.384093	-2.127150
C	4.616243	-0.987580	-0.245410
H	4.406473	-1.574957	-1.144041
H	4.387087	-1.575566	0.647081
C	6.058590	-0.540435	-0.211503
H	6.700040	-1.420698	-0.254376
H	6.269226	0.078738	-1.089700
O	6.363037	0.132609	0.984023
H	5.871050	0.959155	1.003868
H	-4.637695	1.418913	0.112175
K	-4.697365	-1.886394	0.146306

Irg-Li⁺
-775.1708162

C	1.342155	1.217425	0.066773
C	-0.021653	1.386329	-0.011650
C	-0.905934	0.298168	0.034660
C	-0.357528	-0.991513	0.168279
C	0.998629	-1.175349	0.247601
H	1.991074	2.079133	0.028540
H	-0.429902	2.382265	-0.112472
H	-0.982910	-1.869308	0.212043
H	1.426461	-2.162767	0.351265
C	-2.326458	0.600756	-0.060850
O	-2.709103	1.769088	-0.172523
C	1.867114	-0.074412	0.195652
O	3.164712	-0.349449	0.278088
O	-4.657866	0.255304	-0.157542
C	-3.318031	-1.418081	-1.234354
H	-3.337673	-0.842991	-2.160084
H	-2.412346	-2.016689	-1.222811
H	-4.169982	-2.101027	-1.228470
C	-3.415053	-0.486541	-0.030555
C	-3.453391	-1.209173	1.312186
H	-4.305396	-1.891864	1.327516
H	-2.556261	-1.793081	1.493942
H	-3.566337	-0.491313	2.124622
C	4.120451	0.714709	0.213141
H	3.977714	1.386792	1.063887
H	3.987896	1.260771	-0.724032
C	5.487132	0.072474	0.247042
H	6.241328	0.859516	0.251779
H	5.595425	-0.508502	1.168639
O	5.717543	-0.712533	-0.894999
H	5.151589	-1.489336	-0.856696
H	-5.391180	-0.369756	-0.148683
Li	-4.482131	2.086707	-0.293575

Chapter 3: Irgacure 2959 Clusters Supporting Information

Irg-Na⁺
-929.9107329

C	-1.566339	1.159384	-0.126269
C	-0.192016	1.240947	-0.063401
C	0.619631	0.099445	-0.067851
C	-0.013689	-1.153654	-0.142494
C	-1.381342	-1.251948	-0.205593
H	-2.156427	2.063260	-0.121148
H	0.280914	2.211426	-0.008237
H	0.550416	-2.072781	-0.152537
H	-1.872056	-2.213587	-0.264002
C	2.067842	0.321008	0.007798
O	2.512910	1.462456	0.066401
C	-2.175669	-0.097691	-0.195721
O	-3.492725	-0.291048	-0.258069
O	4.376233	-0.214223	0.106428
C	2.908518	-1.712481	1.261985
H	2.995048	-1.102195	2.161080
H	1.952682	-2.226225	1.289652
H	3.695635	-2.469323	1.277866
C	3.077039	-0.841843	0.019048
C	3.037429	-1.624149	-1.291646
H	3.823722	-2.381913	-1.279851
H	2.090398	-2.130100	-1.451437
H	3.213514	-0.953677	-2.132944
C	-4.372491	0.835821	-0.232528
H	-4.194656	1.461157	-1.112083
H	-4.195565	1.412322	0.678978
C	-5.779229	0.285804	-0.229808
H	-6.480899	1.119453	-0.259424
H	-5.934772	-0.323048	-1.126426
O	-6.048892	-0.437892	0.944068
H	-5.511511	-1.235825	0.943729
H	5.031932	-0.920612	0.116284
H	4.595755	2.003952	0.197160
Na	4.595755	2.003952	0.197160

M06-2X/def2-SVP

Irg-Ca²⁺-Irg
-2211.0082943

C	-5.850140	-1.004236	-0.717433
C	-4.609021	-0.447578	-0.504715
C	-4.357558	0.463770	0.553296
C	-5.441245	0.782866	1.416303
C	-6.685538	0.239489	1.214961
H	-5.992729	-1.747971	-1.497474
H	-3.783390	-0.721256	-1.160972
H	-5.323133	1.467022	2.253772
H	-7.526318	0.483621	1.863645
C	-3.021660	0.984341	0.668320
O	-2.126307	0.647104	-0.139918
C	-6.919042	-0.652485	0.138856
O	-8.160035	-1.073291	0.019668
O	-1.186274	2.246863	1.515210
C	-2.691238	1.350983	3.160604

Chapter 3: Irgacure 2959 Clusters Supporting Information

H	-2.112567	0.417897	3.200988
H	-2.288546	2.051547	3.907977
H	-3.723550	1.122724	3.444448
C	-2.602218	1.978839	1.770883
C	-3.335667	3.312460	1.641670
C	-8.617385	-1.860278	-1.081629
H	-8.075994	-1.580519	-1.997576
H	-9.673687	-1.592438	-1.203146
C	-8.488320	-3.337270	-0.796960
H	-9.009202	-3.559575	0.150354
H	-9.006561	-3.880860	-1.606856
O	-7.121802	-3.653805	-0.731628
C	5.674084	-1.263714	0.785216
C	4.479948	-0.661268	0.458849
C	4.283590	0.016244	-0.772227
C	5.380177	0.067548	-1.675449
C	6.575474	-0.532628	-1.366895
H	5.810713	-1.718608	1.763103
H	3.655975	-0.692196	1.171130
H	5.307091	0.573913	-2.635482
H	7.420116	-0.508558	-2.054863
C	2.989509	0.600939	-1.001163
O	2.078334	0.504966	-0.147288
C	6.743563	-1.219366	-0.138776
O	7.917339	-1.790420	0.027144
O	1.244029	1.788616	-2.106865
C	3.464230	2.648015	-2.431834
H	4.526855	2.435143	-2.586054
H	3.369138	3.273065	-1.533313
H	3.110249	3.221560	-3.301841
C	2.635434	1.372913	-2.289275
C	2.669748	0.466678	-3.518520
H	2.313246	1.024822	-4.397634
H	3.680830	0.111109	-3.741075
H	2.025079	-0.410549	-3.370059
C	8.226791	-2.635993	1.136270
H	7.332332	-3.196103	1.446816
H	8.969752	-3.346115	0.754203
C	8.808026	-1.847845	2.285271
H	9.171518	-2.570506	3.037358
H	9.675930	-1.275087	1.915409
O	7.803463	-1.008577	2.793772
H	-3.204184	3.729695	0.633843
H	-2.932705	4.026196	2.376076
H	-4.409333	3.214259	1.830694
H	-7.019240	-4.576253	-0.473009
H	8.176992	-0.441101	3.476957
H	0.983019	2.257874	-2.913168
H	-0.884147	2.849120	2.211202
Ca	-0.001139	1.266597	-0.220997

Irg-Mg²⁺-Irg
-1733.4747146

C	5.803733	-0.913058	-0.464025
C	4.496003	-0.611697	-0.165179
C	4.089734	0.690847	0.235115
C	5.091345	1.700855	0.306408
C	6.399968	1.413861	0.017082
H	6.070355	-1.901275	-0.830435

Chapter 3: Irgacure 2959 Clusters Supporting Information

H	3.737159	-1.389168	-0.249248
H	4.853337	2.721833	0.597130
H	7.178435	2.173895	0.077439
C	2.704485	0.885570	0.527360
O	1.888668	-0.073190	0.450237
C	6.786439	0.101210	-0.360198
O	8.071877	-0.062848	-0.567238
O	0.685718	1.977288	1.138475
C	2.225242	3.288087	-0.159346
H	1.780452	2.910249	-1.090243
H	1.698058	4.206109	0.141439
H	3.266582	3.557006	-0.363818
C	2.114293	2.248020	0.952425
C	2.655149	2.709645	2.303167
C	8.670270	-1.333964	-0.836930
H	8.134175	-2.125866	-0.293572
H	9.687836	-1.258823	-0.436045
C	8.713550	-1.614927	-2.319609
H	9.229709	-0.778882	-2.822249
H	9.316566	-2.527974	-2.469544
O	7.393034	-1.765479	-2.772044
Mg	0.001160	0.133929	0.816110
C	-5.665673	0.329895	-1.250517
C	-4.395439	0.246700	-0.730949
C	-4.033808	-0.730951	0.236088
C	-5.046492	-1.632255	0.672576
C	-6.316238	-1.563481	0.161101
H	-5.925548	1.127373	-1.942085
H	-3.637041	0.956360	-1.060431
H	-4.845193	-2.401216	1.415326
H	-7.098358	-2.252316	0.479041
C	-2.680789	-0.731265	0.696148
O	-1.851043	0.112155	0.259141
C	-6.649380	-0.593071	-0.819627
O	-7.880544	-0.655702	-1.269621
O	-0.731451	-1.375403	1.889873
C	-2.798175	-1.556242	3.101814
H	-3.860375	-1.820641	3.085510
H	-2.709967	-0.513741	3.437100
H	-2.302941	-2.208705	3.836233
C	-2.142865	-1.739287	1.735419
C	-2.173165	-3.171922	1.209043
H	-1.681273	-3.839860	1.932282
H	-3.196620	-3.534056	1.068497
H	-1.649956	-3.242844	0.245494
C	-8.367987	0.152523	-2.344594
H	-7.564292	0.336535	-3.072531
H	-9.145480	-0.453186	-2.824639
C	-8.956422	1.445443	-1.833654
H	-9.445602	1.949955	-2.685652
H	-9.732864	1.208523	-1.085969
O	-7.914939	2.210816	-1.284907
H	2.512299	1.930461	3.064410
H	2.121860	3.618126	2.620381
H	3.722150	2.949973	2.257233
H	7.392173	-1.873776	-3.729560
H	-8.279826	3.008838	-0.886749
H	-0.296548	-2.006858	2.480930
H	0.223592	2.802503	1.344959

Chapter 3: Irgacure 2959 Clusters Supporting Information

Irg-Zn ²⁺ -Irg			
-3312.5273206			
C	-5.513417	-1.080433	-0.812777
C	-4.276770	-0.524027	-0.585429
C	-4.027521	0.352051	0.506657
C	-5.111329	0.630575	1.387575
C	-6.350318	0.085487	1.171546
H	-5.654026	-1.795637	-1.619344
H	-3.452066	-0.767639	-1.254517
H	-4.993930	1.282053	2.250810
H	-7.190194	0.297006	1.832751
C	-2.703207	0.875827	0.638453
O	-1.813266	0.555251	-0.196253
C	-6.582190	-0.767863	0.061475
O	-7.818228	-1.189542	-0.068464
O	-0.879748	2.133004	1.513813
C	-2.351416	1.152133	3.136449
H	-1.743401	0.237096	3.132965
H	-1.966605	1.833966	3.909819
H	-3.375213	0.880337	3.412608
C	-2.288112	1.837394	1.773567
C	-3.033864	3.166961	1.692220
C	-8.275648	-1.954143	-1.187699
H	-7.740872	-1.646545	-2.098301
H	-9.334596	-1.691938	-1.295931
C	-8.129106	-3.435479	-0.936258
H	-8.651063	-3.687282	0.003020
H	-8.636224	-3.966326	-1.761363
O	-6.758416	-3.732450	-0.871697
C	5.337598	-1.506647	0.532927
C	4.148248	-0.837015	0.366677
C	3.948373	0.107592	-0.677340
C	5.039220	0.355015	-1.558845
C	6.228565	-0.309693	-1.408900
H	5.478574	-2.173753	1.379654
H	3.330327	-1.023540	1.061919
H	4.962496	1.066326	-2.378299
H	7.067433	-0.137774	-2.082733
C	2.665792	0.735247	-0.757984
O	1.762596	0.430891	0.068593
C	6.399648	-1.261990	-0.370679
O	7.564376	-1.866760	-0.355930
O	0.931117	2.170430	-1.534104
C	3.153644	3.053984	-1.681632
H	4.214133	2.870763	-1.880643
H	3.060501	3.457252	-0.664242
H	2.804103	3.812524	-2.397682
C	2.311503	1.789386	-1.829773
C	2.311302	1.182892	-3.231012
H	1.970432	1.935653	-3.957835
H	3.309420	0.853860	-3.537157
H	1.637508	0.316102	-3.272562
C	7.882790	-2.940394	0.534072
H	6.987175	-3.549155	0.726429
H	8.613577	-3.551247	-0.008720
C	8.485842	-2.425579	1.818709
H	8.845866	-3.297891	2.392468
H	9.358131	-1.796191	1.571648
O	7.495822	-1.705003	2.505756
H	-2.897363	3.620841	0.701367

Chapter 3: Irgacure 2959 Clusters Supporting Information

H	-2.639848	3.854755	2.455119
H	-4.107554	3.051502	1.869984
H	-6.641773	-4.660551	-0.640296
H	7.879474	-1.305554	3.294284
H	0.605540	2.781566	-2.210416
H	-0.520995	2.681838	2.225800
Zn	-0.002358	1.205444	-0.038210

SCS-CC2/def2-TZVP

Irg-H⁺

-766.9682243176

C	1.2791163	1.2379393	0.0623355
C	-0.0809288	1.4290299	-0.0192574
C	-0.9883206	0.3360490	0.0304817
C	-0.4557042	-0.9754777	0.1706814
C	0.8990207	-1.1732665	0.2523315
H	1.9405806	2.0922431	0.0242393
H	-0.4686506	2.4353736	-0.1222870
H	-1.1017809	-1.8398482	0.2157186
H	1.3165543	-2.1673229	0.3594541
C	-2.3702673	0.6059553	-0.0658534
O	-2.7456155	1.8435380	-0.2056991
C	1.7880675	-0.0738892	0.1979302
O	3.0743538	-0.3757031	0.2844836
O	-4.7058964	0.4331413	-0.0955332
C	-3.4925362	-1.3474539	-1.2122910
H	-3.4812115	-0.7868279	-2.1509165
H	-2.6201835	-1.9978039	-1.1959601
H	-4.3827790	-1.9817404	-1.1839725
C	-3.5292273	-0.3987170	-0.0166551
C	-3.5824153	-1.1066090	1.3364086
H	-4.4733477	-1.7366266	1.3586245
H	-2.7072219	-1.7285632	1.5170592
H	-3.6618763	-0.3708922	2.1391058
C	4.0654636	0.6923725	0.2229207
H	3.9301305	1.3470304	1.0886973
H	3.9269567	1.2431028	-0.7098072
C	5.4186331	0.0186952	0.2384881
H	6.1835305	0.7979064	0.2610874
H	5.5222197	-0.5887079	1.1438089
O	5.6350797	-0.7383783	-0.9372050
H	5.1759459	-1.5833251	-0.8409275
H	-5.2838323	0.1137666	-0.8048215
H	-3.7455396	1.7992957	-0.2486220

Irg-K⁺

-1365.8202382511

C	1.8009837	-1.1156382	-0.1638548
C	0.4159968	-1.1051037	-0.1081131
C	-0.3207053	0.0924842	-0.0805238
C	0.4009183	1.3049816	-0.1147934
C	1.7811093	1.3093942	-0.1701757
H	2.3237518	-2.0620933	-0.1847222
H	-0.1213106	-2.0452583	-0.0842155
H	-0.0969385	2.2630406	-0.0984143
H	2.3342772	2.2410811	-0.1968451
C	-1.7856867	-0.0356784	-0.0171595

Chapter 3: Irgacure 2959 Clusters Supporting Information

O	-2.3116575	-1.1578925	0.0109541
C	2.4985079	0.1018658	-0.1933813
O	3.8370305	0.2178212	-0.2465997
O	-4.0586349	0.6596239	0.0770512
C	-2.4900832	2.0212872	1.2853706
H	-2.6280536	1.3928526	2.1680024
H	-1.4983684	2.4656082	1.3344220
H	-3.2228123	2.8333808	1.3196361
C	-2.7083011	1.1965442	0.0172703
C	-2.5994504	2.0106494	-1.2717154
H	-3.3318905	2.8234486	-1.2496054
H	-1.6153011	2.4531618	-1.4094377
H	-2.8133179	1.3751057	-2.1338720
C	4.6289055	-0.9899297	-0.2522344
H	4.4095595	-1.5660540	-1.1574729
H	4.3960531	-1.5786042	0.6393582
C	6.0739718	-0.5471873	-0.2237299
H	6.7121407	-1.4312018	-0.2773893
H	6.2826051	0.0828505	-1.0959618
O	6.3976834	0.1133231	0.9873326
H	5.9144130	0.9511109	0.9965846
H	-4.6387346	1.4369963	0.0958792
K	-4.7601690	-1.9040966	0.1410689

Irg-Li⁺

-773.9881517999

C	1.3473987	1.2175765	0.0670080
C	-0.0228787	1.3900936	-0.0125546
C	-0.9143585	0.2987592	0.0342975
C	-0.3648367	-0.9969565	0.1699905
C	0.9991231	-1.1812844	0.2507496
H	1.9944302	2.0830495	0.0279191
H	-0.4273691	2.3896709	-0.1146238
H	-0.9892958	-1.8770167	0.2142671
H	1.4232532	-2.1730387	0.3557004
C	-2.3333660	0.6038186	-0.0625460
O	-2.7169424	1.7890114	-0.1781996
C	1.8735174	-0.0796536	0.1983399
O	3.1777880	-0.3690567	0.2833715
O	-4.6755323	0.2571514	-0.1585537
C	-3.3255414	-1.4194772	-1.2352506
H	-3.3419667	-0.8432454	-2.1627294
H	-2.4187634	-2.0201880	-1.2216220
H	-4.1797919	-2.1029032	-1.2331331
C	-3.4192801	-0.4872556	-0.0304762
C	-3.4609373	-1.2092561	1.3135385
H	-4.3158831	-1.8915141	1.3330779
H	-2.5628302	-1.7959009	1.4940023
H	-3.5703960	-0.4893306	2.1273329
C	4.1335930	0.7167108	0.2172701
H	3.9870330	1.3799308	1.0759573
H	3.9899960	1.2634572	-0.7182582
C	5.5031369	0.0773983	0.2453521
H	6.2549875	0.8689266	0.2522872
H	5.6159458	-0.5126972	1.1618002
O	5.7432112	-0.7007272	-0.9132699
H	5.1862760	-1.4891899	-0.8568966
H	-5.3967435	-0.3894634	-0.1455731
Li	-4.5228890	2.1083528	-0.3022162

Chapter 3: Irgacure 2959 Clusters Supporting Information

Irg-Na⁺
-928.5092012318

C	-1.5719498	1.1593065	-0.1258067
C	-0.1909457	1.2440390	-0.0616928
C	0.6278230	0.0988238	-0.0659336
C	-0.0072005	-1.1605923	-0.1417653
C	-1.3824384	-1.2590165	-0.2063768
H	-2.1597748	2.0669407	-0.1208035
H	0.2783066	2.2185645	-0.0055452
H	0.5561752	-2.0817469	-0.1516005
H	-1.8697530	-2.2252860	-0.2653351
C	2.0741420	0.3235394	0.0100402
O	2.5216960	1.4823399	0.0708332
C	-2.1827382	-0.1032996	-0.1971411
O	-3.5071561	-0.3104881	-0.2620643
O	4.3937406	-0.2123638	0.1065603
C	2.9171053	-1.7142126	1.2628386
H	2.9982229	-1.1022164	2.1638064
H	1.9614891	-2.2330583	1.2876800
H	3.7086282	-2.4694601	1.2828574
C	3.0807162	-0.8425182	0.0189897
C	3.0440328	-1.6234927	-1.2934794
H	3.8355782	-2.3789480	-1.2880591
H	2.0969501	-2.1349980	-1.4498753
H	3.2128926	-0.9496544	-2.1362660
C	-4.3847748	0.8380920	-0.2364942
H	-4.2027578	1.4545302	-1.1230740
H	-4.1974372	1.4138942	0.6738290
C	-5.7946158	0.2927420	-0.2297176
H	-6.4929284	1.1311797	-0.2627182
H	-5.9546119	-0.3247700	-1.1208868
O	-6.0758427	-0.4224458	0.9602913
H	-5.5502419	-1.2340686	0.9420554
H	5.0349159	-0.9394143	0.1139562
Na	4.6440924	2.0202788	0.1999059

SCS-CC2/def2-SVP

Irg-Ca²⁺-Irg
-2206.4285966040

C	-5.9496515	-0.9220823	-0.7885784
C	-4.6868123	-0.4099282	-0.5434437
C	-4.4152006	0.4631384	0.5517675
C	-5.5056773	0.7908105	1.4144697
C	-6.7716812	0.2911418	1.1778266
H	-6.0978953	-1.6307807	-1.5995791
H	-3.8636269	-0.6907366	-1.2017943
H	-5.3803631	1.4452422	2.2745489
H	-7.6113370	0.5453653	1.8269697
C	-3.0648647	0.9346076	0.6987363
O	-2.1621460	0.5959891	-0.1270471
C	-7.0232946	-0.5640478	0.0699611
O	-8.2881863	-0.9365575	-0.0671678
O	-1.1789348	2.0959437	1.6206910
C	-2.7500924	1.1994250	3.2132612
H	-2.2143191	0.2395067	3.2195927
H	-2.3191885	1.8511508	3.9894234
H	-3.7948419	1.0100615	3.4808537

Chapter 3: Irgacure 2959 Clusters Supporting Information

C	-2.6238712	1.8708606	1.8460695
C	-3.2951218	3.2411583	1.7575422
C	-8.7456451	-1.7249944	-1.1886251
H	-8.1707275	-1.4720880	-2.0904166
H	-9.7885012	-1.4171471	-1.3344408
C	-8.6749450	-3.2019105	-0.8786107
H	-9.2355759	-3.3953115	0.0524517
H	-9.1802629	-3.7412857	-1.7008733
O	-7.3122944	-3.5596467	-0.7593993
C	5.7988158	-1.2314527	0.8157004
C	4.5784158	-0.6621248	0.4937378
C	4.3408840	-0.0196865	-0.7577812
C	5.4267841	0.0313085	-1.6845712
C	6.6480029	-0.5369010	-1.3776319
H	5.9523427	-1.6594315	1.8032298
H	3.7689643	-0.6942309	1.2242566
H	5.3291809	0.5090889	-2.6571476
H	7.4790352	-0.5095456	-2.0845087
C	3.0296735	0.5273553	-0.9787960
O	2.1264999	0.4357523	-0.0914388
C	6.8570659	-1.1881082	-0.1309622
O	8.0581897	-1.7292127	0.0176711
O	1.2176053	1.6380022	-2.0910679
C	3.4148190	2.5483599	-2.4825054
H	4.4800894	2.3621849	-2.6545711
H	3.3174523	3.1921424	-1.5967275
H	3.0233749	3.0894407	-3.3580027
C	2.6321777	1.2505016	-2.2851204
C	2.6626043	0.3118489	-3.4910568
H	2.2625883	0.8303712	-4.3764655
H	3.6798876	-0.0156264	-3.7293647
H	2.0507854	-0.5807386	-3.2973144
C	8.4160521	-2.5121528	1.1784425
H	7.5407046	-3.0632890	1.5495478
H	9.1572827	-3.2310596	0.8078491
C	9.0238232	-1.6420455	2.2535602
H	9.4186371	-2.3097205	3.0414121
H	9.8728017	-1.0852313	1.8202424
O	8.0162794	-0.7766544	2.7384676
H	-3.1318999	3.6835607	0.7644579
H	-2.8697593	3.9136310	2.5186789
H	-4.3744805	3.1810318	1.9318205
H	-7.2667386	-4.4865056	-0.4921198
H	8.4196432	-0.1723533	3.3746272
H	0.9440980	2.0715662	-2.9159807
H	-0.8800657	2.6614302	2.3515585
Ca	0.0061404	1.1529592	-0.1561411

Irg-Mg²⁺-Irg

-3307.4194248534

C	5.7500851	-0.9269474	-0.5915716
C	4.4606347	-0.6111067	-0.2039327
C	4.1056588	0.6833027	0.2880101
C	5.1415628	1.6677960	0.3567085
C	6.4328296	1.3631140	-0.0225188
H	5.9634149	-1.9054356	-1.0145401
H	3.6807632	-1.3693109	-0.2860414
H	4.9499218	2.6777609	0.7130658
H	7.2309596	2.1051634	0.0353969
C	2.7425761	0.8931240	0.6645395

Chapter 3: Irgacure 2959 Clusters Supporting Information

O	1.8906030	-0.0556386	0.5716358
C	6.7680863	0.0613536	-0.4923799
O	8.0479338	-0.1097621	-0.7778595
O	0.7728340	1.9951563	1.4552252
C	2.2790260	3.3465447	0.1453779
H	1.7802771	3.0258976	-0.7802719
H	1.7810033	4.2531836	0.5228413
H	3.3137107	3.6117114	-0.0961317
C	2.2114246	2.2431083	1.1996802
C	2.8304583	2.6168171	2.5452187
C	8.5895066	-1.3867848	-1.1921572
H	8.0516831	-2.2048572	-0.6935387
H	9.6269175	-1.3725745	-0.8362854
C	8.5495387	-1.5252309	-2.6959124
H	9.0757625	-0.6655060	-3.1458796
H	9.1041310	-2.4438331	-2.9617943
O	7.1933827	-1.5815385	-3.0908749
Mg	0.0017327	0.1752325	1.0501070
C	-5.5652240	0.2227885	-1.3913870
C	-4.3243898	0.1730969	-0.7826181
C	-4.0286204	-0.7401531	0.2765928
C	-5.0788862	-1.6114635	0.7064517
C	-6.3196171	-1.5743092	0.1037640
H	-5.7638492	0.9712224	-2.1544402
H	-3.5433643	0.8595121	-1.1122215
H	-4.9345964	-2.3301079	1.5104750
H	-7.1234877	-2.2416564	0.4191073
C	-2.7080146	-0.7086229	0.8233183
O	-1.8374970	0.1104238	0.3693751
C	-6.5866441	-0.6692462	-0.9626422
O	-7.7983192	-0.7709133	-1.4825917
O	-0.8316149	-1.2575075	2.2005505
C	-2.9862052	-1.3569972	3.2763233
H	-4.0441702	-1.6316104	3.2094909
H	-2.9227806	-0.2900960	3.5331048
H	-2.5373630	-1.9455969	4.0911200
C	-2.2454444	-1.6369427	1.9701473
C	-2.2353140	-3.1064495	1.5525027
H	-1.7849933	-3.7170359	2.3505555
H	-3.2480817	-3.4839843	1.3767279
H	-1.6524518	-3.2407570	0.6301921
C	-8.2230167	0.0088957	-2.6258923
H	-7.3752866	0.1776785	-3.3040900
H	-8.9626642	-0.6249330	-3.1301386
C	-8.8549841	1.3082830	-2.1852610
H	-9.2888832	1.7895435	-3.0809142
H	-9.6781020	1.0834034	-1.4849851
O	-7.8491504	2.0986095	-1.5833024
H	2.7151817	1.7927882	3.2635165
H	2.3309052	3.5112864	2.9479330
H	3.8976170	2.8439355	2.4519997
H	7.1604515	-1.6063430	-4.0558121
H	-8.2610445	2.9033127	-1.2433184
H	-0.4609957	-1.8465288	2.8766876
H	0.3635945	2.8263889	1.7433397

Irg-Zn²⁺-Irg

-1729.1795236511

C	-5.5514185	-1.0726853	-0.8449888
C	-4.3038104	-0.5238460	-0.6113064

Chapter 3: Irgacure 2959 Clusters Supporting Information

C	-4.0480317	0.3541955	0.4878124
C	-5.1393875	0.6406502	1.3675208
C	-6.3895280	0.1013225	1.1427320
H	-5.6869350	-1.7795211	-1.6597698
H	-3.4799565	-0.7750800	-1.2805082
H	-5.0236620	1.2896550	2.2329938
H	-7.2289574	0.3213834	1.8045037
C	-2.7204022	0.8672659	0.6255738
O	-1.8220058	0.5297807	-0.2215790
C	-6.6270499	-0.7533264	0.0289894
O	-7.8786516	-1.1610025	-0.0973879
O	-0.8788542	2.1171155	1.5015145
C	-2.3629599	1.1443484	3.1281791
H	-1.7627998	0.2234025	3.1180996
H	-1.9648944	1.8208334	3.9004729
H	-3.3889849	0.8839191	3.4083611
C	-2.3010486	1.8265726	1.7625271
C	-3.0310676	3.1661173	1.6825728
C	-8.3255222	-1.9690516	-1.2123373
H	-7.7691608	-1.7001018	-2.1207692
H	-9.3791275	-1.6943064	-1.3446216
C	-8.1999716	-3.4404500	-0.8941488
H	-8.7502471	-3.6501839	0.0395168
H	-8.6869340	-4.0020627	-1.7124060
O	-6.8241678	-3.7435249	-0.7773024
C	5.3584262	-1.5445590	0.5177436
C	4.1612098	-0.8722680	0.3531276
C	3.9634546	0.0959558	-0.6801989
C	5.0661829	0.3603158	-1.5525832
C	6.2634376	-0.3092049	-1.4022613
H	5.4834583	-2.2291547	1.3529294
H	3.3394793	-1.0760232	1.0408229
H	4.9965749	1.0833976	-2.3624791
H	7.1056591	-0.1210019	-2.0702801
C	2.6800342	0.7216166	-0.7596071
O	1.7626058	0.3877121	0.0683685
C	6.4333697	-1.2806408	-0.3753270
O	7.6121486	-1.8800212	-0.3716069
O	0.9380077	2.1782944	-1.5106445
C	3.1657434	3.0642861	-1.6400023
H	4.2262615	2.8899097	-1.8482175
H	3.0717633	3.4401502	-0.6115452
H	2.8083095	3.8399233	-2.3344488
C	2.3302676	1.7971656	-1.8129839
C	2.3269424	1.2207781	-3.2280155
H	1.9789343	1.9850365	-3.9402866
H	3.3264383	0.9019612	-3.5416765
H	1.6545915	0.3526540	-3.2808859
C	7.9380549	-2.9511896	0.5459794
H	7.0441357	-3.5547670	0.7550577
H	8.6647332	-3.5664928	0.0015348
C	8.5536602	-2.4050402	1.8127633
H	8.9145155	-3.2647908	2.4066369
H	9.4260771	-1.7841422	1.5446629
O	7.5622782	-1.6599970	2.4914754
H	-2.8928719	3.6117946	0.6875138
H	-2.6234435	3.8545836	2.4385536
H	-4.1049600	3.0617466	1.8677635
H	-6.7399550	-4.6684391	-0.5122823
H	7.9678529	-1.2568340	3.2697900

H	0.6195663	2.7945342	-2.1884464
H	-0.5228638	2.6555028	2.2253379
Zn	-0.0040546	1.1707908	-0.0444192

References

- Hansen, C. S.; Kirk, B. B.; Blanksby, S. J.; O'Hair, R. A.; Trevitt, A. J., UV photodissociation action spectroscopy of haloanilinium ions in a linear quadrupole ion trap mass spectrometer. *Journal of the American Society for Mass Spectrometry* **2013**, *24* (6), 932-940.
- Marlton, S. J.; McKinnon, B. I.; Ucur, B.; Maccarone, A. T.; Donald, W. A.; Blanksby, S. J.; Trevitt, A. J., Selecting and identifying gas-phase protonation isomers of nicotineH⁺ using combined laser, ion mobility and mass spectrometry techniques. *Faraday Discussions* **2019**, *217*, 453-475.
- Ly, T.; Julian, R. R., Residue-specific radical-directed dissociation of whole proteins in the gas phase. *Journal of the American Chemical Society* **2008**, *130* (1), 351-358.
- Ly, T.; Zhang, X.; Sun, Q.; Moore, B.; Tao, Y.; Julian, R. R., Rapid, quantitative, and site specific synthesis of biomolecular radicals from a simple photocaged precursor. *Chemical Communications* **2011**, *47* (10), 2835-2837.
- Frisch, M. J.; Trucks, G. W.; Schlegel, H. B.; Scuseria, G. E.; Robb, M. A.; Cheeseman, J. R.; Scalmani, G.; Barone, V.; Petersson, G. A.; Nakatsuji, H.; Li, X.; Caricato, M.; Marenich, A. V.; Bloino, J.; Janesko, B. G.; Gomperts, R.; Mennucci, B.; Hratchian, H. P.; Ortiz, J. V.; Izmaylov, A. F.; Sonnenberg, J. L.; Williams-Young, D.; Ding, F.; Lipparini, F.; Egidi, F.; Goings, J.; Peng, B.; Petrone, A.; Henderson, T.; Ranasinghe, D.; Zakrzewski, V. G.; Gao, J.; Rega, N.; Zheng, G.; Liang, W.; Hada, M.; Ehara, M.; Toyota, K.; Fukuda, R.; Hasegawa, J.; Ishida, M.; Nakajima, T.; Honda, Y.; Kitao, O.; Nakai, H.; Vreven, T.; Throssell, K.; Montgomery Jr., J. A.; Peralta, J. E.; Ogliaro, F.; Bearpark, M. J.; Heyd, J. J.; Brothers, E. N.; Kudin, K. N.; Staroverov, V. N.; Keith, T. A.; Kobayashi, R.; Normand, J.; Raghavachari, K.; Rendell, A. P.; Burant, J. C.; Iyengar, S. S.; Tomasi, J.; Cossi, M.; Millam, J. M.; Klene, M.; Adamo, C.; Cammi, R.; Ochterski, J. W.; Martin, R. L.; Morokuma, K.; Farkas, O.; Foresman, J. B.; Fox, D. J. *Gaussian 16*, Wallingford, CT, 2016.
- Zhao, Y.; Truhlar, D. G., The M06 suite of density functionals for main group thermochemistry, thermochemical kinetics, noncovalent interactions, excited states, and transition elements: two new functionals and systematic testing of four M06-class functionals and 12 other functionals. *Theoretical Chemistry Accounts: Theory, Computation, and Modeling (Theoretica Chimica Acta)* **2008**, *120* (1), 215-241.
- Weigend, F.; Ahlrichs, R., Balanced basis sets of split valence, triple zeta valence and quadruple zeta valence quality for H to Rn: Design and assessment of accuracy. *Physical Chemistry Chemical Physics* **2005**, *7* (18), 3297-3305.
- Weigend, F., Accurate Coulomb-fitting basis sets for H to Rn. *Physical chemistry chemical physics* **2006**, *8* (9), 1057-1065.
- Smith, C.; Hall, G., The approximation of electron densities. *Theoretica Chimica Acta* **1986**, *69* (1), 63-69.
- Hall, G.; Smith, C., Fitting electron densities of molecules. *International Journal of Quantum Chemistry* **1984**, *25* (5), 881-890.

11. Christiansen, O.; Koch, H.; Jørgensen, P., The second-order approximate coupled cluster singles and doubles model CC2. *Chemical Physics Letters* **1995**, *243* (5-6), 409-418.
12. Grimme, S., Improved second-order Møller–Plesset perturbation theory by separate scaling of parallel-and antiparallel-spin pair correlation energies. *The Journal of Chemical Physics* **2003**, *118* (20), 9095-9102.
13. Hättig, C.; Weigend, F., CC2 excitation energy calculations on large molecules using the resolution of the identity approximation. *The Journal of Chemical Physics* **2000**, *113* (13), 5154-5161.
14. TURBOMOLE V7.2 2017, a development of University of Karlsruhe and Forschungszentrum Karlsruhe GmbH, 1989-2009, TURBOMOLE GmbH, since 2007; available from <http://www.turbomole.com>.
15. Kulesza, A. J.; Titov, E.; Daly, S.; Włodarczyk, R.; Megow, J.; Saalfrank, P.; Choi, C. M.; MacAleese, L.; Antoine, R.; Dugourd, P., Excited States of Xanthene Analogues: Photofragmentation and Calculations by CC2 and Time-Dependent Density Functional Theory. *ChemPhysChem* **2016**, *17* (19), 3129-3138.
16. Matthews, E.; Dessent, C. E., Locating the proton in nicotinamide protomers via low-resolution UV action spectroscopy of electrosprayed solutions. *The Journal of Physical Chemistry A* **2016**, *120* (46), 9209-9216.
17. McNaught, A. D.; Wilkinson, A., *IUPAC. Compendium of Chemical Terminology, 2nd ed. (the "Gold Book")*. . Blackwell Science Oxford: 1997; Vol. 1669.

This page has been intentionally left blank.

PROTOMERS OF QUINAZOLINEH⁺

4. QuinazolineH⁺

This chapter discusses the separation and spectroscopy of quinazolineH⁺ protomers. The contents are reproduced verbatim from the peer-reviewed and publication:

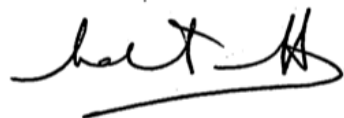
Marlton, S.J., McKinnon, B.I., Ucur, B., Bezzina, J.P., Blanksby, S.J. and Trevitt, A.J., 2020. Discrimination between protonation isomers of quinazoline by ion mobility and uv-photodissociation action spectroscopy. *The journal of physical chemistry letters*, 11(10), pp.4226-4231.

Author Contributions

S.J.P Marlton performed all calculations and experiments presented in this work. S.J.P Marlton prepared the manuscript with input from all authors. B, I, McKinnon contributed to data analysis and conception of the computational strategy. B, Ucur contributed to development and implementation of the FAIMS experimental method. J,P, Bezzina contributed to initial photodissociation action spectroscopy experiments without FAIMS separation.

Certification

I, Prof. Adam J. Trevitt, as Samuel J. P. Marlton's primary supervisor, and the principal investigator for this project, agree with and certify the author contributions described above.

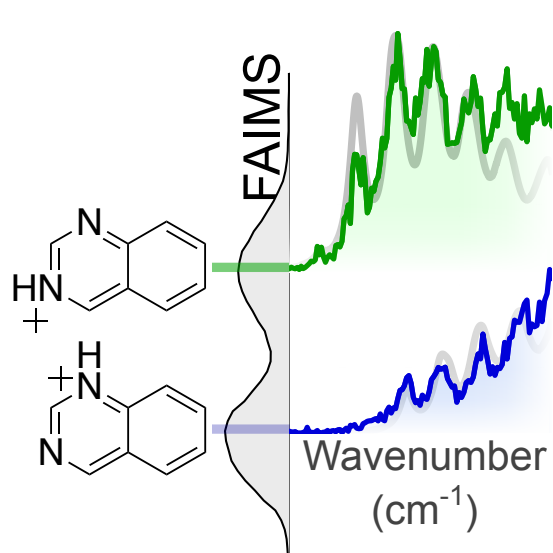


Adam J. Trevitt

07/12/2021

4.1 Abstract

The influence of oriented electric fields on chemical reactivity and photochemistry is an area of increasing interest. Within a molecule, different protonation sites offer the opportunity to control the location of charge and thus orientation of electric fields. New techniques are thus needed to discriminate between protonation isomers in order to understand this effect. This investigation reports the UV-photodissociation action spectroscopy of two protonation isomers (protomers) of 1,3-diazanaphthalene (quinazoline) arising from protonation of a nitrogen at either the 1- or 3-position. It is shown that these protomers are separable by field-asymmetric ion mobility spectrometry (FAIMS) with confirmation provided by UV-photodissociation (PD) action spectroscopy. Vibronic features in the UVPD action spectra and computational input allow assignment of the origin transitions to the S₁ and S₅ states of both protomers. These experiments also provide vital benchmarks for protomer-specific calculations and examination of isomer-resolved reaction kinetics and thermodynamics.



4.2 Introduction

There is expanding interest in the role oriented electric fields can play in influencing chemical reactivity and photochemistry.¹⁻⁶ The application of such fields can be achieved by an external source or by positioning charge on (or near) a molecule. One of the fundamental chemical agents bearing charge is the proton. In mass spectrometry, it is well known that electrospray ionization of biologically relevant molecules can protonate molecules at various sites. This is exploited in H⁺ driven fragmentation, where multiple protonation isomers give rise to a spread of product ions that facilitate structural elucidation.⁷ From both analytical and fundamental perspectives, there are prevailing questions about the underlying mechanisms of electrospray ionization requiring new experimental strategies capable of separating, assigning and selecting protonation isomers (termed protomers) for detailed study.

Combined laser photodissociation and mass spectrometry, in the form of infrared multiphoton dissociation (IRMPD)⁸⁻¹² or UV-Vis photodissociation (PD) action spectroscopy¹³⁻²⁰ has allowed the detection and assignment of protomers. Variations in protonation site has been shown to affect non-radiative excited-state lifetimes,^{17, 18, 21} photo-isomerisation perpendencies,²² photofragment distributions,^{13, 20, 23} as well as spectroscopic profiles.^{13, 16, 19, 20, 23} In most of these studies, the protomer ion populations are co-located and their spectroscopy is sufficiently different to allow identification.

Field-asymmetric waveform ion mobility spectrometry (FAIMS)²⁴⁻²⁷ has been successfully deployed to separate protomer ions for subsequent analysis.²⁸⁻³¹ Several groups have coupled FAIMS with UV PD³²⁻³⁴ or IRMPD^{35, 36} for isomer analysis (not necessarily protomers). More recently, our group has combined FAIMS and UV laser spectroscopy to separate and assign the two dominant gas-phase protomers of the small-molecule ion nicotineH⁺.²⁰ In the nicotine case, protomers arise from protonation of different function groups: pyridine and pyrrolidine. In the present study, to demonstrate FAIMS separation of protomers with all local chemical functional groups retained, this paper targets quinazoline protonated on either the 1-nitrogen (1QZH⁺) or the 3-nitrogen (3QZH⁺) atom. Quinazoline is a fundamental aromatic chromophore with two non-degenerate protonatable nitrogens, with very similar stabilities, and these systems are small enough to allow detailed treatment with quantum chemical calculations for assignment of vibronic spectra and, in turn, provides valuable benchmarking data. To our knowledge there are no reported spectra of protonated diazanaphthalenes in the literature, while

spectra of protonated azanaphthalenes (quinoline and isoquinoline)^{34, 37, 38} as well as protonated diazines (pyrimidine, pyrazine and pyridazine)³⁹ have been reported.

The experimental setup combined cylindrical geometry field-asymmetric waveform ion mobility spectrometry (FAIMS, Thermo Fisher Scientific) with a linear ion trap mass spectrometry (LTQ XL Thermo Fisher Scientific) equipped with a tuneable UV-VIS mid-band OPO nanosecond-pulse laser system (Spectra-Physics QuantaRay INDI). Ions generated by electrospray ionization (ESI) are carried by a flow of N₂ buffer gas between two electrodes across which a time-varying asymmetric potential is applied, oscillating between a “high-field” voltage and a “low-field” voltage. The high-field voltage is termed the dispersion voltage (DV). In FAIMS, ions are laterally displaced (relative to the flow of ions) by differences in their combined high-field and low-field mobility. By simultaneously applying a DC compensation voltage (CV) across the electrodes, the lateral displacement of ions can be altered to allow each trajectory, in turn, to be directed towards the inlet of the mass spectrometer.²⁴⁻²⁷ To subsequently obtain a photodissociation action spectrum, *m/z* selected ions were isolated in the ion trap and subjected to a single laser pulse (directed through the ion trap *via* a quartz window mounted on the back of the mass spectrometer vacuum housing) after which the ions are scanned out of the ion trap to record a product mass spectrum. Photoproduct yields are recorded over a range of wavelengths and collated to produce a photodissociation action spectrum.

4.3 Results and Discussion

Figure 4.1 shows the FAIMS ionogram of singly protonated quinazoline ion (*m/z* 131) revealing two broad peaks centred at compensation voltages of -8 and -3 V. As shown in Figure 4.1, quinazoline can be protonated at either the 1-nitrogen (1QZH⁺) or the 3-nitrogen (3QZH⁺) and, as will be demonstrated herein, the two FAIMS separated peaks arise from these two protomers. The separation of the two protomers of quinazolineH⁺ can be rationalised by dipole moment calculations, shown in Figure 4.1B, which predict that 3QZH⁺ has a significantly larger dipole moment (4.7 D) compared to 1QZH⁺ (2.6 D). Dipole moment is a key parameter for FAIMS separation.^{28, 31} Figure 4.1B shows the peak positions as a function of dispersion voltage (full ionograms are provided in Figure 4.4 of the Supporting Information). The blue trace levels off around 4400 V and is consistent with increased “hard-sphere” collisional interactions of type B ions,⁴⁰ due to relatively minor buffer gas interactions.^{41, 42} The green trace (ending at CV -8 V) continues its trend towards negative CV values and is consistent with

the strong buffer gas interaction of a type A ion^{40, 42} in this voltage range. Molecules with larger dipole-moments experience a greater degree of buffer-gas clustering.²⁸ Using similar reasoning to Campbell *et al.*²⁸ and Walker *et al.*³¹ it is expected that 1QZH⁺ (2.6 D) experiences weaker interactions with the N₂ buffer gas than 3QZH⁺ (4.7 D) and, as such, it is likely that 3QZH⁺ is the peak at -8 V and 1QZH⁺ is the peak at -3 V. Further evidence substantiating this assignment will be obtained from photodissociation action spectroscopy.

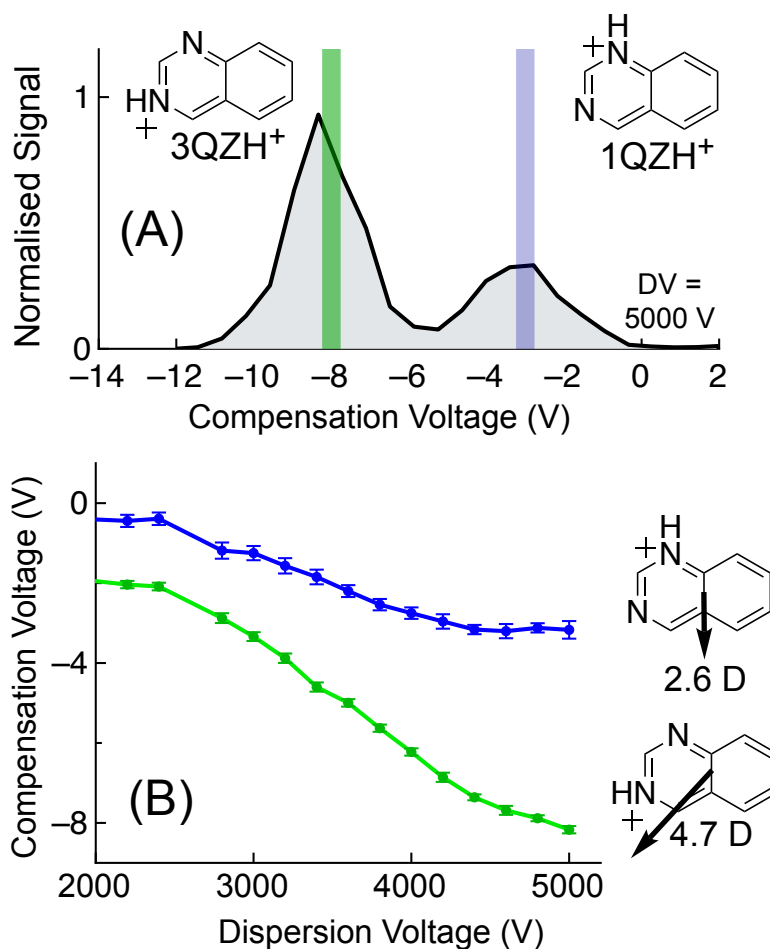


Figure 4.1: (A) FAIMS ionogram following the m/z 131 signal of singly protonated quinazoline. Spectra are acquired using $DV = 5000$ V. The peaks observed at -8 V and -3 V are assigned to protomers of QZH⁺. Further evidence substantiating the FAIMS protomer assignment is obtained from photodissociation action spectroscopy. Figure 4.1(B): Dispersion plot following QZH⁺ (m/z 131) in N₂ buffer gas. The green trace is assigned as 3QZH⁺ and the blue trace is assigned as 1QZH⁺. Errors are 2σ as determined by fitting gaussians to FAIMS peaks. Dipole moments are calculated using CAM-B3LYP/aug-cc-pVDZ.

UVPD of QZH⁺ protomers leads to photoproducts at m/z 104 and m/z 77 in each case with distinctly different product branching ratios. The PD product mass spectra and photoproduct branching ratios are provided in Section SI.2 of the Supporting Information (Figure 4.5) along with energy calculations of plausible photoproduct pathways (Figure 4.6). Since the photoproduct at m/z 104 is plausibly cyanobenzeneH⁺, an action spectrum of this photoproduct was also scanned and compared to an authentic sample (Figure 4.7); although the spectra are similar the match is not exact suggesting that other energetically accessible isomers (*e.g.*, isocyanobenzeneH⁺ or linear isomers) may also contribute to the photoproduct ion population. Photodissociation action spectra of QZH⁺ (following formation of a m/z 104 ion) scanning from 25000 – 45000 cm⁻¹ (385 – 222 nm) are shown in Figure 4.2 with: (A) no FAIMS selection, (B) FAIMS compensation voltage –8 V and (C) compensation voltage at –3 V. There are two main bands in both cases at low and high energy within this range. The low energy band signal is significantly magnified (as indicated) and a full PD spectrum with no FAIMS selection is provided in Figure 4.8 of the Supporting Information. The dotted vertical lines in Figure 4.2, for both the high energy and low energy bands, are to emphasise peaks in Figure 4.2B that are totally absent from the spectrum in Figure 4.2C. For both the highlighted bands, the first vibronic peak is blue-shifted in the spectrum plotted in (C) compared to (B), which indicates successful FAIMS separation of isomeric ions.

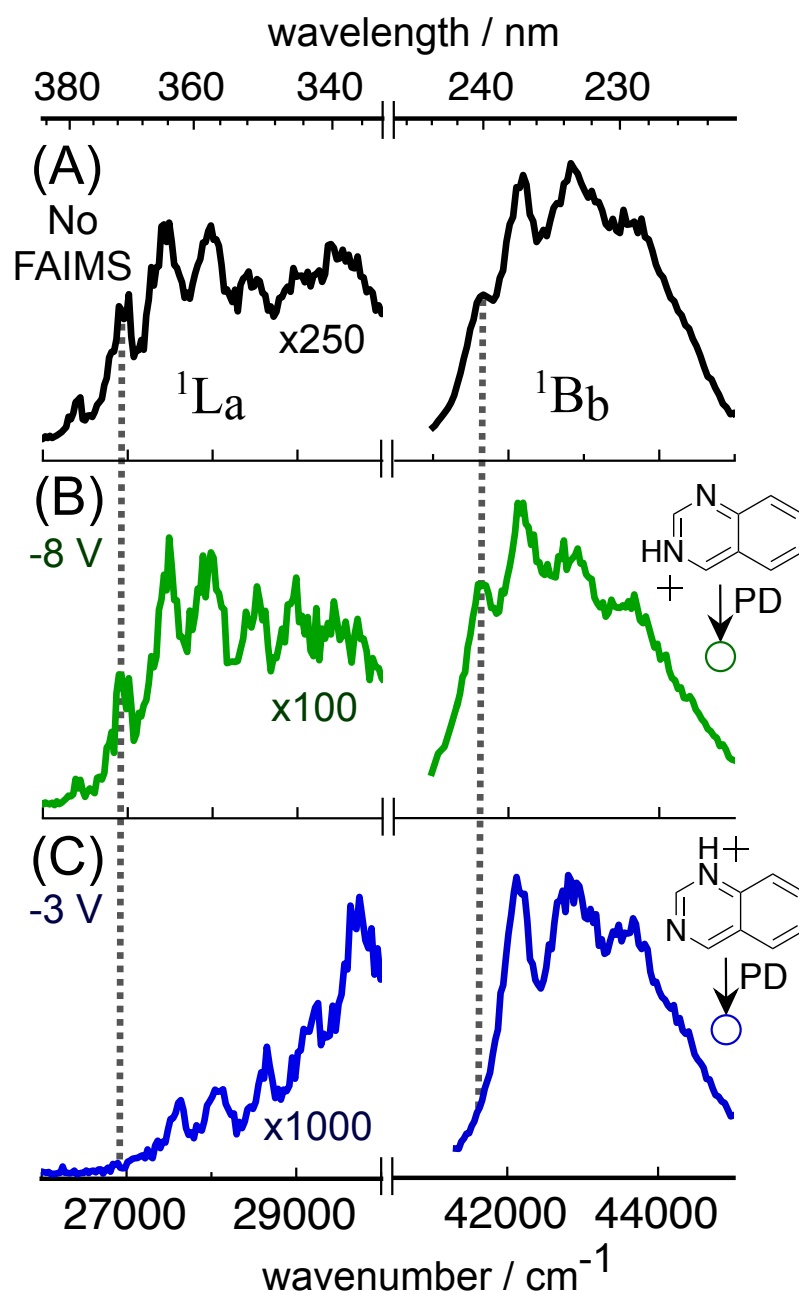


Figure 4.2: Photodissociation action spectra of QZH⁺ with (A): no FAIMS selection, (B): FAIMS CV = -8 V and (C): FAIMS CV = -3V.

To consolidate the protomer assignments, the action spectra are compared to predicted vertical and zero-point energy corrected adiabatic (0-0) electronic transitions for the two suspected protonation isomers. The calculated 0-0 and vertical transition energies, oscillator strengths and orbital contributions using time-dependent density-functional theory TD-DFT (CAM-B3LYP) are shown in Table 4.1 for 3QZH⁺ and Table 4.2 for 1QZH⁺. For images of the key molecular orbitals and their full transition contributions see Figure 4.9 and Tables 4.3 and 4.4 in the Supporting Information. For both cases, calculations predict there are five singlet electronic states in the relevant photon energy range, with S₁, S₃ and S₅ as the ¹ππ* transitions

and S₂ and S₄ as ¹nπ* transitions. In Platt's notation,⁴³ the S₁ state of both protomers is an ¹L_a state, the S₃ is an ¹L_b state and the S₅ is an ¹B_b state (see Section SI.6 of the Supporting Information for full assignment details). Transitions to the ¹B_b (S₅) state are predicted to have the greatest oscillator strengths and, along with the predicted transition energy (44000–46000 cm⁻¹), these are assigned as strong high-energy bands in Figure 4.2. The ¹L_a transitions have oscillator strengths about an order-of-magnitude weaker than ¹B_b transitions. Calculated transition dipoles for these states are provided in Figure 4.11, (Supporting Information). Higher level multistate complete-active-space second-order perturbation theory electronic energy calculations (MS-CASPT2) using complete active space self-consistent field (CASSCF(12,11)) geometries and zero-point energy corrections for both protomers are used to gain a more accurate prediction of the origin energy (active space orbitals are shown in Figure 4.10 of Supporting Information).⁴⁴ The experimental 0-0 transition energies are assigned to the apex of first major peak in the FAIMS-resolved action spectra (Figure 4.2B and C) and are tabulated in Table 4.2 along with MS-CASPT2 values for 0-0 transition energies. The MS-CASPT2 0-0 transition energies for the 1QZH⁺ protomer are blue shifted compared to 3QZH⁺ for both the low and high energy bands. Comparing MS-CASPT2 to the experimental values in Table 4.2, there is good agreement. Therefore, based on the 0-0 transition energies, the FAIMS peaks at CV -3 V is assigned to the 1QZH⁺ protomer and CV -8 V is assigned to 3QZH⁺. With these protonation-isomer specific experiments it is thus possible to benchmark calculations for these small electronic energy differences for protonation isomers. Furthermore, it is notable that the stability difference between two protomers is calculated at only 135 cm⁻¹ (1.6 kJ/mol), in favour of 3QZH⁺, which is on the order of these uncertainty for these calculations (see Figure 4.6).

Table 4.1: 3QZH⁺: Experimental adiabatic transition (0-0) energies, MS-CASPT2 adiabatic transition energies, and CAM-B3LYP adiabatic and vertical transition energies, oscillator strength, and key orbital contributions (> 20 %). H = HOMO, L = LUMO. Structures with imaginary frequencies are shown in square brackets. The * denotes states that did not converge.

3QZH ⁺ Transition from S ₀ (¹ A) to:	Experimental 0-0 (cm ⁻¹)	MS-CASPT2 Adiabatic Transition Energies (cm ⁻¹)	CAM-B3LYP Adiabatic/Vertical Transition Energies (cm ⁻¹)	Oscillator Strength	Orbitals Involved in Transition (TD-DFT)
S ₁ (¹ L _a)	26900	26650	27519/30993	0.040	L (π*) ← H (π)
S ₂	-		[30247]/36433	0.0010	L (π*) ← H-2 (n)
S ₃ (¹ L _b)	-	34681	*/37699	0.016	L (π*) ← H-1 (π) L+1 (π*) ← H (π)
S ₄	-		*/42169	0.0016	L+1 (π*) ← H-2 (n)
S ₅ (¹ B _b)	41600	42587	[44470]/46596	0.69	L (π*) ← H-1 (π) L+1 (π*) ← H (π)

Table 4.2: 1QZH⁺: Experimental adiabatic transition (0-0) energies, MS-CASPT2 adiabatic transition energies, and CAM-B3LYP adiabatic and vertical transition energies, oscillator strength, and key orbital contributions (> 20 %). H = HOMO, L = LUMO. Structures with imaginary frequencies are shown in square brackets. The * denotes states that did not converge

1QZH ⁺ Transition from S ₀ (¹ A) to:	Experimental 0-0 (cm ⁻¹)	MS-CASPT2 Adiabatic Transition Energies (cm ⁻¹)	CAM-B3LYP Adiabatic/Vertical Transition Energies (cm ⁻¹)	Oscillator Strength	Orbitals Involved in Transition (TD-DFT)
S ₁ (¹ L _a)	27600	28424	[29003]/32942	0.028	L (π*) ← H (π)
S ₂			27041/33261	0.0002	L (π*) ← H-2 (n)
S ₃ (¹ L _b)		*	35937/37598	0.078	L (π*) ← H-1 (π) L+1 (π*) ← H (π)
S ₄			[41570]/46300	0.0036	L+1 (π*) ← H-2 (n)
S ₅ (¹ B _b)	42100	43303	[44769]/47447	0.63	L (π*) ← H-1 (π) L+1 (π*) ← H (π)

Figures 4.3A–D contain the experimental PD action spectra of the lower energy band at (A) FAIMS CV -8 V (assigned to 3QZH⁺) and (C) CV -3 V (assigned to 1QZH⁺), following the photoproduct yield of m/z 104 and m/z 77 photoproducts. Also shown are Franck-Condon (FC) simulations for the transition to the ¹L_a (S₁) state of the corresponding protomer calculated using the CASSCF(12,11) method with a 0.90 scaling factor applied to the excited state vibrational wavenumbers, shown as stick spectra and simulated spectra convoluted with 220 cm⁻¹ FWHM Lorentzian functions to aid the comparison. For room temperature ions, the width of peaks could be due to rotational envelopes, unaccounted for combination bands and lifetime broadening. PD in this low energy region appears to be non-linear suggesting some fragmentation arises from multiphoton process (see Figure 4.12).

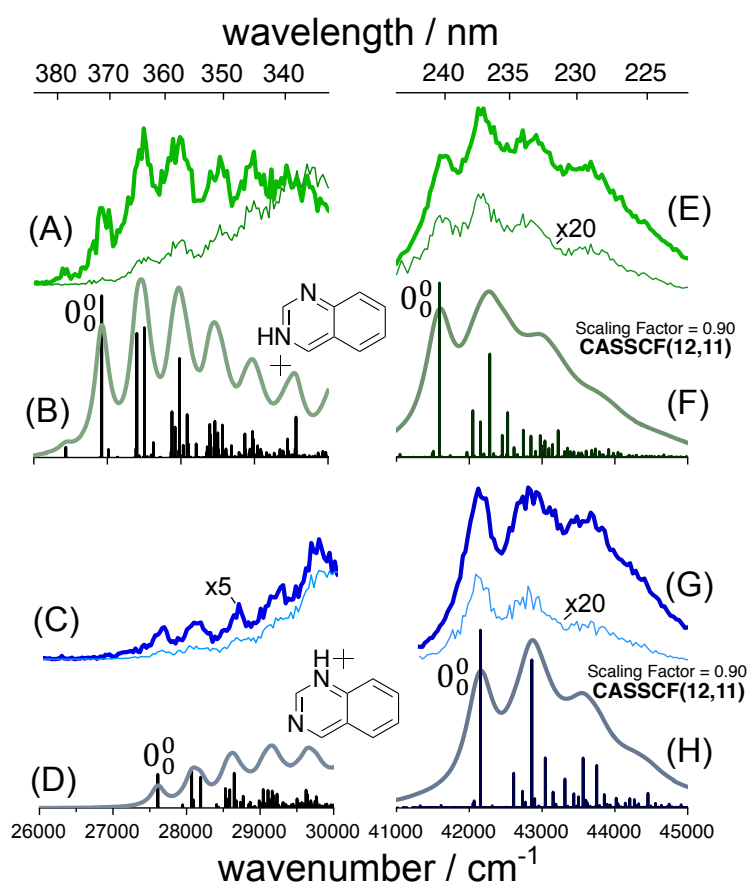


Figure 4.3: Photodissociation action spectra of QZH⁺ at CV -8 V (A and E) and -3 V (C and G) following the yield of m/z 104 (thick line) and m/z 77 (thin line). Franck-Condon simulations of vibronic transitions to the S₁ (¹L_a) state for (B) 3QZH⁺ and (D) 1QZH⁺ and the S₅ (¹B_b) state for (F) 3QZH⁺ and (H) 1QZH⁺ are shown as sticks and also convoluted with Lorentzian functions (FWHM 220 cm⁻¹ for S₁ and 440 cm⁻¹ for S₅). CASSCF(12,11) calculations are shifted to match the experimental origin and vibrations scaled by 0.90 as described in the text.

Previous studies have shown that the vibronic spectrum of neutral quinazoline is dominated by in plane (a') vibrational modes^{45, 46} and the same situation applies here. The vibrational assignments for the transition with the dominant FC intensities are provided in Section SI.8 of the Supporting Information. CASSCF calculations involved in Franck-Condon simulations optimised to planar C_s geometries with all real frequencies. In contrast, CAM-B3LYP optimisations for the 1L_a state of 1QZH⁺ lead to a geometry with an imaginary frequency, which broke C_s symmetry, however, any effects of plane buckling appear to be too subtle to be observed experimentally here (see Section SI.9 of Supporting Information). Overall, there is good alignment between the features in the experimental spectra and the simulations.

Figures 4.3E–H show the photodissociation action spectra of the $^1B_b \leftarrow ^1A$ ($S_5 \leftarrow S_0$) transition using -8 V compensation voltage (Figure 4.3E, assigned to 3QZH⁺) and -3 V compensation voltage (Figure 4.3G, assigned to 1QZH⁺) and FC simulations are shown both as stick spectra and simulated spectra (convoluted with Lorentzian functions of FWHM 440 cm^{-1}). Compared with low energy transition (Figures 4.3A–D), these bands are around two orders of magnitude greater intensity and show only broad features. Relative to MS-CASPT2 0-0 transition energies, Franck-Condon simulations have been shifted by (B) -273 cm^{-1} , (D) 814 cm^{-1} , (F) 997 cm^{-1} and (H) 1151 cm^{-1} to align with experimental peaks. Aligning FC simulations results in good agreement between the simulations and the spectra consistent with all the previous assignments.

4.4 Conclusion

In summary, these experiments show that FAIMS can separate protonation isomers and select the desired protomer for subsequent experimentation. In summary, these experiments show that combined FAIMS and UVPD can clearly separate and select protonation isomers for a case where the isomers differ by which aromatic nitrogen is protonated while retaining the total number of each type of functional group (*i.e.*, one N-H in each structure). These protonation isomers have almost indistinguishable stability. In addition to providing spectroscopic details and vital benchmarks for protomer-specific calculations, the ability to completely resolve these protomers opens future possibilities for examining ion-molecule measurements on selected protomers,²⁸⁻³¹ *e.g.* measurement of proton affinities and protomer-specific reaction kinetics.

Acknowledgements

Funding from the Australian Research Council Discovery Program (DP170101596) is gratefully acknowledged. SM, BM, BU, JB each acknowledge support from Australian Government Research Training Program Scholarships. AT also acknowledges key support from UOW SMAH research funding. The authors also grateful to Profs C. Jouvét and C. Dedonder (CNRS, Aix Marseille Université) and Prof J Bouwman (Leiden) and Prof P. Mayer (University of Ottawa) for helpful discussions. Computing resources provided by NCMAS from the NCI National Facility (Canberra, Australia).

References

1. Ciampi, S.; Darwish, N.; Aitken, H. M.; Díez-Pérez, I.; Coote, M. L., Harnessing electrostatic catalysis in single molecule, electrochemical and chemical systems: a rapidly growing experimental tool box. *Chemical Society Reviews* **2018**, *47* (14), 5146-5164.
2. Shaik, S.; Ramanan, R.; Danovich, D.; Mandal, D., Structure and reactivity/selectivity control by oriented-external electric fields. *Chemical Society Reviews* **2018**, *47* (14), 5125-5145.
3. Stuyver, T.; Danovich, D.; Joy, J.; Shaik, S., External electric field effects on chemical structure and reactivity. *Wiley Interdisciplinary Reviews: Computational Molecular Science* **2019**, e1438.
4. Aragonés, A. C.; Haworth, N. L.; Darwish, N.; Ciampi, S.; Bloomfield, N. J.; Wallace, G. G.; Díez-Pérez, I.; Coote, M. L., Electrostatic catalysis of a Diels–Alder reaction. *Nature* **2016**, *531* (7592), 88-91.
5. Hill, N. S.; Coote, M. L., Internal Oriented Electric Fields as a Strategy for Selectively Modifying Photochemical Reactivity. *Journal of the American Chemical Society* **2018**, *140* (50), 17800-17804.
6. Blyth, M. T.; Noble, B. B.; Russell, I. C.; Coote, M. L., Oriented Internal Electrostatic Fields Cooperatively Promote Ground- and Excited-State Reactivity: A Case Study in Photochemical CO₂ Capture. *Journal of the American Chemical Society* **2019**, *142* (1), 606-613.
7. Wysocki, V. H.; Tsapralis, G.; Smith, L. L.; Brechi, L. A., Mobile and localized protons: a framework for understanding peptide dissociation. *Journal of Mass Spectrometry* **2000**, *35* (12), 1399-1406.
8. Nei, Y.-w.; Akinyemi, T.; Steill, J.; Oomens, J.; Rodgers, M., Infrared multiple photon dissociation action spectroscopy of protonated uracil and thiouracils: Effects of thioketo-substitution on gas-phase conformation. *International Journal of Mass Spectrometry* **2010**, *297* (1), 139-151.
9. Langer, J.; Günther, A.; Seidenbecher, S.; Berden, G.; Oomens, J.; Dopfer, O., Probing Protonation Sites of Isolated Flavins Using IR Spectroscopy: From Lumichrome to the Cofactor Flavin Mononucleotide. *ChemPhysChem* **2014**, *15* (12), 2550-2562.
10. Warnke, S.; Seo, J.; Boschmans, J.; Sobott, F.; Scrivens, J. H.; Bleiholder, C.; Bowers, M. T.; Gewinner, S.; Schöllkopf, W.; Pagel, K., Protomers of benzocaine: solvent and permittivity dependence. *Journal of the American Chemical Society* **2015**, *137* (12), 4236-4242.
11. Patrick, A. L.; Cismesia, A. P.; Tesler, L. F.; Polfer, N. C., Effects of ESI conditions on kinetic trapping of the solution-phase protonation isomer of p-aminobenzoic acid in the gas phase. *International Journal of Mass Spectrometry* **2017**, *418*, 148-155.

12. Bell, M. R.; Cruzeiro, V. W. D.; Cismesia, A. P.; Tesler, L. F.; Roitberg, A. E.; Polfer, N. C., Probing the Structures of Solvent-Complexed Ions Formed in Electrospray Ionization Using Cryogenic Infrared Photodissociation Spectroscopy. *The Journal of Physical Chemistry A* **2018**, *122* (37), 7427-7436.
13. Matthews, E.; Dessent, C. E., Experiment and theory confirm that UV laser photodissociation spectroscopy can distinguish protomers formed via electrospray. *Physical Chemistry Chemical Physics* **2017**, *19* (26), 17434-17440.
14. Sheldrick, A.; Müller, D.; Günther, A.; Nieto, P.; Dopfer, O., Optical spectroscopy of isolated flavins: photodissociation of protonated lumichrome. *Physical Chemistry Chemical Physics* **2018**, *20* (11), 7407-7414.
15. Matthews, E.; Cercola, R.; Dessent, C., Protomer-Dependent Electronic Spectroscopy and Photochemistry of the Model Flavin Chromophore Alloxazine. *Molecules* **2018**, *23* (8), 2036.
16. Noble, J. A.; Broquier, M.; Gregoire, G.; Soorkia, S.; Pino, G.; Marceca, E.; Dedonder-Lardeux, C.; Juvet, C., Tautomerism and electronic spectroscopy of protonated 1- and 2-aminonaphthalene. *Physical Chemistry Chemical Physics* **2018**, *20* (9), 6134-6145.
17. Féraud, G.; Berdakin, M.; Dedonder, C.; Juvet, C.; Pino, G. A., Excited States of Proton-Bound DNA/RNA Base Homodimers: Pyrimidines. *The Journal of Physical Chemistry B* **2014**, *119* (6), 2219-2228.
18. Broquier, M.; Soorkia, S.; Pino, G. A.; Dedonder-Lardeux, C.; Juvet, C.; Gregoire, G., Excited State Dynamics of Cold Protonated Cytosine Tautomers: Characterization of Charge Transfer, Inter System Crossing and Internal Conversion Processes. *The Journal of Physical Chemistry A* **2017**, *121* (34), 6429-6439.
19. Féraud, G.; Esteves-Lopez, N.; Dedonder-Lardeux, C.; Juvet, C., UV spectroscopy of cold ions as a probe of the protonation site. *Physical Chemistry Chemical Physics* **2015**, *17* (39), 25755-25760.
20. Marlton, S. J.; McKinnon, B. I.; Ucur, B.; Maccarone, A. T.; Donald, W. A.; Blanksby, S. J.; Trevitt, A. J., Selecting and identifying gas-phase protonation isomers of nicotineH⁺ using combined laser, ion mobility and mass spectrometry techniques. *Faraday Discussions* **2019**, *217*, 453-475.
21. Berdakin, M.; Féraud, G.; Dedonder-Lardeux, C.; Juvet, C.; Pino, G. A., Excited states of protonated DNA/RNA bases. *Physical Chemistry Chemical Physics* **2014**, *16* (22), 10643-10650.
22. Bull, J. N.; Coughlan, N. J.; Bieske, E. J., Protomer-Specific Photochemistry Investigated Using Ion Mobility Mass Spectrometry. *The Journal of Physical Chemistry A* **2017**, *121* (32), 6021-6027.
23. Matthews, E.; Dessent, C. E., Locating the proton in nicotinamide protomers via low-resolution UV action spectroscopy of electrosprayed solutions. *The Journal of Physical Chemistry A* **2016**, *120* (46), 9209-9216.
24. Shvartsburg, A. A.; Tang, K.; Smith, R. D., Modeling the resolution and sensitivity of FAIMS analyses. *Journal of the American Society for Mass Spectrometry* **2004**, *15* (10), 1487-1498.
25. Shvartsburg, A. A., *Differential ion mobility spectrometry: nonlinear ion transport and fundamentals of FAIMS*. CRC Press: 2008.
26. Shvartsburg, A. A.; Seim, T. A.; Danielson, W. F.; Norheim, R.; Moore, R. J.; Anderson, G. A.; Smith, R. D., High-definition differential ion mobility spectrometry with resolving power up to 500. *Journal of the American Society for Mass Spectrometry* **2012**, *24* (1), 109-114.
27. Gabelica, V.; Shvartsburg, A. A.; Afonso, C.; Barran, P.; Benesch, J. L.; Bleiholder, C.; Bowers, M. T.; Bilbao, A.; Bush, M. F.; Campbell, J. L., Recommendations

for Reporting Ion Mobility Mass Spectrometry Measurements. *Mass spectrometry reviews* **2019**, *38* (3), 291-320.

28. Campbell, J. L.; Le Blanc, J. Y.; Schneider, B. B., Probing electrospray ionization dynamics using differential mobility spectrometry: the curious case of 4-aminobenzoic acid. *Analytical Chemistry* **2012**, *84* (18), 7857-7864.
29. Campbell, J. L.; Yang, A. M.-C.; Melo, L. R.; Hopkins, W. S., Studying gas-phase interconversion of tautomers using differential mobility spectrometry. *Journal of The American Society for Mass Spectrometry* **2016**, *27* (7), 1277-1284.
30. Anwar, A.; Psutka, J.; Walker, S. W.; Dieckmann, T.; Janizewski, J. S.; Campbell, J. L.; Hopkins, W. S., Separating and probing tautomers of protonated nucleobases using differential mobility spectrometry. *International Journal of Mass Spectrometry* **2017**, *429*, 174-181.
31. Walker, S. W.; Mark, A. E.; Verbuyst, B.; Bogdanov, B.; Campbell, J. L.; Hopkins, W. S., Characterizing the Tautomers of Protonated Aniline Using Differential Mobility Spectrometry and Mass Spectrometry. *The Journal of Physical Chemistry A* **2018**, *122* (15), 3858-3865.
32. Papadopoulos, G.; Svendsen, A.; Boyarkin, O. V.; Rizzo, T. R., Conformational distribution of bradykinin [bk+ 2 H]²⁺ revealed by cold ion spectroscopy coupled with FAIMS. *Journal of the American Society for Mass Spectrometry* **2012**, *23* (7), 1173-1181.
33. Voronina, L.; Rizzo, T. R., Spectroscopic studies of kinetically trapped conformations in the gas phase: the case of triply protonated bradykinin. *Physical Chemistry Chemical Physics* **2015**, *17* (39), 25828-25836.
34. Coughlan, N. J.; Carr, P. J.; Walker, S. C.; Zhou, C.; Guna, M.; Campbell, J. L.; Hopkins, W. S., Measuring Electronic Spectra of Differential Mobility-Selected Ions in the Gas Phase. *Journal of the American Society for Mass Spectrometry* **2020**.
35. Berthias, F.; Maatoug, B.; Glish, G. L.; Moussa, F.; Maitre, P., Resolution and Assignment of Differential Ion Mobility Spectra of Sarcosine and Isomers. *Journal of The American Society for Mass Spectrometry* **2018**, *29* (4), 752-760.
36. Schindler, B.; Depland, A. D.; Renois-Predelus, G.; Karras, G.; Concina, B.; Celep, G.; Maurelli, J.; Loriot, V.; Constant, E.; Bredy, R.; Bordas, C.; Lépine, F.; Compagnon, I., FAIMS-MS-IR spectroscopy workflow: a multidimensional platform for the analysis of molecular isoforms. *International Journal for Ion Mobility Spectrometry* **2017**, *20* (3), 119-124.
37. Féraud, G.; Domenianni, L.; Marceca, E.; Dedonder-Lardeux, C.; Jouvét, C., Photodissociation Electronic Spectra of Cold Protonated Quinoline and Isoquinoline in the Gas Phase. *The Journal of Physical Chemistry A* **2017**, *121* (13), 2580-2587.
38. Hansen, C. S.; Blanksby, S. J.; Trevitt, A. J., Ultraviolet photodissociation action spectroscopy of gas-phase protonated quinoline and isoquinoline cations. *Physical Chemistry Chemical Physics* **2015**, *17* (39), 25882-25890.
39. Marchetti, B.; Karsili, T. N.; Ashfold, M. N.; Domcke, W., A 'bottom up', ab initio computational approach to understanding fundamental photophysical processes in nitrogen containing heterocycles, DNA bases and base pairs. *Physical Chemistry Chemical Physics* **2016**, *18* (30), 20007-20027.
40. Purves, R. W.; Guevremont, R., Electrospray ionization high-field asymmetric waveform ion mobility spectrometry– mass spectrometry. *Analytical Chemistry* **1999**, *71* (13), 2346-2357.
41. Hopkins, W. S., Determining the properties of gas-phase clusters. *Molecular Physics* **2015**, *113* (21), 3151-3158.
42. Liu, C.; Le Blanc, J. Y.; Shields, J.; Janiszewski, J. S.; Ieritano, C.; Gene, F. Y.; Hawes, G. F.; Hopkins, W. S.; Campbell, J. L., Using differential mobility spectrometry to

measure ion solvation: an examination of the roles of solvents and ionic structures in separating quinoline-based drugs. *Analyst* **2015**, *140* (20), 6897-6903.

43. Platt, J. R., Classification of spectra of cata-condensed hydrocarbons. *The Journal of Chemical Physics* **1949**, *17* (5), 484-495.

44. Loos, P.-F.; Scemama, A.; Jacquemin, D., The Quest for Highly Accurate Excitation Energies: A Computational Perspective. *The Journal of Physical Chemistry Letters* **2020**, *11* (6), 2374-2383.

45. Hasegawa, Y.; Amako, Y.; Azumi, H., The Ultraviolet Absorption Spectrum of Quinazoline Vapor Due to the n- π^* Transition. *Bulletin of the Chemical Society of Japan* **1968**, *41* (11), 2608-2611.

46. Glass, R.; Robertson, L.; Merritt, J., High-Resolution Electronic Absorption Spectra of Diazanaphthalenes in the Vapor Phase. *The Journal of Chemical Physics* **1970**, *53* (10), 3857-3863.

Chapter 4

Supporting Information

4.SI.1 Detailed Experimental

4.SI.1.1 Materials

Quinazoline (99% purity), methanol of HPLC grade and formic acid of LC/MS grade were purchased from Sigma Aldrich and used without further purification. Samples of 1 μ M quinazoline were prepared in methanol with 1% (v/v) formic acid.

4.SI.1.2 Cylindrical FAIMS-Photodissociation Action Spectroscopy

The field asymmetric waveform ion mobility spectrometry (FAIMS) coupled with photodissociation mass spectrometry equipment and methods have been previously outlined in detail.^{1,2} FAIMS experiments coupled with mass spectrometry were performed using a linear ion-trap mass spectrometry (LTQ XL Thermo Fisher Scientific) with a cylindrical geometry FAIMS attachment positioned between an ESI source and the linear ion-trap mass spectrometer. The process of ion separation by FAIMS has been described elsewhere.^{3,4} Ions are carried by a flow of inert gas between two electrodes across which an asymmetric voltage is applied, sequentially creating a “high-field” when a high voltage is applied and a “low-field” when a low voltage of opposite polarity is applied. Ions are laterally displaced (relative to the flow of ions) by their differences in high-field and low-field mobility. By applying a DC compensation voltage (CV) across the electrodes, the displacement of any ion can be selectively corrected allowing each trajectory, in turn, to be directed towards the inlet to the mass spectrometer for subsequent detection. Isomer populations resolved by the CV spectrum can then be isolated by m/z in the linear ion trap.

The FAIMS carrier gas was 100% N₂ at a flow rate of 3.5 L/min. Dispersion voltage was set to 5000 V. The outer electrode temperature was 70 °C and the inner electrode temperature was 90 °C. The ESI spray voltage was set to 4.5 kV.

As described by Julian and co-workers,⁵ the linear ion-trap mass spectrometer has been coupled with a Nd:YAG (Spectra-Physics QuantaRay INDI) laser generating third harmonic

(355 nm) light that pumps a mid-band optical parametric oscillator (OPO) (GWU-Lasertechnik Flexiscan) with a linewidth of ~ 7 cm⁻¹. Second harmonic generation (SHG) of the visible light OPO output allows access to 340-213 nm photons and sum frequency mixing (SFM) of 355 nm photons with visible light OPO output allows access to 390-300 nm photons. Laser powers ranged from 0.3 mJ to 1.5 mJ per laser pulse in the 340-213 nm (SHG) range and ranged from 1 mJ to 3 mJ per laser pulse in the 390-300 nm (SFM) range as recorded with a power meter (Gentec UP17P-6SW5).

To obtain a photodissociation action spectrum, an ion population was selected by CV and guided into the ion trap. These ions were *m/z* selected and subjected to a single laser pulse directed through the ion trap *via* a quartz window mounted on the back of the mass spectrometer vacuum housing. After one laser pulse, the ions are scanned out of the ion trap to record a mass spectrum. The photoproduct signal is reported as photoproduct intensity divided by the total ion count of the mass spectrum. Photoproduct signal is recorded over a range of 385-333 nm at a step size of 0.4 nm, (each step an average of 270 PD mass spectra when -3 CV was used or 113 mass spectra for -8 CV) and 244-222 nm at a step size of 0.2 nm (each step an average of 120 PD mass spectra) over the ranges of interest. The process of scanning the laser wavelength and timing with the mass spectrometry is controlled using a custom LABVIEW program (National Instruments) developed in-house. All action spectra were power normalised to the laser power spectrum.

4.SI.1.3 Computational Details.

Density functional theory (DFT), time dependent density functional theory (TDDFT) employing the CAM-B3LYP method,⁶ MP2,⁷⁻¹¹ and EOM-CCSD¹²⁻¹⁵ calculations were performed with the Gaussian16 program package,¹⁶ CC2¹⁷ calculations with the resolution of the identity approximation¹⁸ were performed with the TURBOMOLE (V7.2) package.¹⁹ DLPNO-CCSD(T)²⁰ calculations were performed with the ORCA (4.1.1) package.^{21, 22} CASSCF²³⁻²⁸ and MS-CASPT2^{29, 30} calculations were performed on the OpenMolcas software.³¹ All calculations employed the Dunning's aug-cc-pVDZ basis set.^{32, 33} The active space for both protomers included the full π system (five occupied π orbitals and five unoccupied π^* orbitals) as well as an occupied n orbital creating a (12,11) active space (see Figure 4.10). Vibronic Frank Condon simulations were calculated with PGOPHER³⁴ 7.1 using CASSCF geometries and normal modes with a 0.9 scaling factor at 300 K.

An imaginary level-shift of 0.2 au was employed for CASPT2 calculations to avoid the effects of intruder states. The core orbitals were frozen. CASSCF was used to initially optimise structures using a state averaged wave-function and this was used as the reference for subsequent CASPT2 calculations. CASPT2//CASSCF therefore corresponds to CASSCF geometries and frequencies with CASPT2 energies. All calculations were undertaken on the Australian National Computational Infrastructure (NCI).

4.SI.2 FAIMS Ionograms spectra with varying dispersion voltages

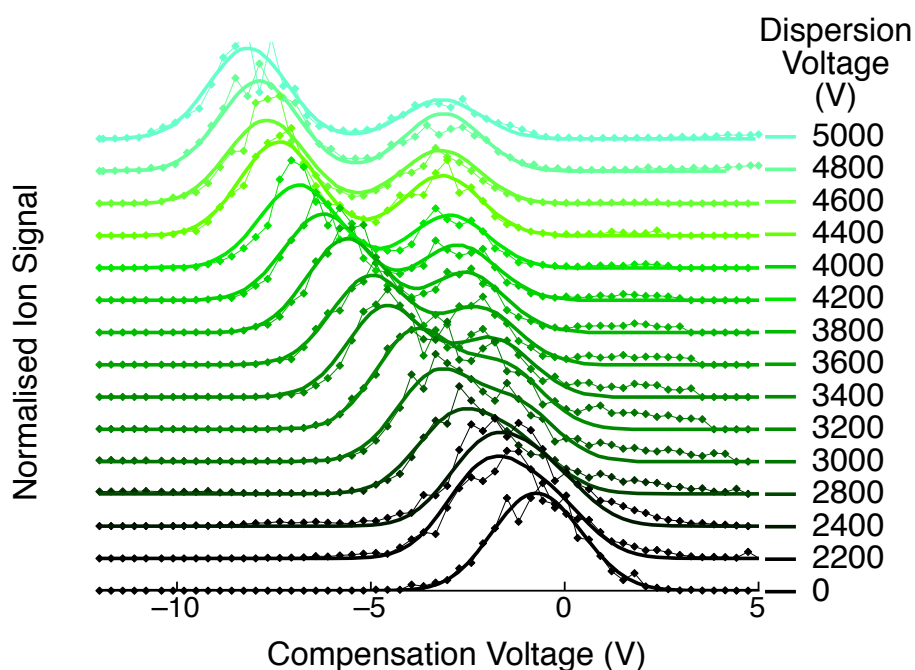


Figure 4.4: Change in FAIMS ionogram following QZH⁺ (m/z 131) with changing dispersion voltage.

4.SI.3 Photodissociation Mass Spectra

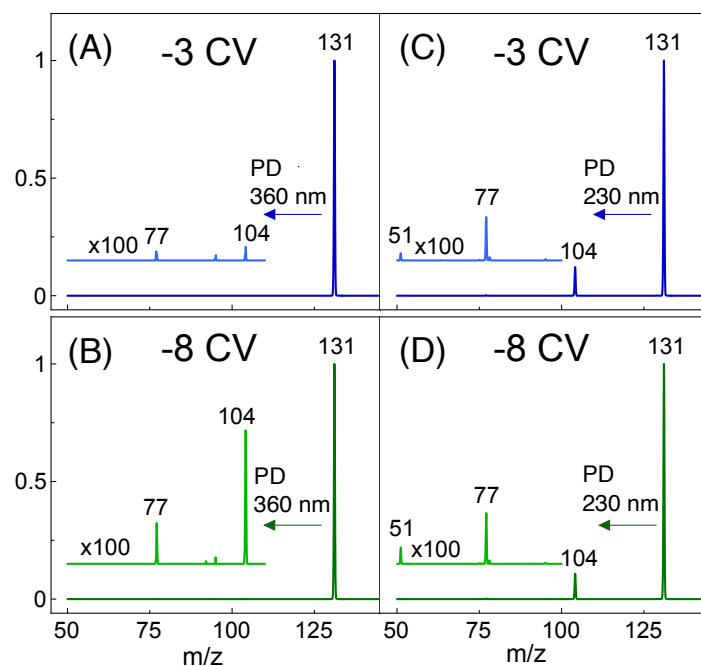


Figure 4.5: Photodissociation mass spectra of QZH⁺ at 360 nm (A and B) and 230 nm (C and D) where blue traces (top) correspond to -3 V compensation voltage (assigned as the 1QZH⁺ protomer) and green traces (bottom) -8 V compensation voltage (assigned as 3QZH⁺ protomer). The branching ratio of photoproducts (m/z 51: m/z 77: m/z 104) is 0.0:1.0:1.0 for 1QZH⁺ and 0.0:1.0:4.0 for 3QZH⁺ at 360 nm and 0.15:1.0:62.0 (1QZH⁺) and 0.3:1.0:48.0 (3QZH⁺) at 230 nm.

Single photon energy PD mass spectra of FAIMS separated QZH⁺ protomers acquired at PD wavelength 360 nm are shown in Figure 4.5 with CV values -3 V (A) and -8 V (B) and also at 230 nm with CV values -3 V (C) and -8 CV (D). These wavelengths correspond to excitation of QZH⁺ to the L_a (S₁) state and B_b (S₅) state, respectively. Following irradiation at 360 nm, both QZH⁺ protomers form product ions at m/z 104 and m/z 77 with the ion at m/z 95 assigned as subsequent H₂O addition (+18 Da) to the m/z 77 product ion. These product ions are also observed at 230 nm (Figures 4.5C and 4.5D) and one additional peak (m/z 51) is present but due to low ion signal, this product ion is not assigned. Figure 4.6 shows the energies of likely products including the low energy products benzonitrileH⁺ (m/z 104) + HCN and phenylium (m/z 77) + NC-CH=NH. Attempts to spectroscopically characterise the m/z 104 fragment from QZH⁺ ions compared to an authentic sample of protonated benzonitrile (m/z 104) were inconclusive (see Figure 4.7). At 230 nm, both protomers have similar m/z 104 and m/z 77

product ion intensities. However, at 360 nm, m/z 104 is the dominant photoproduct for protomer 3QZH⁺ while protomer 1QZH⁺ forms m/z 104 and m/z 77 in similar yields.

4.SI.4 Product Energies and Action Spectrum of Protonated Benzonitrile

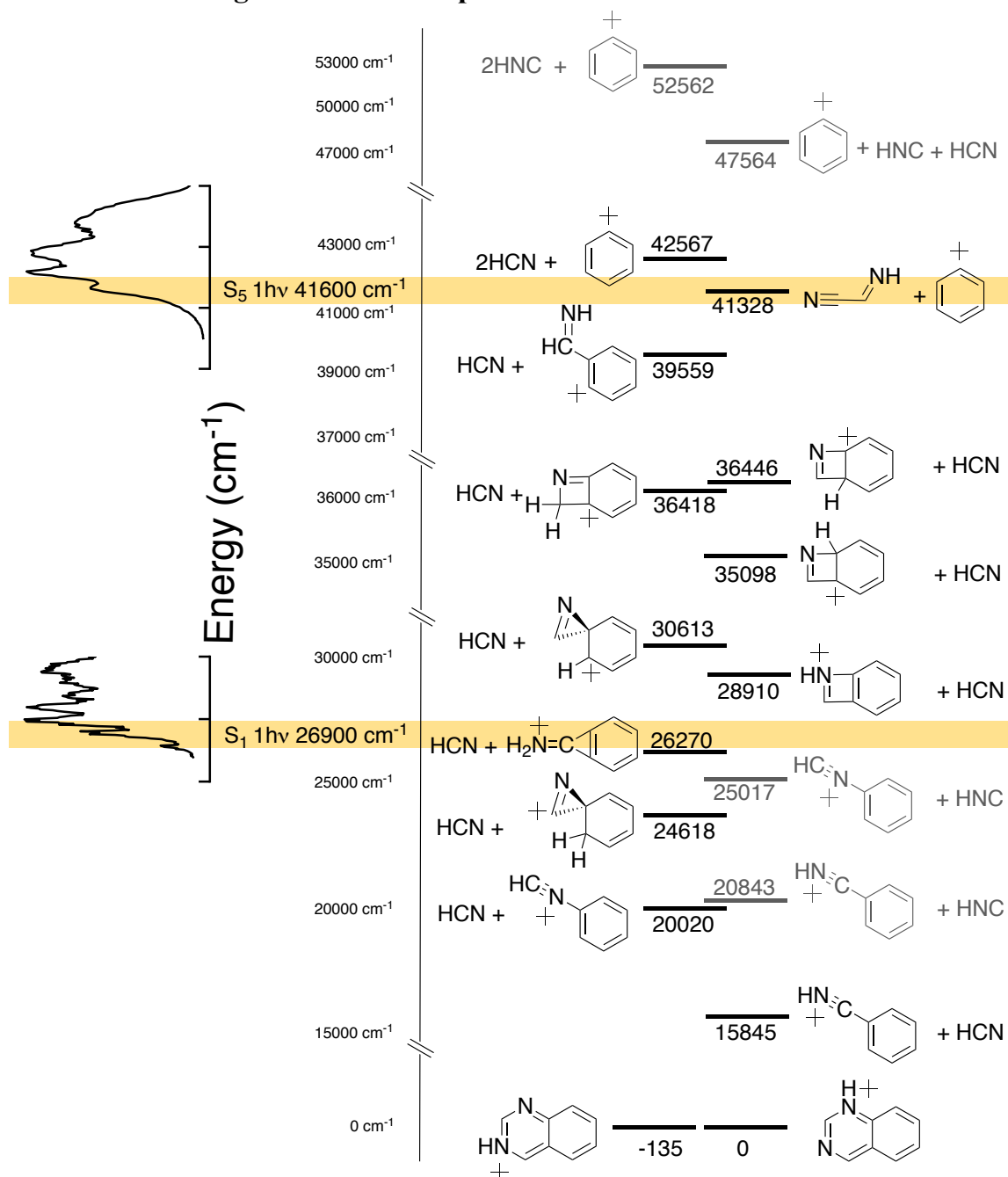


Figure 4.6: Photoproduct energies of most stable plausible m/z 104 and m/z 77 fragments. Energies calculated with DLPNO-CCSD(T)/aug-cc-pVDZ using MP2/aug-cc-pVDZ geometries and zero-point energy correction. Fragments shown in grey form hydrogen isocyanide. S₁ and S₅ photon energies (orange band) shown are origin energies for 3QZH⁺, which has a lower energy origin for both states and action spectra are plotted aligning with product energies.

Energies of possible photoproduct structures relative to the QZH⁺ protomers are shown in Figure 4.6 as calculated with DLPNO-CCSD(T)/aug-cc-pVDZ using MP2/aug-cc-pVDZ geometries and frequencies (Figure 4.6). These energies are compared with the energy of a single photon sufficient to access the L_a state of 3QZH⁺ (26,900 cm⁻¹), the B_b state (41,600 cm⁻¹). If the energy of the neutral fragment and product ion is less than that of a photon, then that product-fragment combination can plausibly be accessed with that photon type, however, entropic factors and barriers on the potential energy surface may block the pathways to low energy products. Formation of the *m/z* 104 photoproduct requires the dissociation of a 27 Da neutral fragment. This is assigned as either hydrogen cyanide (HCN) or hydrogen isocyanide (HNC). DLPNO-CCSD(T)/aug-cc-pVDZ//MP2/aug-cc-pVDZ calculates HCN to be 4,998 cm⁻¹ more energetically favoured than HNC. Formation of the *m/z* 77 photoproduct requires dissociation of either two 27 Da neutral fragments, or one 54 Da neutral fragment. The most energetically stable neutral loss is calculated to be NCCHNH followed by 2HCN. The lowest energy structure after loss of HCN (hydrogen cyanide) from QZH⁺ is protonated benzonitrile, followed by benzo-isonitrile. Both benzonitrile and benzo-isonitrile are lower in energy than the band origin of the ¹L_a ← ¹A₁ transition (to S₁) which is experimentally measured as 26,900 cm⁻¹; hence, formation of either product ion could be accessible with one photon. The relative energy of HNC (hydrogen isocyanide) with benzonitrile or benzo-isonitrile is lower than that of one 26,900 cm⁻¹ photon and could also be accessible. As the energy increases above 24000 cm⁻¹, the number of plausible structures quickly increases.

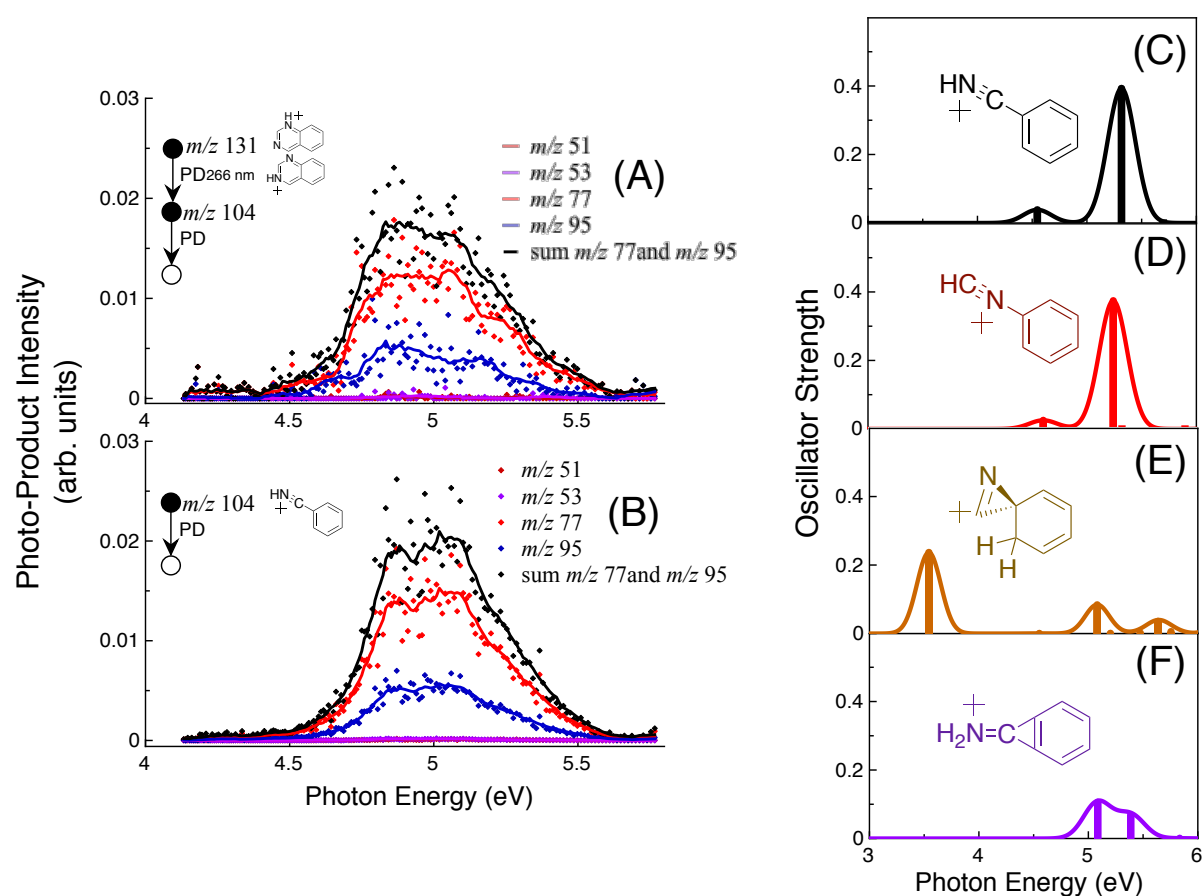


Figure 4.7: (A) PD action scan of the photo-product *m/z* 104 formed from PD of QZH⁺ protomers using 266 nm light. (B) PD action spectra of protonated benzonitrile. (C-F) EOM-CCSD/aug-cc-pVDZ vertical excitation energy calculations of the four lowest energy possible structures of the *m/z* 104 photo-product. The difference between the sum of the photo-product and HCN above QZH⁺ is shown in eV under each structure as calculated with DLPNO-CCSD(T)/aug-cc-pVDZ using MP2/aug-cc-pVDZ structures and frequencies.

Figures 4.7 A and 4.7 B show PD action spectra taken of protonated benzonitrile from an authentic sample compared with the *m/z* 104 fragment formed by photo-dissociating a copopulation of QZH⁺ protomers. Both protonated benzonitrile and the *m/z* 104 product formed from QZH⁺ both have a strong transition around 5.0 eV as well as a minor transition around 4.2 eV. Based on vertical transition energies for the three other lowest energy structures of *m/z* 104 (Figures 4.7 D-F as calculated with EOM-CCSD/aug-cc-pVDZ) and the broad spectra in Figure 4.7 A and B, populations of these fragments cannot be ruled out. Protonated benzonitrile (Figure 4.7 D) and the three-membered ring containing structure in Figure 4.7 E both have observable transitions which overlap with the transitions of protonated benzonitrile.

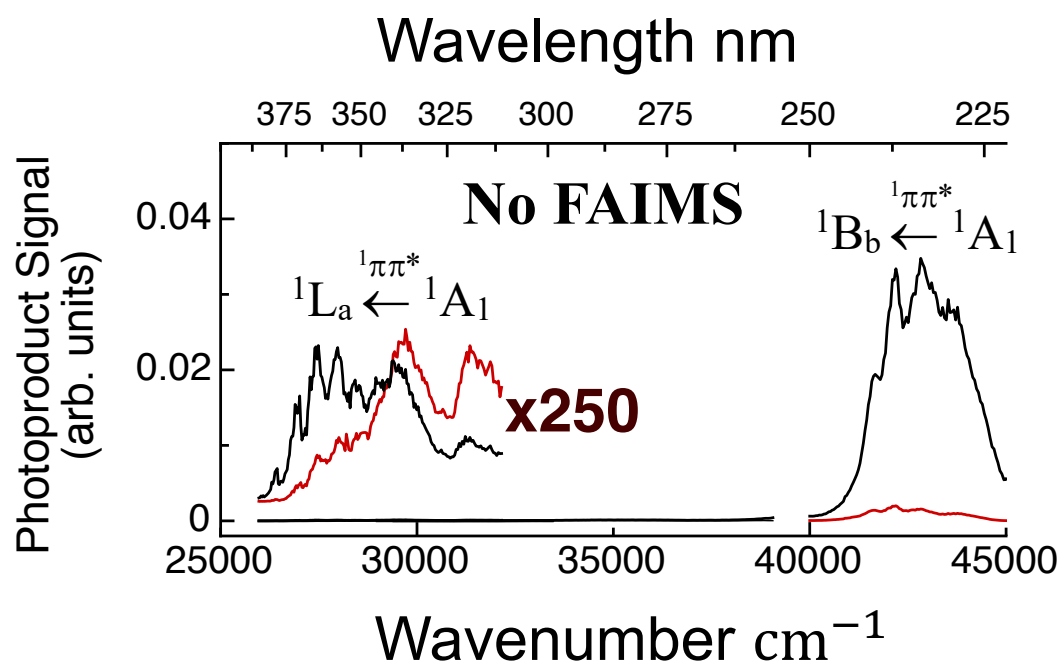
4.SI.5 QZH⁺ action spectrum without FAIMS separation

Figure 4.8: PD action spectra of QZH⁺ without FAIMS separation (both protomers present). Black trace follows formation of *m/z* 104 and red trace follows formation of *m/z* 77.

4.SI.6 Assignments of Transitions and Orbital Analysis

4.SI.6.1 CAM-B3LYP Orbitals

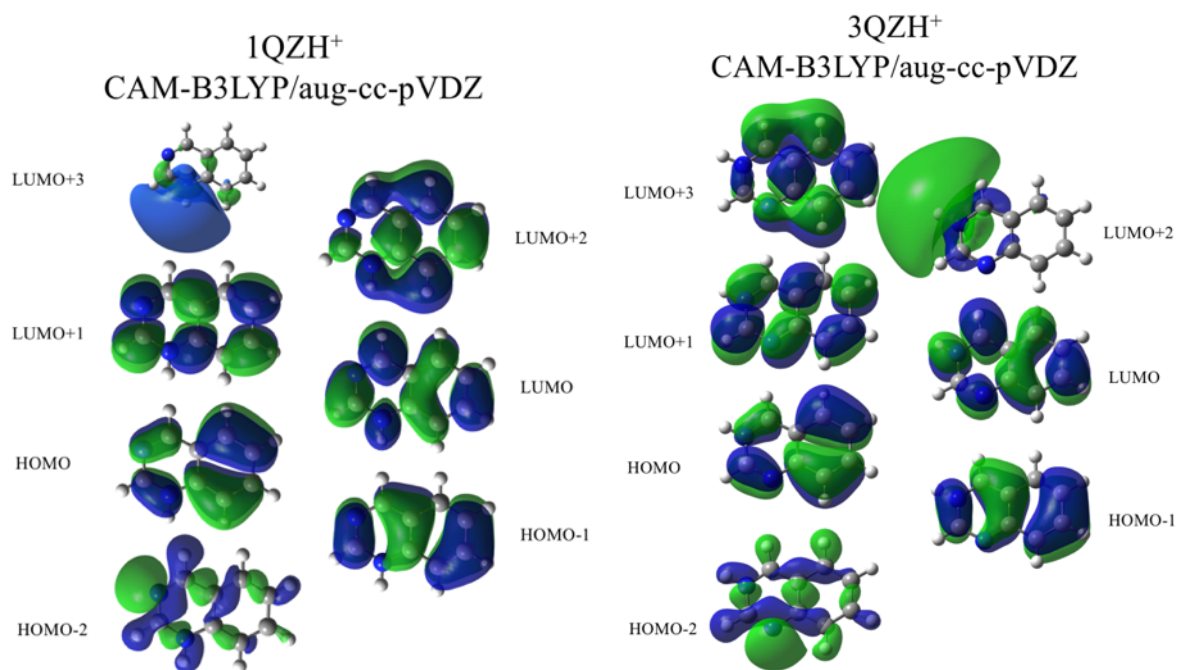


Figure 4.9: Molecular orbitals for 1QZH⁺ and 3QZH⁺ as calculated with CAM-B3LYP/aug-cc-pVDZ.

Table 4.3: Calculated vertical transition energies with key orbital contributions of 3QZH⁺ using CAM-B3LYP. H = HOMO, L = LUMO.

3QZH ⁺ Transition from S ₀ (¹ A ₁) to:	CAM-B3LYP Vertical Transition Energies (cm ⁻¹)	Oscillator Strength (f)	Orbitals Involved in Transition (TD-DFT)	Contribution of Orbital Transitions (%)
S₁ (¹L_a)	30993	0.040	L (π*) ← H (π) L+1 (π*) ← H-1 (π)	97 2
S ₂	36433	0.0010	L (π*) ← H-2 (n)	97
S ₃ (¹ L _b)	37699	0.016	L (π*) ← H-1 (π) L+1 (π*) ← H (π)	56 41
S ₄	42169	0.0016	L+1 (π*) ← H-2 (n)	95
S₅ (¹B_b)	46596	0.69	L (π*) ← H-1 (π) L+1 (π*) ← H (π) L+1 (π*) ← H-1 (π) L+2 (π*) ← H (π) L+2 (π*) ← H-1 (π)	39 46 6 5 2

Table 4.4: Calculated vertical transition energies with key orbital contributions of 1QZH⁺ using CAM-B3LYP. H = HOMO, L = LUMO.

1QZH ⁺ Transition from S ₀ (¹ A ₁) to:	CAM-B3LYP Vertical Transition Energies (cm ⁻¹)	Oscillator Strength (f)	Orbitals Involved in Transition (TD-DFT)	Contribution of Orbital Transitions (%)
S₁ (¹L_a)	32942	0.028	L (π*) ← H (π)	89
S ₂	33261	0.0002	L (π*) ← H-2 (n) L+2 (π*) ← H-2 (n)	95 3
S ₃ (¹ L _b)	37598	0.078	L (π*) ← H-1 (π) L+1 (π*) ← H (π)	72 25
S ₄	46300	0.0036	L+1 (π*) ← H-2 (n) L+10 (π*) ← H-2 (n)	92 4
S₅ (¹B_b)	47447	0.63	L (π*) ← H-1 (π) L+1 (π*) ← H (π) L+2 (π*) ← H-1 (π) L+2 (π*) ← H (π)	23 61 9 2

4.SI.6.2 MS-CASPT2//CASSCF Active Space

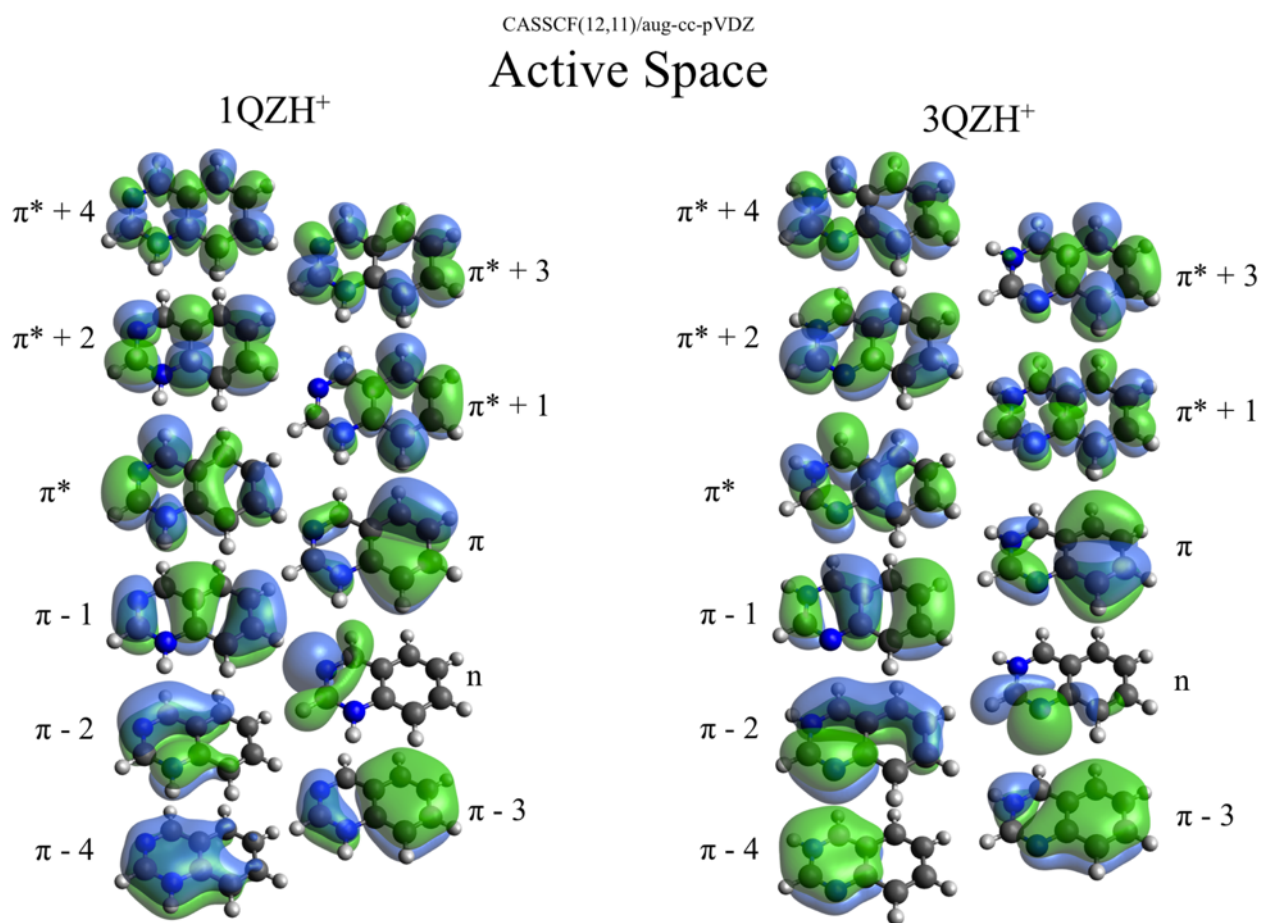


Figure 4.10: Active space of 1QZH⁺ and 3QZH⁺ used for CASSCF(12,11) and CASPT2(12,11) calculations.

4.SI.6.3 Transition Dipoles

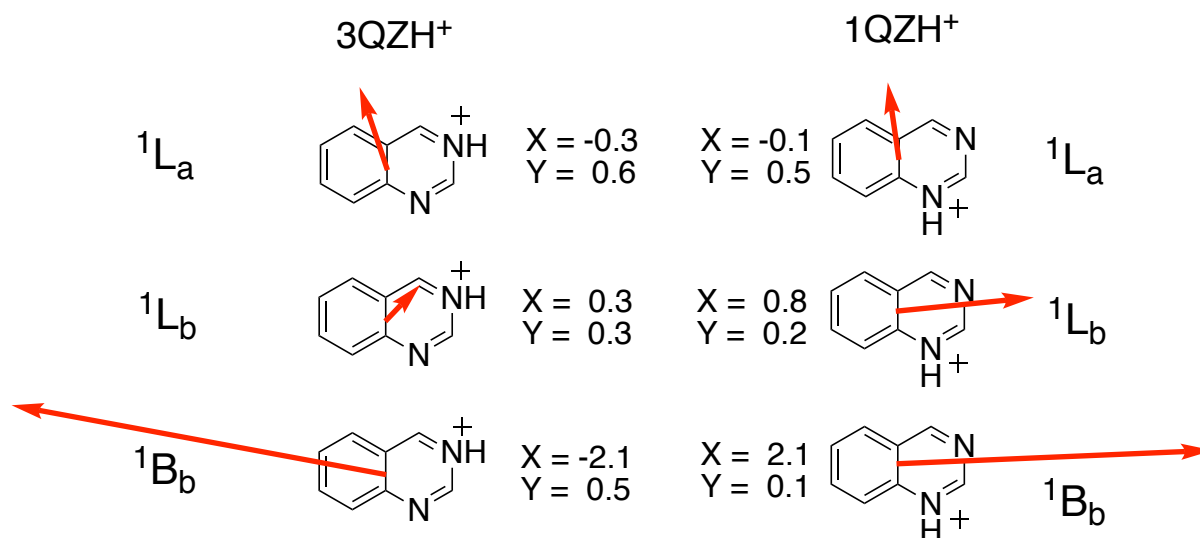


Figure 4.11: Transition dipole moments for the three lowest ¹ππ* transitions of QZH⁺ protomers as calculated with CAM-B3LYP.

4.SI.7 Laser Power Dependence

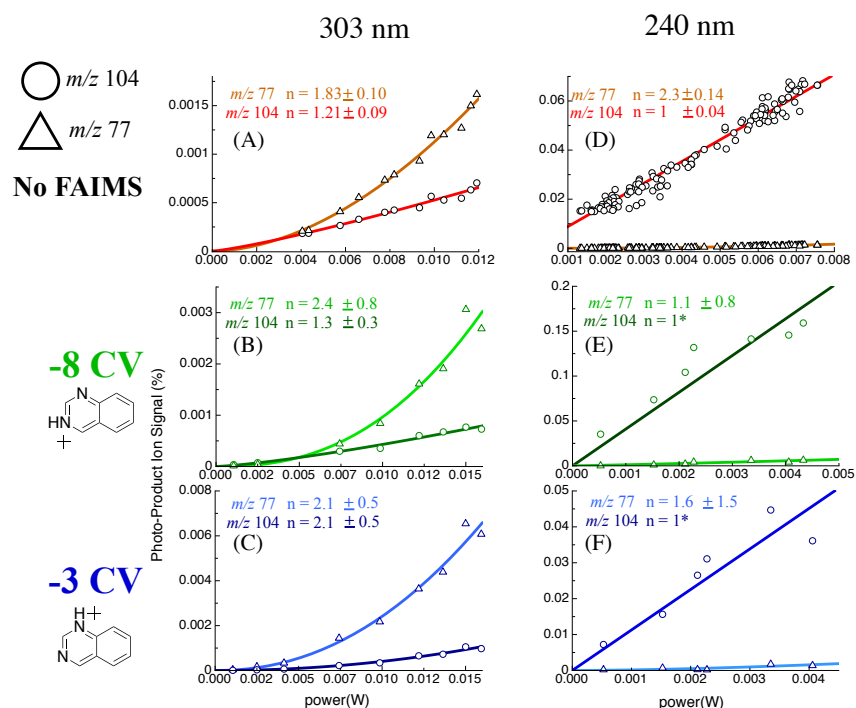


Figure 4.12: Laser power dependence of QZH⁺ at 303 nm (A) without FAIMS, (B) with -3 V compensation voltage, (C) with -8 V compensation voltage and at 240 nm (D) without FAIMS, (E) with -3 V compensation voltage, (F) with -8 V compensation voltage. Circles correspond to photoproduct signal of the *m/z* 104 photoproduct. Triangles correspond to photoproduct signal of the *m/z* 77 photoproduct. Light blue, light green and orange are fits of eq. 4.S1 to data following formation of the *m/z* 77 photoproduct. Dark blue, dark green and red lines are fits of eq. 4.S1 to data following formation of the *m/z* 104 photoproduct.

As laser power intensity (*I*) increases, the absorption (*A*) of an ion population will increase according to the relationship:³⁵

$$A \propto \sigma_1 I^1 + \sigma_2 I^2 + \sigma_3 I^3 + \dots \quad (\text{Equation 4.S1})$$

where σ_n values are the single photon absorption cross section (σ_1), two photon absorption cross section (σ_2), and so on. Fitting the data in equation 9 is fit with a function according to equation (4.S2):

$$y = \sigma I^n \quad (\text{Equation 4.S2})$$

Where *y* is the photoproduct ion signal, *I* is the laser power intensity and σ is a constant.

4.SI.8 Action Spectra with Vibronic Assignments

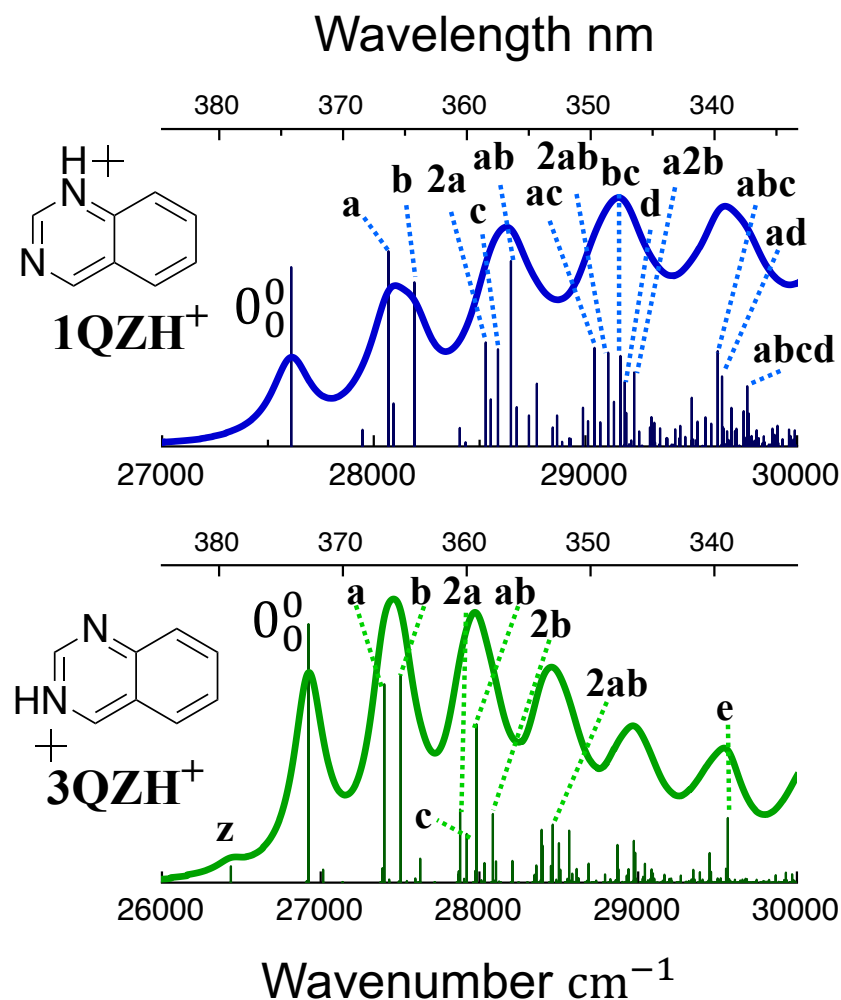


Figure 4.13: ¹L_a region of QZH⁺ including assignments of vibrational quanta. PD action spectra of (A) -8 V and (C) -3 V following the formation of *m/z* 104 (shown in (A) dark green and (C) dark blue) and *m/z* 77 (shown in (A) light green and (C) light blue). Franck-Condon simulations of vibronic transitions for (B) 3QZH⁺ and (D) 1QZH⁺. Calculations were performed using CASSCF(12,11) and vibrations are offset by a scaling factor of 0.90. Transitions are fit with Lorentzians of FWHM 220 cm⁻¹. See Figure 4.15 for vibrations.

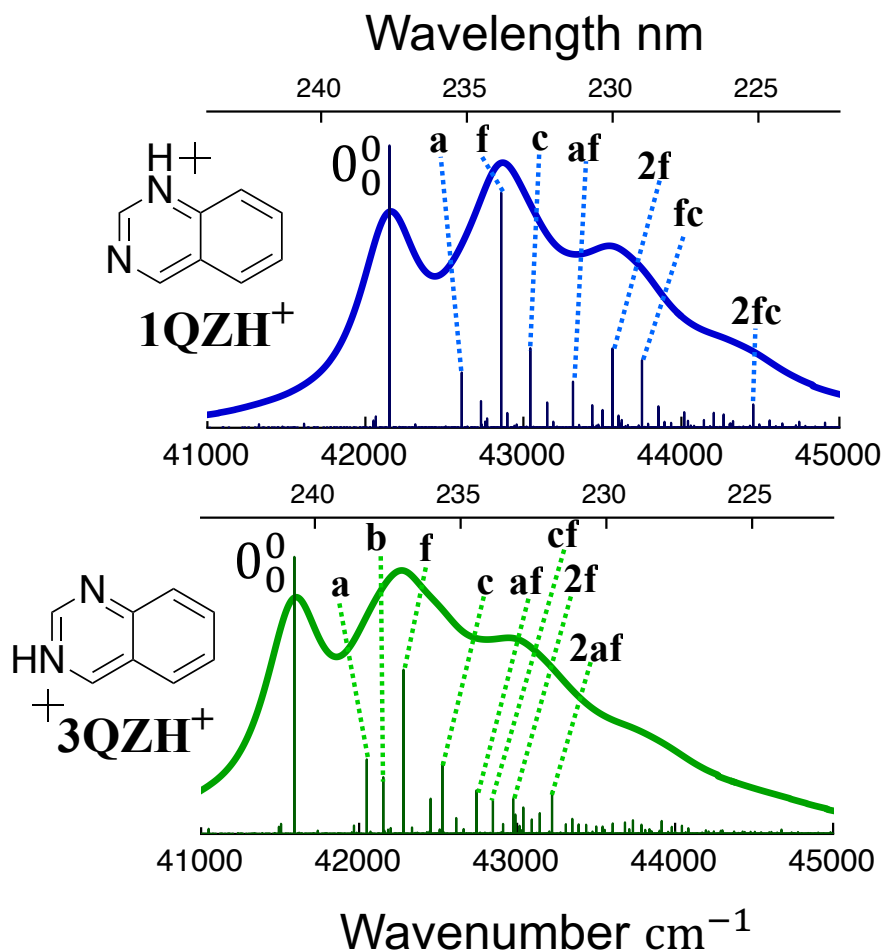


Figure 4.14: 1B_0 region of QZH^+ including assignments of vibrational quanta. PD action spectra of (A) -8 V and (C) -3 V following the formation of m/z 104 (shown in (A) dark green and (C) dark blue) and m/z 77 (shown in (A) light green and (C) light blue). Franck-Condon simulations of vibronic transitions for (B) $3QZH^+$ and (D) $1QZH^+$. Calculations were performed using CASSCF(12,11) and vibrations are offset by a scaling factor of 0.90. Transitions were fitted with Lorentzians of FWHM 440 cm^{-1} . See Figure 4.15 for vibrations.

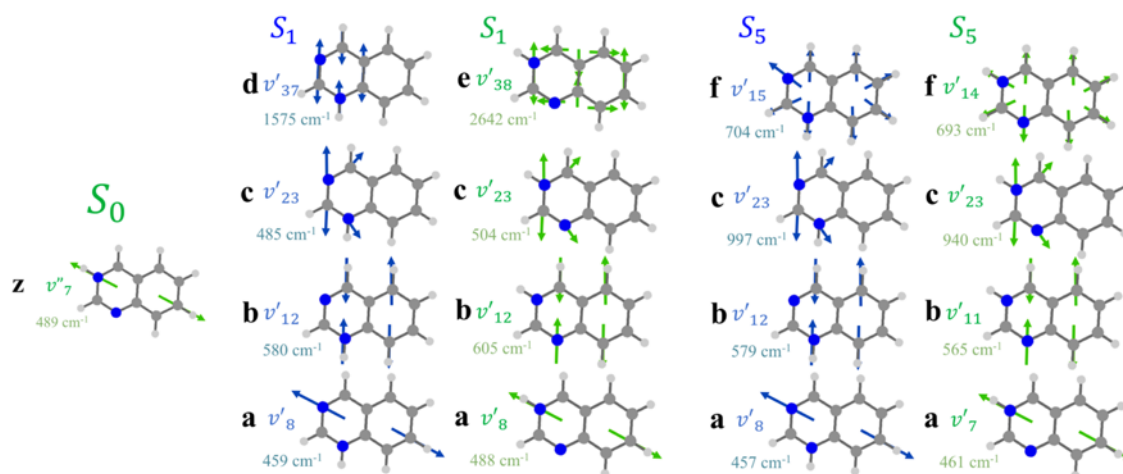


Figure 4.15: Schematic illustration of the optically active vibrational modes of QZH⁺ protomers with energies as calculated using CASSCF(12,11) with a scaling factor of 0.90.

4.SI.9 1QZH⁺ Characterisation of Imaginary Frequency Coordinate

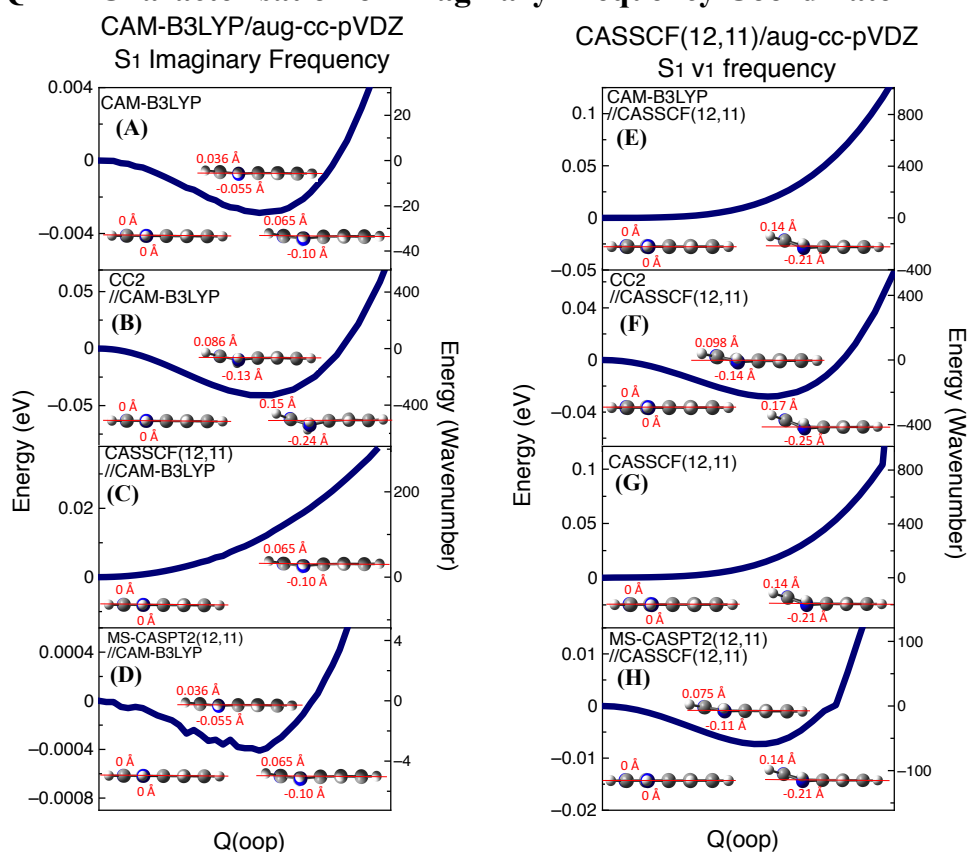


Figure 4.16: (A and E) CAM-B3LYP, (B and F) CC2, (C and G) CASSCF, and (D and H) MS-CASPT2 energies along the (left) CAM-B3LYP L_a imaginary frequency and along the (right) analogous out of plane vibration as calculated with CASSCF(12,11).

While CASSCF optimised to a planar C_s geometry, CAM-B3LYP optimised the ¹L_a state of 1QZH⁺ to a geometry with an imaginary frequency (see Figure 4.16). The imaginary frequency (*i*150 cm⁻¹) corresponds to a buckling of the C2 carbon and N3 nitrogen out of plane, breaking C_s symmetry and creating a prefulvenic, C₁ geometry. Extensive attempts to perform subsequent optimisations after slightly deforming the geometry along the coordinate of the negative frequency led to mixing between the state of interest and a nearby ¹nπ* dark state. Despite the discrepancy between methods concerning whether the ¹L_a excited state of 1QZH⁺ is a minimum (see Figure 4.16), the ZPE corrected 0-0 transition energies using C_s geometries provided excellent agreement to the experimental results in all cases (see Table 1 in main text) and there does not appear to be enough vibronic detail in the spectrum for an excited state double minimum to be observed experimentally. Besides, the Franck-Condon simulations in Figure 4.13 maintain the planar C_s symmetry and reproduce the experimental vibronic structure very well. Optimisations of the ¹L_a state of 3QZH⁺ using CASSCF and CAM-B3LYP converged to planar C_s geometries with all positive frequencies.

References

1. Hansen, C. S.; Kirk, B. B.; Blanksby, S. J.; O'Hair, R. A.; Trevitt, A. J., UV photodissociation action spectroscopy of haloanilinium ions in a linear quadrupole ion trap mass spectrometer. *Journal of the American Society for Mass Spectrometry* **2013**, *24* (6), 932-940.
2. Marlton, S. J.; McKinnon, B. I.; Ucur, B.; Maccarone, A. T.; Donald, W. A.; Blanksby, S. J.; Trevitt, A. J., Selecting and identifying gas-phase protonation isomers of nicotineH⁺ using combined laser, ion mobility and mass spectrometry techniques. *Faraday Discussions* **2019**, *217*, 453-475.
3. Buryakov, I.; Krylov, E.; Nazarov, E.; Rasulev, U. K., A new method of separation of multi-atomic ions by mobility at atmospheric pressure using a high-frequency amplitude-asymmetric strong electric field. *International Journal of Mass Spectrometry and Ion Processes* **1993**, *128* (3), 143-148.
4. Shvartsburg, A. A., *Differential ion mobility spectrometry: nonlinear ion transport and fundamentals of FAIMS*. CRC Press: 2008.
5. Ly, T.; Julian, R. R., Residue-specific radical-directed dissociation of whole proteins in the gas phase. *Journal of the American Chemical Society* **2008**, *130* (1), 351-358.
6. Yanai, T.; Tew, D. P.; Handy, N. C., A new hybrid exchange–correlation functional using the Coulomb-attenuating method (CAM-B3LYP). *Chemical Physics Letters* **2004**, *393* (1), 51-57.
7. Head-Gordon, M.; Pople, J. A.; Frisch, M. J., MP2 energy evaluation by direct methods. *Chemical Physics Letters* **1988**, *153* (6), 503-506.
8. Sæbø, S.; Almlöf, J., Avoiding the integral storage bottleneck in LCAO calculations of electron correlation. *Chemical Physics Letters* **1989**, *154* (1), 83-89.
9. Frisch, M. J.; Head-Gordon, M.; Pople, J. A., A direct MP2 gradient method. *Chemical Physics Letters* **1990**, *166* (3), 275-280.
10. Frisch, M. J.; Head-Gordon, M.; Pople, J. A., Semi-direct algorithms for the MP2 energy and gradient. *Chemical Physics Letters* **1990**, *166* (3), 281-289.
11. Head-Gordon, M.; Head-Gordon, T., Analytic MP2 frequencies without fifth-order storage. Theory and application to bifurcated hydrogen bonds in the water hexamer. *Chemical Physics Letters* **1994**, *220* (1-2), 122-128.
12. Koch, H.; Jørgensen, P., Coupled cluster response functions. *The Journal of Chemical Physics* **1990**, *93* (5), 3333-3344.
13. Stanton, J. F.; Bartlett, R. J., The equation of motion coupled-cluster method. A systematic biorthogonal approach to molecular excitation energies, transition probabilities, and excited state properties. *The Journal of Chemical Physics* **1993**, *98* (9), 7029-7039.
14. Koch, H.; Kobayashi, R.; Sanchez de Merás, A.; Jørgensen, P., Calculation of size-intensive transition moments from the coupled cluster singles and doubles linear response function. *The Journal of Chemical Physics* **1994**, *100* (6), 4393-4400.
15. Goings, J. J.; Caricato, M.; Frisch, M. J.; Li, X., Assessment of low-scaling approximations to the equation of motion coupled-cluster singles and doubles equations. *The Journal of Chemical Physics* **2014**, *141* (16), 164116.
16. Frisch, M. J.; Trucks, G. W.; Schlegel, H. B.; Scuseria, G. E.; Robb, M. A.; Cheeseman, J. R.; Scalmani, G.; Barone, V.; Petersson, G. A.; Nakatsuji, H.; Li, X.; Caricato, M.; Marenich, A. V.; Bloino, J.; Janesko, B. G.; Gomperts, R.; Mennucci, B.; Hratchian, H. P.; Ortiz, J. V.; Izmaylov, A. F.; Sonnenberg, J. L.; Williams-Young, D.; Ding, F.; Lipparini, F.; Egidi, F.; Goings, J.; Peng, B.; Petrone, A.; Henderson, T.; Ranasinghe, D.; Zakrzewski, V. G.; Gao, J.; Rega, N.; Zheng, G.; Liang, W.; Hada, M.;

Ehara, M.; Toyota, K.; Fukuda, R.; Hasegawa, J.; Ishida, M.; Nakajima, T.; Honda, Y.; Kitao, O.; Nakai, H.; Vreven, T.; Throssell, K.; Montgomery Jr., J. A.; Peralta, J. E.; Ogliaro, F.; Bearpark, M. J.; Heyd, J. J.; Brothers, E. N.; Kudin, K. N.; Staroverov, V. N.; Keith, T. A.; Kobayashi, R.; Normand, J.; Raghavachari, K.; Rendell, A. P.; Burant, J. C.; Iyengar, S. S.; Tomasi, J.; Cossi, M.; Millam, J. M.; Klene, M.; Adamo, C.; Cammi, R.; Ochterski, J. W.; Martin, R. L.; Morokuma, K.; Farkas, O.; Foresman, J. B.; Fox, D. J. *Gaussian 16*, Wallingford, CT, 2016.

17. Christiansen, O.; Koch, H.; Jørgensen, P., The second-order approximate coupled cluster singles and doubles model CC2. *Chemical Physics Letters* **1995**, *243* (5-6), 409-418.
18. Hättig, C.; Weigend, F., CC2 excitation energy calculations on large molecules using the resolution of the identity approximation. *The Journal of Chemical Physics* **2000**, *113* (13), 5154-5161.
19. TURBOMOLE V7.2 2017, a development of University of Karlsruhe and Forschungszentrum Karlsruhe GmbH, 1989-2009, TURBOMOLE GmbH, since 2007; available from <http://www.turbomole.com>.
20. Riplinger, C.; Neese, F., An efficient and near linear scaling pair natural orbital based local coupled cluster method. *The Journal of chemical physics* **2013**, *138* (3), 034106.
21. Neese, F., The ORCA program system. *Wiley Interdisciplinary Reviews: Computational Molecular Science* **2012**, *2* (1), 73-78.
22. Neese, F., Software update: the ORCA program system, version 4.0. *Wiley Interdisciplinary Reviews: Computational Molecular Science* **2018**, *8* (1), e1327.
23. Hegarty, D.; Robb, M. A., Application of unitary group methods to configuration interaction calculations. *Molecular Physics* **1979**, *38* (6), 1795-1812.
24. Eade, R. H.; Robb, M. A., Direct minimization in mc scf theory. The quasi-newton method. *Chemical Physics Letters* **1981**, *83* (2), 362-368.
25. Schlegel, H. B.; Robb, M. A., MC SCF gradient optimization of the H₂CO→H₂+CO transition structure. *Chemical Physics Letters* **1982**, *93* (1), 43-46.
26. Bernardi, F.; Bottoni, A.; McDouall, J. J.; Robb, M. A.; Schlegel, H. B. In *MCSCF gradient calculation of transition structures in organic reactions*, Faraday Symposia of the Chemical Society, Royal Society of Chemistry: 1984; pp 137-147.
27. Frisch, M.; Ragazos, I. N.; Robb, M. A.; Schlegel, H. B., An evaluation of three direct MC-SCF procedures. *Chemical Physics Letters* **1992**, *189* (6), 524-528.
28. Yamamoto, N.; Vreven, T.; Robb, M. A.; Frisch, M. J.; Schlegel, H. B., A direct derivative MC-SCF procedure. *Chemical Physics Letters* **1996**, *250* (3-4), 373-378.
29. Andersson, K.; Malmqvist, P. A.; Roos, B. O.; Sadlej, A. J.; Wolinski, K., Second-order perturbation theory with a CASSCF reference function. *Journal of Physical Chemistry* **1990**, *94* (14), 5483-5488.
30. Andersson, K.; Malmqvist, P. Å.; Roos, B. O., Second-order perturbation theory with a complete active space self-consistent field reference function. *The Journal of Chemical Physics* **1992**, *96* (2), 1218-1226.
31. Fdez. Galván, I.; Vacher, M.; Alavi, A.; Angeli, C.; Aquilante, F.; Autschbach, J.; Bao, J. J.; Bokarev, S. I.; Bogdanov, N. A.; Carlson, R. K., OpenMolcas: From source code to insight. *Journal of Chemical Theory and Computation* **2019**, *15* (11), 5925-5964.
32. Dunning Jr, T. H., Gaussian basis sets for use in correlated molecular calculations. I. The atoms boron through neon and hydrogen. *The Journal of Chemical Physics* **1989**, *90* (2), 1007-1023.
33. Woon, D. E.; Dunning Jr, T. H., Gaussian basis sets for use in correlated molecular calculations. III. The atoms aluminum through argon. *The Journal of Chemical Physics* **1993**, *98* (2), 1358-1371.

Chapter 4: QuinazolineH⁺ Supporting Information

34. Western, C. M., PGOPHER: A program for simulating rotational, vibrational and electronic spectra. *Journal of Quantitative Spectroscopy and Radiative Transfer* **2017**, *186*, 221-242.
35. Bhawalkar, J.; He, G.; Prasad, P., Nonlinear multiphoton processes in organic and polymeric materials. *Reports on Progress in Physics* **1996**, *59* (9), 1041.

This page has been intentionally left blank.

PROTOMERS OF NICOTINEH⁺

5. NicotineH⁺

This chapter discusses the separation and spectroscopy of nicotine⁺ protomers. The contents are reproduced verbatim from the peer-reviewed and publication:

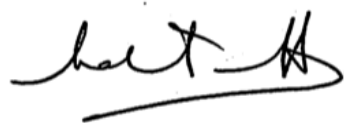
Marlton, S.J., McKinnon, B.I., Ucur, B., Maccarone, A.T., Donald, W.A., Blanksby, S.J. and Trevitt, A.J., 2019. Selecting and identifying gas-phase protonation isomers of nicotineH⁺ using combined laser, ion mobility and mass spectrometry techniques. *Faraday discussions*, 217, pp.453-475.

Author Contributions

S.J.P Marlton performed all calculations and experiments presented in this work. S.J.P Marlton prepared the manuscript with input from all authors. B McKinnon contributed to data analyses as well as the conception and implementation of the computational strategy. B, Ucur contributed to development and implementation of the cylindrical FAIMS experimental method. A,T, Maccarone contributed instrumentation setup and interpretation of the linear DMS experimental method.

Certification

I, Prof. Adam J. Trevitt, as Samuel J. P. Marlton's primary supervisor, and the principal investigator for this project, agree with and certify the author contributions described above.



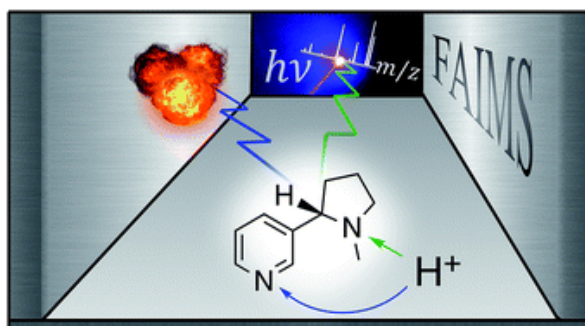
Adam J. Trevitt

07/12/2021

5.1 Abstract

The detection and assignment of protonation isomers, or protomers, of gas-phase ions remains a challenge in mass spectrometry. With the emergence of ion-mobility techniques combined with tuneable-laser photodissociation spectroscopy, new experimental combinations are possible to now meet this challenge. In this paper, the differences in fragmentation and electronic spectroscopy of singly protonated (*S*)-nicotine (nicH⁺) ions are analysed using action spectroscopy in the ultraviolet region and field asymmetric ion mobility spectrometry (FAIMS). Experiments are supported by quantum chemical calculations (DFT, TD-DFT and CC2) of both spectroscopic and thermochemical properties.

ESI of (*S*)-nicotine from different solvents leads to different populations of two nicH⁺ protomers corresponding to protonation on the pyridine nitrogen and pyrrolidine nitrogen, respectively. FAIMS gives partial resolution of these protomers and enables characteristic product ions to be identified for each isomer as verified directly by analysis of product-ion specific action spectroscopy. It is shown that while characteristic, these product ions are not exclusive to each protomer. Calculations of vertical electronic transitions assist in rationalising the photodissociation action spectra. The integration of photodissociation action spectroscopy with FAIMS-mass spectrometry is anticipated to be a useful approach for separating and assigning protonation isomers of many other small molecular ions.



5.2 Introduction

Detection and assignment of protonation site isomers (protomers) generated by electrospray ionisation (ESI) is a challenge for mass spectrometry. Not only are protomers isomers—and therefore unable to be mass-resolved by mass spectrometry—changes in ESI conditions are observed to affect relative protomer populations.¹⁻¹⁴ This can be an analytical problem when protomers dissociate to different product ions under activation, a phenomenon that can confound assignment by comparison to reference spectra. Differences in the photodissociation of protomers have been used to assign protomer populations,¹⁰⁻²⁶ although it is difficult to predict how the electronic spectroscopy and photodissociation will be affected by differences in protonation site. Hence, analysing the photodissociation of selected protomers, can provide insights into the effects of protonation on excited quantum states of ions while progressing towards the use of photo-dissociation as a method to disambiguate and assign protomers.

Previous studies have taken advantage of the differences in photoactivity of protomers and made assignments by comparing theoretical transition simulations to experimental results obtained by UV photodissociation action spectroscopy,^{13-17, 24, 25} or IRMPD.^{10, 11, 18-23} Dessent and co-workers have demonstrated the potential for moderate-resolution UV action spectra, coupled with TD-DFT analysis, to detect and assign protomers of nicotinamide and *p*-aminobenzoic acid.^{12, 26} These studies reported different action spectrum profiles of O-protonated or N-protonated isomers. To further explore this technique, we investigate two N-protonated protomers of (*S*)-nicotine, in which the pyridine nitrogen or the pyrrolidine nitrogen atoms are protonated.

(*S*)-Nicotine is the bioactive agonist in tobacco²⁷ and it is suggested that the bioactive form of (*S*)-nicotine is singly protonated on the pyrrolidine nitrogen. This bioactivity arises as the cationic quaternary amino nitrogen is chemically similar to the cationic quaternary amino nitrogen of acetylcholine.^{28, 29} Its bioactivity manifests when pyrrolidine protonated (*S*)-nicotine binds to the neuronal acetylcholine receptors in the brain.²⁸⁻³⁰ At physiological pH, (*S*)-nicotine is singly protonated. As an interesting aside, cigarettes and electronic cigarettes³¹ vaporise nicotine using different mechanisms and El Hellani *et al.* suggest that analytical studies do not adequately consider whether nicotine is sampled as a neutral species as a singly- or doubly- protonated ion.³²

Theoretical studies have predicted that both protomers of (*S*)-nicotine are likely present in the gas phase^{28, 33, 34} and this is supported by experiment.^{21, 28, 35} Product ions arising from collision induced dissociation (CID) have been explained to arise from either nicH⁺ protonated on the pyridine nitrogen (PYRO-nicH⁺) or pyrrolidine nitrogen (PYRI-nicH⁺).³⁵ What is unclear from CID studies however, is whether both protomers are present in the gas phase or whether tautomerisation proceeds dissociation upon CID. An IRMPD spectrum of gas phase nicH⁺ provided experimental evidence for the presence of PYRI-nicH⁺, however, the presence or absence of PYRO-nicH⁺ could not be confirmed.²¹ By comparing experimental gas-phase basicity measurements to theoretical predictions, it was estimated that protomers formed in approximately a 2:1 ratio of PYRO-nicH⁺:PYRI-nicH⁺ from gas phase proton-transfer equilibrium between a (*S*)-nicotine and several reference compounds.²⁸ Because of the differences between formation of nicH⁺ through proton-transfer and formation by ESI, it is difficult to predict whether the 2:1 ratio will translate to ESI and how solvent conditions might modulate protomer populations in the gas phase.

Several theoretical studies are reported on neutral and protonated (*S*)-nicotine. These include the calculation of optimised ground-state structures and energies for isolated nicH⁺,^{21, 28, 33, 34} and solution-phase nicH⁺.^{28, 33} Calculations uniformly predict the presence of both protomers of nicH⁺ in the gas-phase.^{21, 28, 33, 34} Although the electronic transitions of neutral (*S*)-nicotine have also been calculated at high levels of theory,³⁶ an analysis of the gas-phase electronic transitions of nicH⁺ is absent from the literature.

The photo-stability and absorption properties of neutral (*S*)-nicotine have been subjected to several studies over several decades, including IR,³⁷ electron-induced dissociation³⁸ and UV absorption spectra of solution phase (*S*)-nicotine in various protonated forms.³⁹⁻⁴¹ To our knowledge, there are no reported UV photodissociation studies of singly protonated (*S*)-nicotine in the literature.

For various ions, relative protomer populations have been obtained by comparing relative ion signal after separation using ion mobility mass spectrometry (IMS).^{2, 7, 9, 11, 42-45} The preponderance of these studies have employed classical drift-IMS (or closely related traveling-wave variants) that separate ions based on different collision-cross sections in a uniform electric field. In contrast, field asymmetric waveform ion mobility spectrometry (FAIMS) differs from drift-IMS in that, while drift-IMS typically separates ions depending on their ion

mobility in the direction of ion flow, FAIMS separates species depending on both their high- and low-field ion mobility in fields applied orthogonal to the direction of ion transmission. FAIMS has proven to be a powerful tool for separating and analysing protomer populations at atmospheric pressure prior to detection by mass spectrometry.^{1, 4, 6, 8, 46} Relative-energy calculations are typically coupled with FAIMS analysis to rationalise experimental results. However, it has been shown that theoretical results cannot reliably predict the relative protomer populations generated by ESI. For example, protomer populations can be shifted by changing ESI conditions¹⁻¹⁴ and less stable isomers can be kinetically trapped by the ESI process.^{4, 6, 9, 47, 48} Furthermore, the relative energies of protomers can depend strongly on different levels of theory and basis sets, which can result in the prediction of different lowest energy protomers using different computational approaches.^{14, 49} Here, we report the integration of FAIMS, ion-trap mass spectrometry and UVPD action spectroscopy to detect and assign the protonation isomers of protonated nicotine generated from ESI.

5.3 Experimental

5.3.1 Materials

(*S*)-Nicotine sample of ($\geq 99\%$ purity), acetonitrile, methanol and formic acid of LC/MS grade were purchased from Sigma Aldrich and used without further purification. Samples 1 μM (*S*)-nicotine were prepared in either methanol or acetonitrile with 1% (v/v) formic acid.

5.3.2 Cylindrical FAIMS-Mass Spectrometry

Field asymmetric waveform ion mobility spectrometry (FAIMS) experiments coupled with mass spectrometry were performed using a linear ion-trap mass spectrometer (LTQ XL Thermo Fischer Scientific) with a cylindrical geometry FAIMS attachment (Thermo Fischer Scientific). The FAIMS electrodes are positioned between the ESI source and the inlet transfer capillary of the mass spectrometer. The FAIMS carrier gas was 50 % N₂ and 50 % He at a total flow rate of 3.5 L/min. The dispersion voltage was set to -5000 V. The compensation voltage (CV) was scanned from -30 to -7 V at a step size of 0.3 V. The outer electrode temperature was 90 °C and the inner electrode temperature was 70 °C. The ESI spray voltage was set to 6 kV. The underlying process of ion separation by FAIMS has been described in detail elsewhere.^{50, 51} Briefly, a gas flow carries ions through two electrodes across which an asymmetric voltage alternating between high and low voltage of opposite polarity is applied. Due to their

differences in high-field and low-field ion mobility, ions are separated on laterally displaced trajectories. By scanning a DC compensation voltage (CV) across the electrodes, these displacements can be selectively corrected allowing each trajectory, in turn, to be directed towards the inlet to the mass spectrometer for subsequent detection. With the ion-trap mass spectrometer set to detect a mass-to-charge (m/z) population of interest, a CV scan can provide details of isomer populations—protonation isomers are targeted in this study—by resolving subsequent populations in the CV spectrum. It is noted that this FAIMS geometry is designed to enhanced ion transmission efficiency, compared to planar-FAIMS (see below), but with some sacrificed resolution.⁵²⁻⁵⁴

5.3.3 Planar-FAIMS-Mass Spectrometry

Additional FAIMS experiments were performed on a commercial triple-quadrupole mass spectrometer (SCIEX 5500) equipped with a pair of planar FAIMS electrodes (SCIEX SelexION); herein referred to as planar-FAIMS. Planar FAIMS geometries tend to offer better mobility resolution at the expense of transmission.⁵²⁻⁵⁴ The conditions were as follows: the separation voltage (SV) was set to 4500 V, the compensation voltage (CV) was scanned from -3 to 20 V at a step size of 0.1 V. The DMS temperature was set at 150 °C, DMS offset was set at a value of -3 V, nitrogen was used as a transport gas. IonSpray Voltage was set to 5500 V, the source temperature was 32 °C the curtain gas pressure was set to 20 psi, nebulizing gas pressure of 15 psi, source gas 2 was set to zero, declustering potential was set to 150 V and nitrogen was used as a collision gas with the collision energy parameter set to 2. Although there is no laser photodissociation capabilities on this platform so only CID activation is reported, planar-FAIMS instruments have higher resolution and peak capacity than cylindrical-FAIMS.

5.3.4 Photodissociation Action Spectroscopy

The photo-dissociation action spectroscopy equipment and methods used here have been described in detail elsewhere and will only be outlined briefly.⁵⁵ Experiments were performed on a linear quadrupole ion trap mass spectrometer (Thermo Fisher Scientific LTQ XL), that has been modified to permit photodissociation experiments as described by Julian and co-workers.⁵⁶ This instrument is coupled to a tuneable laser system comprising a Nd:YAG (Spectra-Physics QuantaRay INDI) laser generating third harmonic (355 nm) light that pumps a mid-band optical parametric oscillator (OPO) (GWU-Lasertechnik FlexiScan) with a linewidth of ~ 7 cm⁻¹. Second harmonic generation (SHG) of the visible light OPO output

allows access to 305-213 nm photons. Laser powers typically ranged from 0.5 mJ to 1.5 mJ per pulse within this region, recorded with a power meter (Gentec UP17P-6SW5).

To obtain a photodissociation action spectrum, m/z -selected ions are subjected to a single laser pulse which is directed through the ion trap via a quartz window mounted on the back of the mass spectrometer vacuum housing. This laser pulse overlaps the trapped ion population with very good efficiency.⁵⁷ After one laser pulse, the ions are scanned out of the ion trap to record a mass spectrum. The photofragment signal is reported as photofragment intensity divided by the total ion count of the mass spectrum. The photofragment signal is recorded over a range of wavelength values (305-213 nm) at a set step size (1 nm), each step taking approximately ninety PD mass spectra, *i.e.*, 90 laser shots at one per mass spectrum. The process of scanning the laser wavelength and controlling the mass spectrometry is controlled using a custom LABVIEW program (National Instruments) developed in-house. All action spectra were power normalised to the laser power spectrum. For power dependence experiments, a power attenuator (STANDA 10MVAA) was installed in the beam path of a 266 nm set wavelength Nd:YAG laser (Continuum, MINILITE) and the linear response to power at this wavelength is included in the supporting information (Figure S7).

5.3.5 Computational Details

All calculations were performed with the Gaussian16 program package,⁵⁸ with the exception of CC2 calculations which were performed with the TURBOMOLE (V7.2) package⁵⁹ on the Australian National Computational Infrastructure. Density functional theory (DFT) and time dependant density functional theory (TD-DFT) calculations utilised several methods and the aug-cc-pVDZ basis set.^{60, 61} Conformational minima of (*S*)-nicotine were located using M06-2X⁶² by optimising the *cis* and *trans* forms of both protomers then deforming and scanning the pyrrolidine dihedral labelled ν_2 shown in Figure 5.10. The χ dihedral angle of each of the minima was subsequently scanned and optimised. Conformers found with M06-2X were re-optimised using CAM-B3LYP⁶³ and ω B97X-D⁶⁴ and these optimised structures were used to calculate the vertical electronic transition energies. Further analysis with the CC2 method utilised the cc-pVDZ basis set.^{60, 61} The lowest energy conformer for each protomer (as calculated with M06-2X) was re-optimised using MP2.⁶⁵⁻⁶⁹ These geometries were used to calculate vertical excitation energies with the CC2 method⁷⁰ which employ the resolution-of-the-identity approximation.⁷¹

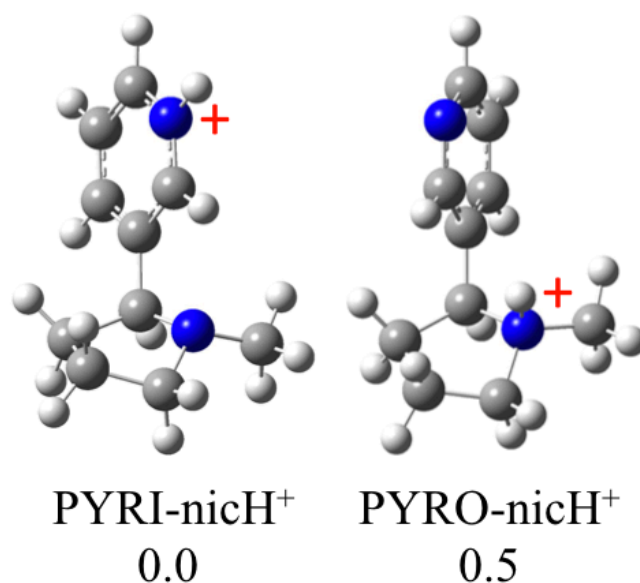


Figure 5.1: Optimised structures for the lowest energy conformers of the two protomers of nicH⁺. Their relative energies are given in kcal/mol as calculated using M06-2X/aug-cc-pVDZ.

5.4 Results and Discussion

5.4.1 Calculations

Optimised structures for the electronic (S_0) ground-state nicH⁺ were first located using the M06-2X method and subsequently optimised using both CAM-B3LYP and ω B97X-D with the aug-cc-pVDZ basis set in all cases. Results indicate that both the pyrrolidine nitrogen and pyridine nitrogen are energetically plausible protonation sites for singly protonated (*S*)-nicotine (see Table 5.3 and 5.4) as the minimum structure and conformation in each case differ by only 0.5 kcal/mol, in favour of pyridine-protonation (Figure 1), which is in accord with the 0.45 kcal/mol calculated by Yoshida *et al.* using MP2/6-31G(d,p).³⁴ Previous theoretical studies using B3LYP calculated proton affinity differences and free energy differences of less than 3 kcal/mol between protomers.^{28, 33}

It is well known that proton affinity is an oversimplified predictor for ESI generated gas-phase protomer populations, and this is well evidenced by reports showing that protomer populations can vary drastically with ESI and source conditions.^{3, 12-14, 25, 26} Furthermore, cases are reported that show predictions with different computational methods can scramble the order of proton affinities, thus making it tricky to confidently predict the most stable gas-phase protomer.^{13, 14,}
⁴⁹ Therefore, for mass spectrometry, experimental tools that detect and assign protonation isomers are vital for validation of computational methods.

As is discussed later, the computational predictions of two optically-active electronic transitions for PYRO-nicH⁺ and PYRI-nicH⁺ aid in the assignment of the action spectra. Conformational variations do not affect the assignments as the transition energies remain essentially consistent over several conformation scans (see Figure 5.12). It is therefore sufficient here to consider the global minimum conformation of each protomer in the analysis of photodissociation action spectra.

5.4.2 Photodissociation and Collision-Induced Dissociation

The PD and CID mass spectra of nicH⁺ (m/z 163), without FAIMS selection, are shown in Figure 5.2. Several of these product ions have been assigned to be characteristic of a particular protomer based on mechanistic arguments which are summarised below.³⁵ As will be explained in more detail, the characteristic product ions targeted in this study are m/z 84 and m/z 80 for the PYRI-nicH⁺ protomer and m/z 132 and m/z 130 for the PYRO-nicH⁺ protomer. For these product mass spectra in Figure 5.2, the same product ions are detected for both CID and PD methods, but since PD provides a more uniform distribution of abundance across these product ions, in particular by enhancing key product ions, only PD product spectra used herein (unless otherwise noted).

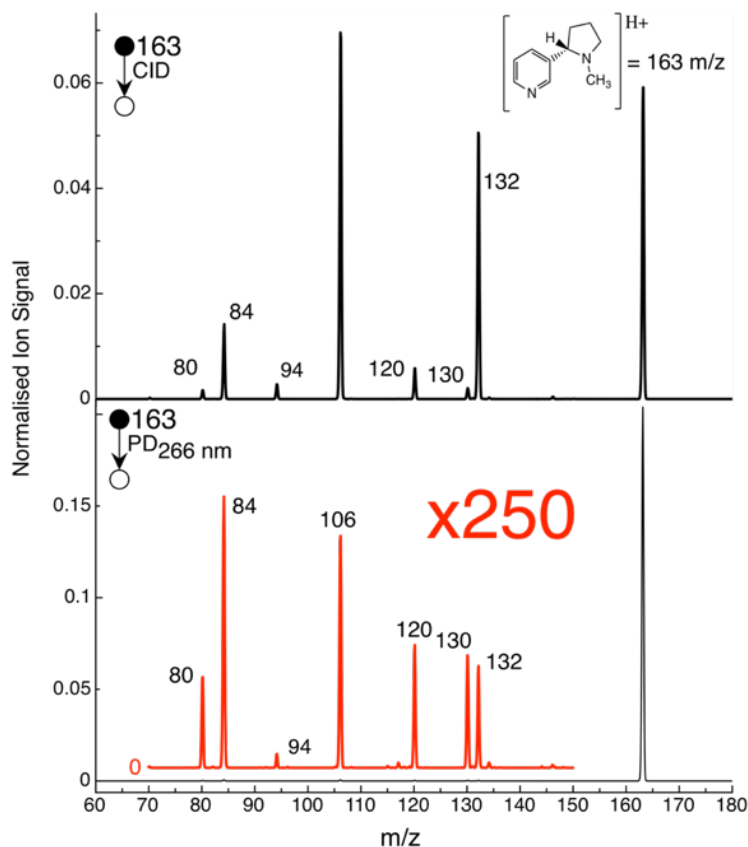


Figure 5.2: (top) The CID and (bottom) PD ($\lambda=266$ nm) product mass spectra of nicH^+ (m/z 163). Spectra are normalised to the total ion count.

The links between individual product ions of nicH^+ to precursor protomers have been explored by previous groups.³⁵ Product ions m/z 84 and m/z 80 have been assigned to the PYRI- nicH^+ precursor ion product ions at and m/z 117, m/z 130 and m/z 132 product ions have been assigned to the PYRO- nicH^+ precursor ion. The product ion at m/z 106 has been assigned to the PYRO- nicH^+ precursor ion, but as will be shown here, it appears to be formed from both protomers. Although some mechanistic explanation does exist, a comprehensive computational analysis would be useful to better explore the mechanism leading to each product ion.

Variations in relative protomer populations will result in changes in the relative populations of characteristic product ions and studies have documented that protomer population can be altered by changing the ESI solvent.^{1, 10-12} In this context, Figure 5.3A plots PD (266 nm) mass spectra of nicH^+ acquired from either methanol or acetonitrile as the ESI solvent. In Figure 5.3B, the difference mass spectrum of the two mass spectra in Figure 5.3A is shown, in which positive peaks are enhanced in the case of methanol as the ESI solvent and negative peaks are enhanced with acetonitrile. The m/z 84 and m/z 80 product ions—which are the purported

characteristic products for the PYRI-nicH⁺ protomer—are favoured in methanol relative to acetonitrile while the opposite is true for the *m/z* 132 and 130 product ions purportedly characteristic products of PYRO-nicH⁺. Thus, the PYRI-nicH⁺ protomer appears to be significantly enhanced using methanol as an ESI solvent and PYRO-nicH⁺ is enhanced with acetonitrile. There remains a question whether these pairs of characteristic product ions are exclusive to each protomer. To explore this, one would need to isolate pure populations of each protomer within the ion trap, for subsequent activation and analysis, and thus complete separation of these isomers is desired.

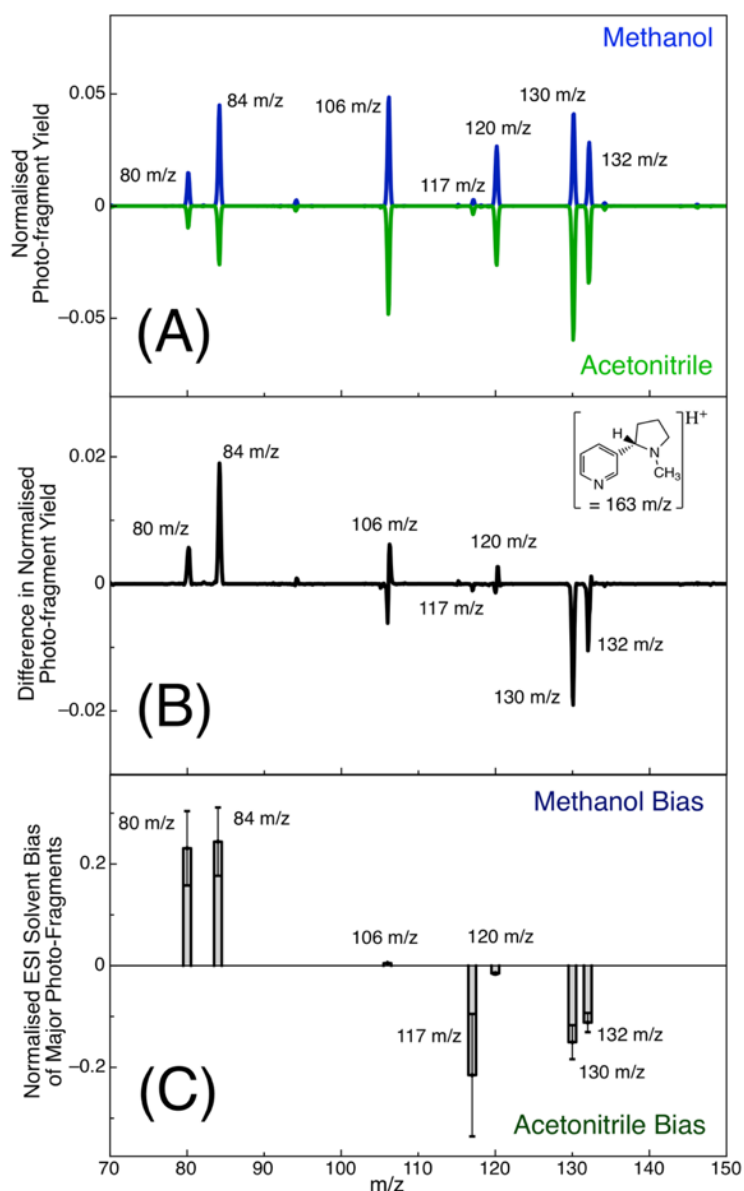


Figure 5.3: (A) The PD (266 nm) spectrum of nicH⁺ with methanol (blue line) and acetonitrile (green line) as the ESI solvent. (B) A difference spectrum (methanol – acetonitrile). (C) Bias calculated for the seven major photoproduct ions as calculated using Eq. (5.1).

To better quantify the link between product ions and protomers, bias values, as defined by Equation 5.1 were calculated.

$$\text{BIAS} = \frac{I_{\text{MeOH}} - I_{\text{ACN}}}{I_{\text{MeOH}} + I_{\text{ACN}}} \quad (\text{Eq.5.1})$$

Bias values are used to quantify the proportional change of product ion populations between mass spectra taken under two different sets of conditions, as the difference in fragment intensity between two mass spectra (such as that plotted in Figure 5.3B) does not clearly communicate the relative magnitude of change in ion population. Bias as defined here by Eq. 5.1, where I_{ACN} is the signal of a fragment using acetonitrile as an ESI solvent and I_{MeOH} is the signal intensity from the same peak using methanol as the ESI solvent. Mass spectra are normalised to their total product ion count before respective I values are calculated. In this case, Bias values will therefore be 1 if the product ion is only detected with methanol as the ESI solvent and, at the other extreme, will be -1 if the product ion is only detected when acetonitrile is used. If a bias value of a fragment is 0 then the abundance of that ion is the same in both experiments. Bias values for the two ESI solvent spectra are plotted for the seven most abundant product ions in Figure 5.3C. The product ions with the strongest methanol bias are m/z 84 and m/z 80, which are characteristic of PYRI-nicH⁺. The product ions with the strongest acetonitrile bias are m/z 132, m/z 130 and m/z 117 and are characteristic of PYRO-nicH⁺. Despite the m/z 117 product ion having a low abundance compared to other products (Figure 3A), it has a relatively large acetonitrile bias (-0.2 ± 0.1), albeit with a large uncertainty. In contrast, product ions at m/z 106 and m/z 120 high signal intensity compared to other products yet are rather insensitive to ESI solvent with bias values of -0.0048 ± 0.0003 and 0.15 ± 0.03 , respectively. These findings suggest that this pair of product ions are likely common to both protomers.

5.4.3 Action Spectroscopy

To date, the assignment of characteristic product ions to respective protomers of nicH⁺ emanates from mechanistic arguments in the literature.³⁵ While it is true that there is no major controversy surrounding these assignments, although we have reported above that m/z 106 responds as a common product ion, no direct evidence exists that supports these protomer assignments, thus, a direct measure of spectroscopic signatures would fulfil this requirement. Using UVPD action spectroscopy, the photoproduct yield of the m/z 132 product ion (green

line) and the m/z 84 product ion (blue line) are shown in Figure 5.4. Acetonitrile is used as the ESI solvent in Figure 5.4A, whereas methanol was used in Figure 5.4B.

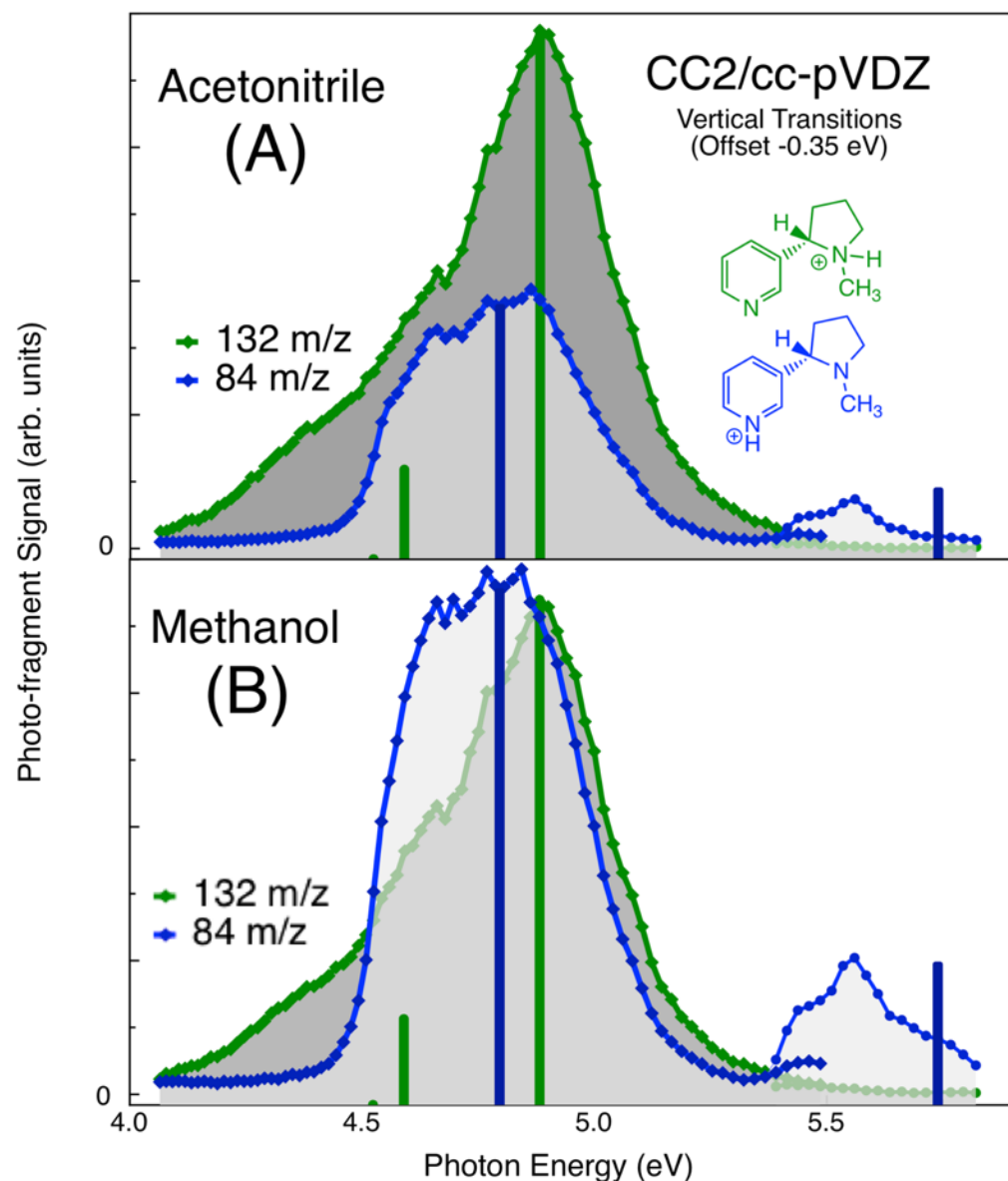


Figure 5.4: UVPD action spectra of nicH^+ generated by (A) ESI from acetonitrile with 1% formic acid and (B) methanol with 1% formic acid. The spectra follow the signal of the m/z 84 product ion (blue trace) and the m/z 132 product ion (green trace). Vertical bars represent vertical transition energies as calculated with CC2/cc-pVDZ based on geometries optimised with MP2/cc-pVDZ for PYRI- nicH^+ (blue bars) and PYRO- nicH^+ (green bars). Calculated transitions are all offset by -0.35 eV relative to their predicted values. Additional scans over the high energy portion of the spectra (*ca.* 5.5 eV) are appended to both (A) and (B).

The UVPD trace following formation of the m/z 132 product ion (green trace in Figure 5.4) shows a strong transition centred at approximately 4.9 eV but there is a tailing-shoulder on the low-energy side of this main peak. This shoulder is distinct from the action spectrum following the m/z 84 fragment (blue trace in Figure 5.4), which reveals a strong band centred around 4.8

eV but essentially no signal between 4 and 4.4 eV. Also notable is a weak feature centred around 5.5 eV for the m/z 84 product-ion. Additional scans over this feature were performed and are added to both (A) and (B) in Figure 5.4 (blue circles). These scans confirm that this high-energy band is almost exclusive to the m/z 84 product ion. Two general features, (i) signal—or otherwise—between 4.0-4.4 eV and (ii) the high-energy feature centred at 5.5 eV, appear to discriminate between the two protomers. Comparing the two solvent cases (A and B in Figure 5.4), the relative abundance of the product ions changes but the general peak shape of the respective fragment ions remains the same.

5.4.4 Action Spectroscopy Compared to Calculations

Ground state DFT and MP2 as well as excited-state TD-DFT and CC2 calculations were performed to rationalise the differences in the UVPD action spectra of nicH⁺ protomers. The CC2 and CAM-B3LYP predictions are listed in Table 5.1 (PYRO-nicH⁺) and Table 5.2 (PYRI-nicH⁺), which also includes the orbital and state analysis for CAM-B3LYP. Other TD-DFT (M06-2X and ω B97X-D) predictions are shown in Figure 5.13 and included in Tables S3 and S4 and these are generally in accord with the CAM-B3LYP results. Natural transition orbital (NTO) analysis was performed with CAM-B3LYP, the output of which is shown in Figure 5.5. We predominantly discuss the CC2 and CAM-B3LYP output here.

The vertical electronic excitation energies of PYRO-nicH⁺ (green) and PYRI-nicH⁺ (blue) calculated by the CC2 method, and shifted by -0.35 eV to align with the main features in the experimental spectra, are plotted in Figure 5.4 along with the experimental spectra. The computational predictions were uniformly shifted by -0.35 eV to align with the main features in the experimental data. It was observed by Kulesza *et al.* that CC2 calculations accurately predict vertical transition energies, as compared with experimental PD action spectroscopy of cations, while TD-DFT overestimates these energies by approximately 0.5 eV.⁷² Although we note that it can be somewhat subjective to assign the “vertical transition energy” from an experimental spectrum, there is little doubt that CC2 offers significant improvement on transition energy predictions in many published studies of aromatic ions.^{13, 73} For the CAM-B3LYP method, comparisons are generally good with -0.5 eV shift applied to the predicted values. Many attempts to optimise excited states geometries, to obtain adiabatic (0-0) transition energies, were unsuccessful due to state mixing between the optical bright states and lower-lying dark states. It should be noted that different basis sets were utilised for the CC2 (cc-

pVDZ) and TD-DFT (aug-cc-pVDZ) methods and warrants further investigation and comparison.

For the PYRO-nicH⁺ protomer, all computational methods predict a strong transition at around 5.23 - 5.52 eV, corresponding to the S₃←S₀ transition for all methods, and a relatively weaker transition at around 4.46 - 4.95 eV corresponding to the S₁←S₀ transition for the TD-DFT methods and S₂←S₀ in the case of CC2. Together these transitions manifest in the experimental action spectrum following the evolution of *m/z* 132 in the form of a major peak with a shoulder on the red-side as followed in the green trace in Figure 5.4, both A and B. A very strong transition is predicted at 6.45 eV (6.13 eV for CAM-B3LYP) but is not observed in the experimental spectra and is probably just outside of the experimental window when considering the aforementioned -0.35 eV and -0.5 eV shifts.

Table 5.1: Calculated vertical transition energies and key orbitals for the (*W*, *trans*, *anti*) PYRO-nicH⁺ using CC2/cc-pVDZ and CAM-B3LYP/aug-cc-pVDZ. H = HOMO and L = LUMO.

PYRO-nicH ⁺ State:	CC2 Transition Energies (eV)	CC2 Oscillator Strength (f)	CAM-B3LYP Transition Energies (eV)	CAM-B3LYP Oscillator Strength (f)	CAM-B3LYP Orbitals	CAM-B3LYP Contribution (%)
S ₁	4.87	0.00001	4.89	0.0036	L← H	60
					L+1← H	4
					L+2← H	30
					L+3← H	2
S ₂	4.94	0.0035	5.02	0.0001	L← H	3
					L+1← H	90
S ₃	5.23	0.021	5.52	0.04	L+1← H-2	26
					L← H-1	48
					L+2← H-1	21
S ₄	6.45	0.97	6.13	0.063	L← H-2	12
					L+2← H-2	5
					L+1← H-1	78
S ₅	7.23	0.70	6.74	0.0115	L← H	30
					L+2← H	47
					L+3← H	6
					L+5← H	7

For PYRI-nicH⁺, a strong transition is predicted around 5.15 - 5.19 eV which corresponds to the S₃←S₀ transition for all methods and this is assigned to the major peak in the *m/z* 84 action spectrum in Figure 5.4 (both A and B). The higher energy transition centred around 5.5 eV in Figure 5.4 is assigned to the S₄←S₀ for the CC2 method but assigned as the S₅←S₀ for the TD-DFT methods.

Table 5.2: Calculated vertical transition energies and key orbitals for (*S*, *trans*, *anti*) PYRI-nicH⁺ using CC2/cc-pVDZ and CAM-B3LYP/aug-cc-pVDZ. H = HOMO and L = LUMO.

PYRI-nicH ⁺ State:	CC2 Transition Energies (eV)	CC2 Oscillator Strength (f)	CAM-B3LYP Transition Energies (eV)	CAM-B3LYP Oscillator Strength (f)	CAM-B3LYP Orbitals	CAM-B3LYP Contribution (%)
S ₁	3.29	0.00006	3.27	0.0005	L ← H	98
S ₂	4.27	0.0006	4.31	0.0014	L+1 ← H	96
S ₃	5.15	0.11	5.19	0.13	L ← H-4	4
					L+1 ← H-4	3
S ₄	6.09	0.029	5.81	0.0004	L+1 ← H-1	87
					L+2 ← H	77
					L+4 ← H	15
S ₅	6.62	0.0092	6.04	0.012	L ← H-5	9
					L ← H-4	40
					L ← H-1	4
					L+1 ← H-1	39

Natural transition orbitals (NTO)⁷⁴ are a way of rationalising electronic transitions and thus NTOs calculated with CAM-B3LYP/aug-cc-pVDZ are presented in Figure 5.5 and can be compared with the results in Tables 1 and 2. Using this method it is evident that both protomers have an S₃←S₀ transition of π*←π character and these transitions have the highest oscillator strength within this part of the UV spectrum but a major difference is the evidence for charge transfer in the S₃ ← S₀ for the PYRI-nicH⁺ protomer. The feature on the red edge of the PYRO-

nicH⁺ action spectrum, assigned to the S₁←S₀ transition (S₂←S₀ for CC2), and has π*←n character and by inspection is reminiscent of the π*←n (S₁←S₀) for neutral pyridine. This transition is assigned to the shoulder observed *m/z* 132 product action spectra in Figure 5.4. Pyridine protonation, PYRI-nicH⁺, eliminates this π*←n transition and therefore no analogous transition is present in this case.

The high-energy feature of PYRI-nicH⁺ is assigned to the S₅ ← S₀ transition (S₄ ← S₀ for CC2) has mostly π*←π character associated with the pyridine ring but with some charge-transfer (CT), as shown in Figure 5.5. The presence of charge-transfer character in the PYRI-nicH⁺ case dramatically increases the oscillator strength relative to all other relevant transitions in this energy range (Table 2).

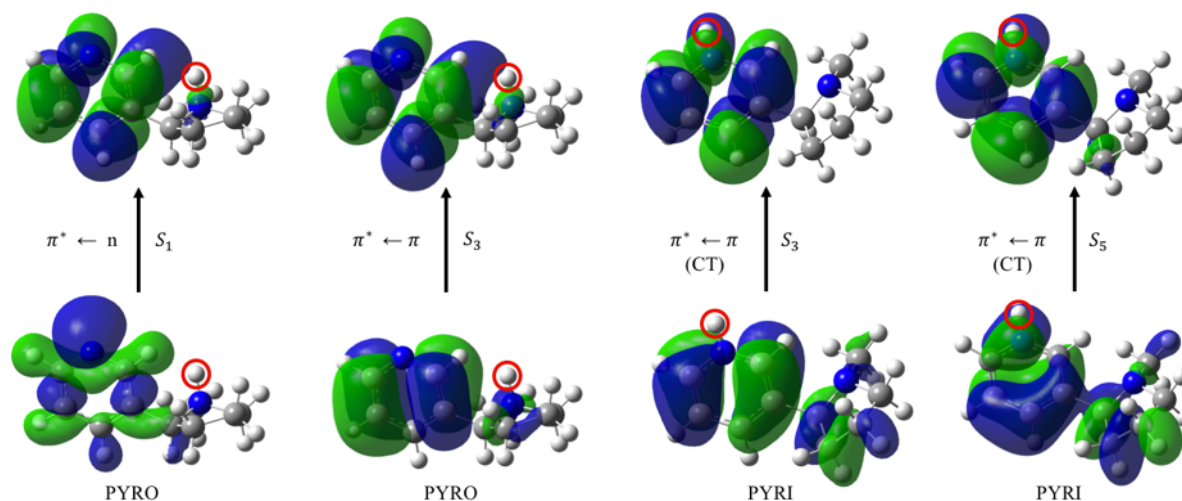


Figure 5.5: Calculated natural transition orbitals (NTOs) for the major transitions using CAM-B3LYP/aug-cc-pVDZ. The charging proton is circled in red.

It is plausible that charge-transfer accounts for the red-shift of the S₃ ← S₀ transition as the excited state π*-system of PYRI-nicH⁺ can be stabilised relative to the ground state π system by increasing the localisation of the electrons around the charged site. Protonation on a heterocyclic nitrogen in a chromophore has been observed to red shift π*←π transitions for protonated lumichrome²⁴ as well as other types of protonation on aromatic chromophores red shifted transition energies relative to their neutral (unprotonated) forms.^{13, 14, 75} Neutral (*S*)-nicotine has a calculated S₃ ← S₀ vertical transition of π*←π character at 5.42 eV with CAM-B3LYP/aug-cc-pVDZ³⁶ compared to 5.19 eV predicted of the PYRI-nicH⁺ protomer for the analogous transition and is closer to the S₃ ← S₀ transition of PYRO-nicH⁺ (5.52 eV). When

the pyridine ring is not protonated, as is the case of PYRO-nicH⁺, the chromophore has closer resemblance to that of neutral pyridine and hence the $\pi^* \leftarrow \pi$ transition more closely resembles neutral pyridine and higher in energy than the $\pi^* \leftarrow \pi$ transition of PYRI-nicH⁺.

The action spectra of all photofragment ions are shown in intensity image plots in Figure 5.14. Characteristic PYRO-nicH⁺ product ions, m/z 130 and m/z 132 are detected across a wider range of photon energies than m/z 80 and m/z 84, which is characteristic of PYRI-nicH⁺. A difference intensity plot comparing the two ESI solvents (acetonitrile subtracted by methanol plot) is shown in Figure 5.14C. Across all wavelengths, the characteristic product ions of PYRO-nicH⁺ are dominant when acetonitrile is used as the ESI solvent whereas characteristic product ions of PYRI-nicH⁺ dominate when methanol is used as an ESI solvent. The action spectra images reveal that the PYRO-nicH⁺ ion photodissociates across a wider wavelength range (*i.e.*, it has a wider band) than PYRI-nicH⁺. Secondly, the two protomers have characteristic photo-product branching ratios and hence when protomer populations shift in the different solvents, there is a change in relative fragment populations, however one needs to keep in mind the relative absorption and dissociation efficiencies of each protomer at each photon energy.

5.4.5 FAIMS

Figure 6A shows the FAIMS ‘ionogram’ of nicH⁺ (m/z 163) obtained using methanol as the ESI solvent. There is a wide region of signal from -30 V to -18 V of relatively low signal intensity and a relatively high intensity region from -18 V to -8 V. Some separation of the two protomers by FAIMS is achieved by analysing the photodissociation spectrum of nicH⁺ and tracking the formation of two protomer characteristic photoproducts as shown in Figure 5.6B. The blue trace from -18 V to -12 V is the m/z 84 photoproduct ion signal and has a maximum at -15 V. The green trace from -18 V to -8 V is the abundance of the m/z 132 photoproduct ions and has a maximum at -13 V. To probe the action spectra of these FAIMS selected nicH⁺ ions to verify the separation of protomers, the changes in relative intensity of product ions at these compensation voltage values are plotted as action spectra profiles in Figures 5.6C and 5.6D. These data reveal a clear reversal of product ion abundance ratios between CV values of -16.5 V and -11.5 V, respectively. There is also a difference in the shape of the bands, with the m/z 132+130 action spectrum having a sharp point but a tailing low-energy shoulder. To better compare the band shapes in both cases, the bands are normalised to the same intensity value

(Figure S6) revealing similarities between the two bands particularly in the distinctive region between 4.0-4.5 eV. To explain this point, inspection of Figure 5.6(D) and Figure 5.15(A) shows that at a FAIMS set voltage of -11.5V, where we expect a significant enhancement of the PYRO-nicH⁺ protomer in the ion trap. The product-ion action spectrum of *m/z* 84 actually begins to show some resemblance of the the PYRO-nicH⁺ protomer as is most noticeable in that 4.0-4.5 eV region. This is despite that the *m/z* 84 photoproduct is assigned to be largely characteristic of the PYRI-nicH⁺ protomer (as shown in Figure 5.4). These results are direct evidence that under photoexcitation, there are common photodissociation pathways from these two protomers. To quantify this, the absorption and dissociation cross-section values for both protomers are required, across this photon range, however these values are unknown.

Ultimately, the evidence suggests that bias values of 1 or -1 might not be possible for nicH⁺. Looking at the bias values for this FAIMS selection, PD product mass spectra for nicH⁺ ions for FAIMS CV values of -11.5 V and -16.5 V are shown in Figure 5.7 A with bias values calculated and shown in Figure 5.7 B. The larger bias values for product ions of *m/z* 80, *m/z* 84, *m/z* 130, and *m/z* 132 achieved by FAIMS illustrates that, in this case, the protomer populations are shifted more dramatically than by changing ESI solvent. However, due to decreased ion signal, the FAIMS bias had more statistical uncertainty than the solvent bias but presumably this could be improved with increased acquisitions. Ultimately, the same characteristic product ions are present as discussed earlier, in accord with the above assignments.

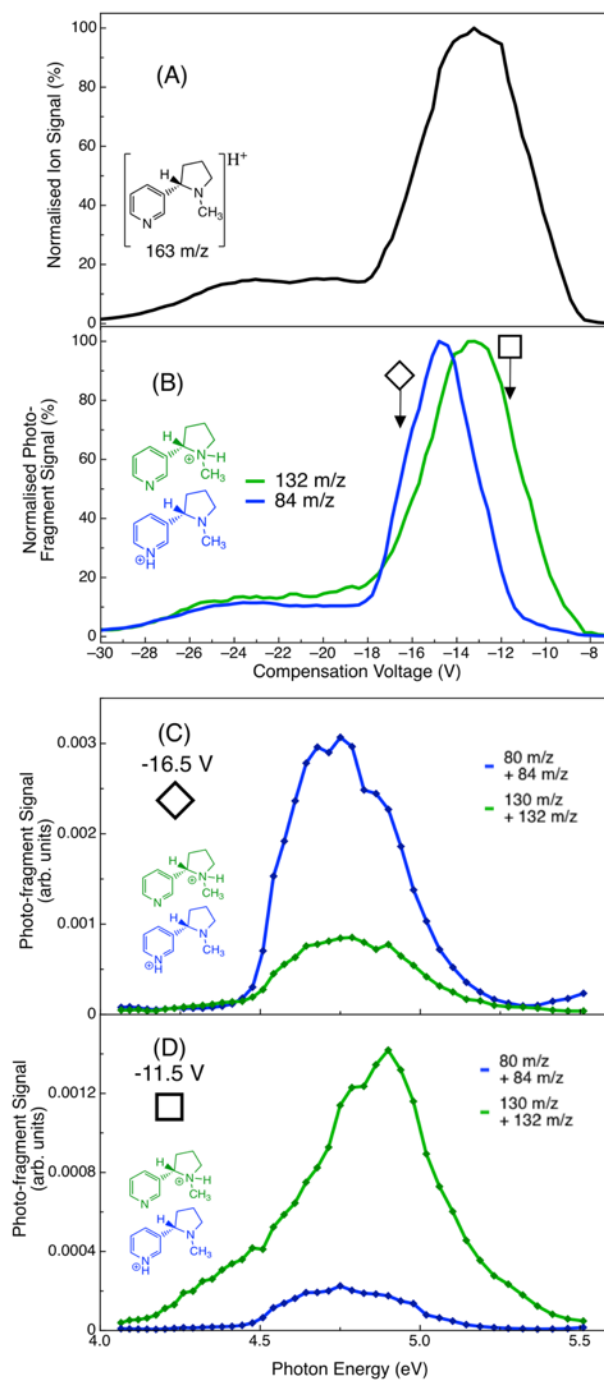


Figure 5.6: (A) Cylindrical-FAIMS ionogram of m/z 163 nicH⁺. (B) Cylindrical-FAIMS ionogram of photoproducts (PD 266 nm) for m/z 132 (green line) and m/z 84 (blue line). (C) FAIMS-modulated action spectra of photoproducts assigned to PYRO-nicH⁺ (m/z 130 + 132 in green) and PYRI-nicH⁺ (m/z 80 + 84 in blue) acquired at FAIMS CV voltages of -16.5 V (B) and -11.5 V (D). The square and diamond symbols link the compensation voltage value used for the respective action scans to the position on the FAIMS ionogram.

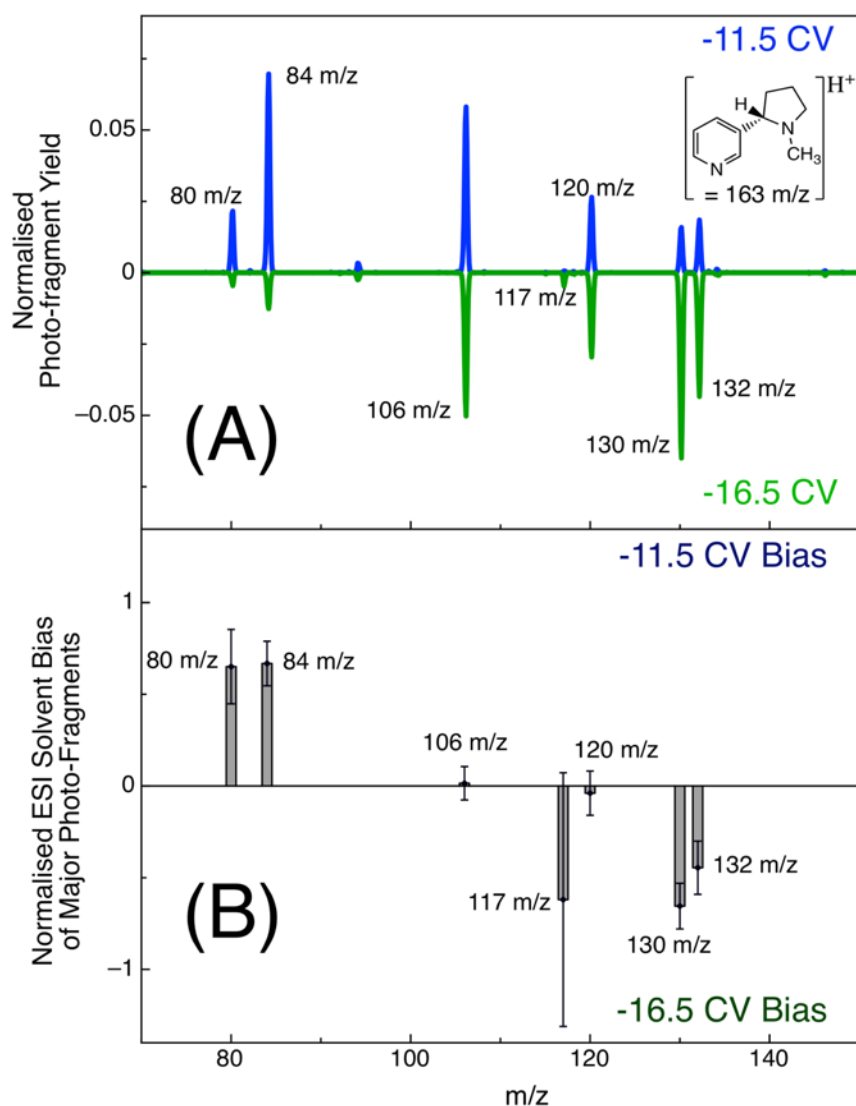


Figure 5.7: (A) PD mass spectra of nicH⁺ with FAIMS CV voltages -11.5 V (blue) and -16.5 V (green). (B) Bar graph showing the bias values of several photo-products to formation from nicH⁺ with a CV voltage of -11.5 V and -16.5 V.

To further explore if complete separation of nicH⁺ protomer is possible, experiments on a planar-FAIMS system were performed, however, only CID activation was available on this triple-quadrupole mass spectrometer. As shown in Figure 5.8, this planar-FAIMS system afforded almost complete separation of protomers by CV. Parking the CV at +4.5 V and +6.5 V and acquiring CID product spectra provided a significantly improved bias analysis, shown in Figure 5.9, but characteristic peaks still fall short of +1 and -1. Action spectroscopy would be required here to unequivocally determine if these protomers give rise to exclusive product ions. Do the protomers isomerise before dissociation? Do they have some common product ions? The answers to these questions will depend on the activation method (*i.e.*, laser versus

collision) and furthermore depend on the laser wavelength and the CID strategy (ion-trap resonant excitation versus beam-type collisions).

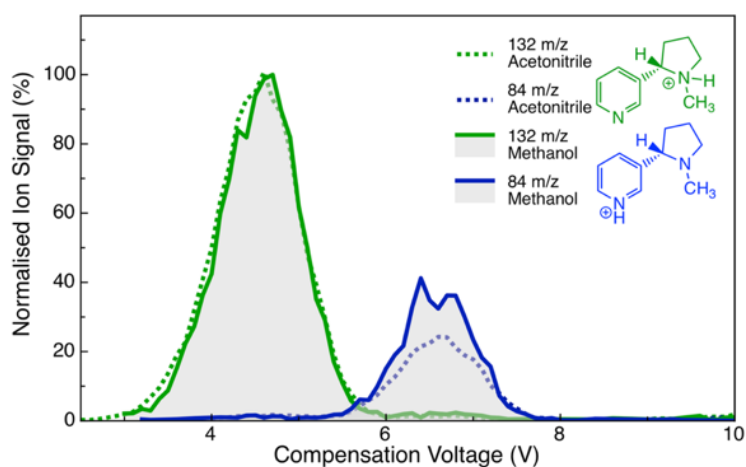


Figure 5.8: Planar-FAIMS multiple-reaction monitoring scans following the formation of the m/z 84 CID product ions (red) from and m/z 132 (blue) which correspond to fragmentation from different promoters of nicH^+ (m/z 163) comparing acetonitrile (dashed-line) and methanol (solid line) as the solvent.

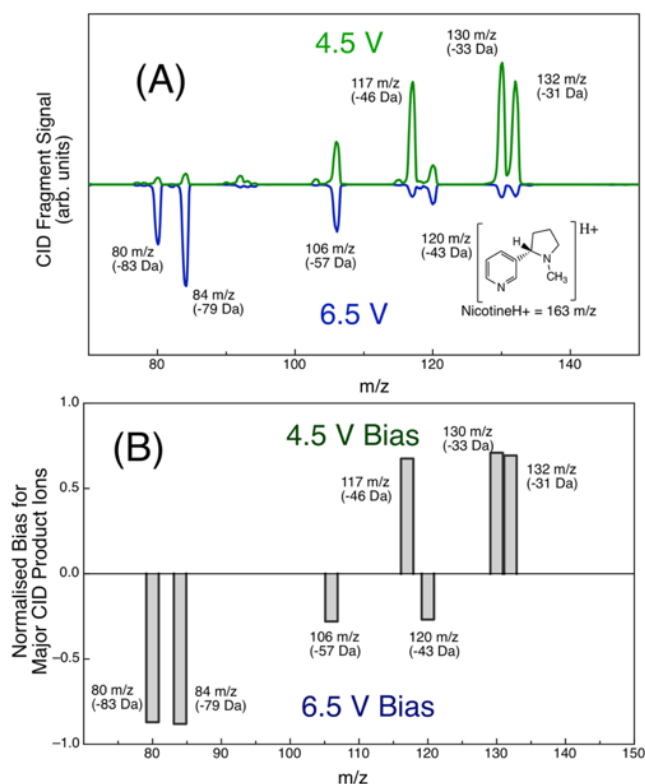


Figure 5.9: (A) CID spectra of planar-FAIMS separated nicH^+ protomers in a SCIEX 5500 with SelexION attachment. The green spectrum originates from ions isolated at 4.5 CV and are assigned as pyrrolidine protonated nicH^+ . The inverted blue spectrum originates from ions isolated at 6.5 CV and are assigned as pyridine protonated nicH^+ . (B) Bar graph showing the bias of several CID product ions to formation from nicH^+ with a CV voltage of 4.5 V and 6.5 V.

5.5 Conclusions

Wavelength-dependent photodissociation and product ion branching ratios, which are observed in the PD mass spectra of nicH⁺, confirm both the presence of two nicH⁺ protomers in the gas phase. These protomers have distinguishable photodissociation characteristics and characteristic—although it appears not exclusive—product ions. Separation of nicH⁺ protomers via FAIMS and analysis of separated species with PD mass spectrometry validated the assignments of the two nicH⁺ protomers. Although both protomers appear to be formed in both solvents, relative protomer populations were shifted by changing ESI solvent (methanol and acetonitrile), with protonation being favoured on the pyridine nitrogen in methanol and at the on the pyrrolidine nitrogen in acetonitrile. Quantum chemical calculations supported the assignments of the protomers and their PD action spectra. It is anticipated that the integration of ion photodissociation action spectroscopy with the methods of ion mobility and mass spectrometry should be useful in the future for determining the impact of protonation sites on the photochemistry and photodissociation of many other protonation isomers.

Acknowledgements

The authors thank the Australian Research Council for funding through the Discovery (DP170101596) and Linkage Programs (LP110200648). With also thank Dr Alan Maccarone (UOW) for outstanding instrumental and technique support.

References

1. Campbell, J. L.; Le Blanc, J. Y.; Schneider, B. B., Probing electrospray ionization dynamics using differential mobility spectrometry: the curious case of 4-aminobenzoic acid. *Analytical Chemistry* **2012**, *84* (18), 7857-7864.
2. Xia, H.; Attygalle, A. B., Effect of electrospray ionization source conditions on the tautomer distribution of deprotonated p-hydroxybenzoic acid in the gas phase. *Analytical Chemistry* **2016**, *88* (11), 6035-6043.
3. Attygalle, A. B.; Xia, H.; Pavlov, J., Influence of Ionization Source Conditions on the Gas-Phase Protomer Distribution of Anilinium and Related Cations. *Journal of The American Society for Mass Spectrometry* **2017**, *28* (8), 1575-1586.
4. Campbell, J. L.; Yang, A. M.-C.; Melo, L. R.; Hopkins, W. S., Studying gas-phase interconversion of tautomers using differential mobility spectrometry. *Journal of The American Society for Mass Spectrometry* **2016**, *27* (7), 1277-1284.
5. Tian, Z.; Kass, S. R., Gas-Phase versus liquid-Phase structures by electrospray ionization mass spectrometry. *Angewandte Chemie International Edition* **2009**, *48* (7), 1321-1323.
6. Anwar, A.; Psutka, J.; Walker, S. W.; Dieckmann, T.; Janizewski, J. S.; Campbell, J. L.; Hopkins, W. S., Separating and probing tautomers of protonated nucleobases using

differential mobility spectrometry. *International Journal of Mass Spectrometry* **2017**, *429*, 174-181.

7. Xia, H.; Attygalle, A. B., Transformation of the gas-phase favored O-protomer of p-aminobenzoic acid to its unfavored N-protomer by ion activation in the presence of water vapor: A n ion-mobility mass spectrometry study. *Journal of Mass Spectrometry* **2018**, *53* (4), 353-360.
8. Walker, S. W.; Mark, A. E.; Verbuyst, B.; Bogdanov, B.; Campbell, J. L.; Hopkins, W. S., Characterizing the Tautomers of Protonated Aniline Using Differential Mobility Spectrometry and Mass Spectrometry. *The Journal of Physical Chemistry A* **2018**, *122* (15), 3858-3865.
9. Xia, H.; Attygalle, A. B., Untrapping Kinetically Trapped Ions: The Role of Water Vapor and Ion-Source Activation Conditions on the Gas-Phase Protomer Ratio of Benzocaine Revealed by Ion-Mobility Mass Spectrometry. *Journal of The American Society for Mass Spectrometry* **2017**, *28* (12), 2580-2587.
10. Patrick, A. L.; Cismesia, A. P.; Tesler, L. F.; Polfer, N. C., Effects of ESI conditions on kinetic trapping of the solution-phase protonation isomer of p-aminobenzoic acid in the gas phase. *International Journal of Mass Spectrometry* **2017**, *418*, 148-155.
11. Warnke, S.; Seo, J.; Boschmans, J.; Sobott, F.; Scrivens, J. H.; Bleiholder, C.; Bowers, M. T.; Gewinner, S.; Schöllkopf, W.; Pagel, K., Protomers of benzocaine: solvent and permittivity dependence. *Journal of the American Chemical Society* **2015**, *137* (12), 4236-4242.
12. Matthews, E.; Dessent, C. E., Experiment and theory confirm that UV laser photodissociation spectroscopy can distinguish protomers formed via electrospray. *Physical Chemistry Chemical Physics* **2017**, *19* (26), 17434-17440.
13. Noble, J. A.; Broquier, M.; Gregoire, G.; Soorkia, S.; Pino, G.; Marceca, E.; Dedonder-Lardeux, C.; Juvet, C., Tautomerism and electronic spectroscopy of protonated 1- and 2-aminonaphthalene. *Physical Chemistry Chemical Physics* **2018**, *20* (9), 6134-6145.
14. Noble, J. A.; Dedonder-Lardeux, C.; Mascetti, J.; Juvet, C., Electronic Spectroscopy of Protonated 1-Aminopyrene in a Cold Ion Trap. *Chemistry—An Asian Journal* **2017**, *12* (13), 1523-1531.
15. Broquier, M.; Soorkia, S.; Pino, G. A.; Dedonder-Lardeux, C.; Juvet, C.; Gregoire, G., Excited State Dynamics of Cold Protonated Cytosine Tautomers: Characterization of Charge Transfer, Inter System Crossing and Internal Conversion Processes. *The Journal of Physical Chemistry A* **2017**, *121* (34), 6429-6439.
16. Féraud, G.; Esteves-Lopez, N.; Dedonder-Lardeux, C.; Juvet, C., UV spectroscopy of cold ions as a probe of the protonation site. *Physical Chemistry Chemical Physics* **2015**, *17* (39), 25755-25760.
17. Berdakin, M.; Féraud, G.; Dedonder-Lardeux, C.; Juvet, C.; Pino, G. A., Excited states of protonated DNA/RNA bases. *Physical Chemistry Chemical Physics* **2014**, *16* (22), 10643-10650.
18. Langer, J.; Günther, A.; Seidenbecher, S.; Berden, G.; Oomens, J.; Dopfer, O., Probing Protonation Sites of Isolated Flavins Using IR Spectroscopy: From Lumichrome to the Cofactor Flavin Mononucleotide. *ChemPhysChem* **2014**, *15* (12), 2550-2562.
19. Peckelsen, K.; Martens, J.; Czypiel, L.; Oomens, J.; Berden, G.; Gründemann, D.; Meijer, A. J.; Schäfer, M., Ergothioneine and related histidine derivatives in the gas phase: tautomer structures determined by IRMPD spectroscopy and theory. *Physical Chemistry Chemical Physics* **2017**, *19* (34), 23362-23372.
20. Gregoire, G.; Gageot, M.; Marinica, D.; Lemaire, J.; Schermann, J.; Desfrancois, C., Resonant infrared multiphoton dissociation spectroscopy of gas-phase protonated

- peptides. Experiments and Car–Parrinello dynamics at 300 K. *Physical Chemistry Chemical Physics* **2007**, *9* (24), 3082-3097.
21. Seydou, M.; Grégoire, G.; Liquier, J.; Lemaire, J.; Schermann, J. P.; Desfrancois, C., Experimental observation of the transition between gas-phase and aqueous solution structures for acetylcholine, nicotine, and muscarine ions. *Journal of the American Chemical Society* **2008**, *130* (12), 4187-4195.
22. Salpin, J. Y.; Guillaumont, S.; Tortajada, J.; MacAleese, L.; Lemaire, J.; Maitre, P., Infrared spectra of protonated uracil, thymine and cytosine. *ChemPhysChem* **2007**, *8* (15), 2235-2244.
23. Nei, Y.-w.; Akinyemi, T.; Steill, J.; Oomens, J.; Rodgers, M., Infrared multiple photon dissociation action spectroscopy of protonated uracil and thiouracils: Effects of thioketo-substitution on gas-phase conformation. *International Journal of Mass Spectrometry* **2010**, *297* (1), 139-151.
24. Sheldrick, A.; Müller, D.; Günther, A.; Nieto, P.; Dopfer, O., Optical spectroscopy of isolated flavins: photodissociation of protonated lumichrome. *Physical Chemistry Chemical Physics* **2018**, *20* (11), 7407-7414.
25. Féraud, G.; Berdakin, M.; Dedonder, C.; Jouvet, C.; Pino, G. A., Excited States of Proton-Bound DNA/RNA Base Homodimers: Pyrimidines. *The Journal of Physical Chemistry B* **2014**, *119* (6), 2219-2228.
26. Matthews, E.; Dessent, C. E., Locating the proton in nicotinamide protomers via low-resolution UV action spectroscopy of electrosprayed solutions. *The Journal of Physical Chemistry A* **2016**, *120* (46), 9209-9216.
27. Pontieri, F. E.; Tanda, G.; Orzi, F.; Di Chiara, G., Effects of nicotine on the nucleus accumbens and similarity to those of addictive drugs. *Nature* **1996**, *382* (6588), 255-257.
28. Graton, J.; Berthelot, M.; Gal, J.-F.; Girard, S.; Laurence, C.; Lebreton, J.; Le Questel, J.-Y.; Maria, P.-C.; Nauš, P., Site of protonation of nicotine and nornicotine in the gas phase: pyridine or pyrrolidine nitrogen? *Journal of the American Chemical Society* **2002**, *124* (35), 10552-10562.
29. Petrick, L.; Destailats, H.; Zouev, I.; Sabach, S.; Dubowski, Y., Sorption, desorption, and surface oxidative fate of nicotine. *Physical Chemistry Chemical Physics* **2010**, *12* (35), 10356-10364.
30. Celie, P. H.; van Rossum-Fikkert, S. E.; van Dijk, W. J.; Brejc, K.; Smit, A. B.; Sixma, T. K., Nicotine and carbamylcholine binding to nicotinic acetylcholine receptors as studied in AChBP crystal structures. *Neuron* **2004**, *41* (6), 907-914.
31. Glasser, A. M.; Collins, L.; Pearson, J. L.; Abudayyeh, H.; Niaura, R. S.; Abrams, D. B.; Villanti, A. C., Overview of electronic nicotine delivery systems: a systematic review. *American Journal of Preventive Medicine* **2017**, *52* (2), e33-e66.
32. El-Hellani, A.; El-Hage, R.; Baalbaki, R.; Salman, R.; Talih, S.; Shihadeh, A.; Saliba, N. A., Free-base and protonated nicotine in electronic cigarette liquids and aerosols. *Chemical Research in Toxicology* **2015**, *28* (8), 1532-1537.
33. Gageot, M.-P.; Cimas, A.; Seydou, M.; Kim, J.-Y.; Lee, S.; Schermann, J.-P., Proton transfer from the inactive gas-phase nicotine structure to the bioactive aqueous-phase structure. *Journal of the American Chemical Society* **2010**, *132* (51), 18067-18077.
34. Yoshida, T.; Farone, W. A.; Xantheas, S. S., Isomers and conformational barriers of gas-phase nicotine, nornicotine, and their protonated forms. *The Journal of Physical Chemistry B* **2014**, *118* (28), 8273-8285.
35. Williams, J. P.; Nibbering, N. M.; Green, B. N.; Patel, V. J.; Scrivens, J. H., Collision-induced fragmentation pathways including odd-electron ion formation from desorption electrospray ionisation generated protonated and deprotonated drugs derived from tandem accurate mass spectrometry. *Journal of Mass Spectrometry* **2006**, *41* (10), 1277-1286.

36. Egidi, F.; Segado, M.; Koch, H.; Cappelli, C.; Barone, V., A benchmark study of electronic excitation energies, transition moments, and excited-state energy gradients on the nicotine molecule. *The Journal of Chemical Physics* **2014**, *141* (22), 224114.
37. Eddy, C. R.; Eisner, A., Infrared spectra of nicotine and some of its derivatives. *Analytical Chemistry* **1954**, *26* (9), 1428-1431.
38. Ryszka, M.; Alizadeh, E.; Li, Z.; Ptasińska, S., Low-energy electron-induced dissociation in gas-phase nicotine, pyridine, and methyl-pyrrolidine. *The Journal of Chemical Physics* **2017**, *147* (9), 094303.
39. Swain, M. L.; Eisner, A.; Woodward, C.; Brice, B., Ultraviolet absorption spectra of nicotine, nornicotine and some of their derivatives. *Journal of the American Chemical Society* **1949**, *71* (4), 1341-1345.
40. Clayton, P. M.; Vas, C. A.; Bui, T. T.; Drake, A. F.; McAdam, K., Spectroscopic investigations into the acid–base properties of nicotine at different temperatures. *Analytical Methods* **2013**, *5* (1), 81-88.
41. Clayton, P. M.; Vas, C. A.; Bui, T. T.; Drake, A. F.; McAdam, K., Spectroscopic studies on nicotine and nornicotine in the UV region. *Chirality* **2013**, *25* (5), 288-293.
42. Boschmans, J.; Jacobs, S.; Williams, J. P.; Palmer, M.; Richardson, K.; Giles, K.; Laphorn, C.; Herrebout, W. A.; Lemièrre, F.; Sobott, F., Combining density functional theory (DFT) and collision cross-section (CCS) calculations to analyze the gas-phase behaviour of small molecules and their protonation site isomers. *Analyst* **2016**, *141* (13), 4044-4054.
43. Lalli, P. M.; Iglesias, B. A.; Toma, H. E.; Sa, G. F.; Daroda, R. J.; Silva Filho, J. C.; Szulejko, J. E.; Araki, K.; Eberlin, M. N., Protomers: formation, separation and characterization via travelling wave ion mobility mass spectrometry. *Journal of Mass Spectrometry* **2012**, *47* (6), 712-719.
44. Laphorn, C.; Dines, T. J.; Chowdhry, B. Z.; Perkins, G. L.; Pullen, F. S., Can ion mobility mass spectrometry and density functional theory help elucidate protonation sites in 'small' molecules? *Rapid Communications in Mass Spectrometry* **2013**, *27* (21), 2399-2410.
45. Bull, J. N.; Coughlan, N. J.; Bieske, E. J., Protomer-Specific Photochemistry Investigated Using Ion Mobility Mass Spectrometry. *The Journal of Physical Chemistry A* **2017**, *121* (32), 6021-6027.
46. Cruz-Ortiz, A. F.; Rossa, M.; Berthias, F.; Berdakin, M.; Maitre, P.; Pino, G. A., Fingerprints of Both Watson–Crick and Hoogsteen Isomers of the Isolated (Cytosine-Guanine) H⁺ Pair. *The journal of physical chemistry letters* **2017**, *8* (22), 5501-5506.
47. Papadopoulos, G.; Svendsen, A.; Boyarkin, O. V.; Rizzo, T. R., Conformational distribution of bradykinin [bk+ 2 H]²⁺ revealed by cold ion spectroscopy coupled with FAIMS. *Journal of the American Society for Mass Spectrometry* **2012**, *23* (7), 1173-1181.
48. Voronina, L.; Rizzo, T. R., Spectroscopic studies of kinetically trapped conformations in the gas phase: the case of triply protonated bradykinin. *Physical Chemistry Chemical Physics* **2015**, *17* (39), 25828-25836.
49. Russo, N.; Toscano, M.; Grand, A.; Mineva, T., Proton affinity and protonation sites of aniline. Energetic behavior and density functional reactivity indices. *The Journal of Physical Chemistry A* **2000**, *104* (17), 4017-4021.
50. Buryakov, I.; Krylov, E.; Nazarov, E.; Rasulev, U. K., A new method of separation of multi-atomic ions by mobility at atmospheric pressure using a high-frequency amplitude-asymmetric strong electric field. *International Journal of Mass Spectrometry and Ion Processes* **1993**, *128* (3), 143-148.
51. Shvartsburg, A. A., *Differential ion mobility spectrometry: nonlinear ion transport and fundamentals of FAIMS*. CRC Press: Boca Raton, FL, 2009.

52. Guevremont, R.; Purves, R. W., Atmospheric pressure ion focusing in a high-field asymmetric waveform ion mobility spectrometer. *Review of Scientific Instruments* **1999**, *70* (2), 1370-1383.
53. Krylov, E., Comparison of the planar and coaxial field asymmetrical waveform ion mobility spectrometer (FAIMS). *International Journal of Mass Spectrometry* **2003**, *225* (1), 39-51.
54. Shvartsburg, A. A.; Li, F.; Tang, K.; Smith, R. D., High-resolution field asymmetric waveform ion mobility spectrometry using new planar geometry analyzers. *Analytical Chemistry* **2006**, *78* (11), 3706-3714.
55. Hansen, C. S.; Kirk, B. B.; Blanksby, S. J.; O'Hair, R. A.; Trevitt, A. J., UV photodissociation action spectroscopy of haloanilinium ions in a linear quadrupole ion trap mass spectrometer. *Journal of the American Society for Mass Spectrometry* **2013**, *24* (6), 932-940.
56. Ly, T.; Julian, R. R., Residue-specific radical-directed dissociation of whole proteins in the gas phase. *Journal of the American Chemical Society* **2008**, *130* (1), 351-358.
57. Ly, T.; Zhang, X.; Sun, Q.; Moore, B.; Tao, Y.; Julian, R. R., Rapid, quantitative, and site specific synthesis of biomolecular radicals from a simple photocaged precursor. *Chemical Communications* **2011**, *47* (10), 2835-2837.
58. Frisch, M. J.; Trucks, G. W.; Schlegel, H. B.; Scuseria, G. E.; Robb, M. A.; Cheeseman, J. R.; Scalmani, G.; Barone, V.; Petersson, G. A.; Nakatsuji, H.; Li, X.; Caricato, M.; Marenich, A. V.; Bloino, J.; Janesko, B. G.; Gomperts, R.; Mennucci, B.; Hratchian, H. P.; Ortiz, J. V.; Izmaylov, A. F.; Sonnenberg, J. L.; Williams-Young, D.; Ding, F.; Lipparini, F.; Egidi, F.; Goings, J.; Peng, B.; Petrone, A.; Henderson, T.; Ranasinghe, D.; Zakrzewski, V. G.; Gao, J.; Rega, N.; Zheng, G.; Liang, W.; Hada, M.; Ehara, M.; Toyota, K.; Fukuda, R.; Hasegawa, J.; Ishida, M.; Nakajima, T.; Honda, Y.; Kitao, O.; Nakai, H.; Vreven, T.; Throssell, K.; Montgomery Jr., J. A.; Peralta, J. E.; Ogliaro, F.; Bearpark, M. J.; Heyd, J. J.; Brothers, E. N.; Kudin, K. N.; Staroverov, V. N.; Keith, T. A.; Kobayashi, R.; Normand, J.; Raghavachari, K.; Rendell, A. P.; Burant, J. C.; Iyengar, S. S.; Tomasi, J.; Cossi, M.; Millam, J. M.; Klene, M.; Adamo, C.; Cammi, R.; Ochterski, J. W.; Martin, R. L.; Morokuma, K.; Farkas, O.; Foresman, J. B.; Fox, D. J. *Gaussian 16*, Wallingford, CT, 2016.
59. TURBOMOLE V7.2 2017, a development of University of Karlsruhe and Forschungszentrum Karlsruhe GmbH, 1989-2009, TURBOMOLE GmbH, since 2007; available from <http://www.turbomole.com>.
60. Woon, D. E.; Dunning Jr, T. H., Gaussian basis sets for use in correlated molecular calculations. III. The atoms aluminum through argon. *The Journal of Chemical Physics* **1993**, *98* (2), 1358-1371.
61. Dunning Jr, T. H., Gaussian basis sets for use in correlated molecular calculations. I. The atoms boron through neon and hydrogen. *The Journal of Chemical Physics* **1989**, *90* (2), 1007-1023.
62. Zhao, Y.; Truhlar, D. G., The M06 suite of density functionals for main group thermochemistry, thermochemical kinetics, noncovalent interactions, excited states, and transition elements: two new functionals and systematic testing of four M06-class functionals and 12 other functionals. *Theoretical Chemistry Accounts: Theory, Computation, and Modeling (Theoretica Chimica Acta)* **2008**, *120* (1), 215-241.
63. Yanai, T.; Tew, D. P.; Handy, N. C., A new hybrid exchange–correlation functional using the Coulomb-attenuating method (CAM-B3LYP). *Chemical Physics Letters* **2004**, *393* (1), 51-57.

64. Chai, J.-D.; Head-Gordon, M., Long-range corrected hybrid density functionals with damped atom–atom dispersion corrections. *Physical Chemistry Chemical Physics* **2008**, *10* (44), 6615-6620.
65. Frisch, M. J.; Head-Gordon, M.; Pople, J. A., A direct MP2 gradient method. *Chemical Physics Letters* **1990**, *166* (3), 275-280.
66. Head-Gordon, M.; Pople, J. A.; Frisch, M. J., MP2 energy evaluation by direct methods. *Chemical Physics Letters* **1988**, *153* (6), 503-506.
67. Sæbø, S.; Almlöf, J., Avoiding the integral storage bottleneck in LCAO calculations of electron correlation. *Chemical Physics Letters* **1989**, *154* (1), 83-89.
68. Frisch, M. J.; Head-Gordon, M.; Pople, J. A., Semi-direct algorithms for the MP2 energy and gradient. *Chemical Physics Letters* **1990**, *166* (3), 281-289.
69. Head-Gordon, M.; Head-Gordon, T., Analytic MP2 frequencies without fifth-order storage. Theory and application to bifurcated hydrogen bonds in the water hexamer. *Chemical Physics Letters* **1994**, *220* (1-2), 122-128.
70. Christiansen, O.; Koch, H.; Jørgensen, P., The second-order approximate coupled cluster singles and doubles model CC2. *Chemical Physics Letters* **1995**, *243* (5-6), 409-418.
71. Hättig, C.; Weigend, F., CC2 excitation energy calculations on large molecules using the resolution of the identity approximation. *The Journal of Chemical Physics* **2000**, *113* (13), 5154-5161.
72. Kulesza, A. J.; Titov, E.; Daly, S.; Włodarczyk, R.; Megow, J.; Saalfrank, P.; Choi, C. M.; MacAleese, L.; Antoine, R.; Dugourd, P., Excited States of Xanthene Analogues: Photofragmentation and Calculations by CC2 and Time-Dependent Density Functional Theory. *ChemPhysChem* **2016**, *17* (19), 3129-3138.
73. Garcia, R. L.; Nieuwjaer, N.; Desfrancois, C.; Lecomte, F.; Leite, S.; Manil, B.; Broquier, M.; Grégoire, G., Vibronic spectra of protonated hydroxypyridines: contributions of prefulvenic and planar structures. *Physical Chemistry Chemical Physics* **2017**, *19* (12), 8258-8268.
74. Martin, R. L., Natural transition orbitals. *The Journal of chemical physics* **2003**, *118* (11), 4775-4777.
75. Alata, I.; Omidyan, R.; Broquier, M.; Dedonder, C.; Dopfer, O.; Jouvét, C., Effect of protonation on the electronic structure of aromatic molecules: naphthaleneH⁺. *Physical Chemistry Chemical Physics* **2010**, *12* (43), 14456-14458.

Chapter 5

Supporting Information

5.SI NicotineH⁺ Supporting Information

Table 5.3: Relative energies of different conformers of PYRO-nicH⁺ relative to the PYRI-nicH⁺ (*S*, *trans*, *anti*) global minimum in kcal/mol as calculated with four different DFT levels of theory with the aug-cc-pVDZ basis set as well as the MP2 method with the cc-pVDZ basis set. Omitted values converged to another structure upon optimisation. Labels are according to the naming system implemented by Yoshida *et al.* [REF 34 in main text] and represents (pyrrolidine ring conformational region, relative placement of the methyl group to the pyridine ring, χ angle region).

PYRO	M06-2X	CAM-B3LYP	ω B97X-D	MP2
(<i>N</i> , <i>cis</i> , <i>anti</i>)	3.1	-	4.2	-
(<i>W</i> , <i>cis</i> , <i>anti</i>)	2.7	5.3	4.1	-
(<i>W</i> , <i>cis</i> , <i>syn</i>)	2.4	5.1	3.8	-
(<i>W</i> , <i>trans</i> , <i>anti</i>)	0.5	2.5	1.6	0.7
(<i>W</i> , <i>trans</i> , <i>syn</i>)	0.5	2.5	1.6	-

Table 5.4: Relative energies of different conformers of PYRI-nicH⁺ relative to the PYRI-nicH⁺ (*S*, *trans*, *anti*) global minimum in kcal/mol as calculated with four different DFT levels of theory with the aug-cc-pVDZ basis set as well as the MP2 method with the cc-pVDZ basis set. Omitted values converged to another structure upon optimisation. Labels are according to the naming system implemented by Yoshida *et al.* [REF 34 in main text] and represents (pyrrolidine ring conformational region, relative placement of the methyl group to the pyridine ring, χ angle region).

PYRI	M06-2X	CAM-B3LYP	ω B97X-D	MP2
(<i>N</i> , <i>cis</i> , <i>anti</i>)	6.0	6.0	5.7	-
(<i>N</i> , <i>cis</i> , <i>syn</i>)	5.6	5.9	5.4	-
(<i>S</i> , <i>cis</i> , <i>anti</i>)	5.4	-	5.3	-
(<i>E</i> , <i>cis</i> , <i>anti</i>)	5.1	6.3	5.2	-
(<i>W</i> , <i>trans</i> , <i>syn</i>)	1.1	1.0	1.1	-
(<i>W</i> , <i>trans</i> , <i>anti</i>)	0.2	-	-	-
(<i>S</i> , <i>trans</i> , <i>anti</i>)	0	0	0	0

Table 5.5: Experimental and Calculated vertical transition energies for the (*W*, *trans*, *anti*) isomer of PYRO-nicH⁺. TD-DFT calculations were performed with M06-2X and ω B97X-D with the aug-cc-pVDZ basis set.

PYRO	M06-2X		ω B97X-D	
PYRO	Transition	Calculated	Transition	Calculated
Transition	Energies	Oscillator	Energies	Oscillator
from S ₀ to:	(eV)	Strength (f)	(eV)	Strength (f)
S ₁	4.67	0.0030	4.88	0.0034
S ₂	5.04	0	5.01	0.0001
S ₃	5.59	0.043	5.52	0.040
S ₄	6.23	0.079	6.15	0.062
S ₅	6.69	0.066	7.02	0.39

Table 5.6: Experimental and Calculated vertical transition energies for the (*S*, *trans*, *anti*) isomer of PYRI-nicH⁺. TD-DFT calculations were done with M06-2X and ω B97X-D with the aug-cc-pVDZ basis set.

PYRI	M06-2X		ω B97X-D	
	Transition Energies (eV)	Calculated Oscillator Strength (f)	Transition Energies (eV)	Calculated Oscillator Strength (f)
Transition from S ₀ to:				
S ₁	3.41	0.0018	3.30	0.0005
S ₂	4.40	0.0014	4.34	0.0012
S ₃	5.24	0.13	5.19	0.13
S ₄	5.79	0.0004	6.04	0.010
S ₅	6.10	0.016	6.13	0.0027

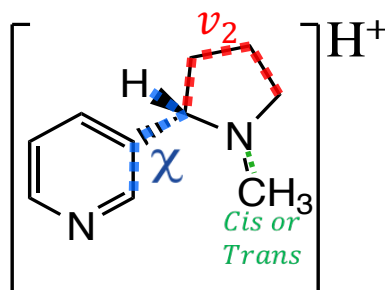


Figure 5.10: Structure of (*S*)-(-)-Nicotine including degrees of freedom which differentiate the conformers.

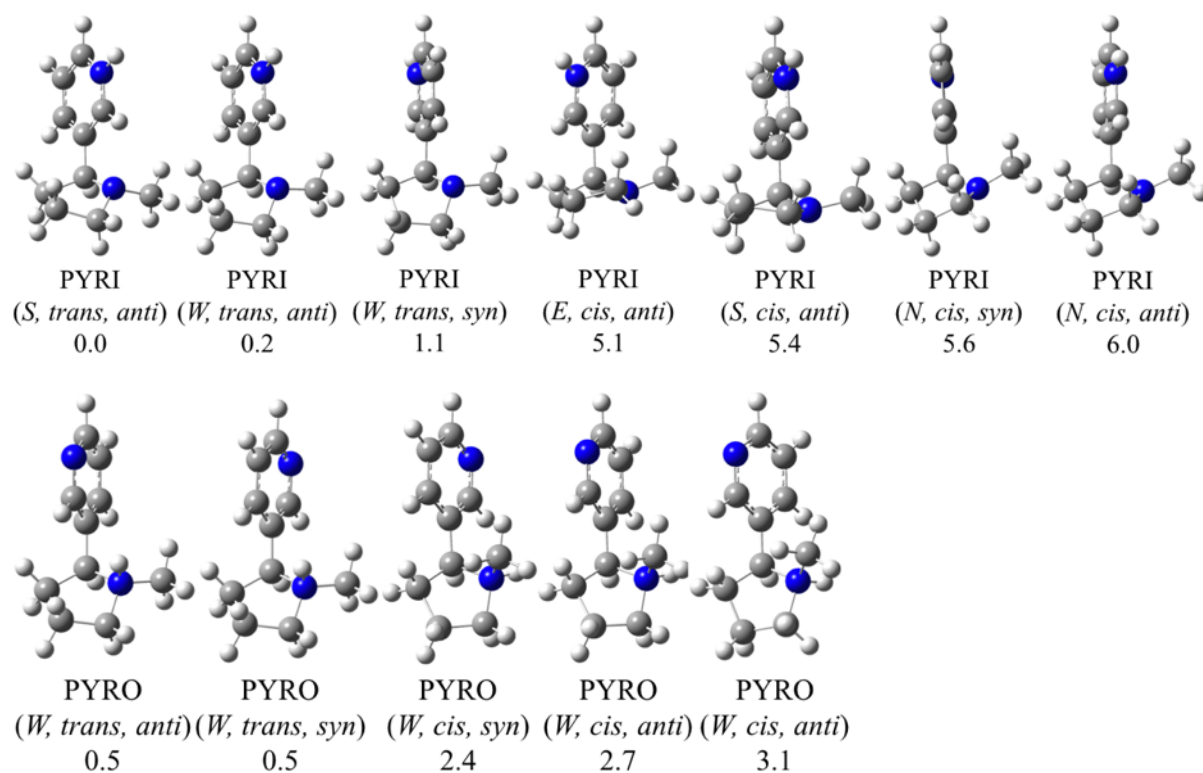


Figure 5.11: Optimised structures for twelve conformers of nicH⁺ their relative energies in kcal/mol as calculated using M06-2X/aug-cc-pVDZ.

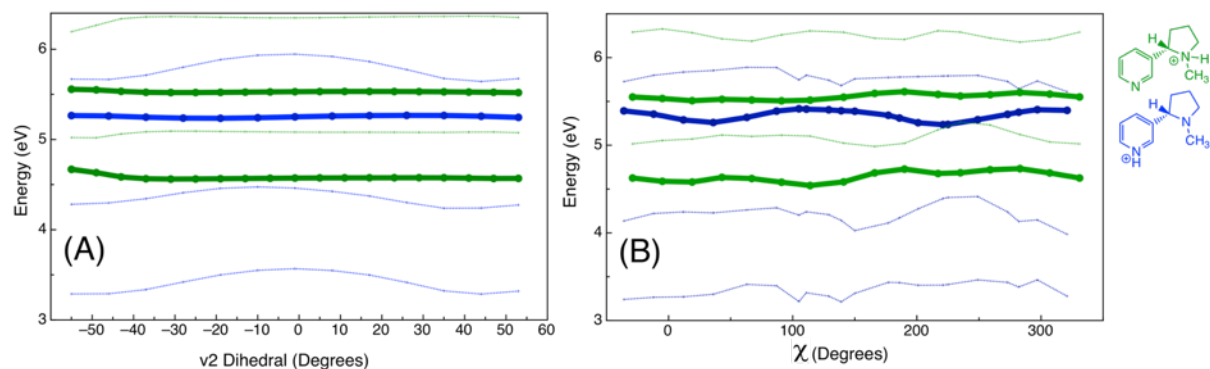


Figure 5.12: Electronic excitation energies of the first four states of protonated PYRI-nicH⁺ (blue) and PYRO-nicH⁺ (green) as the pyrrolidine ν_2 angle (A) or χ angle (B) was scanned. Transition energies were calculated using M06-2X/aug-cc-pVDZ. States of interest are plotted with bold lines. The -0.5 eV shift applied in the TD-DFT simulated electronic spectra was not applied to values presented in this table.

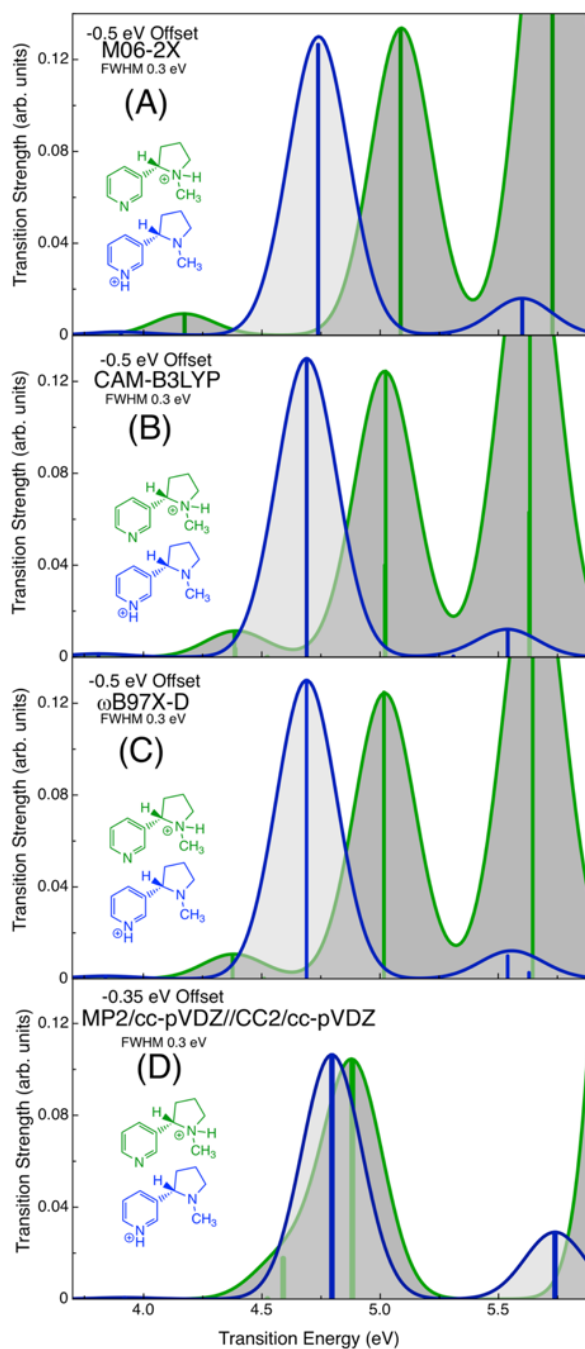


Figure 5.13: Calculated TD-DFT vertical transition energies for PYRI-nicH⁺ (blue) and PYRO-nicH⁺ (green). Three TD-DFT levels of theory were used (A) M06-2X, (B) CAM-B3LYP, (C) ω B97X-D, all with the aug-cc-pVDZ basis set. The transitions were fitted with Gaussian functions with a FWHM of 0.3 eV. Transitions have been offset -0.5 eV, as explained in the text. (D) Shows transitions calculated using CC2/cc-pVDZ from geometries which were optimised using MP2/cc-pVDZ. CC2 transitions have been offset by -0.35 eV as explained in the text.

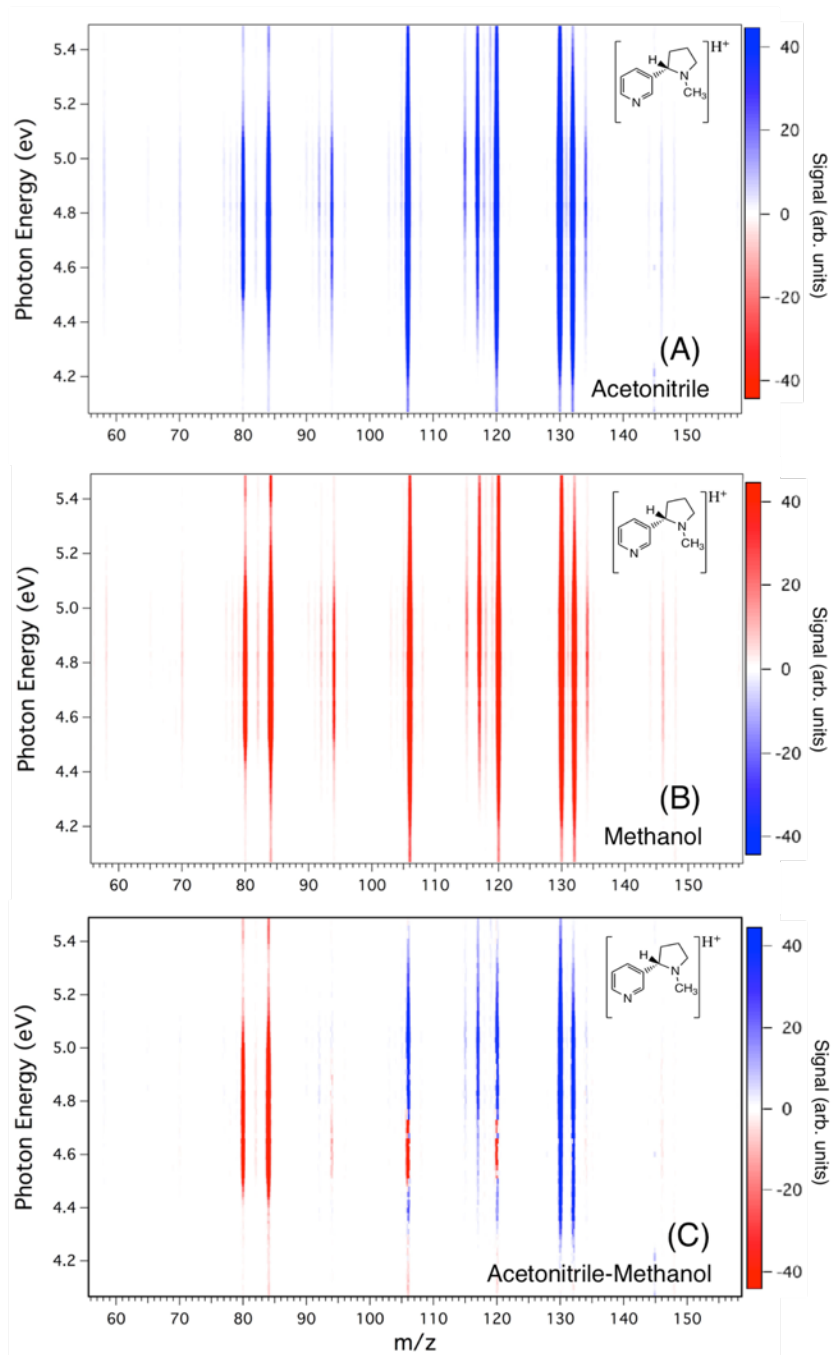


Figure 5.14: Intensity photodissociation action plots showing the changing intensities of all nicotineH⁺ photodissociation fragments between 60 m/z and 150 m/z. ESI solvents (A) acetonitrile and (B) methanol were used. The difference between image (A) and (B) is plotted in (C).

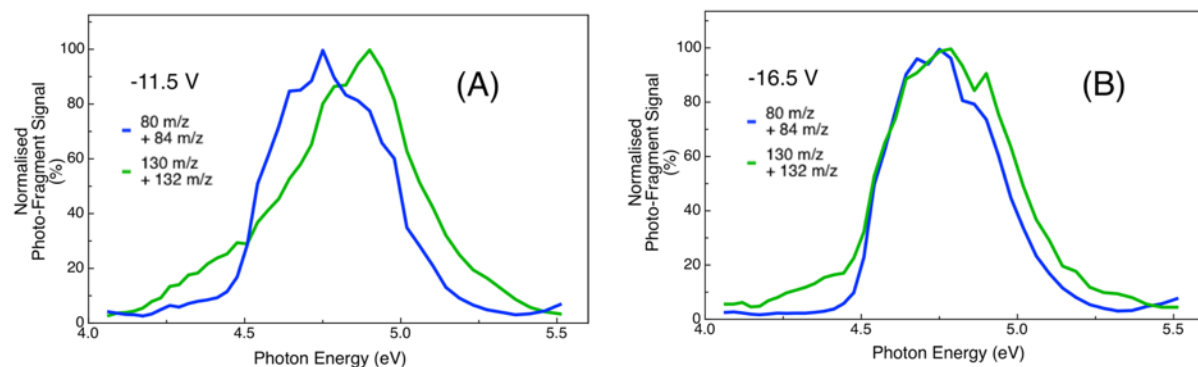


Figure 5.15: Normalised action spectra of fragments of nicH⁺ after partial separation of the protomers of nicH⁺ by FAIMS at -11.5 V (A) and -16.5 V (B).

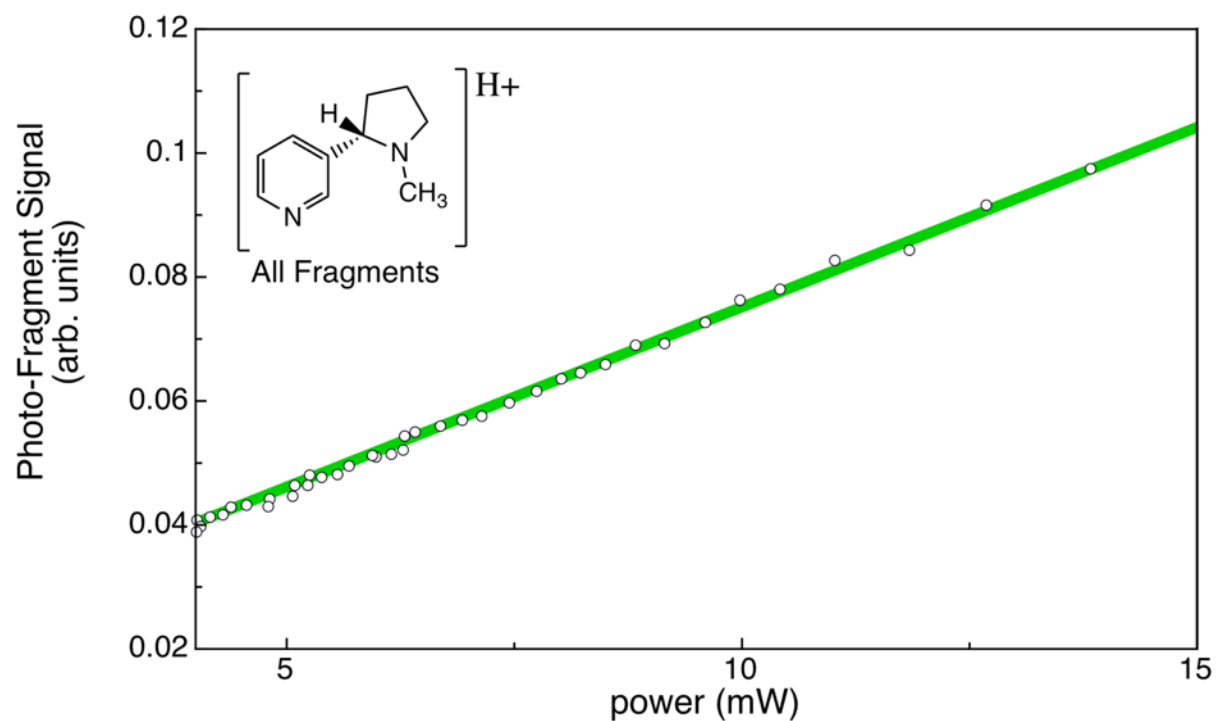


Figure 5.16: Power dependence experiments showing change in 266 nm photo-fragment signal with increasing laser power for all photoproduct ions.

This page has been intentionally left blank.

INDAZOLEH⁺ AND
BENZIMIDAZOLEH⁺

6. IndazoleH⁺ and BenzimidazoleH⁺

This chapter discusses the role of the N-N bond in the excited state dynamics of indazoleH⁺ in comparison to its isomer benzimidazoleH⁺. The contents are reproduced verbatim from the peer-reviewed and publication:

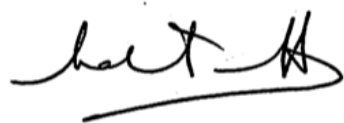
Marlton, S.J., McKinnon, B.I., Greißel, P., Shiels, O.J., Ucur, B. and Trevitt, A.J., **2021**. Picosecond Excited-State Lifetimes of Protonated Indazole and Benzimidazole: The Role of the NN bond. *The Journal of Chemical Physics*. 155, 184302

Author Contributions

S.J.P Marlton performed all calculations and action spectroscopy experiments presented in this work. Pump-probe photodissociation experiments were performed by S.J.P Marlton, P. Greißel and B.I. McKinnon. S.J.P Marlton prepared the manuscript with input from all authors. B, Ucur contributed to calculations of the transition densities of the excited states. O,J, Shiels contributed to interpreting the rates and barriers.

Certification

I, Prof. Adam J. Trevitt, as Samuel J. P. Marlton's primary supervisor, and the principal investigator for this project, agree with and certify the author contributions described above.

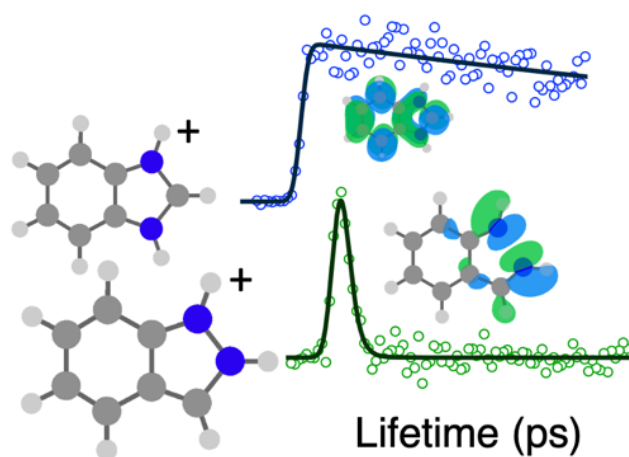


Adam J. Trevitt

07/12/2021

6.1 Abstract

Certain chemical groups give rise to characteristic excited-state deactivation mechanisms. Here we target the role of a protonated N-N chemical group in the excited-state deactivation of protonated indazole by comparison to its isomer that lacks this group, protonated benzimidazole. Gas-phase protonated indazole and protonated benzimidazole ions are investigated at room temperature using picosecond laser pump-probe photodissociation experiments in a linear ion-trap. Excited state lifetimes are measured across a range of pump energies (4.0 – 5.4 eV). The $^1\pi\pi^*$ lifetimes of protonated indazole range from 390 ± 70 ps using 4.0 eV pump energy to ≤ 18 ps using 4.6 eV pump energy. The $^1\pi\pi^*$ lifetimes of protonated benzimidazole are systematically longer, ranging from 3700 ± 1100 ps at 4.6 eV pump energy to 400 ± 200 ps at 5.4 eV. Based on these experimental results, and accompanying quantum chemical calculations and potential energy surfaces (MS-CASPT2), the shorter lifetimes of protonated indazole are attributed to $\pi\sigma^*$ state mediated elongation of the protonated N-N bond.

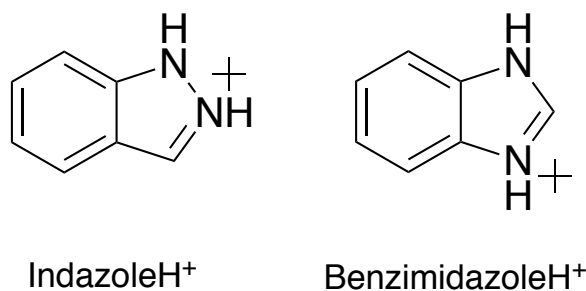


6.2 Introduction

The interplay between chemical structure, excited-state dynamics and non-radiative decay is central to understanding photostability. Particular non-radiative pathways arise when certain chemical groups are present. For example, molecules with OH and NH bonds are known to have dissociative $\pi\sigma^*$ states that lead to H atom loss,¹⁻⁴ halogen atoms bound to aromatic chromophores reliably undergo homolysis through $\pi\sigma^*$ states⁵—a process that has been exploited in mass spectrometry to make site-selected radical ions.^{6, 7} Norrish photochemistry is a well-known process characteristic of aldehydes and ketones.⁸⁻¹¹ A detailed study of pyrazole has pointed out that a $\pi\sigma^*$ state mediated dissociation of the N-N bond prevails after photoexcitation² suggesting that this could be a more general characteristic pathway.

For molecules bearing an N-N bond, photo-induced cleavage of this bond has been flagged as a practical tool in synthesis.^{12, 13} For tetrazoles, five membered heterocycles containing four N atoms and one C atom, it is known that electron attachment cleaves the N-N bond.¹⁴ Photoinduced cleavage of N-N bonds initiate photoligation reactions.¹⁵ Cationic tetrazolium dyes are used in MTT assays, which are widely used to assess cell viability because MTT changes colour (and breaks an N-N bond) when chemically reduced in a viable cell.¹⁶⁻¹⁸ The N-N bond occurs in drug molecules like allopurinol and important photochemical molecules like benzotriazole dyes.^{19, 20} Although the excited state deactivation for N-N bond containing six-membered rings has been investigated for molecules like pyridazine,²¹⁻²⁴ these studies focused on the interplay of $\pi\pi^*$ and $n\pi^*$ states rather than the possible role of photo-induced N-N bond dissociation. Overall, however, the non-radiative decay mechanism for photoactivated N-N bond dissociation has not been extensively studied.

In this paper, we target the excited-state deactivation pathways of protonated indazole (indazoleH⁺) and protonated benzimidazole (benzimidazoleH⁺) in the gas phase. These ions are structural isomers that vary in the position of the nitrogen atoms. The nitrogen atoms are placed at either the 1 and 2 positions for indazoleH⁺ or at the 1 and 3 positions for benzimidazoleH⁺ (Scheme 1). As will be shown, the presence of an N-N bond in indazoleH⁺ results in a particular UV excited-state deactivation mechanism, which results in lifetimes *ca.* two order of magnitude shorter compared with benzimidazoleH⁺.



Scheme 1: Structures of indazoleH⁺ and benzimidazoleH⁺.

Indazole and benzimidazole are fundamental chromophores and are structurally similar to pyrazole, purine-based nucleobases and are building blocks for many photoactive molecules (including photoactive molecules in cationic form²⁵⁻²⁷). Neutral indazole²⁸⁻³⁸ and benzimidazole^{32, 36, 39-52} have been extensively studied—especially with focus on steady-state spectroscopy of the first two $^1\pi\pi^*$ states (1L_b and 1L_a according to Platt's notation) rather than the excited state deactivation pathways.

Although there have been many studies of their neutral counterparts, there are only a few studies on the photoproperties of indazoleH⁺ and benzimidazoleH⁺. The solution phase UV absorption of benzimidazoleH⁺^{52, 53} and the solution phase fluorescence of benzimidazoleH⁺⁵⁴ and indazoleH⁺³¹ are reported. Ground state vibrational spectroscopy using infrared multi-photon dissociation (IRMPD) of indazoleH⁺ in the gas phase confirmed protonation occurs on the N atom lone pair.³⁵ A recent study observed the formation of benzimidazoleH⁺ from photodissociation of the neutral benzimidazole dimer, involving excited-state charge-coupled proton transfer.⁵⁵ To our knowledge, the non-radiative decay of electronically photoexcited indazoleH⁺ and benzimidazoleH⁺ has not been studied.

A $\pi\sigma^*$ mediated N-N bond dissociation process is believed to dominate for photoexcited pyrazole (analogous to the five-membered ring of neutral indazole).² This pathway is barrierless and calculated to proceed on a timescale of *ca.* 130 fs,² in agreement with the experimental measurement lifetimes of 50-160 fs for photon energies > 5 eV.⁵⁶ It should be noted, however, that there is some disagreement over the dominant process responsible for the observed pyrazole lifetimes.^{2, 56, 57} It remains that this N-N bond dissociation pathway is an interesting observation that warrants further investigation.

A more common deactivation pathway for aromatic heterocycles is out-of-plane (OOP) ring puckering leading to a conical intersection (CI) between a ¹ππ* state and the ground state. For example, indole,^{58, 59} pyrazole,^{4, 57, 60} imidazole^{3, 57, 60-63} and protonated pyridine⁶⁴ all undergo OOP ring deformation to non-radiatively decay to the ground state.

To study these photodissociation pathways, we undertake gas-phase pump-probe photodissociation experiments of protonated indazole (indazoleH⁺) and protonated benzimidazole (benzimidazoleH⁺). Experimental results reported here are supported by multi-reference and coupled cluster quantum chemical calculations. It will be shown that benzimidazoleH⁺ has an excited state lifetime that is two orders of magnitude longer than that of indazoleH⁺, since indazoleH⁺ decays on the picosecond timescale *via* a πσ* state driven N-N bond cleavage.

6.3 Experimental

Indazole and benzimidazole were purchased from AKSCIENTIFIC and used without further purification. Solutions of either indazole or benzimidazole were made up to a concentration of *ca.* 1 μM in HPLC grade methanol with 1 % (v/v) formic acid.

6.3.1 Photodissociation action spectroscopy mass spectrometry

The experimental setup utilised for photodissociation (PD) and PD action spectroscopy are described in detail elsewhere.⁶⁵ A linear ion trap mass spectrometer (Thermo LTQ XL) was coupled to a tuneable wavelength laser system composed of an Nd:YAG laser (Spectra-Physics QuantaRay INDI), which pumped an optical parametric oscillator (GWU Flexiscan). Following electrospray ionisation (ESI), protonated ions are guided into the ion trap where they are *m/z* selected and stored for 220 ms. During this storage time, the ions are irradiated by a single nanosecond laser pulse, which accesses the trap through a quartz window on the rear of the mass spectrometer. This setup provides very good overlap between the ion cloud and the laser beam.⁷ After *ca.* 50 ms the ions are scanned out of the ion trap and a mass spectrum is recorded. This process is repeated over photon wavelengths 400 – 230 nm for protonated imidazole and 320 – 230 nm for protonated benzimidazole at a 2 nm step size with *ca.* 100 mass spectra recorded and averaged at each wavelength. The photoproduct ion signal is normalised to the total ion count and the laser power. The laser power is measured after each action scan using a power meter (Gentec 11MAESTRO).

6.3.2 Photodissociation pump-probe spectroscopy mass spectrometry

Pump-probe photodissociation (PD) experiments were undertaken using an equivalent setup to that used for action spectroscopy in a different—but similar—ion trap mass spectrometer (Thermo LTQ VELOS operated in the low-pressure ion trap) and, in this setup, two picosecond laser pulses are directed through the ion trap. A schematic of the experimental setup is shown in Figure 6.1. Picosecond pulses are generated with a laser (PL2251, EKSPLA) composed of a passively mode-locked diode-pumped master oscillator with Nd:YVO₄ gain medium, a diode pumped Nd:YAG regenerative amplifier and flash-lamp pumped Nd:YAG power amplifier. The third harmonic output (355 nm) was used to pump an optical parametric generator (PG401 OPG, EKSPLA). This setup outputs picosecond pulses of tuneable wavelength in the 213 – 340 nm and 370 – 700 nm range with a linewidth of *ca.* 10 cm⁻¹ and a repetition rate of 20 Hz. For pump-probe PD experiments, this tuneable output of the OPG is the *pump* pulse and the 532 nm output from the Nd:YAG pump-laser is the *probe* pulse (see inset of Figure 6.1). The delay between the pump and probe pulses is controlled using a mechanical delay stage (ODL220 Thorlabs).

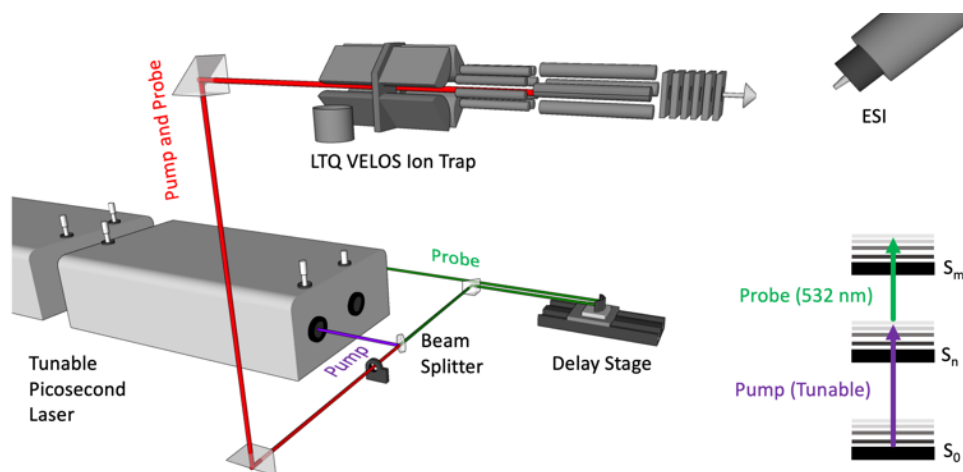


Figure 6.1: Schematic of the experimental setup.

Ions are generated, isolated, and stored in the ion trap using the same method as described above for PD action spectroscopy, except for the ion storage time (110 ms for pump-probe experiments). Only one pump laser pulse and a one probe pulse irradiate the ions during the ion storage time. The ions are then scanned out of the ion trap and a mass spectrum is acquired. This is repeated to record photodissociation mass spectra across a range of pump-probe delay

times. Delays (between pump and probe) either ranged from –300 to 1200 ps at a step size of 13.3 ps, or ranged from –70 to 690 ps at a step size of 6.7 ps. At each delay step, *ca.* 100 mass spectra were recorded, averaged, and normalised to the total ion count.

Tuneable pump-pulse energies were *ca.* 0.1 mJ (depending on the wavelength) and probe-pulse energy was *ca.* 2.5 mJ. The laser cross correlation (instrument response function) was 13 ± 3 ps. Collisions between an ion in the trap and the He buffer gas (*ca.* 400 μ Torr for similar arrangements⁶⁶) are expected to occur on the microsecond timescale within the low pressure ion trap of the dual-trap LTQ VELOS Pro (Thermo Scientific). Our experiments are, therefore, expected to be collision-free on the nanosecond and picosecond timescales relevant in this study.

6.3.3 Computational Details

Optimisation of ground state and excited state geometries were undertaken using time-dependant density functional theory (TD-DFT) employing the wB97X-D functional⁶⁷ with the aug-cc-pVDZ basis set^{68, 69} using the Gaussian16.⁷⁰ Vibrational frequencies were calculated at the optimised geometries to confirm the geometries correspond to minima by the absence of imaginary frequencies. Electronic energies of optimised structures were re-calculated with the coupled cluster singles doubles and non-iterative triples CCSDR(3)^{71, 72} method using the TZVP⁷³ basis set using the Dalton package,⁷⁴ with virtual orbitals above 98 eV and core orbitals frozen. Transition densities were calculated using these wB97X-D/aug-cc-pVDZ ground state geometries with the double hybrid ω B2PLYP method,⁷⁵ employing the aug-cc-pVTZ basis set⁶⁸ in the ORCA/4.2.1 package.⁷⁶

CASSCF⁷⁷⁻⁸² and MS-CASPT2^{83, 84} calculations were undertaken using the OpenMolcas package⁸⁵ with the cc-pVDZ basis set. For CASSCF optimisations and subsequent MS-CASPT2 energies of excited states that retained the same symmetry as the ground state, an active space CASSCF(10,9) was employed with the full π system only. CASSCF calculations involved a state averaged wavefunction including four states. Core orbitals were frozen. To avoid intruder states, an imaginary level-shift of 0.02 au was employed for MS-CASPT2 calculations.

The CASSCF(12,11)/cc-pVDZ method and basis set was used to optimise the ground state and excited states without symmetry constraints. To confirm that the optimised ground and excited states correspond to true minima, vibrational frequencies for these states were calculated. CASSCF(12,11) calculations employed an active space of 12 electrons and 11 orbitals including four π orbitals, three π^* orbitals, two σ orbitals and two corresponding σ^* orbitals. One of the σ orbitals and one corresponding σ^* orbital were rotated out of the active space of indazoleH⁺ and replaced with a different σ orbital and σ^* orbital in order to correctly describe the minimum energy crossing points (MECPs) between $\pi\sigma^*$ states and the S₀ state along the C-N bond or second N-H bond elongation coordinates (see Figures 6.S1 and 6.S2 of Supporting Information). This method, basis set, and active space were also used to optimise eight MECPs between S₁ states and the S₀ ground state, (which will be referred to here as S₁/S₀ in general; or $^1\pi\sigma^*/S_0$, $^1L_b/S_0$ or $^1L_a/S_0$ MECPs depending on the character of the states involved), as well as between S₁ and S₂ states, (S₁/S₂ in general; or $^1L_b/^1\pi\sigma^*$ or $^1L_a/^1\pi\sigma^*$ MECPs), for both indazoleH⁺ and benzimidazoleH⁺. The electronic energies of these structures were then calculated using MS-CASPT2/cc-pVDZ. Unless otherwise stated, the MS-CASPT2 energies reported here correspond to relative electronic energies that are not zero-point energy corrected to allow straightforward comparison between energies of stationary points with energies at crossing points. Triplet electronic states were calculated using the same method, basis set, and active space as singlet states. Attempts to optimise $^1L_a/^3\pi\sigma^*$ crossing points were unsuccessful due to nearby $^1\pi\sigma^*$ and $^3\pi\pi^*$ states.

Energy surfaces were calculated by interpolating the optimised ground state geometry to an optimised crossing-point geometry. This was performed by either linear interpolation of internal coordinates or a curved interpolation of internal coordinates. Detailed descriptions of these interpolation procedures can be found in Section SI.2 of the Supporting Information. Briefly, for linear interpolation of internal coordinates, each atom is progressed along a path between an initial and final structure in a linear path. For curved interpolation of internal coordinates, each atom is stepped along a path between the initial and final structure where the path that each atom takes is a quarter-ellipse. The curved interpolation of internal coordinates was deployed to avoid very short bond lengths (leading to large, erroneous barriers) that appear when attempting to linearly interpolate two significantly distorted geometries.

6.4 Results and Discussion

6.4.1 Photodissociation Action Spectroscopy

Photodissociation action spectra of room temperature benzimidazoleH⁺ and indazoleH⁺ ions are shown in Figure 6.2. These spectra track the formation of the m/z 92 product ion arising from 27 Da loss—presumably HCN or HNC. The photodissociation of benzimidazoleH⁺ onsets at *ca.* 4.5 eV (270 nm), whereas the photodissociation of indazoleH⁺ begins *ca.* 4.0 eV (310 nm). No H atom loss is observed. This H loss channel is important for indole⁵⁹ and protonated *n*-azaindoles⁸⁶ (isomeric to indazoleH⁺ and benzimidazoleH⁺) and is an important channel for non-radiative decay of imidazole and pyrazole,^{3, 4, 56, 57, 60-63} so it is notably absent for indazoleH⁺ and benzimidazoleH⁺.

The photodissociation action spectra are dominated by ¹pp* states, labelled here with Platt notation.⁸⁷ Details of Platt notation assignments are provided in Supporting Information Section SI.3 and are based upon transition densities and orbital contributions.^{88, 89} The first singlet excited state (S₁) of indazoleH⁺ is the ¹L_a state—presumably responsible for the onset of the spectrum—while the ¹L_b state is observed around 4.7 eV. This ordering is a reversal of the ordering reported for the neutral (*i.e.* not protonated) form.^{29, 32-34, 36} The rather broad photodissociation band for benzimidazoleH⁺ is attributed to overlapping ¹L_b and ¹L_a states. It is not possible to assign this broad band because the dip in signal at ~4.9 eV occurs at a region of a UV crystal change of the OPO laser. Calculated transition energies of the ¹L_a and ¹L_b states of both indazoleH⁺ and benzimidazoleH⁺ are shown in Table 6.2 in Supporting Information. For benzimidazoleH⁺, the CCSDR(3) calculated vertical transition energies to the ¹L_b and ¹L_a states are 5.04 eV and 5.41 eV, respectively. However, when the excited state is optimised maintaining C_{2v} symmetry the ¹L_a state has a lower calculated adiabatic transition energy (4.79 eV) than ¹L_b (4.81 eV). The states of indazoleH⁺ are probably distinguishable in the action spectrum, with calculated adiabatic transition energies (maintaining C_s symmetry) are more separated at 4.21 eV for ¹L_a and 4.89 eV for ¹L_b. The key result from these photodissociation action spectra are that the indazoleH⁺ spectrum onsets at lower energy than benzimidazoleH⁺ and that both the ¹L_a and ¹L_b states can be populated in this UV region depending on the photon energy.

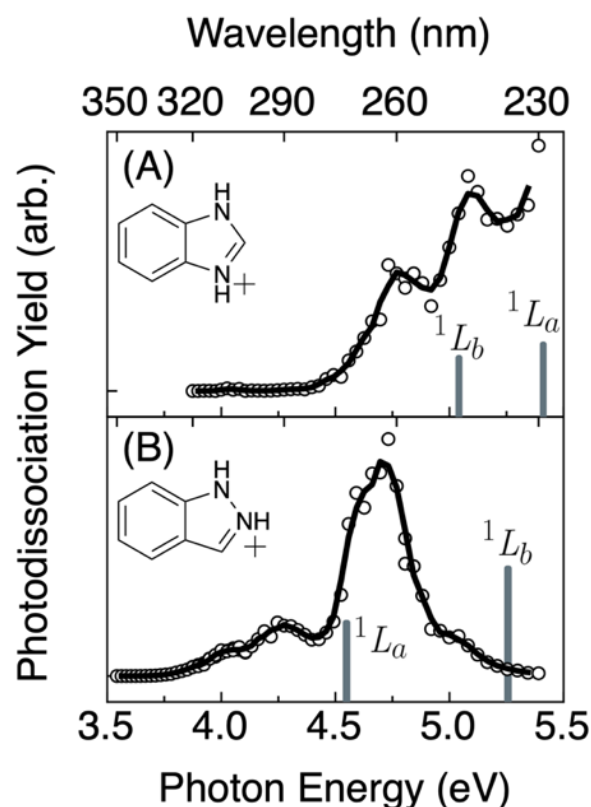


Figure 6.2: UV Photo-dissociation action spectra of benzimidazoleH⁺ (top) and indazoleH⁺ (bottom) following loss of HCN (27 Da) to form the *m/z* 92 photoproduct. The black trace follows a rolling average of the three adjacent data points. Unshifted vertical transition energies calculated using CCSDR(3)/TZVP employing ω B97X-D/aug-cc-pVDZ geometries are shown (vertical bars).

6.4.2 Pump-Probe PD

As mentioned, the major photoproduct observed for benzimidazoleH⁺ and indazoleH⁺ is *m/z* 92, which corresponds to a loss of 27 Da (HCN or HNC). For indazoleH⁺, a *m/z* 91 photoproduct corresponding to loss of N₂ is observed at lower photon energies (< 4 eV) but becomes an increasingly minor product at photon energies > 4 eV (see Figure 6.12 in Supporting Information). A low signal photoproduct is observed at *m/z* 65 for both indazoleH⁺ and benzimidazoleH⁺ corresponds to loss of 54 Da (2HCN or H₂C₂N₂) presumably is C₅H₅⁺ and the structure of this ion is unknown (e.g. cyclic or linear). The loss of these HCN neutral fragments occur for similar protonated nitrogen containing heterocycles.^{86, 90-92} It is observed that when tandem pump (260 nm) and probe (532 nm) laser pulses are used, the *m/z* 65 photoproduct intensity increases. As evidenced by the action spectra in Figure 6.2, no PD of benzimidazoleH⁺ or indazoleH⁺ occurs from the 532 nm probe pulse alone and therefore the increase in *m/z* 65 signal from the 260 nm (pump) + 532 nm (probe) pulses is interpreted as transient absorption of the 532 nm photons enhancing the formation of the *m/z* 65 photoproduct. For individual PD mass spectra see Figure 6.13 in Supporting Information.

Pump-probe PD plots of indazoleH⁺ are shown in Figure 6.3 following the formation of the *m/z* 65 photoproduct as a function of pump-probe delay, scanning pump wavelengths between 4.00 – 4.77 eV (310 – 260 nm). Probe pulse is fixed at 532 nm. The plots for benzimidazoleH⁺ are shown in Figure 6.4, following the formation of the *m/z* 65 photoproduct with the exception of pump photon of 4.6 eV, which tracks the *m/z* 92 photoproduct. The range of pump energies for benzimidazoleH⁺ is 4.6 – 5.4 eV (270 – 230 nm). All pump-probe PD experiments employed a probe energy of 2.33 eV (532 nm).

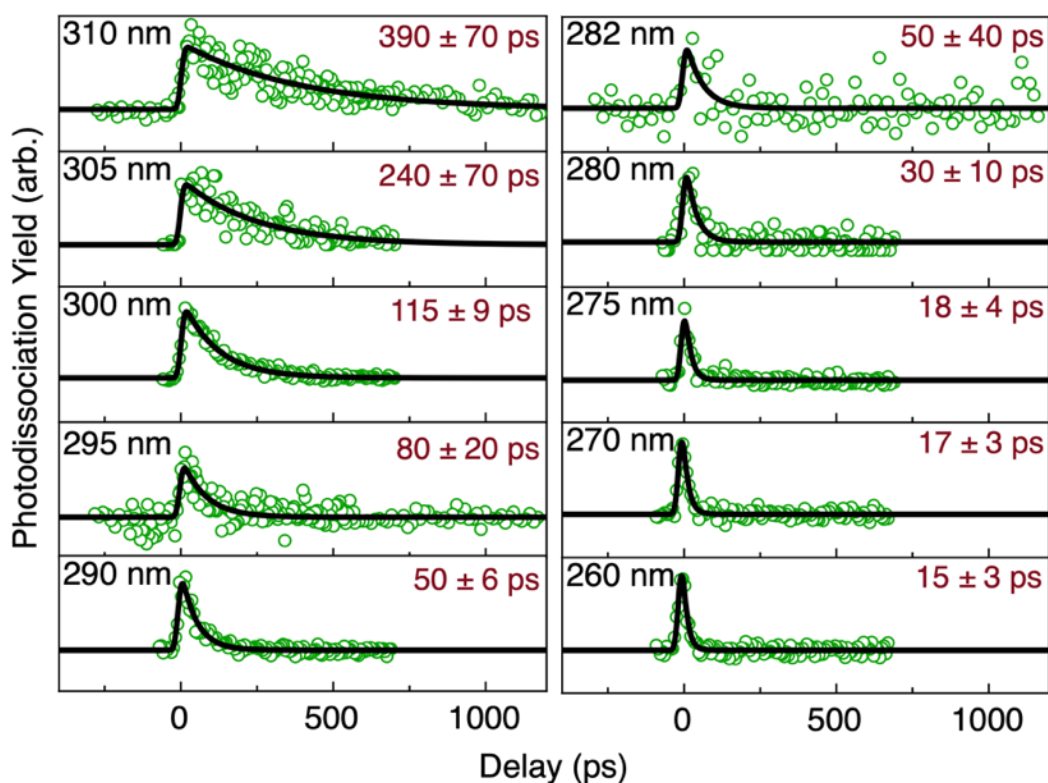


Figure 6.3: Pump-probe photodissociation spectra of indazoleH⁺ following the *m/z* 65 photoproduct. Pump photon energies are indicated. Probe photon energy is 2.33 eV (532 nm). Several traces are truncated to a maximum delay of 690 ps by experimental limitations early in the data collection. Multiple repeat experiments are combined and presented for data corresponding to pump energies of 4.0 eV (310 nm), 4.2 eV (295 nm) and 4.6 eV (270 nm). Individual experiments are presented in Figure 6.14 of Supporting Information.

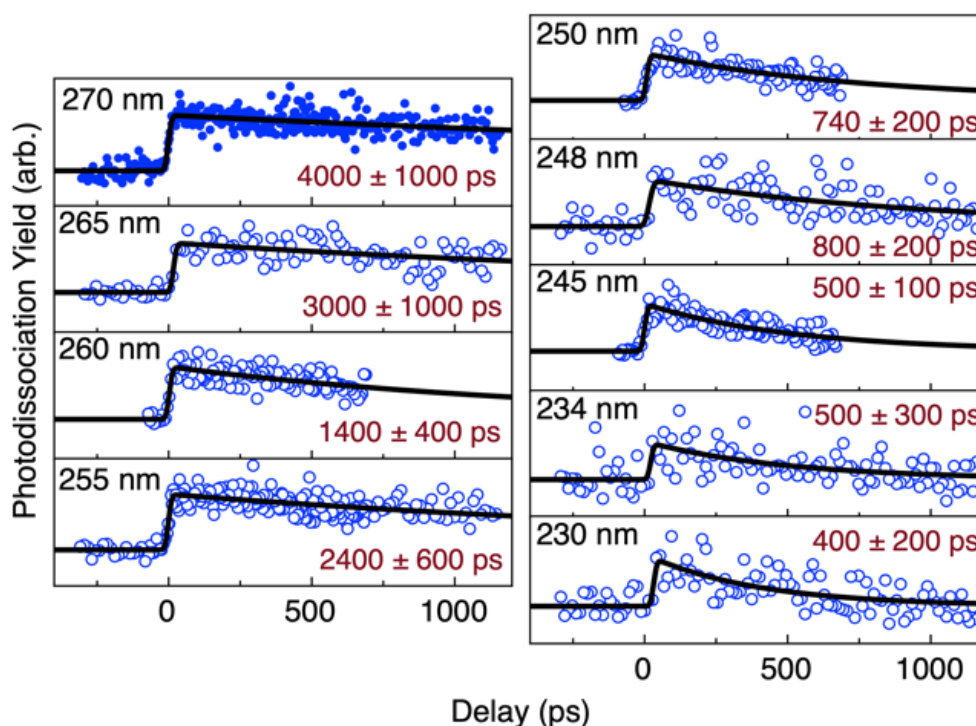


Figure 6.4: Pump-probe photodissociation spectra of benzimidazoleH⁺ following the m/z 65 photoproduct for all pump wavelengths except 4.6 eV (270 nm), which follows the 92 m/z fragment (solid circles). Pump photon energies are indicated. Probe photon energy is 2.33 eV (532 nm). Several traces are truncated to a maximum delay of 690 ps by experimental limitations earlier in the data collection. Multiple repeat experiments are combined and presented for data taken using 4.6 eV (270 nm) and 4.9 eV (255 nm) pump photons. Individual experiments are presented in Figure 6.15 of Supporting Information.

Following Soorkia *et al.*,⁹³ the pump-probe PD plots are fit to Equation 1, where t_0 represents the 0 time delay between pulses, t is the pump-probe delay. This equation is an error response function (erf) that accounts for the temporal widths of the pump and probe laser pulses (with a cross-correlation of $l_0 = 13$ ps) and an exponential decay giving the time constant τ , which is the excited-state lifetime.

$$S(t) = 1/2 \left[1 + \operatorname{erf}\left(\frac{t-t_0}{l_0}\right) \right] \exp\left(-\frac{t-t_0}{\tau}\right) \quad \dots(1)$$

The fitted indazoleH⁺ lifetimes range from 390 ± 70 ps at 4.00 eV (310 nm) to ≤ 18 ps at 4.77 eV (260 nm). BenzimidazoleH⁺ lifetimes range from 3700 ± 1100 ps at 4.60 eV (270 nm) to 400 ± 200 ps at 5.40 eV (230 nm). All lifetimes are summarised in Figure 6.5, with indazoleH⁺ (green) and benzimidazoleH⁺ (blue). As the pump pulse energy increases the lifetimes consistently decrease. The lifetimes of indazoleH⁺ are significantly and consistently shorter

than benzimidazoleH⁺ across all energies. The error bars in Figure 6.5 are reported as $\pm 2\sigma$ extracted from the Levenberg-Marquardt fit of the decay data.

A plot of the decay lifetimes as a function of photon energy relative to the calculated 0-0 value, which can be interpreted as excess energy, is shown in Figure 6.16 in Supporting Information. It is clear from both Figures 6.5 and 6.S9 that indazoleH⁺ has a shorter lifetime by *ca.* x100 than benzimidazoleH⁺ even when they have the same internal energy relative to the excited state origin. To explore the origins of this difference, quantum chemical calculations using the MS-CASPT2 method are now reported and discussed.

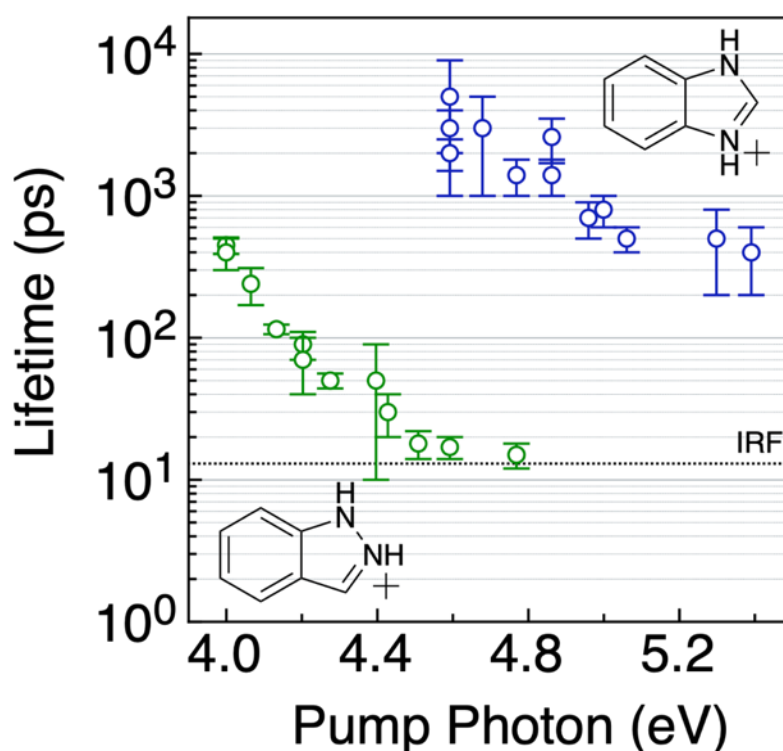


Figure 6.5: Plot of the decay lifetime of benzimidazoleH⁺ (blue) and indazoleH⁺ (green) as a function of pump photon energy. The dotted line indicates the instrument response function (IRF), which corresponds to the 13 ps laser cross-correlation.

6.4.3 Minimum Energy Crossing Points and PES

As established from the experimental pump-probe PD results, the excited-state lifetimes of indazoleH⁺ are consistently shorter than those of benzimidazoleH⁺. To guide the explanation of this observation, minimum energy crossing points (MECPs) between relevant excited states and the S₀ ground state have been located. The structures of these S₁/S₀ MECPs and MS-CASPT2/cc-pVDZ energy values along interpolated pathways from the optimised ground state

(S₀) to these S₁/S₀ MECPs are shown in Figure 6.17 and Figure 6.18 in Supporting Information. Based on their barrier heights, most of the pathways are unfavourable and will therefore not be further discussed.

The most favourable calculated pathway from the excited state to the ground state is shown for both indazoleH⁺ (Figure 6.6A) and benzimidazoleH⁺ (Figure 6.7). The pathway for indazoleH⁺ involves elongating the N-N bond described by a ¹πσ* state (green trace in Figure 6.6A) or a ³πσ* state (purple trace) and will be referred to as the indazoleH⁺-NN pathway. The two relevant pathways are: (i) ¹L_a → ¹πσ* → S₀ or (ii) ¹L_a → ³πσ* → S₀. Ultimately, the formation of the *m/z* 65 product ion presumably proceeds off the activated ground-state although data presented here do not provide any direct insight into this.

Pathway (i) starts on the ¹L_a state and leads to a MECP between the ¹L_a and the ¹πσ* state (referred to as a ¹L_a/¹πσ* MECP) followed by a MECP between the ¹πσ* and the ground state (referred to as a ¹πσ*/S₀ MECP). Both the ¹L_a/¹πσ* and ¹πσ*/S₀ MECP points in Figure 6.6A correspond to optimised geometries using the CASSCF(12,11)/cc-pVDZ level of theory. Notably, from to the ground state geometry, there is only a small nuclear displacement required to reach the ¹L_a/¹πσ* MECP (3.45 Å amu^{1/2}) and ¹πσ*/S₀ MECP (5.78 Å amu^{1/2}). The key orbitals involved in the πσ* state are shown in Figure 6.6B.

In the case of (ii), the ¹L_a → ³πσ* → S₀ pathway involves intersystem crossing from the ¹L_a state to the ³πσ* state. The ³πσ* is *ca.* 0.5 eV lower in energy than the ¹πσ* state and, therefore, this pathway is energetically favoured. Intersystem crossing from the ¹L_a (¹ππ*) state to the ³πσ* state should be viable based on the El-Sayed rules.^{94, 95} Quantifying the likelihood that deactivation occurs *via* the ³πσ* state versus the ¹πσ* state is beyond the scope of this study.

Intersystem crossing between ¹ππ* and ³ππ* should be unfavourable according to El-Sayed rules.^{94, 95} Therefore, the only viable path onto the triplet manifold calculated for these molecules is by intersystem crossing from a ¹ππ* state to a ³πσ* state and the ³ππ* states are omitted from Figures 6.6 and 6.7. PESs including ³ππ* states are shown in Supporting Information Figure 6.18.

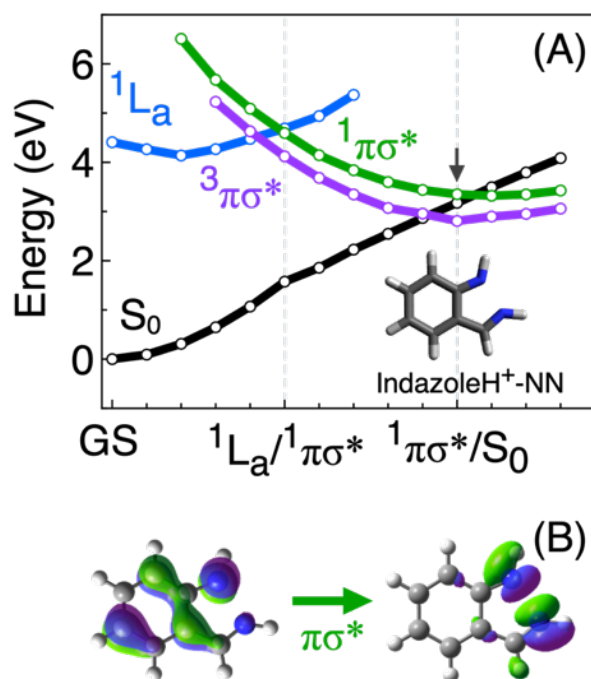


Figure 6.6: Calculated potential energy surface interpolating between the optimised ground state of indazoleH⁺ and several optimised crossing points. Panel (A) is constructed by linear interpolation between the ground state and an optimised $^1L_a/^1\pi\sigma^*$ (S_2/S_1) MECP followed by linear interpolation to an optimised $^1\pi\sigma^*/S_0$ (S_1/S_0) MECP. Ground state and MECP geometries were optimised using CASSCF(12,11)/cc-pVDZ and electronic energies were calculated using MS-CASPT2/cc-pVDZ. (B) MS-CASPT2 calculated key orbitals that contribute to the $\pi\sigma^*$ state for indazoleH⁺ (isovalue = 0.05). The orbitals are presented with the $^1\pi\sigma^*/S_0$ MECP nuclear geometry, which is located in (A) by the arrow.

The most favourable deactivation pathway located for benzimidazoleH⁺ corresponds to an out-of-plane OOP puckering and will be referred to as the benzimidazoleH⁺-OOP pathway. This benzimidazoleH⁺-OOP pathway leads directly to a MECP between the 1L_b state and the S_0 state (referred to as a $^1L_b/S_0$ MECP). The interpolated geometry points plotted between the S_0 state and the $^1L_b/S_0$ MECP do not correspond to the minimum energy path and hence, only serve as upper bounds for the energy barrier of this pathway. The lower bound is the energy of the MECP itself. Therefore, the calculated upper bound for the barrier along the benzimidazoleH⁺-OOP pathway is 5.58 eV and the lower bound is 5.39 eV (taken as the 1L_b energy at the optimised $^1L_b/S_0$ MECP). Comparing the two pathways in Figures 6.6A and 6.7, the benzimidazoleH⁺-OOP pathway appears less favourable than the $^1\pi\sigma^*$ driven indazoleH⁺-NN pathway, which has a maximum barrier energy of 4.64 eV that corresponds to the energy at the optimised $^1L_a/^1\pi\sigma^*$ (S_1/S_2) MECP. The $^3\pi\sigma^*$ driven indazoleH⁺-NN pathway is the most energetically favourable with a maximum barrier of 4.52 eV at the $^1L_a/^3\pi\sigma^*$ crossing point and

attempts to optimise this ${}^1L_a/{}^3\pi\sigma^*$ crossing point were unsuccessful and this barrier energy is an upper bound.

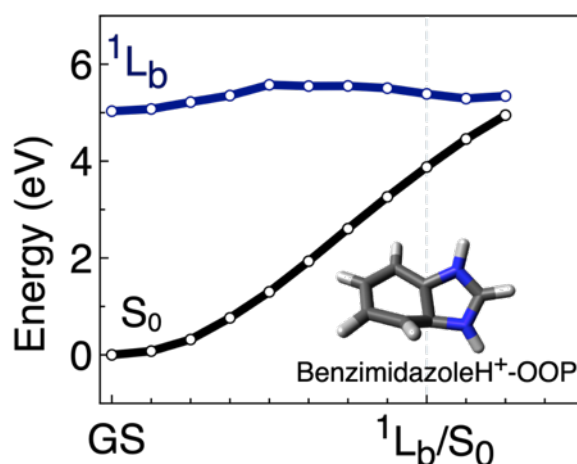


Figure 6.7: Calculated potential energy surfaces interpolating between the optimised ground state of benzimidazoleH⁺ and an optimised ${}^1L_b/S_0$ (S_1/S_0) MECP. This surface is constructed by curved interpolation between the optimised S_0 geometry and an optimised ${}^1L_b/S_0$ (S_1/S_0) MECP. Ground state and MECP geometries were optimised using CASSCF(12,11)/cc-pVDZ and electronic energies were calculated using MS-CASPT2/cc-pVDZ.

The benzimidazoleH⁺-OOP MECP (optimised at the CASSCF level of theory) has an ${}^1L_b - S_0$ energy gap of approximately 1 eV (MS-CASPT2) at the MECP geometry. The ${}^1L_b - S_0$ energy gap only becomes close after extrapolating past the optimised MECP. A similar discrepancy between CASSCF and MS-CASPT2 was observed by other groups for similar OOP crossing points.⁹⁶⁻⁹⁸ It is worth noting that an error of 0.2 eV is typical for MS-CASPT2 and CASSCF geometries compounds this problem.^{99, 100} Nevertheless, even when the accuracy of these methods are accounted for the indazoleH⁺-NN pathway is significantly more energetically favourable than any of the other pathways calculated here.

6.5 Discussion

The pump-probe PD experiments reveal that indazoleH⁺ has an excited-state lifetime in the UV that is approximately two orders of magnitude shorter than that of benzimidazoleH⁺. From the indazoleH⁺ MS-CASPT2 results, the energetically favourable pathways calculated from the 1L_a excited state to the ground state involve elongation of the N-N bond *via* an unbound ${}^1\pi\sigma^*$ or ${}^3\pi\sigma^*$ state. The rate-limiting barrier energy for deactivation through these $\pi\sigma^*$ states occurs where they intersect the 1L_a state, corresponding to an energy of 4.64 eV for the ${}^1L_a/{}^1\pi\sigma^*$

MECP and 4.52 eV for the ${}^1L_a/{}^3\pi\sigma^*$ crossing point. Both indazoleH⁺ pathways are energetically more favourable than the most favourable pathway located for benzimidazoleH⁺, which corresponds to the OOP ring puckering. Therefore, we attribute the much shorter excited state lifetimes observed for indazoleH⁺ to the relatively facile indazoleH⁺-NN pathway, which involves elongation of the N-N bond *via* an unbound ${}^1\pi\sigma^*$ or ${}^3\pi\sigma^*$ state.

The indazoleH⁺-NN pathway is similar to deactivation processes reported for neutral pyrazole.² Deactivation *via* the N-N coordinate, however, is slower for indazoleH⁺ (~10 – 400 ps) compared to pyrazole (~100 fs).^{2, 56} This difference is unsurprising because the deactivation pathway is calculated to be barrierless for pyrazole² but this does not appear to be the case for indazoleH⁺. Nevertheless, these results indicate that a fundamentally facile deactivation pathway involving the $\pi\sigma^*$ state driven nonadiabatic N-N dissociation could be common in N-N bond containing aromatic heterocycles and—as observed for indazoleH⁺—this deactivation pathway can occur for protonated N-N systems.

Determining the key deactivation pathway for benzimidazoleH⁺ is less straightforward. While the benzimidazoleH⁺-OOP pathway is the most favourable of the pathways calculated for benzimidazoleH⁺ in this study, it requires significant deformation of the heavy atoms with a total nuclear displacement of 20.61 Å amu^{1/2}. Higher barriers for excited state deactivation of benzimidazoleH⁺ are consistent with the longer lifetimes observed for benzimidazoleH⁺. However, while it is possible that the deactivation along the benzimidazoleH⁺-OOP pathway occurs for benzimidazoleH⁺ (especially at higher photon energies), it is also possible that deactivation is dominated by other pathways that were not calculated here including fluorescence. When a 4.60 eV (270 nm) pump energy is used, the 532 nm probe pulse increases the total PD yield for benzimidazoleH⁺ by a factor of 5.6 ± 1.2 relative to when only the pump pulse is used, which is consistent with the presence of non-dissociative fluorescence. This argument follows that of Broquier *et al.* for protonated 3-aminopyridine and 2-aminopyridine, where photodissociation yield was increased by introducing a probe pulse and this was interpreted as possible fluorescence deactivation rather than photodissociation.¹⁰¹ In contrast, for indazoleH⁺ no significant increase in the PD yield (1.2 ± 0.2) was measured with the inclusion of the probe pulse (with a pump photon energy of 4.0 eV).

6.6 Conclusions

The UV excited-state lifetime of gas-phase indazoleH⁺ is measured to be about two orders of magnitude shorter than that of its isomer, benzimidazoleH⁺ using pump-probe photodissociation across a range of pump photon energies. By comparison with MS-CASPT2 calculations, this difference in lifetimes is explained by indazoleH⁺ accessing a facile elongation pathway involving a ¹πσ* state or a ³πσ* state that drives non-adiabatic elongation of the N-N bond. This pathway is non-existent for benzimidazoleH⁺ as it contains no N-N bonds. In this UV region, the excited-state lifetime of indazoleH⁺ ranges from 390 ± 70 ps down to ≤ 18 ps and benzimidazoleH⁺ ranges from several nanoseconds to 400 ± 200 ps (depending on the excitation energy). The results presented here show that the UV activated N-N elongation pathway is relevant for protonated systems. Future work is required to reveal the generality of πσ* state-driven N-N elongation pathways and whether it has broader importance for N-N functionalized photoactive heterocycles.

Supporting Information

See Supporting Information for CASSCF active space, interpolation details, Platt notation (L_a and L_b) character analysis, photodissociation mass spectra, averages of pump-probe photodissociation plots, additional MS-CASPT2 deactivation pathways, potential energy surface values and coordinates for optimised geometries.

Acknowledgements

Australian Research Council grant support is gratefully acknowledged (DP200100065). Support for picosecond lasers provided by Australian Research Council LIEF Funding Scheme (LE180100060) and supported by the University of Wollongong. Computational resources accessed through the National Computational Merit Allocation Scheme of the Australian Government through the NCI. S.J.P.M, B.J.M, B.U, and O.J.S acknowledge support provided by the Australian Government Research Training Program Scholarships.

References

1. Sobolewski, A. L.; Domcke, W.; Dedonder-Lardeux, C.; Jouvét, C., Excited-state hydrogen detachment and hydrogen transfer driven by repulsive ¹πσ* states: a new paradigm for nonradiative decay in aromatic biomolecules. *Physical Chemistry Chemical Physics* **2002**, *4* (7), 1093-1100.

2. Xie, B.-B.; Liu, X.-Y.; Fang, Q.; Fang, W.-H.; Cui, G., The position of the N atom plays a significant role for excited-state decay of heterocycles. *The Journal of Physical Chemistry Letters* **2017**, *8* (5), 1019-1024.
3. Devine, A. L.; Cronin, B.; Nix, M. G.; Ashfold, M. N., High resolution photofragment translational spectroscopy studies of the near ultraviolet photolysis of imidazole. *The Journal of chemical physics* **2006**, *125* (18), 184302.
4. King, G. A.; Oliver, T. A.; Nix, M. G.; Ashfold, M. N., Exploring the mechanisms of H atom loss in simple azoles: Ultraviolet photolysis of pyrazole and triazole. *The Journal of chemical physics* **2010**, *132* (6), 02B604.
5. Sage, A. G.; Oliver, T. A.; Murdock, D.; Crow, M. B.; Ritchie, G. A.; Harvey, J. N.; Ashfold, M. N., $n\sigma^*$ and $\pi\sigma^*$ excited states in aryl halide photochemistry: a comprehensive study of the UV photodissociation dynamics of iodobenzene. *Physical Chemistry Chemical Physics* **2011**, *13* (18), 8075-8093.
6. Ly, T.; Julian, R. R., Residue-specific radical-directed dissociation of whole proteins in the gas phase. *Journal of the American Chemical Society* **2008**, *130* (1), 351-358.
7. Narreddula, V. R.; McKinnon, B. I.; Marlton, S. J.; Marshall, D. L.; Boase, N. R.; Poad, B. L.; Trevitt, A. J.; Mitchell, T. W.; Blanksby, S. J., Next-generation derivatization reagents optimized for enhanced product ion formation in photodissociation-mass spectrometry of fatty acids. *Analyst* **2020**, *146*, 156-169.
8. Jockusch, S.; Landis, M. S.; Freiermuth, B.; Turro, N. J., Photochemistry and photophysics of α -hydroxy ketones. *Macromolecules* **2001**, *34* (6), 1619-1626.
9. Hill, N. S.; Coote, M. L., Internal Oriented Electric Fields as a Strategy for Selectively Modifying Photochemical Reactivity. *Journal of the American Chemical Society* **2018**, *140* (50), 17800-17804.
10. Marlton, S. J.; McKinnon, B. I.; Hill, N. S.; Coote, M. L.; Trevitt, A. J., Electrostatically Tuning the Photodissociation of the Irgacure 2959 Photoinitiator in the Gas Phase by Cation Binding. *Journal of the American Chemical Society* **2021**, *143* (5), 2331-2339.
11. Rowell, K. N.; Kable, S. H.; Jordan, M. J., Structural Effects on the Norrish Type I α -Bond Cleavage of Tropospherically Important Carbonyls. *The Journal of Physical Chemistry A* **2019**, *123* (48), 10381-10396.
12. Lebrun, S.; Couture, A.; Deniau, E.; Grandclaude, P., A practical photochemically induced method for NN bond cleavage of N, N-disubstituted hydrazides. *Synlett* **2009**, *2009* (16), 2621-2624.
13. Zhu, M.; Zheng, N., Photoinduced Cleavage of N–N Bonds of Aromatic Hydrazines and Hydrazides by Visible Light. *Synthesis* **2011**, *2011* (14), 2223.
14. Luxford, T.; Fedor, J.; Kočišek, J., Electron attachment to tetrazoles: The influence of molecular structure on ring opening reactivity. *The Journal of Chemical Physics* **2021**, *154* (21), 214303.
15. Marshall, D. L.; Menzel, J. P.; McKinnon, B. I.; Blinco, J. P.; Trevitt, A. J.; Barner-Kowollik, C.; Blanksby, S. J., Laser Photodissociation Action Spectroscopy for the Wavelength-Dependent Evaluation of Photoligation Reactions. *Analytical Chemistry* **2021**.
16. Mosmann, T., Rapid colorimetric assay for cellular growth and survival: application to proliferation and cytotoxicity assays. *Journal of Immunological Methods* **1983**, *65* (1-2), 55-63.
17. Stockert, J. C.; Horobin, R. W.; Colombo, L. L.; Blázquez-Castro, A., Tetrazolium salts and formazan products in Cell Biology: Viability assessment, fluorescence imaging, and labeling perspectives. *Acta Histochemica* **2018**, *120* (3), 159-167.

18. Zhao, J.; Zhu, R.; Zhang, X.; Zhang, B.; Liu, Y.; Li, Y.; Wang, W.; Phillips, D. L., A photoenhanced oxidation of amino acids and the cross-linking of lysozyme mediated by tetrazolium salts. *Physical Chemistry Chemical Physics* **2021**, *23* (6), 3761-3770.
19. Rocks, L.; Faulds, K.; Graham, D.; Parchaňský, V.; Bouř, P.; Blanch, E. W., Through-space transfer of chiral information mediated by a plasmonic nanomaterial. *Nature Chemistry* **2015**, *7* (7), 591-596.
20. Yen, Y. S.; Lee, C. T.; Hsu, C. Y.; Chou, H. H.; Chen, Y. C.; Lin, J. T., Benzotriazole-Containing D- π -A Conjugated Organic Dyes for Dye-Sensitized Solar Cells. *Chemistry—An Asian Journal* **2013**, *8* (4), 809-816.
21. Terazima, M.; Yamauchi, S.; Hirota, N., A time-resolved EPR study of the magnetic and decay properties of short-lived non-phosphorescent $3\pi^*$ pyridazine. *Chemical Physics Letters* **1985**, *120* (3), 321-326.
22. Holt, P. L.; Selco, J. I.; Weisman, R. B., Transient spectroscopy of pyridazine vapor: Photophysics of the S 1 origin. *The Journal of Chemical Physics* **1986**, *84* (4), 1996-2001.
23. Matsumoto, Y.; Kim, S. K.; Suzuki, T., Femtosecond photoelectron imaging of pyridazine: S 1 lifetime and (3s (n- 1), 3p (n- 1)) Rydberg state energetics. *The Journal of Chemical Physics* **2003**, *119* (1), 300-303.
24. Pino, G. A.; Feraud, G.; Broquier, M.; Grégoire, G.; Soorkia, S.; Dedonder, C.; Jouvét, C., Non-radiative processes in protonated diazines, pyrimidine bases and an aromatic azine. *Physical Chemistry Chemical Physics* **2016**, *18* (30), 20126-20134.
25. Jędrzejewska, B.; Ośmiałowski, B.; Zaleśny, R., Application of spectroscopic and theoretical methods in the studies of photoisomerization and photophysical properties of the push-pull styryl-benzimidazole dyes. *Photochemical & Photobiological Sciences* **2016**, *15* (1), 117-128.
26. Jana, P.; Patel, N.; Mukherjee, T.; Soppina, V.; Kanvah, S., A “turn-on” Michler's ketone-benzimidazole fluorescent probe for selective detection of serum albumins. *New Journal of Chemistry* **2019**, *43* (27), 10859-10867.
27. Inouchi, T.; Nakashima, T.; Kawai, T., The Origin of the Emission Properties of π -Conjugated Molecules that have an Acid-responsive Benzimidazole Unit. *Asian Journal of Organic Chemistry* **2013**, *2* (3), 230-238.
28. Byrne, J. P.; Ross, I., Electronic relaxation as a cause of diffuseness in electronic spectra. *Australian Journal of Chemistry* **1971**, *24* (6), 1107-1141.
29. Cané, E.; Trombetti, A.; Velino, B.; Caminati, W., Assignment of the 290-nm electronic band system of indazole [1, 2-benzodiazole] as $\pi^*-\pi$ by rotational band contour analysis. *Journal of Molecular Spectroscopy* **1992**, *155* (2), 307-314.
30. Cané, E.; Palmieri, P.; Tarroni, R.; Trombetti, A., Gas-phase infrared spectrum of indazole. Scaled quantum mechanical force field and complete spectrum assignment. *Journal of the Chemical Society, Faraday Transactions* **1993**, *89* (22), 4005-4011.
31. Catalan, J.; del Valle, J. C.; Claramunt, R. M.; Boyer, G.; Laynez, J.; Gomez, J.; Jimenez, P.; Tomas, F.; Elguero, J., Acidity and Basicity of Indazole and its N-Methyl Derivatives in the Ground and in the Excited State. *The Journal of Physical Chemistry* **1994**, *98* (41), 10606-10612.
32. Berden, G.; Meerts, W. L.; Jalviste, E., Rotationally resolved ultraviolet spectroscopy of indole, indazole, and benzimidazole: Inertial axis reorientation in the S 1 (1 L b) \leftarrow S 0 transitions. *The Journal of Chemical Physics* **1995**, *103* (22), 9596-9606.
33. Jalviste, E.; Temps, F., Vibronic spectroscopy of jet-cooled indazole: S 1 \leftrightarrow S 0 spectra and mode assignments. *The Journal of Chemical Physics* **1999**, *111* (9), 3898-3910.
34. Su, H.; Pradhan, M.; Tzeng, W. B., Mass analyzed threshold ionization spectroscopy of indazole cation. *Chemical physics letters* **2005**, *411* (1-3), 86-90.

35. Oomens, J.; Meijer, G.; von Helden, G., An infrared spectroscopic study of protonated and cationic indazole. *International Journal of Mass Spectrometry* **2006**, *249*, 199-205.
36. Yang, S. C.; Tzeng, W. B., Mass-analyzed threshold ionization of deuterium substituted indazole and benzimidazole and site-specific H/D exchange reaction. *Chemical Physics Letters* **2010**, *501* (1-3), 6-10.
37. Nicken, H.; Temps, F.; Jalviste, E., Dispersed Fluorescence Spectra of 1H- and 1D-Indazole. *Zeitschrift für Physikalische Chemie* **2011**, *225* (11-12), 1457-1469.
38. Catalán, J., On the solvatochromism, dimerization and tautomerism of indazole. *Arkivoc* **2014**, *2*, 57-70.
39. Gordon, R.; Yang, R. F., Vapor absorption spectra of benzoxazole, benzimidazole, and benzothiazole near 2850 Å. *Canadian Journal of Chemistry* **1970**, *48* (11), 1722-1729.
40. Maki, I.; Nishimoto, K.; Sugiyama, M.-a.; Hiratsuka, H.; Tanizaki, Y., Polarized absorption spectra of indole and benzimidazole. *Bulletin of the Chemical Society of Japan* **1981**, *54* (1), 8-12.
41. Anderson, B. E.; Jones, R. D.; Rehms, A. A.; Ilich, P.; Callis, P. R., Polarized two-photon fluorescence excitation spectra of indole and benzimidazole. *Chemical Physics Letters* **1986**, *125* (2), 106-112.
42. Cané, E.; Trombetti, A.; Velino, B.; Caminati, W., Assignment of the 278-nm electronic band system of benzimidazole [1, 3-benzodiazole] as $\pi^*-\pi$ by rotational band contour analysis. *Journal of Molecular Spectroscopy* **1991**, *150* (1), 222-228.
43. Jalviste, E.; Treshchalov, A., Spectroscopy of jet-cooled benzimidazole and benzotriazole. *Chemical Physics* **1993**, *172* (2-3), 325-338.
44. Borin, A. C.; Serrano-Andrés, L., A theoretical study of the absorption spectra of indole and its analogs: indene, benzimidazole, and 7-azaindole. *Chemical Physics* **2000**, *262* (2-3), 253-265.
45. Jacoby, C.; Roth, W.; Schmitt, M., A comparison of intermolecular vibrations and tautomerism in benzimidazole, benzotriazole and their binary water clusters. *Applied Physics B* **2000**, *71* (5), 643-649.
46. Serrano-Andrés, L.; Borin, A. C., A theoretical study of the emission spectra of indole and its analogs: indene, benzimidazole, and 7-azaindole. *Chemical Physics* **2000**, *262* (2-3), 267-283.
47. Schmitt, M.; Krügler, D.; Böhm, M.; Ratzner, C.; Bednarska, V.; Kalkman, I.; Meerts, W. L., A genetic algorithm based determination of the ground and excited (1 L b) state structure and the orientation of the transition dipole moment of benzimidazole. *Physical Chemistry Chemical Physics* **2006**, *8* (2), 228-235.
48. Schwell, M.; Jochims, H.-W.; Baumgärtel, H.; Leach, S., VUV photophysics and dissociative photoionization of pyrimidine, purine, imidazole and benzimidazole in the 7–18 eV photon energy range. *Chemical Physics* **2008**, *353* (1-3), 145-162.
49. Brand, C.; Rolf, J.; Wilke, M.; Schmitt, M., High resolution electronic spectroscopy of vibrationally hot bands of benzimidazole. *The Journal of Physical Chemistry A* **2013**, *117* (48), 12812-12820.
50. Stuhlmann, B.; Gmerek, F.; Krügler, D.; Schmitt, M., Determination of the geometry change of benzimidazole upon electronic excitation from a combined Franck-Condon/rotational constants fit. *Journal of Molecular Structure* **2014**, *1072*, 45-52.
51. Yang, P.; Pang, M.; Li, M.; Shen, W.; He, R., Vibrationally resolved 1Lb (1A') \leftrightarrow S0 (1A') electronic spectra of benzimidazole and indene: Influence of Duschinsky and Herzberg-Teller effects on weak dipole-allowed transitions. *Spectrochimica Acta Part A: Molecular and Biomolecular Spectroscopy* **2015**, *151*, 375-384.

52. Peral, F.; Gallego, E., A study by ultraviolet spectroscopy on self-association of purine, 6-methylpurine, benzimidazole, and imidazo [1, 2-a] pyridine in aqueous solution. *Spectrochimica Acta Part A: Molecular and Biomolecular Spectroscopy* **2000**, *56* (4), 747-759.
53. Jerez, G.; Kaufman, G.; Prystai, M.; Schenkeveld, S.; Donkor, K. K., Determination of thermodynamic pK_a values of benzimidazole and benzimidazole derivatives by capillary electrophoresis. *Journal of Separation Science* **2009**, *32* (7), 1087-1095.
54. Rogers, K. S.; Clayton, C., Effects of pH on benzimidazole fluorescence. *Analytical biochemistry* **1972**, *48* (1), 199-201.
55. D'mello, V. C.; Wategaonkar, S., Characterization and Photofragmentation Studies of the Benzimidazole Homodimer: Evidence for Excited-State Charge-Coupled Proton Transfer. *The Journal of Physical Chemistry A* **2021**.
56. Williams, C. A.; Roberts, G. M.; Yu, H.; Evans, N. L.; Ullrich, S.; Stavros, V. G., Exploring ultrafast H-atom elimination versus photofragmentation pathways in pyrazole following 200 nm excitation. *The Journal of Physical Chemistry A* **2012**, *116* (11), 2600-2609.
57. Symonds, C. C.; Makhov, D. V.; Cole-Filipiak, N. C.; Green, J. A.; Stavros, V. G.; Shalashilin, D. V., Ultrafast photodissociation dynamics of pyrazole, imidazole and their deuterated derivatives using ab initio multiple cloning. *Physical Chemistry Chemical Physics* **2019**, *21* (19), 9987-9995.
58. Giussani, A.; Merchan, M.; Roca-Sanjuan, D.; Lindh, R., Essential on the photophysics and photochemistry of the indole chromophore by using a totally unconstrained theoretical approach. *Journal of Chemical Theory and Computation* **2011**, *7* (12), 4088-4096.
59. Godfrey, T.; Yu, H.; Ullrich, S., Investigation of electronically excited indole relaxation dynamics via photoionization and fragmentation pump-probe spectroscopy. *The Journal of Chemical Physics* **2014**, *141* (4), 044314.
60. Hadden, D. J.; Wells, K. L.; Roberts, G. M.; Bergendahl, L. T.; Paterson, M. J.; Stavros, V. G., Time resolved velocity map imaging of H-atom elimination from photoexcited imidazole and its methyl substituted derivatives. *Physical Chemistry Chemical Physics* **2011**, *13* (21), 10342-10349.
61. Barbatti, M.; Lischka, H.; Salzmann, S.; Marian, C. M., UV excitation and radiationless deactivation of imidazole. *The Journal of Chemical Physics* **2009**, *130* (3), 034305.
62. Crespo-Otero, R.; Barbatti, M.; Yu, H.; Evans, N. L.; Ullrich, S., Ultrafast Dynamics of UV-Excited Imidazole. *ChemPhysChem* **2011**, *12* (17), 3365-3375.
63. Yu, H.; Evans, N. L.; Stavros, V. G.; Ullrich, S., Investigation of multiple electronic excited state relaxation pathways following 200 nm photolysis of gas-phase imidazole. *Physical Chemistry Chemical Physics* **2012**, *14* (18), 6266-6272.
64. Hansen, C. S.; Blanksby, S. J.; Chalyavi, N.; Bieske, E. J.; Reimers, J. R.; Trevitt, A. J., Ultraviolet photodissociation action spectroscopy of the N-pyridinium cation. *The Journal of Chemical Physics* **2015**, *142* (1), 014301.
65. Hansen, C. S.; Kirk, B. B.; Blanksby, S. J.; O'Hair, R. A.; Trevitt, A. J., UV photodissociation action spectroscopy of haloanilinium ions in a linear quadrupole ion trap mass spectrometer. *Journal of The American Society for Mass Spectrometry* **2013**, *24* (6), 932-940.
66. Olsen, J. V.; Schwartz, J. C.; Griep-Raming, J.; Nielsen, M. L.; Damoc, E.; Denisov, E.; Lange, O.; Remes, P.; Taylor, D.; Splendore, M., A dual pressure linear ion trap Orbitrap instrument with very high sequencing speed. *Molecular & Cellular Proteomics* **2009**, *8* (12), 2759-2769.

67. Chai, J.-D.; Head-Gordon, M., Long-range corrected hybrid density functionals with damped atom–atom dispersion corrections. *Physical Chemistry Chemical Physics* **2008**, *10* (44), 6615-6620.
68. Dunning Jr, T. H., Gaussian basis sets for use in correlated molecular calculations. I. The atoms boron through neon and hydrogen. *The Journal of Chemical Physics* **1989**, *90* (2), 1007-1023.
69. Woon, D. E.; Dunning Jr, T. H., Gaussian basis sets for use in correlated molecular calculations. III. The atoms aluminum through argon. *The Journal of Chemical Physics* **1993**, *98* (2), 1358-1371.
70. Frisch, M. J.; Trucks, G. W.; Schlegel, H. B.; Scuseria, G. E.; Robb, M. A.; Cheeseman, J. R.; Scalmani, G.; Barone, V.; Petersson, G. A.; Nakatsuji, H.; Li, X.; Caricato, M.; Marenich, A. V.; Bloino, J.; Janesko, B. G.; Gomperts, R.; Mennucci, B.; Hratchian, H. P.; Ortiz, J. V.; Izmaylov, A. F.; Sonnenberg, J. L.; Williams-Young, D.; Ding, F.; Lipparini, F.; Egidi, F.; Goings, J.; Peng, B.; Petrone, A.; Henderson, T.; Ranasinghe, D.; Zakrzewski, V. G.; Gao, J.; Rega, N.; Zheng, G.; Liang, W.; Hada, M.; Ehara, M.; Toyota, K.; Fukuda, R.; Hasegawa, J.; Ishida, M.; Nakajima, T.; Honda, Y.; Kitao, O.; Nakai, H.; Vreven, T.; Throssell, K.; Montgomery Jr., J. A.; Peralta, J. E.; Ogliaro, F.; Bearpark, M. J.; Heyd, J. J.; Brothers, E. N.; Kudin, K. N.; Staroverov, V. N.; Keith, T. A.; Kobayashi, R.; Normand, J.; Raghavachari, K.; Rendell, A. P.; Burant, J. C.; Iyengar, S. S.; Tomasi, J.; Cossi, M.; Millam, J. M.; Klene, M.; Adamo, C.; Cammi, R.; Ochterski, J. W.; Martin, R. L.; Morokuma, K.; Farkas, O.; Foresman, J. B.; Fox, D. J. *Gaussian 16*, Wallingford, CT, 2016.
71. Christiansen, O.; Koch, H.; Jørgensen, P., Perturbative triple excitation corrections to coupled cluster singles and doubles excitation energies. *The Journal of chemical physics* **1996**, *105* (4), 1451-1459.
72. Christiansen, O.; Koch, H.; Jørgensen, P.; Olsen, J., Excitation energies of H₂O, N₂ and C₂ in full configuration interaction and coupled cluster theory. *Chemical Physics Letters* **1996**, *256* (1-2), 185-194.
73. Schafer, A.; Huber, C.; Ahlrichs, R., Fully optimized contracted Gaussian basis sets of triple zeta valence quality for atoms Li to Kr. *The Journal of Chemical Physics* **1994**, *100* (8), 5829-5835.
74. Aidas, K.; Angeli, C.; Bak, K. L.; Bakken, V.; Bast, R.; Boman, L.; Christiansen, O.; Cimiraglia, R.; Coriani, S.; Dahle, P., The Dalton quantum chemistry program system. *Wiley Interdisciplinary Reviews: Computational Molecular Science* **2014**, *4* (3), 269-284.
75. Casanova-Páez, M.; Dardis, M. B.; Goerigk, L., ωB2PLYP and ωB2GPPLYP: the first two double-hybrid density functionals with long-range correction optimized for excitation energies. *Journal of Chemical Theory and Computation* **2019**, *15* (9), 4735-4744.
76. Neese, F., The ORCA program system. *Wiley Interdisciplinary Reviews: Computational Molecular Science* **2012**, *2* (1), 73-78.
77. Hegarty, D.; Robb, M. A., Application of unitary group methods to configuration interaction calculations. *Molecular Physics* **1979**, *38* (6), 1795-1812.
78. Eade, R. H.; Robb, M. A., Direct minimization in mc scf theory. The quasi-newton method. *Chemical Physics Letters* **1981**, *83* (2), 362-368.
79. Schlegel, H. B.; Robb, M. A., MC SCF gradient optimization of the H₂CO→H₂+CO transition structure. *Chemical Physics Letters* **1982**, *93* (1), 43-46.
80. Bernardi, F.; Bottoni, A.; McDouall, J. J.; Robb, M. A.; Schlegel, H. B. In *MCSCF gradient calculation of transition structures in organic reactions*, Faraday Symposia of the Chemical Society, Royal Society of Chemistry: 1984; pp 137-147.
81. Frisch, M.; Ragazos, I. N.; Robb, M. A.; Schlegel, H. B., An evaluation of three direct MC-SCF procedures. *Chemical Physics Letters* **1992**, *189* (6), 524-528.

82. Yamamoto, N.; Vreven, T.; Robb, M. A.; Frisch, M. J.; Schlegel, H. B., A direct derivative MC-SCF procedure. *Chemical Physics Letters* **1996**, *250* (3-4), 373-378.
83. Andersson, K.; Malmqvist, P. A.; Roos, B. O.; Sadlej, A. J.; Wolinski, K., Second-order perturbation theory with a CASSCF reference function. *Journal of Physical Chemistry* **1990**, *94* (14), 5483-5488.
84. Andersson, K.; Malmqvist, P. Å.; Roos, B. O., Second-order perturbation theory with a complete active space self-consistent field reference function. *The Journal of Chemical Physics* **1992**, *96* (2), 1218-1226.
85. Fdez. Galván, I.; Vacher, M.; Alavi, A.; Angeli, C.; Aquilante, F.; Autschbach, J.; Bao, J. J.; Bokarev, S. I.; Bogdanov, N. A.; Carlson, R. K., OpenMolcas: From source code to insight. *Journal of Chemical Theory and Computation* **2019**, *15* (11), 5925-5964.
86. Noble, J. A.; Marceca, E.; Dedonder, C.; Phasayavan, W.; Féraud, G.; Inceesungvorn, B.; Jouvét, C., Influence of the N atom position on the excited state photodynamics of protonated azaindole. *Physical Chemistry Chemical Physics* **2020**.
87. Platt, J. R., Classification of spectra of cata-condensed hydrocarbons. *The Journal of Chemical Physics* **1949**, *17* (5), 484-495.
88. Livingstone, R.; Schalk, O.; Boguslavskiy, A. E.; Wu, G.; Therese Bergendahl, L.; Stolow, A.; Paterson, M. J.; Townsend, D., Following the excited state relaxation dynamics of indole and 5-hydroxyindole using time-resolved photoelectron spectroscopy. *The Journal of Chemical Physics* **2011**, *135* (19), 194307.
89. Oliver, T. A.; King, G. A.; Ashfold, M. N., Position matters: competing O–H and N–H photodissociation pathways in hydroxy- and methoxy-substituted indoles. *Physical Chemistry Chemical Physics* **2011**, *13* (32), 14646-14662.
90. Marlton, S. J.; McKinnon, B. I.; Ucur, B.; Bezzina, J. P.; Blanksby, S. J.; Trevitt, A. J., Discrimination Between Protonation Isomers of Quinazoline by Ion Mobility and UV-Photodissociation Action Spectroscopy. *The Journal of Physical Chemistry Letters* **2020**.
91. Hansen, C. S.; Blanksby, S. J.; Trevitt, A. J., Ultraviolet photodissociation action spectroscopy of gas-phase protonated quinoline and isoquinoline cations. *Physical Chemistry Chemical Physics* **2015**, *17* (39), 25882-25890.
92. Féraud, G.; Domenianni, L.; Marceca, E.; Dedonder-Lardeux, C.; Jouvét, C., Photodissociation Electronic Spectra of Cold Protonated Quinoline and Isoquinoline in the Gas Phase. *The Journal of Physical Chemistry A* **2017**, *121* (13), 2580-2587.
93. Soorkia, S.; Broquier, M.; Grégoire, G., Conformer- and mode-specific excited state lifetimes of cold protonated tyrosine ions. *The Journal of Physical Chemistry Letters* **2014**, *5* (24), 4349-4355.
94. McNaught, A. D.; Wilkinson, A., *IUPAC. Compendium of Chemical Terminology, 2nd ed. (the "Gold Book")*. . Blackwell Science Oxford: 1997; Vol. 1669.
95. El-Sayed, M., Spin—orbit coupling and the radiationless processes in nitrogen heterocyclics. *The Journal of Chemical Physics* **1963**, *38* (12), 2834-2838.
96. Karsili, T. N.; Marchetti, B.; Ashfold, M. N.; Domcke, W., Ab initio study of potential ultrafast internal conversion routes in oxybenzone, caffeic acid, and ferulic acid: Implications for sunscreens. *The Journal of Physical Chemistry A* **2014**, *118* (51), 11999-12010.
97. Tuna, D.; Sobolewski, A. L.; Domcke, W., Photochemical mechanisms of radiationless deactivation processes in urocanic acid. *The Journal of Physical Chemistry B* **2014**, *118* (4), 976-985.
98. Tuna, D.; Došlić, N.; Mališ, M.; Sobolewski, A. L.; Domcke, W., Mechanisms of Photostability in Kynurenines: A Joint Electronic-Structure and Dynamics Study. *The Journal of Physical Chemistry B* **2015**, *119* (6), 2112-2124.

99. Loos, P.-F.; Scemama, A.; Jacquemin, D., The Quest for Highly Accurate Excitation Energies: A Computational Perspective. *The Journal of Physical Chemistry Letters* **2020**, *11* (6), 2374-2383.
100. Segarra-Martí, J.; Francés-Monerris, A.; Roca-Sanjuán, D.; Merchán, M., Assessment of the potential energy hypersurfaces in thymine within multiconfigurational theory: CASSCF vs. CASPT2. *Molecules* **2016**, *21* (12), 1666.
101. Broquier, M.; Soorkia, S.; Dedonder-Lardeux, C.; Jouvet, C.; Theulé, P.; Grégoire, G., Twisted intramolecular charge transfer in protonated amino pyridine. *The Journal of Physical Chemistry A* **2016**, *120* (21), 3797-3809.

Chapter 6

Supporting Information

6.SI.1 Active Space for CASSCF calculations

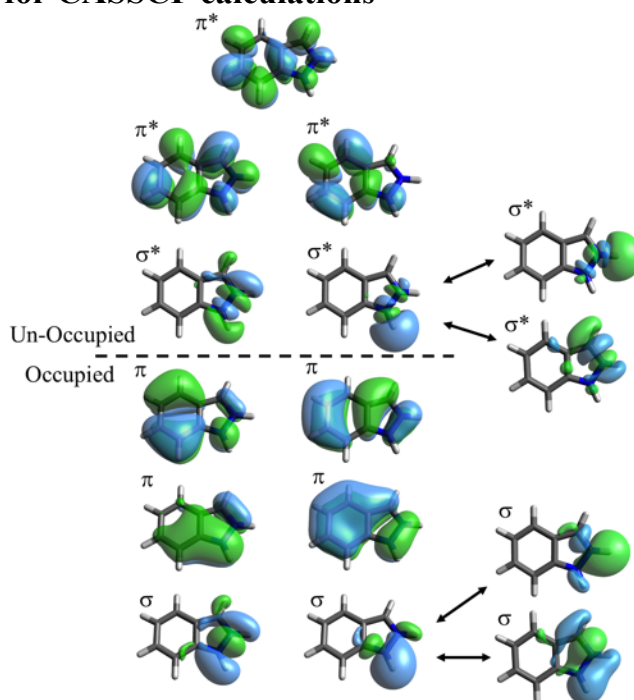


Figure 6.8: Active space for CASSCF(12,11)/cc-pVDZ calculations of indazoleH⁺. The s* and s orbitals on the N₁-H bond were rotated out for s* and s orbitals on either the N₂-H bond or the N₂-C₃ bond to describe states involving these orbitals.

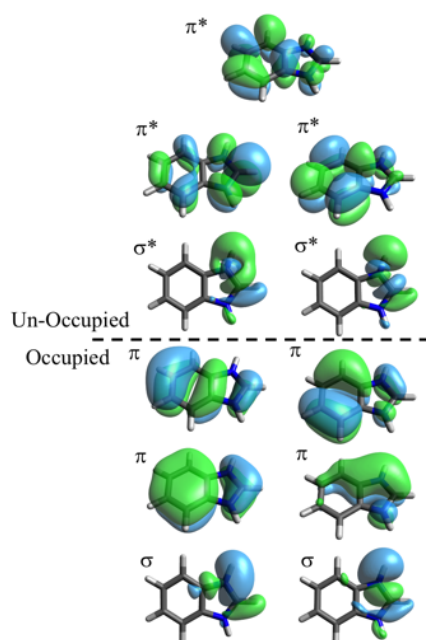


Figure 6.9: Active space for CASSCF(12,11)/cc-pVDZ calculations of benzimidazoleH⁺.

6.SI.2 Additional Details for Linear and Curved Interpolation

Linear interpolation procedure involves moving from an initial geometry x_0 to a final geometry x_f where the geometry change from x_0 to an interpolation step x_n is equal to $(x_f - x_0)(n/f)$ where x_f is the final x position, x_0 is the initial x position, n is the step number, f is the total number of steps. This leads to an interpolation between two geometries with the interpolation path for each atom being a straight line.

The curved interpolation procedure involves stepping between the initial x, y, z geometry to the final x, y, z geometry, whereby interpolation step in the x and y coordinates is scaled by $(1 - \cos(\theta_n))$ and each step in the z direction is scaled by $\sin(\theta_n)$ leading to equations S1-S3:

$$x_n = x_0 + (x_f - x_0)(1 - \cos(\theta_n)) \quad \dots \text{(Eq. S1)}$$

$$y_n = y_0 + (y_f - y_0)(1 - \cos(\theta_n)) \quad \dots \text{(Eq. S2)}$$

$$z_n = z_0 + (z_f - z_0)(\sin(\theta_n)) \quad \dots \text{(Eq. S3)}$$

Where θ_n is:

$$\theta_n = \frac{n\pi}{f^2} \quad \dots \text{(Eq. S4)}$$

for step n , where f is the total number of steps. By doing this, the curved interpolation gives an interpolation path for each atom as a quarter-ellipse. Note that, in the ground state, the molecules are planar in the xy plane.

6.SI.3 Additional Details for L_a and L_b State Character Analysis.

Orbital contributions for the S₁ and S₂ states of indazoleH⁺ and benzimidazoleH⁺ (calculated with CCSDR(3)/TZVP with ω B97X-D/aug-cc-pVDZ geometries and MS-CASPT2/cc-pVDZ with CASSCF geometries) are shown in Figure 6.10. Transition densities calculated using ω B2PLYP/aug-cc-pVTZ for these states are also shown in Figure 6.11. The transition density for a transition to an ¹L_b state should have anti-nodes located on the bonds, while a transition to an ¹L_a state should have anti-nodes located on the atoms.¹ The first two singlet states of benzimidazoleH⁺ have clearly distinguishable ¹L_a and ¹L_b character based on the location of the anti-nodes (especially on the benzene moiety). The S₁ and S₂ states of benzimidazoleH⁺ are assigned as ¹L_b and ¹L_a, respectively. In the C_{2v} point group, the ¹L_b state has A₁ symmetry, and the ¹L_a state has B₂. In contrast, the ¹L_a and ¹L_b character for the indazoleH⁺ states are not clearly distinguishable from the transition densities and so the orbitals involved in the transition must also be analysed.

Based on CCSDR(3)/TZVP calculations for indazoleH⁺, the S₁ has mostly LUMO ← HOMO character characteristic of an ¹L_a state. The S₂ of indazoleH⁺ is dominated by LUMO ← HOMO – 1 which is similar to the expected character of an ¹L_b state, albeit with less LUMO + 1 ← HOMO character than expected. The CCSDR(3)/TZVP results for benzimidazoleH⁺—especially the orbital character of the occupied orbitals and the LUMO + 1 ← HOMO dominated ¹L_b state—are similar to results for indole using EOM-CCSD.² Therefore, the S₁ and S₂ states of indazoleH⁺ are assigned as ¹L_a and ¹L_b, respectively—this is a reversal of the state ordering relative to the neutral form.³⁻⁷

For completeness, the orbital contributions for benzimidazoleH⁺ are also considered; even though the A₁ symmetry state is assigned as the ¹L_b state and the B₂ states is assigned as the ¹L_a state based on their transition densities. The ordering of the HOMO and HOMO – 1 orbitals is reversed for benzimidazoleH⁺ as calculated using CCSDR(3) (but not as calculated with ω B2PLYP) relative to indazoleH⁺, neutral benzimidazole^{8, 9} and similar molecules such as substituted indoles.^{2, 10} Therefore, the assignment of the ¹L_a and ¹L_b states for benzimidazoleH⁺ is based on the character of contributing orbitals rather than their ordering. In the ground state, benzimidazoleH⁺ has C_{2v} symmetry with a ¹B₂ state dominated by a B₁ → A₂ orbital contribution and a ¹A₁ state dominated by B₁ → B₁ and A₂ → A₂ orbital contributions. Based on comparison with the orbitals contributing to the L_a and L_b states of substituted indoles,^{2, 10} the A₁ and B₂ states of benzimidazoleH⁺ are assigned as ¹L_b and ¹L_a, respectively.

There is evidence of the ¹L_a and ¹L_b states of indazoleH⁺ having mixed character. Firstly, the indazoleH⁺ HOMO and HOMO-1 orbitals (calculated using CCSDR(3)/TZVP) do not closely resemble those of the benzimidazoleH⁺ B₂ (p) and A₁ (p) orbitals, whereas the indazoleH⁺ orbitals calculated for indazoleH⁺ using MS-CASPT2 are B₂-like and A₁-like (see Figure 6.10). Secondly, all transitions have some LUMO ← HOMO, LUMO + 1 ← HOMO and LUMO ← HOMO – 1 character except when symmetry is enforced (see Table 6.1). Thirdly, L_a and L_b states were originally defined as having transition densities with maxima over the atoms for L_a states and maxima over the bonds for L_b states¹—this difference is not clear from the transition densities.

Attempts to optimise the minima (to structures without imaginary frequencies) for the S₁ states of indazoleH⁺ and benzimidazoleH⁺ lead to symmetry breaking back to the C₁ point group. Because of the dynamic nature of the states during excited state dynamics—where state crossings mean that electronic states move below what was initially the S₁ and where symmetry is readily broken in the excited state—Platt's notation allows for consistent labelling with these changes.

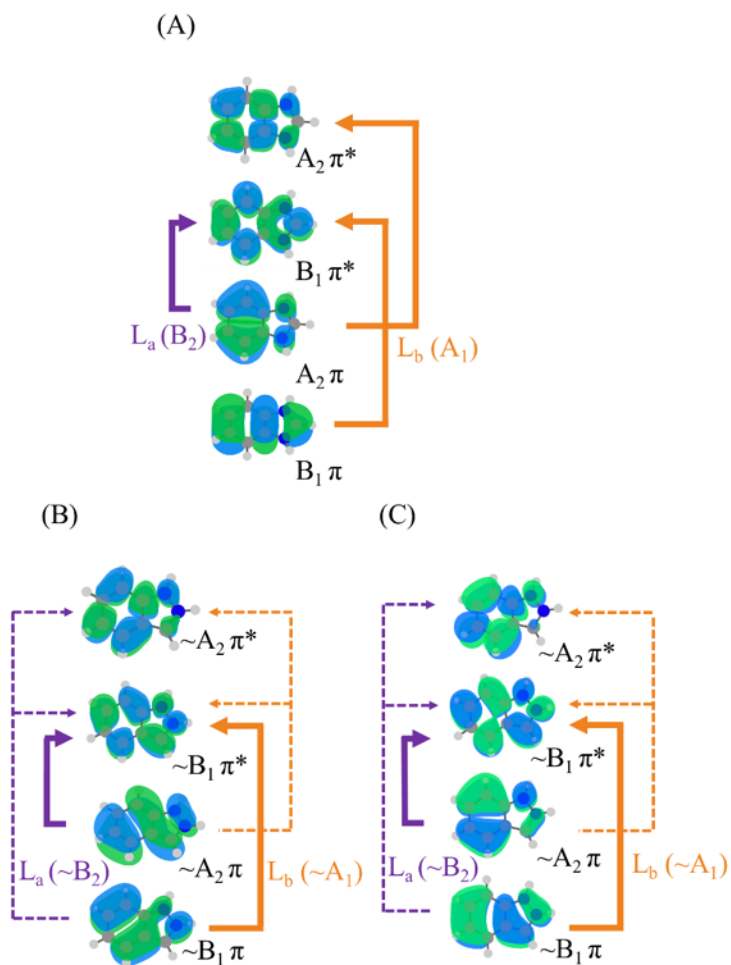


Figure 6.10: The π and π^* orbitals that contribute to the L_a and L_b transitions calculated using (A and B) CCSDR(3)/TZVP and (C) MS-CASPT2/cc-pVDZ//CAS(12,11)/cc-pVDZ. Dotted lines in (B) and (C) correspond to orbital contributions that are much weaker (amplitudes ~ 0.25) than those in bold (amplitudes > 0.5). The ordering of B_1 (p) and A_2 (p) orbitals in (A) have been swapped to simplify comparison to previous studies.

Table 6.1: Amplitudes of orbital contributions to the L_a \rightarrow S₀ and L_b \rightarrow S₀ states of cnH⁺ and nnH⁺ as calculated using CCSDR(3)/TZVP. Where relevant, ω B2PLYP/aug-cc-pVTZ amplitudes are shown in brackets and MS-CASPT2/cc-pVDZ amplitudes for corresponding configurations are shown in square brackets. Contributions with values less than 0.20 are omitted.

Ion	State (symmetry)	L (B ₁) \rightarrow H (A ₂)	L (B ₁) \rightarrow H-1(B ₁)	L+1 (A ₂) \rightarrow H (A ₂)	L+1 (A ₂) \rightarrow H- 1 (B ₁)	L+2 (B ₁) \rightarrow H-1 (B ₁)
cnH ⁺	L _a (B ₂)	0.84 (0.78) [0.78]	- [0.41]	-	-	-
	L _b (A ₁)	- [0.42]	0.70 (0.72) [0.62]	0.49 (0.19) [0.23]	-	-
nnH ⁺	L _a (A')	0.82 (0.93) [0.80]	0.19 - [0.28]	-	0.22	-
	L _b (A')	0.31 - [0.29]	0.76 (0.81) [0.78]	0.20 - [0.27]	-	0.26

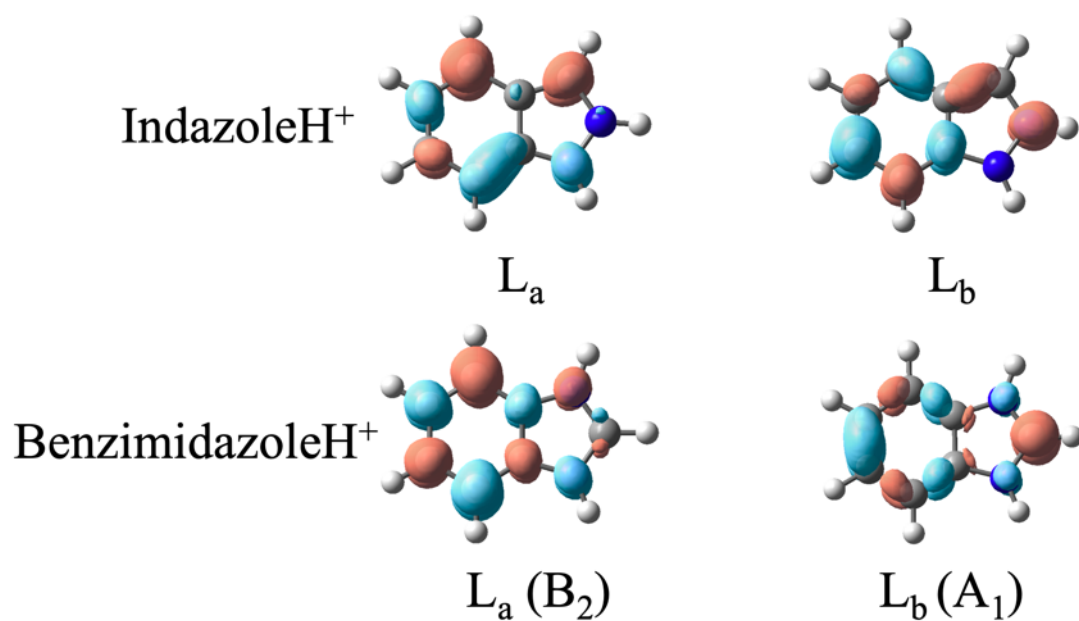


Figure 6.11: ω B2PLYP/aug-cc-pVTZ transition densities for L_a and L_b states of indazoleH⁺ and benzimidazoleH⁺ calculated in ORCA/4.2.1 using ω B97X-D/aug-cc-pVDZ geometries.

Table 6.2: Vertical transition energies and adiabatic transition energies for the ¹L_a—both planar and OOP—and ¹L_b states of benzimidazoleH⁺ and indazoleH⁺ (the OOP ¹L_b state optimisations did not converge). All values are in eV. ^a Planar adiabatic transitions calculated with MS-CASPT2 employed optimised geometries and reference wavefunctions using CASSCF(10,9)/cc-pVDZ with only the full π system active space. ^b The symmetry for MS-CASPT2 vertical transitions is A' due to non-symmetric orbitals in the active space slightly breaking C_{2v} symmetry. Note that all planar “adiabatic” geometries give imaginary frequencies and do not correspond to true minima. The OOP adiabatic for the ¹L_b state of benzimidazoleH⁺ did not converge and so ¹L_b OOP adiabatic energies are not included.

State	indazoleH ⁺			benzimidazoleH ⁺		
	Symmetry	CCSDR(3) (eV)	MS- CASPT2 (eV)	Symmetry	CCSDR(3) (eV)	MS- CASPT2 (eV)
¹ L _a Vertical	C _s (A')	4.55	4.41	C _{2v} (B ₂)	5.41	5.32 ^b
¹ L _a Planar Adiabatic	C _s (A')	4.21	4.02 ^a	C _{2v} (B ₂)	4.79	4.71 ^a
¹ L _a OOP Adiabatic	C ₁ (A)	3.95	3.94	C ₁ (A)	4.62	4.52
¹ L _b Vertical	C _s (A')	5.26	4.98	C _{2v} (A ₁)	5.04	5.03 ^b
¹ L _b Planar Adiabatic	C _s (A')	4.89	5.04 ^a	C _{2v} (A ₁)	4.81	4.87 ^a

6.SI.4 Photodissociation products and Pump-probe PD mass spectra

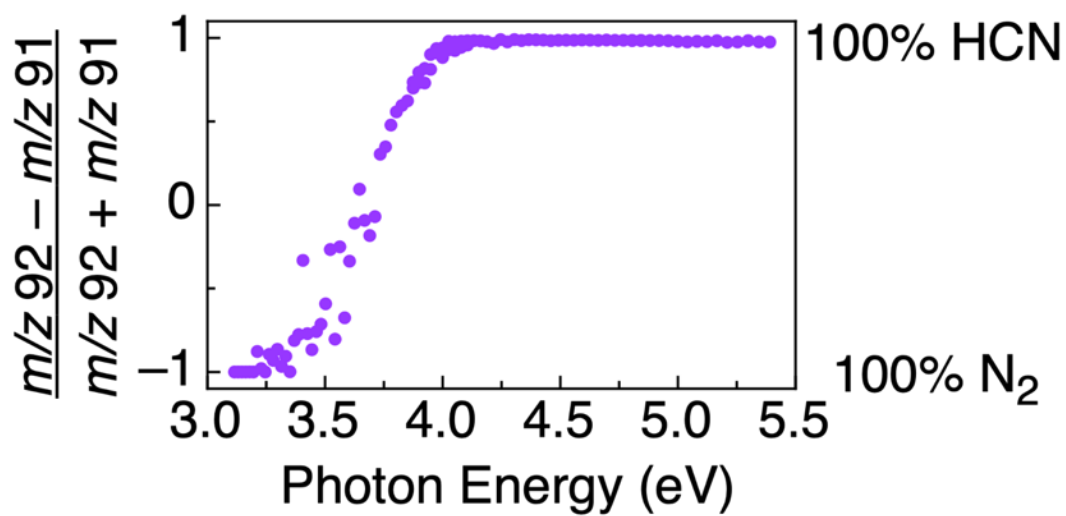


Figure 6.12: Bias between HCN loss and N₂ loss for indazoleH⁺ as a function of photon energy.

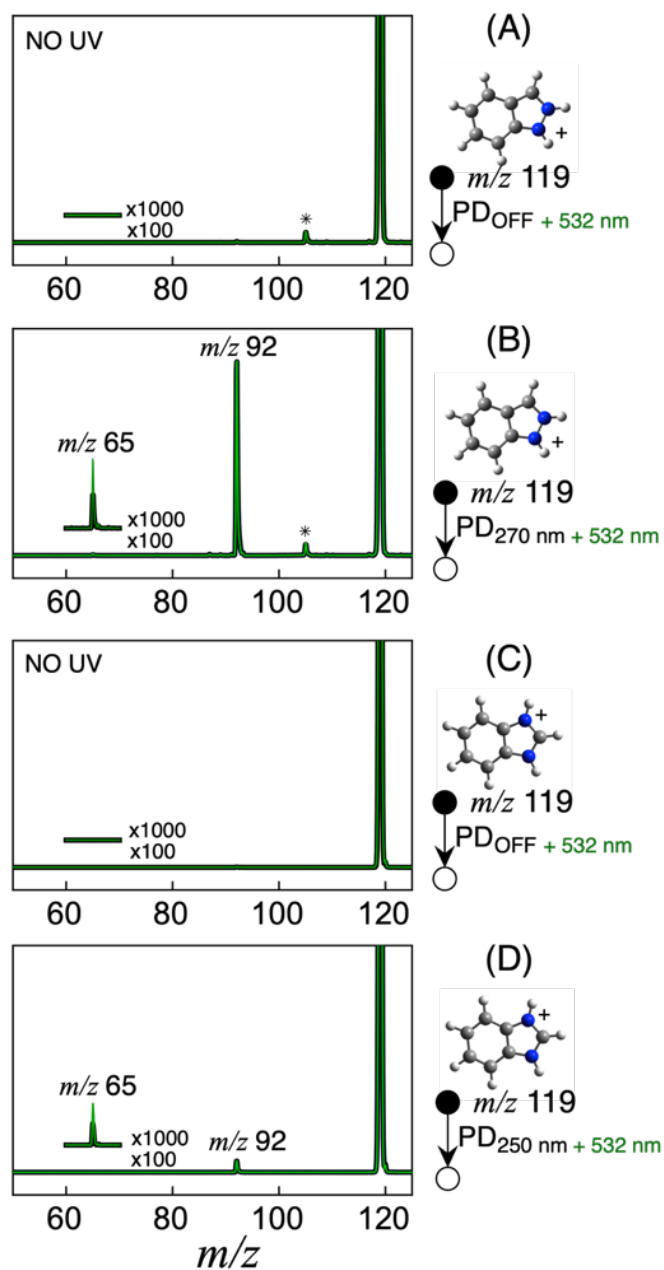


Figure 6.13: PD mass spectrum of indazoleH⁺ using with no laser irradiation (black trace in A), with only 532 nm irradiation (green trace in A), with only 270 nm laser irradiation (black trace in B), and with 270 nm + 532 nm laser irradiation (green trace in B). PD mass spectrum of benzimidazoleH⁺ using with no laser irradiation (black trace in C), with only 532 nm irradiation (green trace in C), with only 250 nm laser irradiation (black trace in D), and with 250 nm + 532 nm laser irradiation (green trace in D). The asterisk at m/z 105 indicates an artefact peak.

SI.5 Single Averages of Pump-Probe Photodissociation Plots

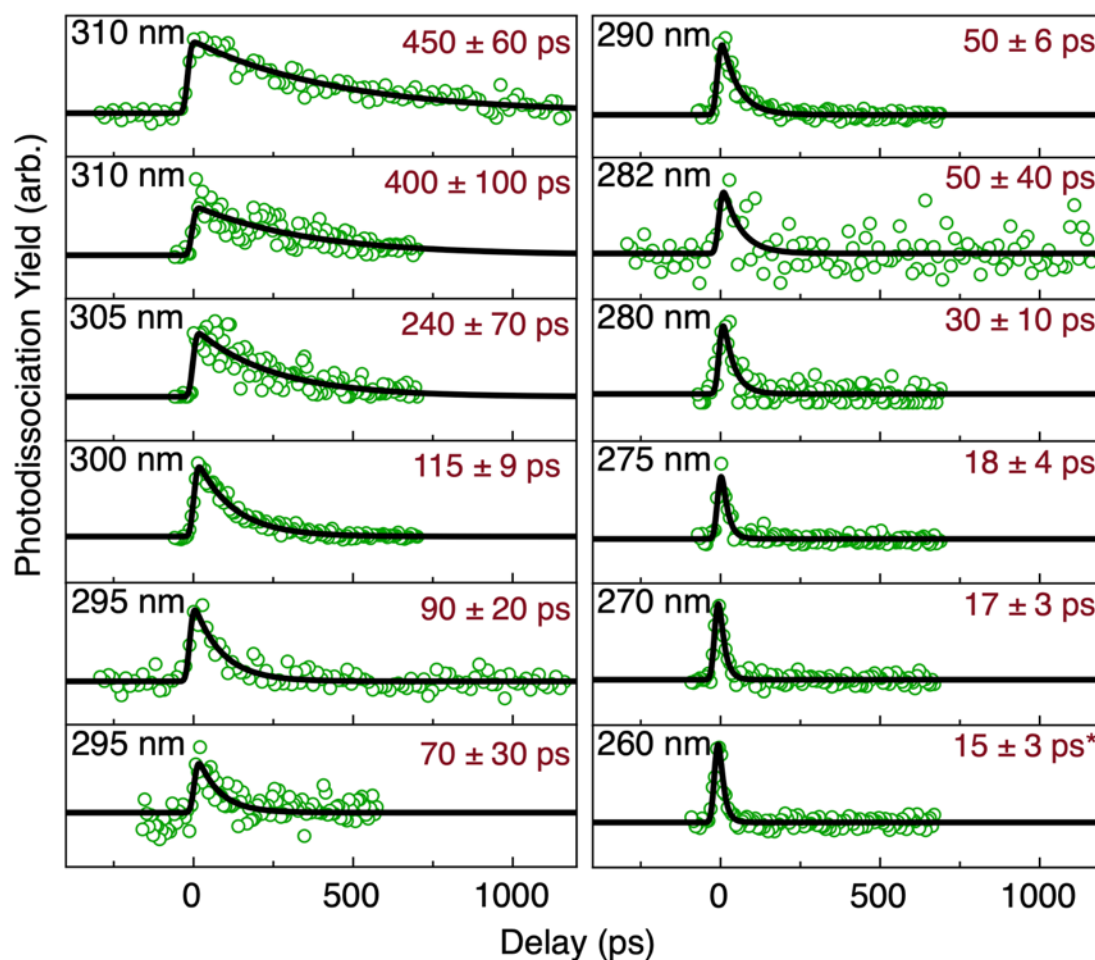


Figure 6.14: Pump-probe photodissociation spectra of indazoleH⁺ following the *m/z* 65 photoproduct. A range of pump photon wavelengths were used with a probe wavelength of 2.33 eV (532 nm). Asterisk denotes measurement affected by the instrument response function (~13 ps). Several data sets are truncated to a maximum delay of 690 ps by experimental limitations earlier in the data collection.

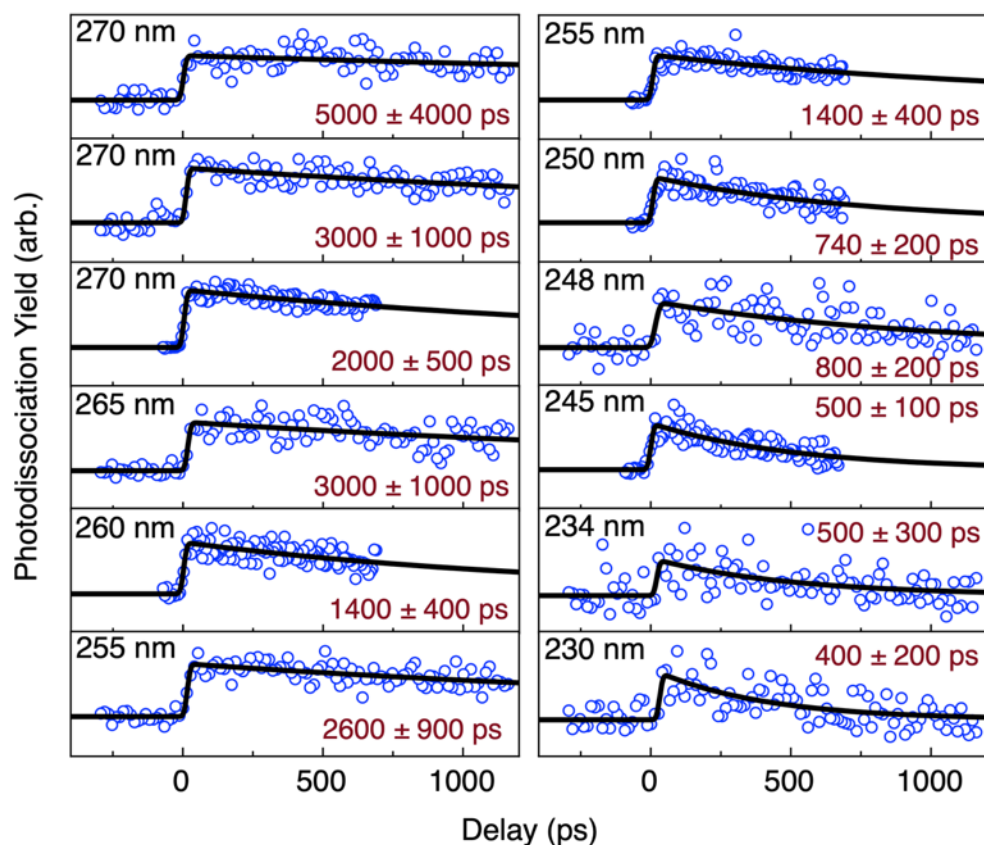


Figure 6.15: Pump-probe photodissociation spectra of indazoleH⁺ following the m/z 65 photoproduct for all pump wavelengths except 4.6 eV (270 nm), which follows the 92 m/z fragment. A range of pump photon wavelengths were used with a probe wavelength of 2.33 eV (532 nm). Several data sets are truncated to a maximum delay of 690 ps by experimental limitations earlier in the data collection.

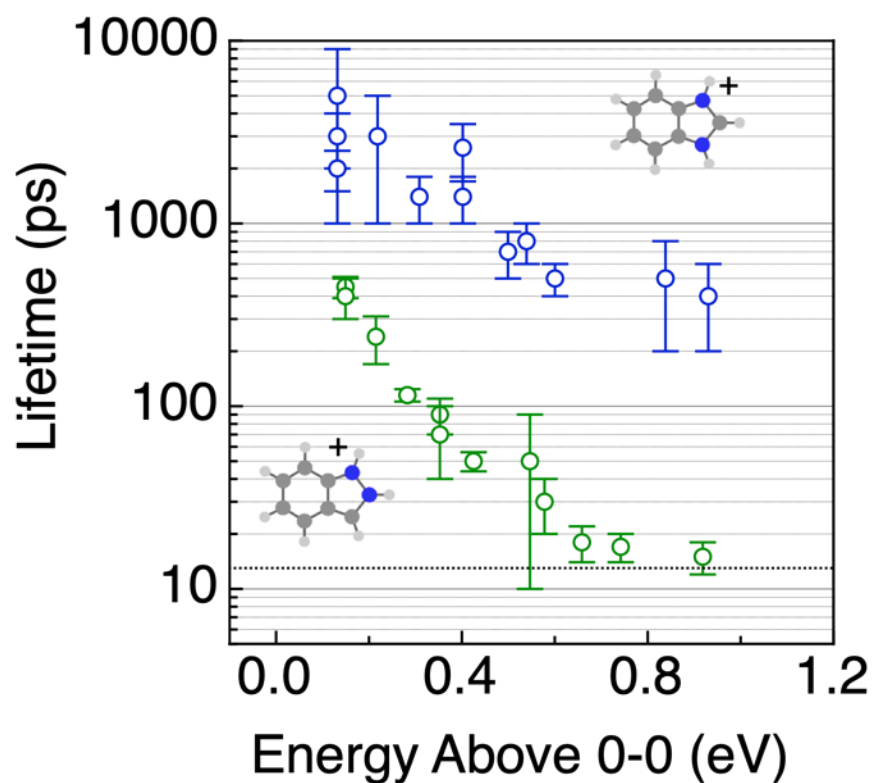


Figure 6.16: (A) Plot of the decay lifetime of benzimidazoleH⁺ (blue) and indazoleH⁺ (green) as a function of the photon energy relative to the calculated zero-point energy corrected 0-0 of the ¹L_a state—this value is 3.85 eV for indazoleH⁺ and 4.46 eV for benzimidazole and these values employed excited state geometries with C₁ symmetry. The dotted line indicates the instrument response function (13 ps). The 0-0 energies were calculated using CCSDR(3)/TZVP electronic energies and ωB97X-D/aug-cc-pVDZ geometries and vibrational frequencies.

6.SI.6 MS-CASPT2 Deactivation pathways

The MECPs are labelled according to the nature of the geometry change relative to the ground state. These geometry are: out of plane ring puckering (OOP), dissociation of the N-N bond in indazoleH⁺ (NN), dissociation of an N-H bond (NH), dissociation of a C-N bond (CN).

The MS-CASPT2/cc-pVDZ energies of these MECPs relative to the optimised ground state are also shown in Figure 6.17, Table 6.3 and Table 6.4. From these MS-CASPT2 results, it is evident that the lowest energy MECP is the indazoleH⁺-NN CI which involves breaking the N-N bond *via* an unbound ¹ $\pi\sigma^*$ state (participating σ^* orbital shown in Figure 6.17). The energy of this indazoleH⁺-NN MECP is 3.26 eV, lower in energy than the other MECPs optimised here by over 1 eV.

MS-CASPT2/cc-pVDZ PESs for pathways from the optimised ground state (S₀) to that of the S₁/S₀ MECPs are shown in Figure 6.18. The maximum energy point of the S₁ state along each potential energy surface for each pathway are shown in Tables 6.S3 and 6.S4.

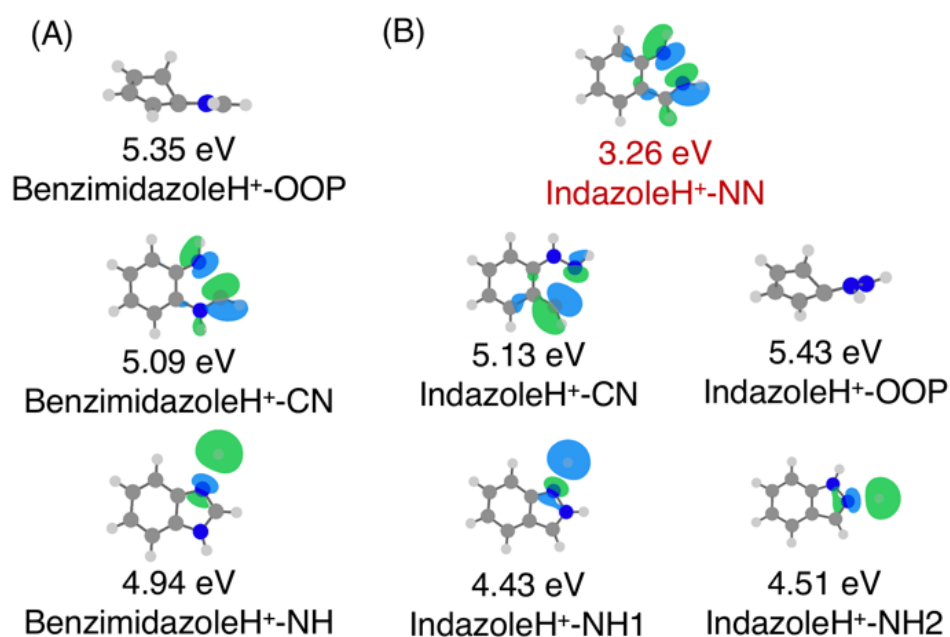


Figure 6.17: Structures of CASSCF(12,11)/cc-pVDZ optimised MECP between excited states and the ground state with—where applicable—the non-bonding σ^* orbital participating in the deactivation for benzimidazoleH⁺ (A) and indazoleH⁺ (B). The MS-CASPT2/cc-pVDZ energies of these S₁/S₀ MECPs are shown.

Table 6.3: MS-CASPT2/cc-pVDZ energies of the S₁/S₀ MECP and maximum energy along the PESs towards optimised CIs for indazoleH⁺. All values are in eV.

	NN	CN	NH1	NH2	OOP
S₁/S₀ MECP	3.26	5.13	4.43	4.51	5.43
Max. Barrier	4.64	6.29	5.85	5.98	5.43
Max. Barrier Relative to Vertical	0.23	1.88	1.44	1.57	0.78

Table 6.4: MS-CASPT2/cc-pVDZ energies of maximum barrier energy along the PESs towards optimised CIs for benzimidazoleH⁺. All values are in eV.

	CN	NH1	OOP
S₁/S₀ MECP	5.09	4.94	5.35
Max. Barrier	6.06	6.52	5.58
Max. Barrier Relative to Vertical	1.03	1.49	0.55

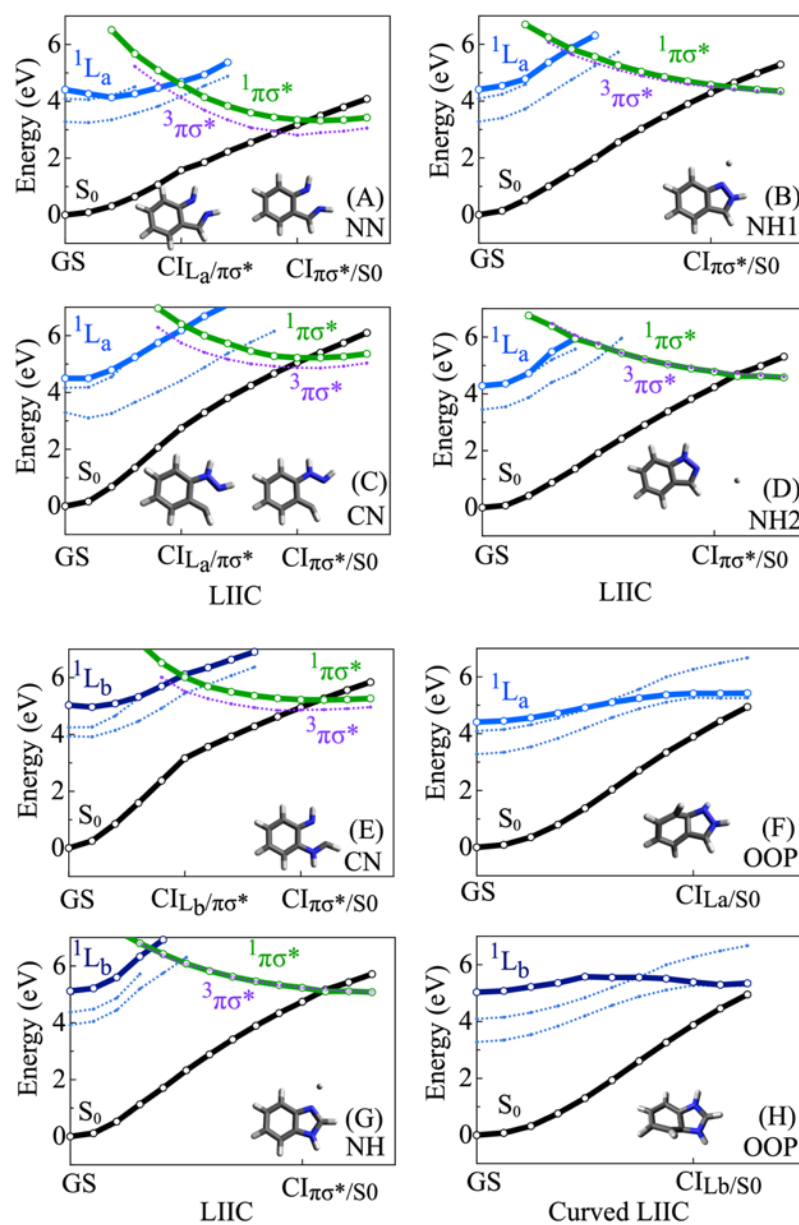


Figure 6.18: Calculated PESs interpolating between the optimised ground state of indazoleH⁺ or benzimidazoleH⁺ and several optimised crossing points. PESs show either linear interpolation between the ground state (GS) and an optimised S₂/S₁ MECP followed by linear interpolation of internal coordinates (LIIC) to an optimised S₁/S₀ MECP (A,C,E), or LIIC directly to an optimised S₁/S₀ MECP (B,D,G), or curvilinear interpolation of internal coordinates (curved LIIC) directly to an optimised S₁/S₀ MECP (F,H). Details of curvilinear interpolation are given in Section SI.3. Ground state and crossing point geometries were optimised using CASSCF(12,11)/cc-pVDZ and electronic energies were calculated using MS-CASPT2/cc-pVDZ. The first two ³ππ* triplet states are thin, blue dotted lines and the first ³πσ* state is represented as purple dotted lines.

References

1. Platt, J. R., Classification of spectra of cata-condensed hydrocarbons. *The Journal of Chemical Physics* **1949**, *17* (5), 484-495.
2. Livingstone, R.; Schalk, O.; Boguslavskiy, A. E.; Wu, G.; Therese Bergendahl, L.; Stolow, A.; Paterson, M. J.; Townsend, D., Following the excited state relaxation dynamics of indole and 5-hydroxyindole using time-resolved photoelectron spectroscopy. *The Journal of Chemical Physics* **2011**, *135* (19), 194307.
3. Cané, E.; Trombetti, A.; Velino, B.; Caminati, W., Assignment of the 290-nm electronic band system of indazole [1, 2-benzodiazole] as $\pi^*-\pi$ by rotational band contour analysis. *Journal of Molecular Spectroscopy* **1992**, *155* (2), 307-314.
4. Berden, G.; Meerts, W. L.; Jalviste, E., Rotationally resolved ultraviolet spectroscopy of indole, indazole, and benzimidazole: Inertial axis reorientation in the S 1 (1 L b)← S 0 transitions. *The Journal of Chemical Physics* **1995**, *103* (22), 9596-9606.
5. Jalviste, E.; Temps, F., Vibronic spectroscopy of jet-cooled indazole: S 1↔ S 0 spectra and mode assignments. *The Journal of Chemical Physics* **1999**, *111* (9), 3898-3910.
6. Su, H.; Pradhan, M.; Tzeng, W. B., Mass analyzed threshold ionization spectroscopy of indazole cation. *Chemical physics letters* **2005**, *411* (1-3), 86-90.
7. Yang, S. C.; Tzeng, W. B., Mass-analyzed threshold ionization of deuterium substituted indazole and benzimidazole and site-specific H/D exchange reaction. *Chemical Physics Letters* **2010**, *501* (1-3), 6-10.
8. Borin, A. C.; Serrano-Andrés, L., A theoretical study of the absorption spectra of indole and its analogs: indene, benzimidazole, and 7-azaindole. *Chemical Physics* **2000**, *262* (2-3), 253-265.
9. Arulmozhiraja, S.; Coote, M. L., 1L a and 1L b states of indole and azaindole: is density functional theory inadequate? *Journal of chemical theory and computation* **2012**, *8* (2), 575-584.
10. Oliver, T. A.; King, G. A.; Ashfold, M. N., Position matters: competing O–H and N–H photodissociation pathways in hydroxy- and methoxy-substituted indoles. *Physical Chemistry Chemical Physics* **2011**, *13* (32), 14646-14662.

SI.7 Potential Energy Surface Values

Q	IndazoleH ⁺ -NN						
	S ₀	¹ L _a	¹ L _b	¹ πσ*	³ πσ*	¹ ππ*	² ππ*
0	0.00	4.41	4.98			3.28	4.09
1	0.09	4.27	4.95			3.25	4.06
2	0.31	4.14	5.49	6.51		3.35	4.20
3	0.65	4.27	5.65	5.68	5.23	3.57	4.51
4	1.07	4.48	6.04	5.09	4.63	3.82	
5	1.57	4.69	6.18	4.59	4.12	4.17	
6	1.86	4.94		4.14	3.68	4.55	
7	2.23	5.37		3.84	3.35	4.88	
8	2.55			3.60	3.07		

Chapter 6: IndazoleH⁺ and BenzimidazoleH⁺ Supporting Information

9	2.87		3.44	2.96
10	3.18		3.35	2.81
11	3.49		3.32	2.90
12	3.79		3.35	2.95
13	4.08		3.43	3.06

Q	IndazoleH ⁺ -CN						
	S ₀	¹ L _a	¹ L _b	¹ πσ*	³ πσ*	¹ ³ ππ*	² ³ ππ*
0	0.00	4.50	5.26			3.30	4.17
1	0.16	4.50	5.28			3.11	4.18
2	0.68	4.79	5.74			3.26	4.55
3	1.35	5.24	6.24			3.65	5.33
4	2.06	5.75	6.75	6.96	6.29	4.03	
5	2.74	6.19	7.17	6.40	5.74	4.42	
6	3.29	6.68	7.46	6.00	5.41	4.88	
7	3.80	7.08		5.73	5.17	5.37	
8	4.24	7.37		5.46	5.01	5.77	
9	4.67			5.28	4.92	6.15	
10	5.05			5.22	4.87		
11	5.40			5.22	4.86		
12	5.74			5.26	4.93		
13	6.10			5.36	5.03		

Q	indazoleH ⁺ -OOP					
	S ₀	¹ L _a	¹ L _b	¹ ³ ππ*	² ³ ππ*	
0	0.00	4.41	4.98	3.28	4.09	
1	0.09	4.45	5.02	3.34	4.15	
2	0.36	4.56	5.26	3.54	4.31	
3	0.80	4.72	5.61	3.84	4.55	
4	1.38	4.92	5.98	4.20	4.84	
5	2.03	5.10	6.40	4.57	5.20	
6	2.70	5.25	6.86	4.88	5.56	
7	3.34	5.37	7.32	5.11	5.99	
8	3.89	5.42	7.66	5.27	6.26	
9	4.45	5.42	7.54	5.25	6.49	
10	4.94	5.43	7.20	5.26	6.67	

IndazoleH⁺-NH₂

Chapter 6: IndazoleH⁺ and BenzimidazoleH⁺ Supporting Information

Q	S ₀	¹ L _a	¹ L _b	¹ πσ*	³ πσ*	¹ ³ ππ*	² ³ ππ*
0	0.00	4.28	5.25			3.45	4.23
1	0.07	4.36	5.34			3.54	4.33
2	0.42	4.72	5.68	6.76		3.87	4.67
3	0.88	5.48		6.39	6.47	4.41	5.21
4	1.36	5.94		5.94	6.07	4.75	5.57
5	1.92			5.71	5.76	5.27	
6	2.42			5.44	5.44	5.96	
7	2.91			5.22	5.22		
8	3.38			5.04	5.04		
9	3.82			4.89	4.93		
10	4.24			4.78	4.81		
11	4.69			4.62	4.72		
12	4.98			4.62	4.65		
13	5.31			4.58	4.60		

IndazoleH ⁺ -NH1							
Q	S ₀	¹ L _a	¹ L _b	¹ πσ*	³ πσ*	¹ ³ ππ*	² ³ ππ*
0	0.00	4.41	4.98			3.28	4.09
1	0.14	4.54	5.11			3.41	4.24
2	0.52	4.78	5.97	6.70		3.73	4.59
3	1.00	5.36		6.24	6.07	4.25	
4	1.49	5.87		5.83	5.64	4.76	
5	1.99	6.31		5.56	5.34	5.24	
6	2.55			5.26	5.10	5.72	
7	3.02			5.04	4.89		
8	3.48			4.85	4.73		
9	3.90			4.70	4.60		
10	4.29			4.58	4.51		
11	4.65			4.48	4.42		
12	4.98			4.40	4.36		
13	5.29			4.35	4.32		

BenzimidazoleH ⁺ -CN							
Q	S ₀	¹ L _a	¹ L _b	¹ πσ*	³ πσ*	¹ ³ ππ*	² ³ ππ*
0	0.00	5.03	5.32			3.94	4.25
1	0.25	4.96	5.29			3.92	4.26
2	0.85	5.09	5.73			4.14	4.65

Chapter 6: IndazoleH⁺ and BenzimidazoleH⁺ Supporting Information

3	1.59	5.32	6.39	7.26		4.46	5.27
4	2.37	5.69	7.06	6.52	6.01	4.92	
5	3.16	6.11	7.70	6.01	5.51	5.45	
6	3.56	6.35		5.69	5.26	5.76	
7	3.93	6.63		5.50	5.08	6.07	
8	4.29	6.91		5.36	4.94	6.37	
9	4.63			5.27	4.85		
10	4.95			5.22	4.86		
11	5.27			5.21	4.87		
12	5.56			5.23	4.91		
13	5.84			5.27	4.96		

 BenzimidazoleH⁺-OOP

Q	S ₀	¹ L _a	¹ L _b	¹ ππ*	³ ππ*	² ³ ππ*
0	0.00	5.03	5.32	3.28	4.09	
1	0.08	5.08	5.33	3.34	4.15	
2	0.32	5.22	5.42	3.54	4.31	
3	0.76	5.35	5.58	3.84	4.55	
4	1.30	5.58	5.77	4.20	4.84	
5	1.93	5.55	6.08	4.57	5.20	
6	2.61	5.55	6.39	4.88	5.56	
7	3.26	5.51	6.63	5.11	5.99	
8	3.88	5.39	6.72	5.27	6.26	
9	4.46	5.29	6.94	5.25	6.49	
10	4.95	5.34	7.21	5.26	6.67	

 BenzimidazoleH⁺-NH

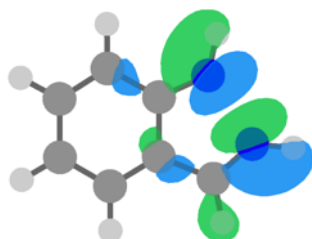
Q	S ₀	¹ L _a	¹ L _b	¹ πσ*	³ πσ*	¹ ³ ππ*	² ³ ππ*
0	0.00	5.12	5.32			3.93	4.37
1	0.11	5.21	5.46			4.05	4.48
2	0.52	5.60	5.80	7.24		4.44	4.87
3	1.13	6.33		6.80	6.78	5.20	5.71
4	1.71	6.92		6.42	6.36	5.75	
5	2.33			6.08	6.06	6.30	
6	2.89			5.82	5.88		
7	3.41			5.62	5.60		
8	3.90			5.46	5.45		
9	4.34			5.33	5.33		

10	4.74	5.23	5.24
11	5.16	5.10	5.17
12	5.43	5.11	5.12
13	5.71	5.08	5.09

SI.8 XYZ Coordinates

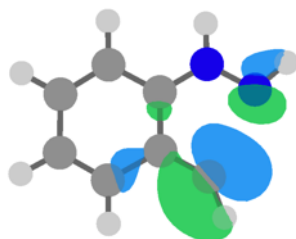
SI.9.1 CASSCF(12,11)/cc-pVDZ

IndazoleH⁺



IndazoleH⁺-NN $\pi\sigma^*/GS$ -377.83298114159174

C	1.69367062	-1.01204973	0.00000441
C	0.30292657	-0.64115971	-0.00008098
C	0.13076520	0.79088425	0.00002683
N	1.25041978	1.46027184	0.00002655
H	1.33508129	2.48505482	0.00008010
H	2.03773441	-2.04269257	-0.00001459
N	2.52295060	-0.06180541	-0.00003874
H	3.52780417	-0.03182964	-0.00011863
C	-0.78583959	-1.50010671	-0.00006576
C	-2.08146442	-0.95392438	0.00002844
H	-0.64334780	-2.57167481	-0.00007293
C	-2.26890507	0.45240019	-0.00009268
H	-2.93903069	-1.60937493	0.00004444
C	-1.20199324	1.32874896	0.00000643
H	-3.27484385	0.84673404	0.00016709
H	-1.35008558	2.39847808	-0.00002198

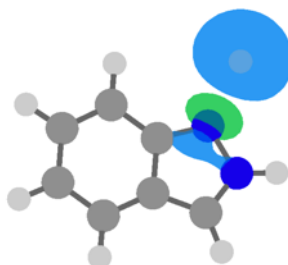


IndazoleH⁺-CN $\pi\sigma^*/GS$

Chapter 6: IndazoleH⁺ and BenzimidazoleH⁺ Supporting Information

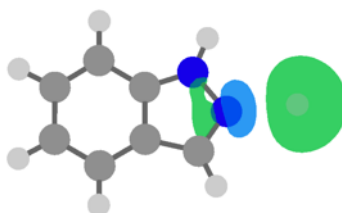
-377.76733778086555

C	1.06618879	1.79678223	-0.00026760
C	0.06872611	0.89813847	-0.00016701
C	0.38645064	-0.52339337	0.00006361
N	1.65771861	-0.90470772	-0.00011667
H	1.85646501	-1.91759191	-0.00005258
H	1.25486508	2.85649107	-0.00038013
N	2.63221923	-0.03093442	-0.00026785
H	3.53981333	-0.47613737	-0.00033226
C	-1.35602136	1.27898670	0.00002655
C	-2.30408523	0.34847802	0.00013797
H	-1.59247091	2.33260334	-0.00001031
C	-1.95579635	-1.07155388	0.00015349
H	-3.34854631	0.62306796	0.00017059
C	-0.65793124	-1.49571634	0.00014868
H	-2.75019055	-1.80384063	0.00042548
H	-0.41296604	-2.54880114	0.00014205



IndazoleH⁺-NH1 $\pi\sigma^*/GS$
-377.79091549334709

C	1.66864849	-0.97909483	0.01604387
C	0.27916799	-0.74346793	0.00695392
C	0.15103712	0.68205791	-0.00302699
N	1.34875405	1.24890701	-0.00034652
H	1.87380433	3.05930547	-0.00928993
H	2.22791523	-1.90171944	0.02513588
N	2.25948162	0.18200169	0.01150509
H	3.24071313	0.38839490	0.01541073
C	-0.84122236	-1.56398089	0.00632064
C	-2.10495847	-0.94074068	-0.00480592
H	-0.75630587	-2.64120445	0.01400013
C	-2.23426739	0.46582334	-0.01456101
H	-2.99361029	-1.55438654	-0.00530351
C	-1.12545859	1.30523851	-0.01402693
H	-3.22440716	0.89752338	-0.02266058
H	-1.21963194	2.38033055	-0.02160834

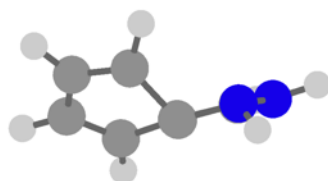


IndazoleH⁺-NH2 $\pi\sigma^*/GS$

Chapter 6: IndazoleH⁺ and BenzimidazoleH⁺ Supporting Information

-377.80086047980848

C	1.61323445	-0.68947763	0.13087902
C	0.22608237	-0.60545898	0.05359258
C	-0.05857194	0.82194964	0.05392638
N	1.12374248	1.43474952	0.11485148
H	1.32725328	2.43798804	0.13832557
H	2.25100633	-1.55576216	0.16368543
N	2.16748047	0.53848970	0.16681511
H	5.86537940	-0.61925772	-0.51651993
C	-0.84871572	-1.55152266	-0.00934640
C	-2.10185962	-1.06624680	-0.05232646
H	-0.64250524	-2.61151553	-0.00836901
C	-2.35466545	0.36251079	-0.05014377
H	-2.95188112	-1.73077931	-0.09357999
C	-1.37040576	1.31400144	-0.00122128
H	-3.38573087	0.68822067	-0.09069738
H	-1.59356207	2.36981099	0.00002216



IndazoleH⁺-OOP L_a/GS
-377.74300432336003

C	1.26600758	-1.09455105	0.45336091
C	0.05805211	-0.61289983	-0.10572451
C	0.36493428	0.69671048	-0.68056112
N	1.73568155	0.94700603	-0.38298096
H	2.31520333	1.16128869	-1.20487396
H	1.45410745	-2.02732135	0.96602065
N	2.21911259	-0.26000390	0.22041329
H	3.15651626	-0.29148568	0.57955276
C	-1.25155459	-1.25957371	-0.31709403
C	-2.33527320	-0.42840187	-0.12680236
H	-1.31334694	-2.27872781	-0.66869449
C	-1.99347015	0.86023534	0.34493460
H	-3.35485850	-0.74683893	-0.27804102
C	-0.60423615	1.20359771	0.32823567
H	-2.70530842	1.55173844	0.76998446
H	-0.17747249	1.81392663	1.11517611

IndazoleH⁺-NN L_a/πσ*
-377.77380526131179

C	1.69301992	-1.03767410	0.00014228
C	0.28995790	-0.71247213	0.00005028
C	0.11984840	0.71927730	-0.00004548
N	1.29080654	1.32445955	-0.00015430
H	1.53367014	2.31901584	-0.00020782
H	2.15733210	-2.00902352	0.00025965
N	2.42670315	0.07660335	0.00007503
H	3.41238785	0.25101236	0.00002802

Chapter 6: IndazoleH⁺ and BenzimidazoleH⁺ Supporting Information

C	-0.79917128	-1.50804565	0.00007926
C	-2.13115418	-0.92918069	0.00002473
H	-0.69885083	-2.58553805	0.00022303
C	-2.30020769	0.45247263	-0.00011926
H	-2.98377692	-1.59090497	0.00004289
C	-1.17429080	1.30842479	-0.00013653
H	-3.29209803	0.87738685	-0.00014088
H	-1.28833473	2.38213805	-0.00024290

IndazoleH⁺-CN L_a/πσ*
-377.69840367552547

C	1.41168515	1.44256698	-0.00000257
C	0.18631935	0.80624873	0.00000980
C	0.26415082	-0.61660228	-0.00005567
N	1.53457142	-1.07369216	-0.00012344
H	1.77669372	-2.07041140	-0.00018111
H	1.81801592	2.43696623	0.00004903
N	2.45849215	-0.13399646	-0.00010599
H	3.42275702	-0.41619291	-0.00016424
C	-1.10971875	1.40746418	0.00010197
C	-2.25733227	0.63030204	0.00008492
H	-1.18429966	2.48600080	0.00014915
C	-2.15264504	-0.75012232	0.00005336
H	-3.22826247	1.10152244	0.00012311
C	-0.88931764	-1.39795614	-0.00006590
H	-3.04304894	-1.36238438	0.00001020
H	-0.83792087	-2.47775284	-0.00010661

Indazole-H⁺ GS
-377.95692379896639

C	1.64099596	-0.96756079	0.00021327
C	0.28828070	-0.73331962	0.00011688
C	0.13372166	0.68017981	-0.00010224
N	1.36059719	1.21499564	-0.00014518
H	1.65502847	2.19331903	-0.00029511
H	2.20125731	-1.88803967	0.00038814
N	2.27337481	0.19836384	0.00006099
H	3.25685769	0.38986817	0.00007407
C	-0.87300620	-1.58385164	0.00020228
C	-2.09914850	-0.96934050	0.00004902
H	-0.76819004	-2.65773563	0.00045903
C	-2.22463492	0.45878876	-0.00010613
H	-2.99913369	-1.56622510	0.00001175
C	-1.13398342	1.30253707	-0.00026652
H	-3.21582063	0.88913300	-0.00034570
H	-1.24035541	2.37683762	-0.00043651

Indazole-H⁺ L_a (C₁)
-377.81166832938595

C	1.70848925	-0.99636664	-0.05544417
C	0.29856170	-0.70252008	0.01046248
C	0.15789730	0.69241781	0.02374784

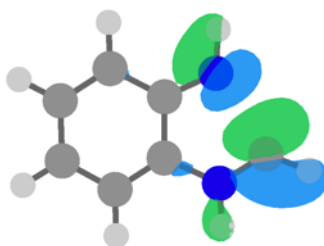
Chapter 6: IndazoleH⁺ and BenzimidazoleH⁺ Supporting Information

N	1.38344121	1.27153967	0.03408809
H	1.57100416	2.09195518	-0.55323749
H	2.19664655	-1.93474675	-0.25565538
N	2.43518467	0.21022545	-0.09492923
H	3.04365861	0.31700403	0.70163377
C	-0.80996747	-1.50394832	-0.01317309
C	-2.13889065	-0.92629884	0.03888354
H	-0.70807416	-2.57923831	-0.09459604
C	-2.27857095	0.43558766	0.05481097
H	-2.99334369	-1.58526819	0.04652150
C	-1.11773555	1.29468978	0.03892254
H	-3.26006530	0.88465891	0.07833365
H	-1.23239468	2.36825864	0.03950901

Indazole-H⁺ L_b (C₁)
-377.76022782167786

C	1.65448594	-0.98734659	0.06041699
C	0.30838136	-0.75070835	0.01119565
C	0.15211159	0.67922524	0.00384268
N	1.37636189	1.21331638	0.02139202
H	1.63490698	2.20154430	0.11112819
H	2.20972031	-1.90833600	0.08134520
N	2.34189547	0.22208050	0.16400888
H	3.19308851	0.39438075	-0.34434819
C	-0.82887385	-1.58452601	-0.01121046
C	-2.17299523	-0.96694945	-0.02567914
H	-0.72553334	-2.65788689	-0.00313002
C	-2.29102677	0.44093966	-0.01714382
H	-3.05137337	-1.58971709	-0.02864533
C	-1.09000214	1.32465775	-0.00042896
H	-3.26304398	0.90914507	-0.02359755
H	-1.19226256	2.39813071	0.00073186

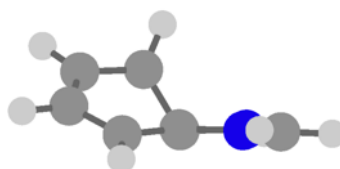
BenzimidazoleH⁺



BenzimidazoleH⁺-CN πσ*/GS

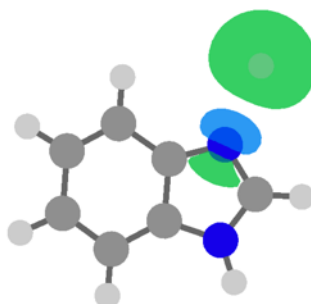
-377.81460838110269

C	-0.33548518	-0.56170308	-0.00289001
C	-0.10002240	0.85281512	-0.00293976
N	-1.17982216	1.59905833	-0.00439576
H	-1.06083172	2.62359295	-0.00447380
H	-1.93243553	-1.90997357	-0.00477008
H	-3.71207976	-0.27266949	-0.00714837
C	0.66664129	-1.48627757	-0.00139052
C	1.99085333	-1.03584803	0.00031648
H	0.45410488	-2.54731152	-0.00106797
C	2.27812801	0.34596094	0.00041788
H	2.79628047	-1.75475717	0.00169124
C	1.26319775	1.28681852	-0.00122894
H	3.30814710	0.67108466	0.00212747
H	1.48109634	2.34500144	-0.00113369
N	-1.70532957	-0.92459245	-0.00463241
C	-2.65004284	-0.06373610	-0.00589577

BenzimidazoleH⁺-OOP L_a/GS

-377.77316849121377

C	-0.35675257	-0.76226008	-0.63067944
C	-0.05298644	0.55908875	-0.08477873
N	-1.28236810	1.09952078	0.35028225
H	-1.43427321	2.01509673	0.78504281
H	-2.32751467	-1.65882774	-0.67724787
H	-3.28753729	0.39250567	0.38064320
C	0.57962991	-1.17121986	0.42285391
C	2.00945293	-0.86402683	0.23894918
H	0.22688645	-1.74450521	1.27207575
C	2.32100042	0.40260145	-0.11143424
H	2.74680609	-1.63785700	0.39957797
C	1.20616878	1.27297083	-0.21643890
H	3.33027896	0.73741759	-0.29659333
H	1.25668585	2.33687693	-0.38569258
N	-1.76100543	-0.89307051	-0.37028073
C	-2.24975969	0.21880150	0.14223578



BenzimidazoleH⁺-CN $\pi\sigma^*/GS$
-377.81100152176714

C	-0.32835718	-0.69574303	-0.00677719
C	-0.09398193	0.72027683	0.00006371
N	-1.35197363	1.28026694	-0.00237135
H	-1.57988803	2.27924763	0.00100335
H	-2.62506837	-2.65691795	-0.02322712
H	-3.30930934	0.44582129	-0.01327320
C	0.76972298	-1.61490194	-0.00640981
C	2.00798384	-1.08413291	0.00049612
H	0.58710399	-2.67848402	-0.01150777
C	2.22994490	0.34412630	0.00732420
H	2.87477091	-1.72895871	0.00110277
C	1.18159455	1.26685684	0.00720054
H	3.24714074	0.70791224	0.01275437
H	1.36234480	2.33124358	0.01243435
N	-1.64214470	-0.91203596	-0.01260474
C	-2.24270382	0.29323392	-0.00998867

BenzimidazoleH⁺-CN $L_a/\pi\sigma^*$
-377.77238945366389

C	-0.33209949	-0.63914576	-0.00453659
C	-0.10805436	0.78101763	-0.00094994
N	-1.22497648	1.46430534	-0.00179563
H	-1.29157497	2.48809650	0.00032436
H	-2.02905161	-1.88611854	-0.01085155
H	-3.60319935	0.06570635	-0.00987241
C	0.68171888	-1.51750897	-0.00430085
C	2.05155192	-1.02796343	-0.00038812
H	0.50181759	-2.58465607	-0.00707454
C	2.30183121	0.33437374	0.00316360
H	2.85779552	-1.74484668	-0.00023840
C	1.23761426	1.26204107	0.00295882
H	3.31858099	0.69713537	0.00610513
H	1.42557720	2.32546823	0.00567253
N	-1.69946509	-0.93727668	-0.00807256
C	-2.52566640	0.08683457	-0.00755808

BenzimidazoleH⁺ GS
-377.99744487150895

C	-0.30356838	-0.69865475	-0.00718619
C	-0.09215675	0.68594626	0.00118767
N	-1.34946871	1.25762428	0.00008588
H	-1.57053645	2.25769742	0.00503222
H	-2.14054229	-1.76418252	-0.01917536
H	-3.34678672	0.45109533	-0.01094010
C	0.75402238	-1.59721761	-0.00865003
C	2.02803251	-1.05588560	-0.00159567
H	0.59277722	-2.66517111	-0.01502086
C	2.24667783	0.34029466	0.00677650
H	2.88045858	-1.71923575	-0.00245726
C	1.19420638	1.24265892	0.00825148
H	3.26051276	0.71238189	0.01218128
H	1.35660176	2.31006611	0.01509531

Chapter 6: IndazoleH⁺ and BenzimidazoleH⁺ Supporting Information

N	-1.66477433	-0.88294779	-0.01270579
C	-2.28305674	0.29299224	-0.00829408

BenzimidazoleH⁺ L_a (C₁)
-377.83787427449107

C	-0.35228018	-0.68380583	0.01804726
C	-0.13874460	0.69694358	0.02772150
N	-1.35432195	1.32278836	0.10522633
H	-1.49261173	2.25038863	-0.30043861
H	-2.08492945	-1.79676522	-0.23295486
H	-3.34281673	0.43507998	0.32393736
C	0.73416136	-1.55915118	0.00157376
C	2.08849465	-1.03847937	0.00390780
H	0.57076872	-2.62848236	-0.01767106
C	2.29678645	0.30836880	0.01981912
H	2.90810742	-1.73988633	-0.01028705
C	1.16635754	1.21837309	0.03950859
H	3.29418174	0.72016204	0.02045022
H	1.33036270	2.28614519	0.05782335
N	-1.68335276	-0.92715918	0.05330741
C	-2.37776415	0.30294179	-0.14738614

SI.9.2 CASSCF(10,9)/cc-pVDZ

IndazoleH⁺

Indazole-H⁺ GS
-377.93467319670231

C	1.55509303	1.14023423	0.00000000
C	0.21215768	0.74950438	0.00000000
C	0.22864980	-0.66439688	0.00000000
N	1.52922768	-1.04659624	0.00000000
H	1.92566859	-1.96599164	0.00000000
H	2.02100269	2.11069601	0.00000000
N	2.29754391	0.03270966	0.00000000
H	3.29753524	-0.04174831	0.00000000
C	-1.03286741	1.45002419	0.00000000
C	-2.17987467	0.69465980	0.00000000
H	-1.06118011	2.52901566	0.00000000
C	-2.13680388	-0.73578666	0.00000000
H	-3.14350755	1.18236915	0.00000000
C	-0.95036777	-1.44083270	0.00000000
H	-3.06920950	-1.28181402	0.00000000
H	-0.92537373	-2.52012961	0.00000000

Indazole-H⁺ L_a (C_s)

Chapter 6: IndazoleH⁺ and BenzimidazoleH⁺ Supporting Information

-377.77108052694484

C	-1.87018097	-0.58146298	0.00000000
C	-0.46407144	-0.65335455	0.00000000
C	0.02761606	0.72222658	0.00000000
N	-1.09077024	1.50769262	0.00000000
H	-1.17430872	2.50278151	0.00000000
H	-2.62392246	-1.34836955	0.00000000
N	-2.20248777	0.72003002	0.00000000
H	-3.11768168	1.12624389	0.00000000
C	0.45363004	-1.69191265	0.00000000
C	1.86935069	-1.36441082	0.00000000
H	0.13869153	-2.72499345	0.00000000
C	2.32845291	-0.01431358	0.00000000
H	2.58255708	-2.17438198	0.00000000
C	1.39265480	1.05683118	0.00000000
H	3.38623186	0.19206452	0.00000000
H	1.71704032	2.08626023	0.00000000

Indazole-H⁺ L_b (C_s)
-377.74518523953378

C	-1.87477102	-0.66231123	0.00000000
C	-0.43024100	-0.66785122	0.00000000
C	-0.04293246	0.71761912	0.00000000
N	-1.13528356	1.46344766	0.00000000
H	-1.20208072	2.46264485	0.00000000
H	-2.60256349	-1.44854359	0.00000000
N	-2.24837382	0.68367449	0.00000000
H	-3.15397457	1.09699739	0.00000000
C	0.54420589	-1.67119249	0.00000000
C	1.94256884	-1.32565198	0.00000000
H	0.24819329	-2.71009159	0.00000000
C	2.30607856	0.01957754	0.00000000
H	2.69439864	-2.09735936	0.00000000
C	1.30449494	1.09499197	0.00000000
H	3.34695321	0.30781361	0.00000000
H	1.61731927	2.12843083	0.00000000

BenzimidazoleH⁺

Benzimidazole-H⁺ GS
-377.98140940453374

C	0.00000000	0.69661652	0.22240961
C	0.00000000	-0.69661652	0.22240961
C	0.00000000	-1.44225640	-0.96909244
C	0.00000000	1.44225640	-0.96909244
C	0.00000000	-0.70875737	-2.14776263
C	0.00000000	0.70875737	-2.14776263
C	0.00000000	0.00000000	2.32035436

Chapter 6: IndazoleH⁺ and BenzimidazoleH⁺ Supporting Information

H	0.00000000	-2.52190915	-0.96941947
H	0.00000000	2.52190915	-0.96941947
H	0.00000000	-1.23163050	-3.09284378
H	0.00000000	1.23163050	-3.09284378
H	0.00000000	2.01708806	1.90911403
H	0.00000000	-2.01708806	1.90911403
H	0.00000000	0.00000000	3.39660267
N	0.00000000	1.07868938	1.55707166
N	0.00000000	-1.07868938	1.55707166

Benzimidazole-H⁺ L_a, B₂ (C_{2v})

-377.80725216628866

C	0.00000000	0.72323963	0.22897531
C	0.00000000	-0.72323963	0.22897531
C	0.00000000	-1.48143480	-0.95232819
C	0.00000000	1.48143480	-0.95232819
C	0.00000000	-0.72217991	-2.18376723
C	0.00000000	0.72217991	-2.18376723
C	0.00000000	0.00000000	2.33625168
H	0.00000000	-2.55940163	-0.94905884
H	0.00000000	2.55940163	-0.94905884
H	0.00000000	-1.24787090	-3.12511126
H	0.00000000	1.24787090	-3.12511126
H	0.00000000	2.02269186	1.92047286
H	0.00000000	-2.02269186	1.92047286
H	0.00000000	0.00000000	3.41136331
N	0.00000000	1.08576119	1.56539337
N	0.00000000	-1.08576119	1.56539337

Benzimidazole-H⁺ L_b, A₁ (C_{2v})

-377.80725289749290

C	0.00000000	0.72311438	0.22722133
C	0.00000000	-0.72311438	0.22722133
C	0.00000000	-1.48126019	-0.95414348
C	0.00000000	1.48126019	-0.95414348
C	0.00000000	-0.72211826	-2.18569320
C	0.00000000	0.72211826	-2.18569320
C	0.00000000	0.00000000	2.33442540
H	0.00000000	-2.55919740	-0.95085862
H	0.00000000	2.55919740	-0.95085862
H	0.00000000	-1.24821458	-3.12676180
H	0.00000000	1.24821458	-3.12676180
H	0.00000000	2.02263986	1.91882871
H	0.00000000	-2.02263986	1.91882871
H	0.00000000	0.00000000	3.40954831
N	0.00000000	1.08570184	1.56373535
N	0.00000000	-1.08570184	1.56373535

SI.9.3 ωB97X-D/aug-cc-pVDZ

Chapter 6: IndazoleH⁺ and BenzimidazoleH⁺ Supporting Information

Indazole-H⁺ GS
-380.1193565

C	1.553092	1.144910	-0.000234
C	0.206908	0.745011	-0.000129
C	0.223490	-0.674203	0.000106
N	1.527467	-1.060561	0.000133
H	1.936488	-1.984716	0.000272
H	2.011805	2.128000	-0.000411
N	2.301782	0.045423	-0.000073
H	3.312023	-0.028084	-0.000090
C	-1.026979	1.442827	-0.000210
C	-2.175868	0.693614	-0.000053
H	-1.053490	2.530729	-0.000390
C	-2.134568	-0.731116	0.000182
H	-3.145324	1.188581	-0.000107
C	-0.954713	-1.441260	0.000266
H	-3.076748	-1.278243	0.000299
H	-0.937671	-2.528995	0.000447

Indazole-H⁺ L_a, (C₁)
-380.0994622

C	-1.592245	1.145386	0.010624
C	-0.244637	0.755999	0.029750
C	-0.220690	-0.655461	0.024231
N	-1.504125	-1.102129	0.043930
H	-1.806472	-1.970175	-0.384915
H	-2.052048	2.125894	0.021619
N	-2.377417	-0.000124	-0.103465
H	-3.208860	-0.073649	0.483534
C	0.980147	1.434179	-0.012849
C	2.208757	0.686549	-0.004058
H	1.018103	2.521262	-0.081848
C	2.212634	-0.697328	-0.004814
H	3.148152	1.237492	-0.004060
C	0.982189	-1.400272	0.014631
H	3.149077	-1.250035	-0.006581
H	0.965916	-2.489324	0.043912

Indazole-H⁺ L_a, A' (C_s)
-380.1079578

C	-1.876750	-0.593275	0.000000
C	-0.474994	-0.641389	0.000000
C	0.000000	0.695252	-0.000000
N	-1.078432	1.510225	0.000000
H	-1.129896	2.518427	0.000000
H	-2.624001	-1.375967	0.000000
N	-2.235644	0.735870	0.000000
H	-3.146361	1.166796	0.000000
C	0.477540	-1.669877	-0.000000
C	1.881191	-1.345166	-0.000000
H	0.173140	-2.716117	0.000000
C	2.323634	-0.035132	-0.000000
H	2.597043	-2.165837	-0.000000

Chapter 6: IndazoleH⁺ and BenzimidazoleH⁺ Supporting Information

C	1.375709	1.022087	-0.000000
H	3.386268	0.194218	-0.000000
H	1.704355	2.060816	-0.000000

Indazole-H⁺ L_b, A' (C_s)

-380.1132958

C	-1.848502	-0.642669	-0.000000
C	-0.423299	-0.668730	-0.000000
C	0.000000	0.733975	-0.000000
N	-1.139874	1.495517	-0.000000
H	-1.253344	2.498598	-0.000000
H	-2.583545	-1.437088	-0.000000
N	-2.223317	0.663323	-0.000000
H	-3.160240	1.046340	-0.000000
C	0.547262	-1.702580	0.000000
C	1.892542	-1.332494	0.000000
H	0.244857	-2.746891	0.000000
C	2.281547	0.039624	0.000000
H	2.669371	-2.094041	0.000000
C	1.323481	1.103828	0.000000
H	3.341080	0.292849	0.000000
H	1.645973	2.142635	0.000000

Benzimidazole-H⁺ GS

-380.1626172

C	0.000000	0.699560	0.214044
C	-0.000000	-0.699560	0.214044
C	0.000000	-1.439168	-0.969521
C	0.000000	-0.705867	-2.145363
C	0.000000	0.705867	-2.145363
C	0.000000	1.439168	-0.969521
C	0.000000	0.000000	2.325945
H	0.000000	-2.527292	-0.972465
H	0.000000	-1.232732	-3.098119
H	0.000000	1.232732	-3.098119
H	0.000000	2.527292	-0.972465
H	0.000000	2.032229	1.907283
H	0.000000	0.000000	3.409524
H	-0.000000	-2.032229	1.907283
N	0.000000	1.083498	1.555106
N	-0.000000	-1.083498	1.555106

Benzimidazole-H⁺ L_a, (C₁)

-380.133757

C	0.246497	-0.697214	-0.018886
C	0.246506	0.697227	-0.018997
N	1.550723	1.110376	-0.022119
H	1.866883	2.061793	0.091818
H	1.866850	-2.061757	0.092352
H	3.399683	-0.000044	-0.324097
C	-0.960083	-1.410781	-0.003521
C	-2.204681	-0.682895	0.005362

Chapter 6: IndazoleH⁺ and BenzimidazoleH⁺ Supporting Information

H	-0.970720	-2.500490	0.004145
C	-2.204672	0.682897	0.005392
H	-3.137156	-1.243285	0.012788
C	-0.960072	1.410787	-0.003426
H	-3.137142	1.243296	0.012859
H	-0.970720	2.500493	0.004679
N	1.550704	-1.110394	-0.022016
C	2.398560	-0.000002	0.103144

Benzimidazole-H⁺ L_b, A₁ (C_{2v})
-380.1562773

C	0.000000	0.729303	0.219699
C	-0.000000	-0.729303	0.219699
C	0.000000	-1.467781	-0.961086
C	0.000000	-0.714673	-2.157057
C	0.000000	0.714673	-2.157057
C	0.000000	1.467781	-0.961086
C	0.000000	0.000000	2.347573
H	0.000000	-2.554486	-0.967543
H	0.000000	-1.235726	-3.112660
H	0.000000	1.235726	-3.112660
H	0.000000	2.554486	-0.967543
H	0.000000	2.053964	1.892173
H	0.000000	0.000000	3.429300
H	-0.000000	-2.053964	1.892173
N	0.000000	1.104409	1.545903
N	-0.000000	-1.104409	1.545903

Benzimidazole-H⁺ L_a, B₂ (C_{2v})
-380.1459937

C	0.000000	0.699489	0.247178
C	-0.000000	-0.699489	0.247178
C	-0.000000	-1.412133	-0.960349
C	-0.000000	-0.682504	-2.206580
C	0.000000	0.682504	-2.206580
C	0.000000	1.412133	-0.960349
C	0.000000	-0.000000	2.391204
H	-0.000000	-2.501768	-0.971570
H	-0.000000	-1.243635	-3.138571
H	0.000000	1.243635	-3.138571
H	0.000000	2.501768	-0.971570
H	0.000000	2.067421	1.873402
H	0.000000	-0.000000	3.467800
H	-0.000000	-2.067421	1.873402
N	0.000000	1.112486	1.549677
N	-0.000000	-1.112486	1.549677

This page has been intentionally left blank.

CONCLUSION

7. Conclusions

7.1 The Effects of Charge

All the photodissociation action spectra reported in this thesis are summarised in Figure 7.1. Charge can influence photoproperties in many ways typically characterised as through-bond or through-space.

The protomers of nicotine (Chapter 5) are an example how charge can affect photochemistry predominantly *via* through-bond effects. The location of the proton was found to alter the relative yield of the product ions because the dissociation mechanisms are often initiated by proton migration. Also, a significant difference arises due to a transition to an $^1n\pi^*$ state is observed in the spectrum of only the pyrrolidine protonated nicotineH⁺ (see Figure 7.1 and Figures 5.4 and 5.5). The $^1n\pi^*$ state arises from electron density shifting from the lone pair of the pyridine ring onto the pyridine π system. This shift is presented as the difference density in Figure 7.2 IV, where the region of increased electron density in the excited state are shown in orange and regions of reduced electron density in the excited state are shown in purple. The $^1n\pi^*$ state is non-existent for the N-protonated pyridine.

The energies of electronic states measured in this thesis are shown in Table 7.1 in comparison with their neutral analogues. For most of these values, the energy of maximum intensity in the spectra (λ_{max}) were compared. Because quinazolineH⁺, quinazoline, indazole and benzimidazole exhibit vibronic structure, the 0-0 energies were used as a point of comparison. Overall, the charge red-shifts the $\pi\pi^*$ states of irgacure complexes, pyridine protonated nicotineH⁺, 1QZH⁺, 3QZH⁺, benzimidazoleH⁺ and indazoleH⁺ (see Table 7.1). These red-shifts are attributed to the electric field arising from the proton (or charged atom) favourably affecting the re-distribution of electron density. In each case, it is important to consider (1) the polarizability of the excited state and (2) the orientation of the electric field.

The systematic study of irgacure 2959 (Chapter 3) provides an example of how charge can impact photochemistry *via* through-space effects. Charged atoms (H⁺, Li⁺, Na⁺, K⁺) impart electric fields that affect the irgacure chromophore by shifting the transition energies. Figure 7.2 I–III depicts the electron density changes arising from the transitions to these states. The $\pi\pi^*$ transition of the irgacure-M⁺ clusters favourably shift the electron density towards the cation (working favourably with the electric field), whereas the $n\pi^*$ state shifts the electron density away from the cation against the electric field. This manifests in red-shifting the $\pi\pi^*$

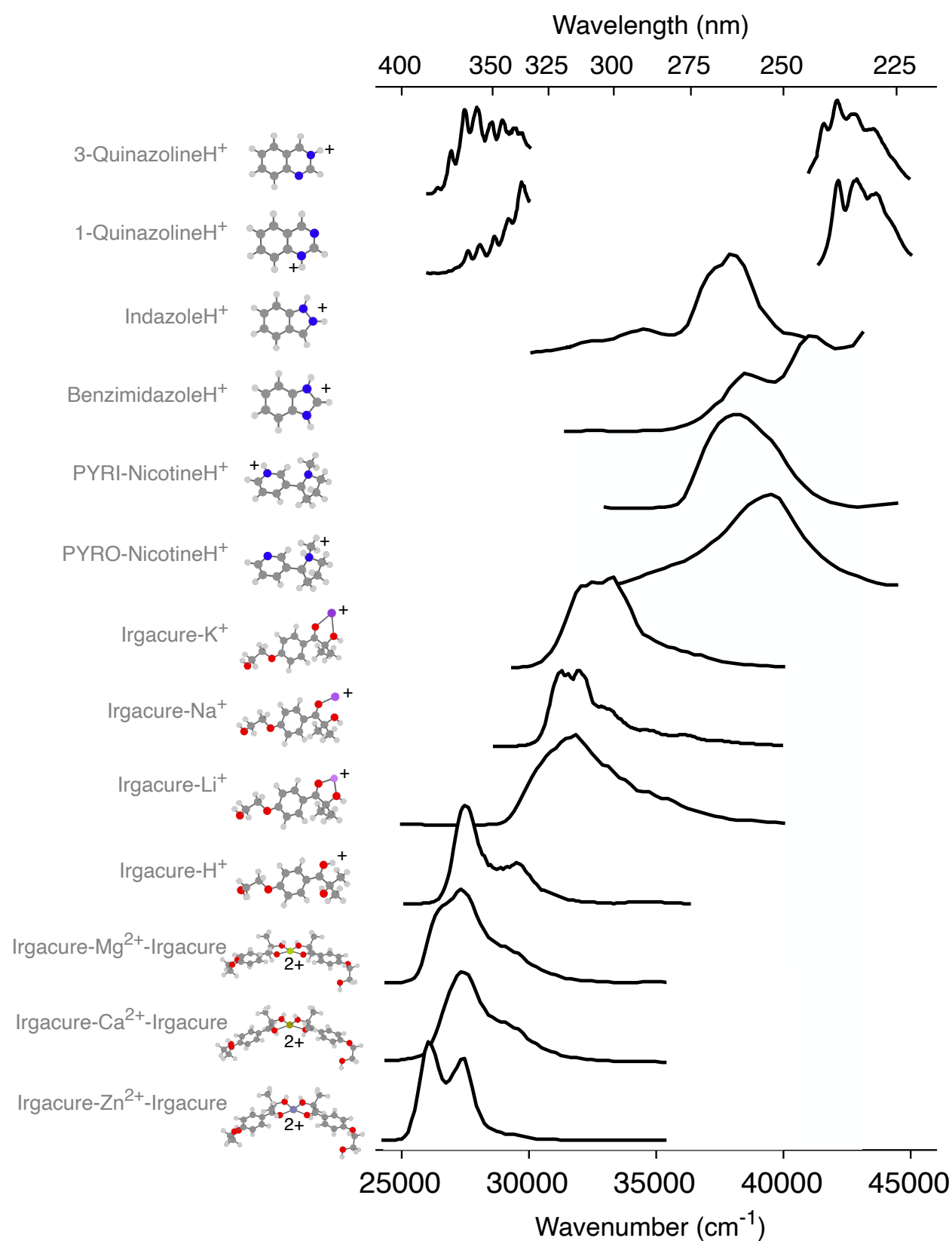


Figure 7.1: Summary of photodissociation action spectra presented in this thesis. From top to bottom: 3-quinazolineH⁺, 1-quinazolineH⁺, indazoleH⁺, benzimidazoleH⁺, PYRI-nicotineH⁺, PYRO-nicotineH⁺, irgacure-K⁺, irgacure-Na⁺, irgacure-Li⁺, irgacure-H⁺, irgacure-Mg²⁺-irgacure, irgacure-Ca²⁺-irgacure, and irgacure-Zn²⁺-irgacure.

state and blue-shifting the $n\pi^*$ state with increasing electric field strength. The red-shift of the $\pi\pi^*$ state is enhanced by the state's polarizability. These shifts are electrostatic and are examples of through space effects.

If electric fields are to be used to optimise photochemical outcomes, the orientation of this field (relative to the chromophore) must be controlled. This was achieved for Irgacure 2959 because the cation binds favourably between the ketone and hydroxide oxygens so that the electric field orientation is locked-in for each metal cation. The desired photochemical outcome for Irgacure is an increase in the yield of the radical photoproducts (formed by α -cleavage), which requires all the participating electronic quantum states to shift harmoniously due to the charges electric field. When the electric field is oriented as depicted in Figure 7.2, the $n\pi^*$ states blue-shifts and the $\pi\pi^*$ states red-shifts so that the dissociative $^3n\pi^*$ state is accessible, thereby each state shifts in the desired direction. This is only possible because of appropriately orientated electric field.

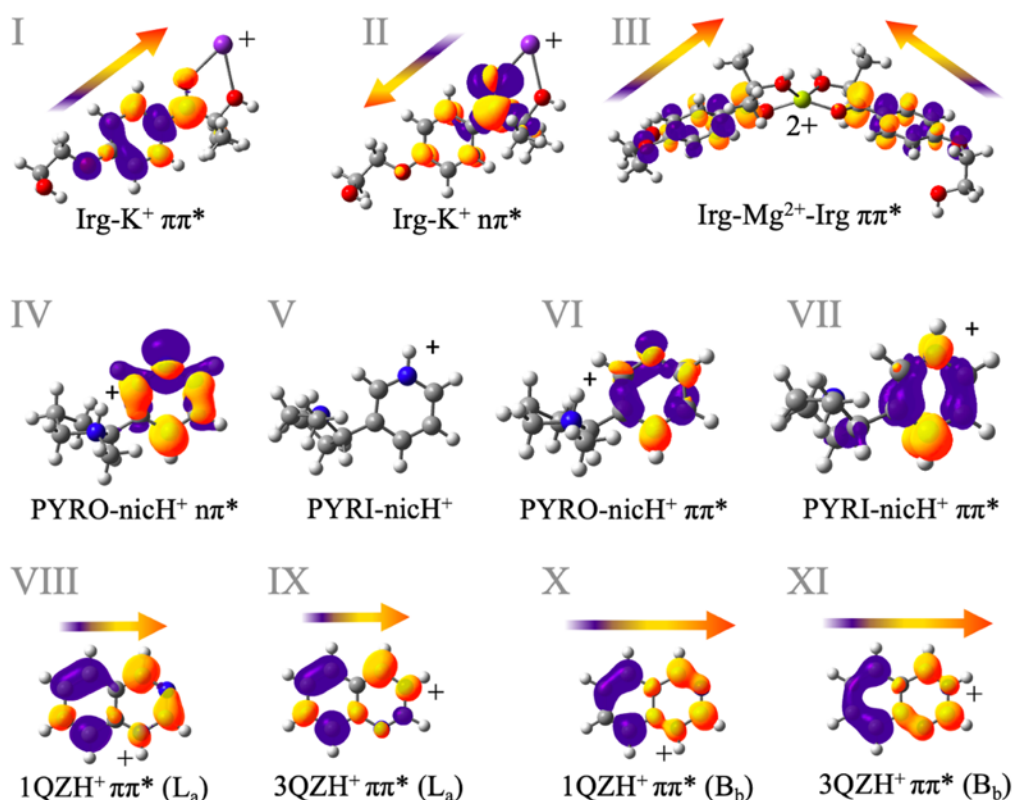


Figure 7.2: Differences in electron density in the ground state and excited state. Purple regions indicate decreased electron density in the excited state and orange regions indicate increased electron density in the excited state. Arrows emphasise the net direction of electron density transfer between the ground and excited state. Calculations employed the SCS-CC2/def2-SVP method.

For quinazolineH⁺ (Chapter 4), it was demonstrated that the two protomers can be selected using the FAIMS ion mobility technique and probed individually (see Figures 4.1 and 4.2). Therefore, serving as a model system to probe the effects of charge location and electronic field orientation. QuinazolineH⁺ protomers are especially good model systems for investigating the effects of electric field orientation because (1) both quinazolineH⁺ protomers have the same *type* of nitrogen protonation site, (2) the protonation sites for quinazolineH⁺ create electric fields that nicely align with either the long axis and short axis of the molecule (see Figure 7.3), and (3) quinazolineH⁺ is a small enough molecule that high level quantum chemical calculations are practical for rationalising experimental results.

Table 7.1: Summary table of neutral and cationic ions spectroscopically probed in this thesis.

Ion	Neutral (cm ⁻¹)	Cation (cm ⁻¹)	Red-Shift (cm ⁻¹)	Neutral Value and Character	Cation Value and Character
PYRI-NicotineH ⁺	38462 ¹⁻³	38100	362	λ_{\max} (¹ $\pi\pi^*$)	λ_{\max} (¹ $\pi\pi^*$)
PYRO-NicotineH ⁺		39500	-1038	λ_{\max} (¹ $\pi\pi^*$)	λ_{\max} (¹ $\pi\pi^*$)
1QZH ⁺	32000 ⁴	29700	2300	0-0 (¹ L _a)	0-0 (¹ L _a)
3QZH ⁺		28000	4000	0-0 (¹ L _a)	0-0 (¹ L _a)
IndazoleH ⁺	34473 ^{5, 6}	31250	3223	0-0 (L _b)	Onset (L _a)
BenzimidazoleH ⁺	36023 ^{7, 8}	35714	309	0-0 (L _b)	Onset (L _b)
Irgacure-H ⁺	36630 ^{9, 10}	27500	9130	λ_{\max} (¹ $\pi\pi^*$)	λ_{\max} (¹ $\pi\pi^*$)
Irgacure-Li ⁺		32000	4630	λ_{\max} (¹ $\pi\pi^*$)	λ_{\max} (¹ $\pi\pi^*$)
Irgacure-Na ⁺		32000	4630	λ_{\max} (¹ $\pi\pi^*$)	λ_{\max} (¹ $\pi\pi^*$)
Irgacure-K ⁺		33300	3330	λ_{\max} (¹ $\pi\pi^*$)	λ_{\max} (¹ $\pi\pi^*$)
Irg-Mg ²⁺ -Irg		27300	9330	λ_{\max} (¹ $\pi\pi^*$)	λ_{\max} (¹ $\pi\pi^*$)
Irg-Zn ²⁺ -Irg		26000	10630	λ_{\max} (¹ $\pi\pi^*$)	λ_{\max} (¹ $\pi\pi^*$)
Irg-Ca ²⁺ -Irg		27300	9330	λ_{\max} (¹ $\pi\pi^*$)	λ_{\max} (¹ $\pi\pi^*$)

In Chapter 6, pump-probe photodissociation of indazoleH⁺ revealed a facile excited state deactivation pathway *via* an $\pi\sigma^*$ state that is dissociative with respect to the N-N bond. In fact, the $\pi\sigma^*$ state transfers electron density towards the positive charge, which may make this state more favourable for protonated N-N bonds than neutral N-N bonds. By breaking the N-N bond the molecule can cross from the $\pi\sigma^*$ state back to the ground state.

The extent to which charge and charge location changes the photoproperties of an ion can vary. For quinazoline, the difference between protomers (*i.e.* charge location) is subtle. The 0-0

transition energies differ by less than 0.1 eV (see Figure 4.3) and the photoproducts are the same for both protomers. For Irgacure, the effect of charge is everything, the $^1\pi\pi^*$ states observed in the spectra shift by over 1 eV relative to the neutral form (see Figure 3.6) and the excited state mechanism that leads to radical photoproducts can be either enhanced or essentially switched off (see Table 3.3). For nicotineH⁺ it is somewhere in-between. Ultimately, the effect of charge is still not predictable, and to characterise these effects for other systems, further experiments and calculations are required.

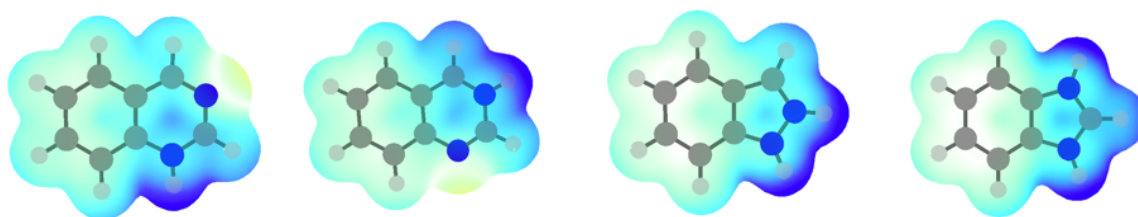


Figure 7.3: Electrostatic potential surfaces for 1QZH⁺, 3QZH⁺, benzimidazoleH⁺ and indazoleH⁺ calculated using ω B97X-D/def2-TZVP, with an iso-value of 0.004 and a range of 0.0 (red) to 0.25 (blue), where darker blue indicates regions of greater positive potential.

7.2 Experimental Results and Quantum Chemical Calculations

The experimental measurements reported in this thesis provide values to compare with computational results (obtained using CC2 and TDDFT). Fifteen $\pi\pi^*$ states from eleven ions different were measured. These feature a diverse range of atoms (H, C, N, O, Li, Na, Mg and Zn). Experimental values—taken from the maximum point in the experimental spectra (λ_{\max})—are compared to TDDFT and SCS-CC2 vertical transition energies. This is because these two properties (vertical transition energies and λ_{\max}) are straightforward to calculate and to extract from experimental data. Even though experimental maxima are often used in comparison with vertical transition energies, the vertical transition energy is not well defined experimentally. Nevertheless, comparison between λ_{\max} and the vertical transition energies identifies some trends. Plotted as green in Figure 7.4 is a comparison between experiment and TDDFT calculations, employing the triple ζ def2-TZVP basis set and the ω B97X-D functional. The blue data compares experiment and the second-order coupled cluster method with spin component scaling (SCS-CC2) and employing the def2-SVP basis set. A comparison between ω B97X-D and SCS-CC2 is shown in purple. Each plot also contains a linear function that has a gradient set to one and a fitted y-axis offset (solid line).

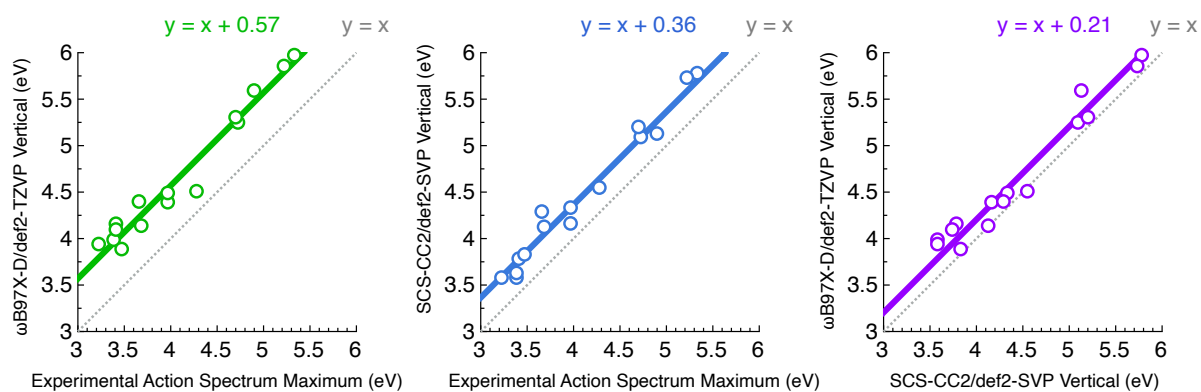


Figure 7.4: Comparisons between ω B97X-D and experiment (green), SCS-CC2 and experiment (blue) and ω B97X-D and SCS-CC2 (purple). The data are presented with a $y = x$ function as a guide for where the data points would lie if there was perfect agreement (grey dotted line). Additionally, the data points are fit with a linear function that has gradient = 1 and a y offset (solid lines).

The results show that ω B97X-D overestimates the experimental maxima by 0.57 eV, SCS-CC2 overestimates the experimental maxima by 0.36 eV. ω B97X-D values are 0.21 eV higher than SCS-CC2. SCS-CC2 is more expensive but generally more accurate than ω B97X-D, and the results in Figure 7.4 reproduce this—even with the smaller basis set for SCS-CC2.

Arguably the most striking results from Figure 7.4 is that both calculated values with ω B97X-D and SCS-CC2 systematically over-estimate the experimental values. The tendency for TDDFT to overestimate excitation energies by 0.5 eV is well known.¹¹⁻¹³ A similar result was observed for Xanthene ions, with TDDFT overestimating the experimental values by *ca.* 0.5 eV and CC2 overestimating by *ca.* 0.3 eV.¹¹ For TDDFT the calculated energies are \sim 0.21 eV above those calculated with SCS-CC2, which further emphasises that TDDFT is overestimating the vertical transition energies of these ions (whether the correct vertical transition energy is closer to the λ_{max} value or to the SCS-CC2 value). These results show that—at least for this reasonably diverse range of aromatic ion $^1\pi\pi^*$ transitions—one can expect TDDFT vertical transition energies to lie approximately 0.57 eV higher in energy than the maximum of the spectrum.

7.3 Implications and Future Directions

The results of this thesis are important because they include the separation of isomers (nicotineH⁺, quinazolineH⁺, and benzimidazoleH⁺ and indazoleH⁺). Distinguishing between isomers is a major bottleneck in metabolomics,¹² lipidomics,¹³ and mass spectrometry imaging.¹⁴ PD action spectroscopy and FAIMS coupled with PD action spectroscopy are useful

methods for distinguishing isomers and this is likely to widen in scope. The fact that different protomers are formed from different ESI solvents is of particular concern for liquid chromatography, which often employs solvent gradients that change over the course of an experiment. Therefore, being aware of the differences between protomers is important for their appropriate analytical detection.

Results for irgacure complexes illustrate how electronic quantum states can be experimentally controlled using internal electric fields to optimise a desired photochemical reaction. The scope of molecular photochemical reactions that could be potentially controlled using electric fields is exciting, as it is straightforward to extend the gas-phase cation binding method (used for irgacure 2959) to other molecules. New targets include the Norrish type-II photo-initiator thioxanthone, and the fundamental acetophenone photo-initiator chromophore (structures shown in Figure 7.5). In fact, acetophenone photochemistry has been recently affected electrostatically by cation binding in the solution-phase.¹⁵ Similar solution-phase experiments on acetophenone derivatives employed Lewis acids to tune photochemistry.¹⁶

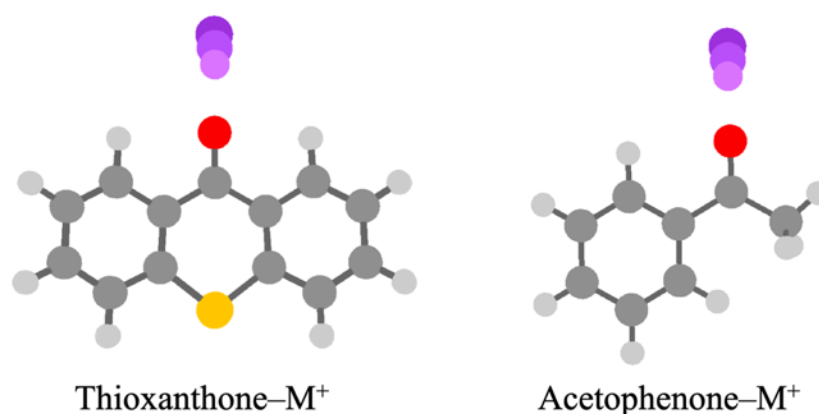


Figure 7.5: Structures of thioxanthone-M⁺ and acetophenone-M⁺.

The pump probe photodissociation experimental setup used here for indazoleH⁺ and benzimidazoleH⁺ can be applied to other ions, including those studied here. Thereby, the effects of charge on excited state dynamics and deactivation mechanisms can be investigated in detail. For irgacure, acetophenone and thioxanthone clusters (Figure 7.5), the excited state lifetimes of different clusters could be measured to see how α -cleavage rates and inter-system crossing rates are connected to the changing energies of the different electronic quantum states under different electric field strengths. Additional ions that could be targeted using pump-probe

photodissociation include MTT, protonated phenylpyrazole, protonated azaindazoles, and protonated allopurinol (Figure 7.6). These molecules all have N-N bonds in various forms. Investigating these ions could determine the generality of the non-radiative deactivation pathway that elongates the N-N bond *via* an unbound $\pi\sigma^*$ state.

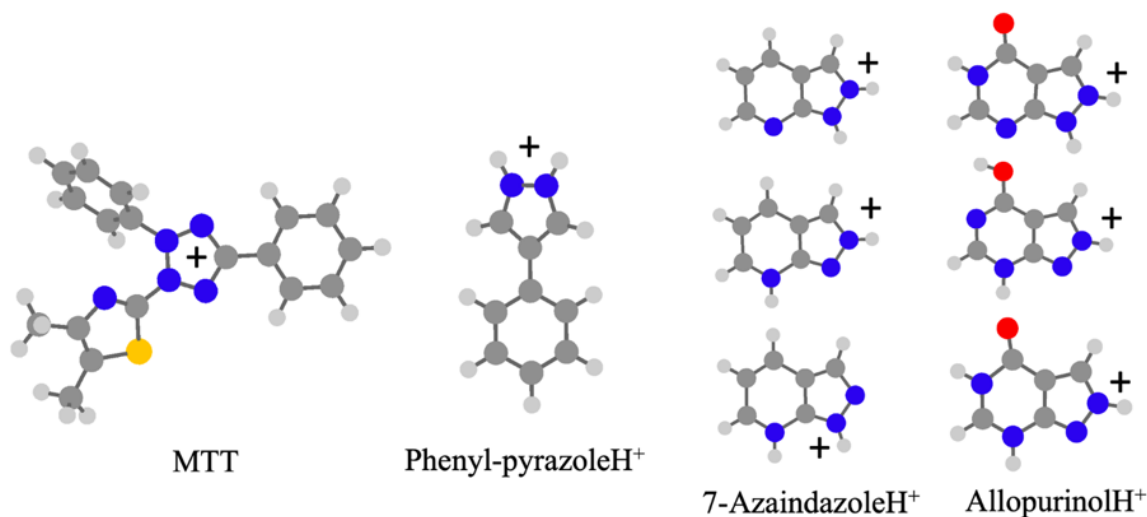


Figure 7.6: Structures of MTT, protonated phenyl-pyrazole, protonated 7-azaindazole protomers and some allopurinol protomers.

Combinations of ion-mobility and pump-probe PD is not yet reported and as such, there is new science to be explored with this combination. The isomer selectivity that ion-mobility afforded to PD action spectroscopy could be extended to pump-probe PD. It is straightforward to extend the experimental setups reported in this thesis to combine FAIMS with pump-probe PD arrangements. These experiments could target protomers of aza-indazoles or protomers of allopurinol to assess if protonation site can affect the N-N bond breaking deactivation pathway; photobiologically relevant flavin isomers are also promising targets; and a huge variety of other isomeric ions. For quinazolineH⁺, it would be possible to separate the two protomers with FAIMS and then analyse them with pump-probe, giving an insight into the different electrostatic effects from charge location on excited state deactivation.

Future work could also target how electrostatic effects from different charge locations can affect ground state chemical reactivity. For example, after separation of quinazoline protomers, will they react with different rates? It is possible to generate distonic radical ions of the two quinazoline protomers (see Figure 7.7) separated using FAIMS. These experiments would have control over the charge location. By observing the reaction kinetics of these distonic radical

protomers in an ion trap, the effects of charge location and through-space electrostatic effects on ground state reactivity would be assessed.

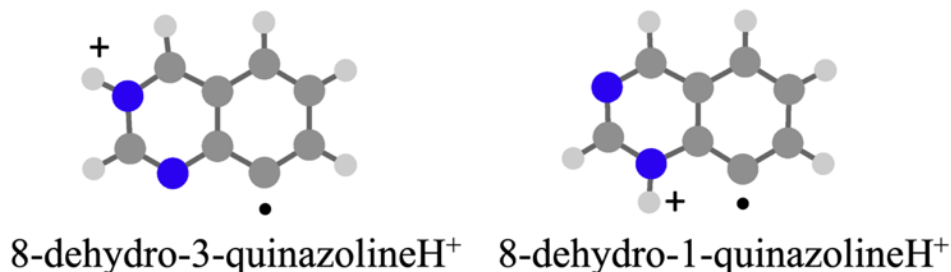


Figure 7.7: Structures of distonic radical ion protomers of protonated dehydro-quinazoline.

Therefore, for all ions investigated here it was helpful to consider the electric field generated from the charge and its push (or pull) on the movement of electron density from the ground state to the excited state. Important factors for these electrostatic shifts are (1) alignment of the electric field, (2) polarizability of the excited state and (3) electric field strength. Through-space and through-bond effects could continue to be useful conceptual tools for conceptualising how charge and charge location affect photochemistry. These effects from charge and charge location can be effectively controlled and probed using combined mass spectrometry, ion-mobility and UV photodissociation techniques.

References

1. Swain, M. L.; Eisner, A.; Woodward, C.; Brice, B., Ultraviolet absorption spectra of nicotine, nornicotine and some of their derivatives. *Journal of the American Chemical Society* **1949**, *71* (4), 1341-1345.
2. Clayton, P. M.; Vas, C. A.; Bui, T. T.; Drake, A. F.; McAdam, K., Spectroscopic investigations into the acid-base properties of nicotine at different temperatures. *Analytical Methods* **2013**, *5* (1), 81-88.
3. Clayton, P. M.; Vas, C. A.; Bui, T. T.; Drake, A. F.; McAdam, K., Spectroscopic studies on nicotine and nornicotine in the UV region. *Chirality* **2013**, *25* (5), 288-293.
4. Hasegawa, Y.; Amako, Y.; Azumi, H., The Ultraviolet Absorption Spectrum of Quinazoline Vapor Due to the n- π^* Transition. *Bulletin of the Chemical Society of Japan* **1968**, *41* (11), 2608-2611.
5. Byrne, J. P.; Ross, I., Electronic relaxation as a cause of diffuseness in electronic spectra. *Australian Journal of Chemistry* **1971**, *24* (6), 1107-1141.

6. Berden, G.; Meerts, W. L.; Jalviste, E., Rotationally resolved ultraviolet spectroscopy of indole, indazole, and benzimidazole: Inertial axis reorientation in the $S_1(1L_b) \leftarrow S_0$ transitions. *The Journal of Chemical Physics* **1995**, *103* (22), 9596-9606.
7. Gordon, R.; Yang, R. F., Vapor absorption spectra of benzoxazole, benzimidazole, and benzothiazole near 2850 Å. *Canadian Journal of Chemistry* **1970**, *48* (11), 1722-1729.
8. Jalviste, E.; Treshchalov, A., Spectroscopy of jet-cooled benzimidazole and benzotriazole. *Chemical Physics* **1993**, *172* (2-3), 325-338.
9. Jockusch, S.; Landis, M. S.; Freiermuth, B.; Turro, N. J., Photochemistry and photophysics of α -hydroxy ketones. *Macromolecules* **2001**, *34* (6), 1619-1626.
10. Liu, M.; Li, M.-D.; Xue, J.; Phillips, D. L., Time-resolved spectroscopic and density functional theory study of the photochemistry of irgacure-2959 in an aqueous solution. *The Journal of Physical Chemistry A* **2014**, *118* (38), 8701-8707.
11. Kulesza, A. J.; Titov, E.; Daly, S.; Włodarczyk, R.; Megow, J.; Saalfrank, P.; Choi, C. M.; MacAleese, L.; Antoine, R.; Dugourd, P., Excited States of Xanthene Analogues: Photofragmentation and Calculations by CC2 and Time-Dependent Density Functional Theory. *ChemPhysChem* **2016**, *17* (19), 3129-3138.
12. Uppal, K.; Walker, D. I.; Liu, K.; Li, S.; Go, Y.-M.; Jones, D. P., Computational metabolomics: a framework for the million metabolome. *Chemical Research in Toxicology* **2016**, *29* (12), 1956-1975.
13. Blanksby, S. J.; Mitchell, T. W., Advances in mass spectrometry for lipidomics. *Annual Review of Analytical Chemistry* **2010**, *3*, 433-465.
14. Paine, M. R.; Poad, B. L.; Eijkel, G. B.; Marshall, D. L.; Blanksby, S. J.; Heeren, R. M.; Ellis, S. R., Mass spectrometry imaging with isomeric resolution enabled by ozone-induced dissociation. *Angewandte Chemie International Edition* **2018**, *57* (33), 10530-10534.
15. Robertson, P. A.; Bishop, H. M.; Orr-Ewing, A. J., Tuning the Excited-State Dynamics of Acetophenone Using Metal Ions in Solution. *The Journal of Physical Chemistry Letters* **2021**, *12*, 5473-5478.
16. Noble, B. B.; Mater, A. C.; Smith, L. M.; Coote, M. L., The effects of Lewis acid complexation on type I radical photoinitiators and implications for pulsed laser polymerization. *Polymer Chemistry* **2016**, *7* (41), 6400-6412.